

Development of a Structural Health Monitoring System to Evaluate Structural Capacity and Estimate Remaining Service Life for Bridges

**Final Report
January 2020**



IOWA STATE UNIVERSITY
Institute for Transportation

Sponsored by
Iowa Department of Transportation
(InTrans Project 10-367)
Federal Highway Administration
Transportation Pooled Fund TPF-5(219)

About the Bridge Engineering Center

The mission of the Bridge Engineering Center (BEC) is to conduct research on bridge technologies to help bridge designers/owners design, build, and maintain long-lasting bridges.

About the Institute for Transportation

The mission of the Institute for Transportation (InTrans) at Iowa State University is to develop and implement innovative methods, materials, and technologies for improving transportation efficiency, safety, reliability, and sustainability while improving the learning environment of students, faculty, and staff in transportation-related fields.

Iowa State University Nondiscrimination Statement

Iowa State University does not discriminate on the basis of race, color, age, ethnicity, religion, national origin, pregnancy, sexual orientation, gender identity, genetic information, sex, marital status, disability, or status as a US veteran. Inquiries regarding nondiscrimination policies may be directed to the Office of Equal Opportunity, 3410 Beardshear Hall, 515 Morrill Road, Ames, Iowa 50011, telephone: 515-294-7612, hotline: 515-294-1222, email: eooffice@iastate.edu.

Disclaimer Notice

The contents of this report reflect the views of the authors, who are responsible for the facts and the accuracy of the information presented herein. The opinions, findings and conclusions expressed in this publication are those of the authors and not necessarily those of the sponsors.

The sponsors assume no liability for the contents or use of the information contained in this document. This report does not constitute a standard, specification, or regulation.

The sponsors do not endorse products or manufacturers. Trademarks or manufacturers' names appear in this report only because they are considered essential to the objective of the document.

Quality Assurance Statement

The Federal Highway Administration (FHWA) provides high-quality information to serve Government, industry, and the public in a manner that promotes public understanding. Standards and policies are used to ensure and maximize the quality, objectivity, utility, and integrity of its information. The FHWA periodically reviews quality issues and adjusts its programs and processes to ensure continuous quality improvement.

Iowa DOT Statements

Federal and state laws prohibit employment and/or public accommodation discrimination on the basis of age, color, creed, disability, gender identity, national origin, pregnancy, race, religion, sex, sexual orientation or veteran's status. If you believe you have been discriminated against, please contact the Iowa Civil Rights Commission at 800-457-4416 or the Iowa Department of Transportation affirmative action officer. If you need accommodations because of a disability to access the Iowa Department of Transportation's services, contact the agency's affirmative action officer at 800-262-0003.

The preparation of this report was financed in part through funds provided by the Iowa Department of Transportation through its "Second Revised Agreement for the Management of Research Conducted by Iowa State University for the Iowa Department of Transportation" and its amendments.

The opinions, findings, and conclusions expressed in this publication are those of the authors and not necessarily those of the Iowa Department of Transportation or the U.S. Department of Transportation Federal Highway Administration.

Technical Report Documentation Page

1. Report No. InTrans Project 10-367	2. Government Accession No.	3. Recipient's Catalog No.	
4. Title and Subtitle Development of a Structural Health Monitoring System to Evaluate Structural Capacity and Estimate Remaining Service Life for Bridges		5. Report Date January 2020	
		6. Performing Organization Code	
7. Author(s) Brent Phares (orcid.org/0000-0001-5894-4774), Sameera Jayathilaka (orcid.org/0000-0002-6417-1154), Yaohua "Jimmy" Deng (orcid.org/0000-0003-0779-6112), Lowell Greimann (orcid.org/0000-0003-2488-6865), and Terry Wipf (orcid.org/0000-0002-1093-0549)		8. Performing Organization Report No. InTrans Project 10-367	
9. Performing Organization Name and Address Bridge Engineering Center Iowa State University 2711 South Loop Drive, Suite 4700 Ames, IA 50010-8664		10. Work Unit No. (TRAIS)	
		11. Contract or Grant No.	
12. Sponsoring Organization Name and Address Iowa Department of Transportation Federal Highway Administration 800 Lincoln Way 1200 New Jersey Avenue, SE Ames, IA 50010 Washington, DC 20590		13. Type of Report and Period Covered Final Report	
		14. Sponsoring Agency Code TPF-5(219)	
15. Supplementary Notes Visit https://intrans.iastate.edu/ for color pdfs of this and other research reports.			
16. Abstract <p>Bridges constitute the most expensive assets, by mile, for transportation agencies around the US and the world. Most of the bridges in the US were constructed between the 1950s and the 1970s. Consequently, an increasing number of bridges are getting old and requiring much more frequent inspections, repairs, or rehabilitations to keep them safe and functional. However, due to constrained construction and maintenance budgets, bridge owners are faced with the difficult task of balancing the condition of their bridges with the cost of maintaining them.</p> <p>Bridge maintenance strategies depend upon information used to estimate future condition and remaining life of bridges. The desire of many departments of transportation (DOTs) is to augment their existing inspection process and maintenance system with a system that can objectively and more accurately quantify the state of bridge health in terms of condition and performance, aid in inspection and maintenance activities, and estimate the remaining life of their bridge inventory in real time. To better manage bridge inventories, tools that can accurately predict the future condition of a bridge, as well as its remaining life, are required.</p> <p>One of the key requirements for an effective infrastructure management system is the establishment of a structural health monitoring (SHM) system. An SHM system traditionally consists of a network of monitoring sensors, data acquisition, and communication hardware and software capable of carrying out bridge condition assessments in real-time and accurately and objectively predicting the health of the infrastructure components and systems.</p> <p>For this project, the research team developed an automated SHM system that could detect bridge damage and estimate load ratings of bridges, as well as models to develop predictions for future condition ratings of bridges. The SHM system and models were then used to develop a bridge maintenance prioritization system for DOTs to augment current bridge management practices.</p>			
17. Key Words bridge condition ratings—condition-based maintenance—load rating factor—SHM-CBM—SHM system—structural health monitoring—truck detection approach		18. Distribution Statement No restrictions.	
19. Security Classification (of this report) Unclassified.	20. Security Classification (of this page) Unclassified.	21. No. of Pages 300	22. Price NA

DEVELOPMENT OF A STRUCTURAL HEALTH MONITORING SYSTEM TO EVALUATE STRUCTURAL CAPACITY AND ESTIMATE REMAINING SERVICE LIFE FOR BRIDGES

**Final Report
January 2020**

Principal Investigator

Brent Phares, Research Associate Professor
Bridge Engineering Center, Iowa State University

Research Assistant

Sameera Jayathilaka

Authors

Brent Phares, Sameera Jayathilaka, Yaohua “Jimmy” Deng,
Lowell Greimann, and Terry Wipf

Sponsored by

Iowa Department of Transportation and FHWA
Pooled Fund Study TPF-5(219): Iowa (lead state), California, Illinois, and Wisconsin

Preparation of this report was financed in part
through funds provided by the Iowa Department of Transportation
through its Research Management Agreement with the
Institute for Transportation
(InTrans Project 10-367)

**A report from
Bridge Engineering Center
Iowa State University**

2711 South Loop Drive, Suite 4700
Ames, IA 50010-8664
Phone: 515-294-8103 / Fax: 515-294-0467
<https://intrans.iastate.edu/>

TABLE OF CONTENTS

ACKNOWLEDGMENTS	XVII
EXECUTIVE SUMMARY	XIX
Objectives	xix
Background.....	xix
Problem Statement.....	xix
Project Description	xix
Key Findings.....	xx
Implementation Readiness and Benefits.....	xxi
CHAPTER 1. INTRODUCTION.....	1
1.1. Background.....	1
1.1.1. Bridge Management Systems	1
1.1.2. Structural Health Monitoring.....	2
1.1.3. Bridge Maintenance Prioritization Strategies	3
1.1.3.1. State of the Practice of Bridge Maintenance Prioritization	3
1.1.3.2. Condition-Based Maintenance Approach.....	4
1.1.4. Financial Justification of SHM Instrumentation.....	4
1.2. Objectives	4
1.3. Report Organization.....	5
CHAPTER 2. LITERATURE REVIEW.....	6
2.1. Pavement Management Systems	6
2.2. Aerospace and Other Vehicle Management Systems.....	6
2.3. Tall Building Management Systems.....	7
2.4. Bridge Management Systems	7
2.4.1. Current Bridge Management Systems	7
2.4.2. Implementation of an SHM System in the BMS	9
2.4.3. Current Bridge Management System of the Iowa DOT	9
2.4.4. SHM Framework for the Iowa DOT.....	10
CHAPTER 3. BRIDGE ENGINEERING CONDITION ASSESSMENT SYSTEM	11
3.1. Introduction to the SHM System, BECAS	11
3.1.1. Bridge Description	12
3.1.2. Bridge Instrumentation	13

3.2. BECAS Software Architecture	14
3.2.1. BECAS Merge	15
3.2.2. BECAS Distributor	15
3.2.3. BECAS Processing Engine	16
3.2.4. BECAS Damage Detection.....	17
3.2.5. BECAS Training.....	17
3.2.6. BECAS Load Rating.....	18
CHAPTER 4. TRUCK DETECTION METHODOLOGY OF SHM SYSTEM	19
4.1. Introduction.....	19
4.2. Truck Detection Methodology.....	19
4.2.1. Single-Truck Event Detection Using Strain Rate Response.....	19
4.2.2. Procedure of Truck Event and Lane Detection.....	21
4.2.3. Truck Axle Detection.....	25
4.2.4. Data Zeroing and Filtering.....	26
4.3. Validation of Truck Detection Approach	29
4.4. Summary and Conclusions	33
CHAPTER 5. STRAIN-BASED BRIDGE DAMAGE DETECTION	34
5.1. Introduction.....	34
5.1.1. Background.....	34
5.2. Literature Review of Damage Detection Methods	35
5.3. Strain-Based Data for Identifying Damage	36
5.3.1. Strain Data Identification.....	36
5.3.2. Truck Parameter Identification	37
5.3.3. Cross Prediction Method.....	37
5.3.4. Experimental Validation.....	39
5.3.5. Orthogonal Regression and Statistical Evolution Approach	40
5.3.6. Damage Detection Approach with F-Test	41
5.3.7. F-Test Control Chart Method.....	44
5.4. Demonstration Bridge on I-80 in Iowa.....	45
5.4.1. Sensor Installation.....	47
5.4.2. Damage Simulation – Level 1 and Level 2.....	48
5.5. Potential Evolution of Damage Detection Approach	49

5.5.1. Influence of Temperature.....	49
5.5.2. Influence of Truck Configuration	53
5.5.3. F-Limit	59
5.5.4. Six Sigma Method.....	59
5.5.5. Base Data Method.....	61
5.5.6. Training Data Method.....	63
5.6. Applications of Data to Evaluate Potential Damage	64
5.6.1. 10°F Temperature Bins and All Five-Axle Trucks.....	65
5.6.1.1. Damage Level 1	65
5.6.1.2. Damage Level 2	70
5.6.2. 2°F Temperature Bins and All Five-Axle Trucks.....	75
5.6.2.1. Damage Level 1	75
5.6.2.2. Damage Level 2	80
5.6.3. 10°F Temperature Bins and Semi-Trucks.....	85
5.6.3.1. Damage Level 1	85
5.6.3.2. Damage Level 2	90
5.6.4. 2°F Temperature Bins and Semi-Trucks	95
5.6.4.1. Damage Level 1	95
5.6.5. Recommendations.....	100
5.6.5.1. 5°F Temperature Bin and All Five-Axle Trucks	100
5.7. Summary and Conclusions	107
CHAPTER 6. LOAD RATING FACTOR DETERMINATION USING AMBIENT	
TRAFFIC	109
6.1. Automated Ambient Traffic Approach.....	109
6.1.1. Bridge Model Calibration and Load Rating.....	109
6.1.2. Process Automation	111
6.1.3. Sampling Strategies	112
6.2. FE Modeling of a Demonstration I-80 Bridge.....	118
6.3. Load Rating Using Traditional Known Truck Approach	123
6.4. Load Rating Using Automated Ambient Traffic Approach	130
6.5. Summary and Conclusions	137
CHAPTER 7. IMPROVED LOAD RATING FACTOR THROUGH BETTER	
CAPACITY ESTIMATION	139

7.1. Overview.....	139
7.1.1. Load Rating Using BECAS SHM System.....	139
7.1.2. Objective.....	142
7.2. Methodology.....	142
7.2.1. Hypothesis.....	142
7.2.2. Monte Carlo Simulation.....	144
7.3. Experimental Program	147
7.3.1. Layout	147
7.3.2. Section Dimensions	149
7.3.3. Material Properties.....	150
7.3.4. Experimental Setup and Instrumentation Plan.....	154
7.4. Moment of Inertia of a Composite Section.....	160
7.4.1. Based on Strength of Materials.....	160
7.4.2. Using Nominal Material Properties	162
7.4.3. Using Measured Material Properties	162
7.4.4. Based on Experimental Results	162
7.5. Flexural Strength of a Composite Section	166
7.5.1. Based on Strength of Materials.....	166
7.5.2. Using Nominal Material Properties	168
7.5.3. Using Measured Material Properties	169
7.5.4. Based on Experimental Results	169
7.6. Validation of the Proposed Method.....	177
7.6.1. Relationship between Capacity and Moment of Inertia.....	177
7.6.2. Improved Load Rating Factor Calculation	178
7.7. Summary and Conclusions	180
7.7.1. Summary.....	180
7.7.2. Conclusions.....	182
CHAPTER 8. PREDICTION OF FUTURE BRIDGE CONDITION RATINGS	183
8.1. Introduction.....	183
8.2. Historical Behavior of Bridges in the US	186
8.2.1. National Bridge Inventory Database.....	186
8.2.2. Historical Bridge Condition Statistics, Iowa and Wisconsin.....	187

8.3. Objective.....	196
8.4. Methodology.....	196
8.4.1. Current Practice Model.....	196
8.4.2. Deterioration Prediction Model.....	201
8.4.3. Probability Theory.....	201
8.4.4. Sojourn Time.....	202
8.4.5. Sojourn Time Database and Characteristics.....	205
8.4.6. Transition Probabilities of Condition Ratings.....	212
8.4.7. Sample Size.....	214
8.4.8. Filtering Methods.....	214
8.5. Validation of Current Practice Model.....	217
8.5.1. Overview of CPM Predictions.....	217
8.5.2. Hindcasting of CPM.....	218
8.5.3. Example Validations of CPM.....	221
8.6. Validation of Deterioration Prediction Model.....	227
8.6.1. Overview of DPM Prediction.....	227
8.6.2. Hindcasting of DPM.....	227
8.6.3. Example Validations of DPM.....	230
8.7. Summary and Conclusion.....	236
8.7.1. Summary.....	236
8.7.2. Conclusions.....	237
CHAPTER 9. SHM-FACILITATED CONDITION-BASED MAINTENANCE PRIORITIZATION SYSTEM.....	238
9.1. Inventory Index.....	238
9.2. SHM Modifier.....	239
9.2.1. Parameters and Weighting Factors Used in the SHMM Calculation.....	240
9.2.1.1. SHMM Parameters F_1 to F_7	240
9.2.1.2. Use of the Weighting Factors γ_1 to γ_7	242
9.2.2. Use of the SHMM Calculation.....	242
9.3. Demonstration Application.....	243
CHAPTER 10. SUMMARY, CONCLUSIONS, AND RECOMMENDATIONS.....	247
10.1. Summary.....	247
10.2. Conclusions.....	248

10.3. Recommendations.....	248
REFERENCES	249
APPENDIX A. DEMONSTRATION OF AUTOMATED SHM SYSTEM FOR BRIDGES....	255
A.1. Demonstration Bridge 1	255
A.1.1. Overall Bridge Description	255
A.1.2. Instrumentation Plan—I-80 Bridge.....	255
A.1.3. Observation Summary of the SHM System.....	256
A.1.3.1. Usage.....	256
A.1.3.2. Load Rating.....	260
A.1.3.3. Behavior Change.....	261
A.2. Demonstration Bridge 2.....	262
A.2.1. Overall Bridge Description	262
A.2.2. Instrumentation Plan—I-280 Bridge.....	263
A.2.3. Observation Summary of the SHM System.....	263
A.2.3.1. Usage.....	263
A.2.3.2. Load Rating.....	267
A.2.3.3. Behavior Change.....	268
A.3. Demonstration Bridge 3.....	270
A.3.1. Overall Bridge Description	270
A.3.2. Instrumentation Plan—US 151 Bridge	271
A.3.3. Observation Summary of the SHM System.....	272
A.3.3.1. Usage.....	272
A.3.3.2. Load Rating.....	276
A.3.3.3. Behavior Change.....	277

LIST OF FIGURES

Figure 3.1. BECAS computer hardware arrangement	12
Figure 3.2. I-80 bridge	12
Figure 3.3. I-80 bridge instrumentation plan girder gauges.....	13
Figure 3.4. I-80 bridge instrumentation plan deck gauges.....	14
Figure 3.5. Screenshot of BECAS Merge	15
Figure 3.6. Screenshot of BECAS Processing Engine.....	16
Figure 3.7. Screenshot of BECAS Damage Detection	17
Figure 3.8. Screenshot of BECAS Load Rating	18
Figure 4.1. Scenarios of trucks traveling on a two-lane bridge	19
Figure 4.2. Deck strain response due to each wheel line	20
Figure 4.3. Deck sensors installed for a two-lane bridge.....	21
Figure 4.4. Algorithm of single-lane event detection of a two-lane bridge.....	22
Figure 4.5. Trucks traveling on a bridge.....	23
Figure 4.6. Truck event window selection of strain rate response.....	24
Figure 4.7. Peak strains induced by a five-axle truck	26
Figure 4.8. Raw, zeroed, and filtered data of a sensor for a five-axle truck event	27
Figure 4.9. Peak strains induced by a five-axle truck	28
Figure 4.10. Two example trucks	29
Figure 4.11. Two deck sensors of south lane – sensor line 2.....	30
Figure 4.12. Two deck sensors of north lane – sensor line 2.....	31
Figure 4.13. Single-truck event due to five-axle truck #1	32
Figure 5.1. Example of matched data from two sensors with applied limits.....	37
Figure 5.2. Example of sample distribution for the combined-sum-residuals	38
Figure 5.3. Sample control chart.....	39
Figure 5.4. Typical installed sacrificial specimen and double curvature bending of sacrificial specimen.....	39
Figure 5.5. Sample standard linear regression and sample orthogonal linear regression	40
Figure 5.6. Example of an orthogonal line fit and an orthogonal residual	41
Figure 5.7. Orthogonal fit lines for the full and reduced models.....	42
Figure 5.8. Graphical representation of the test of hypothesis	43
Figure 5.9. Flow chart for F-test control chart.....	44
Figure 5.10. Example of F_{shm} control chart for web gap sensor 4 at sacrificial specimen vs. sensor in negative moment at bottom flange of north girder	45
Figure 5.11. SHM system components	46
Figure 5.12. I-80 bridge	47
Figure 5.13. Sensor layout for I-80 bridge.....	47
Figure 5.14. Installation of two plates with C-clamps for damage level 1	48
Figure 5.15. Installation of two plates with C-clamps for damage level 2	48
Figure 5.16. Temperature and strain range changes	49
Figure 5.17. Temperature and strain range	50
Figure 5.18. Relationship between strain range and temperature	51
Figure 5.19. Moving average mean and standard deviation for all data and data in 70–80°F temperature bin for B2_BF	52

Figure 5.20. Moving average plots and F_{shm} control chart for B2_BF and C2_BF for all five-axle trucks	54
Figure 5.21. Moving average for mean and standard deviation of B2_BF and C2_BF for semi-trucks	55
Figure 5.22. Moving average for mean and standard deviation of B2_BF and C2_BF for semi-trucks in 70–80°F temperature bin	56
Figure 5.23. Box plots for all five-axle trucks, semi-trucks, all five-axle trucks in 70°F–80°F temperature bin, and semi-trucks in 70°F–80°F temperature bin	57
Figure 5.24. Normal distribution for 3 σ and 6 σ design	59
Figure 5.25. An example of 6 σ method for F_{shm} damage detection approach	60
Figure 5.26. Examples of base data method	61
Figure 5.27. Examples of strain change in percent	62
Figure 5.28. Examples of base data method for F_{shm} damage detection approach	62
Figure 5.29. Examples of training data method for F_{shm} damage detection approach	63
Figure 5.30. Combination of strain data	64
Figure 5.31. F_{shm} control charts for 70°F–80°F temperature bins with all five-axle trucks	68
Figure 5.32. F_{shm} control charts for 30°F–40°F temperature bin with all five-axle trucks	73
Figure 5.33. F_{shm} control charts for 70°F–72°F temperature bin with all five-axle trucks	78
Figure 5.34. F_{shm} control charts for 36°F–38°F temperature bin with all five-axle trucks	83
Figure 5.35. F_{shm} control charts for 70°F–80°F temperature bin with semi-trucks	88
Figure 5.36. F_{shm} control charts for 30°F–40°F temperature bin with semi-trucks	93
Figure 5.37. F_{shm} control charts for 70°F–72°F temperature bin with semi-trucks	98
Figure 5.38. F_{shm} control chart for 35°F–40°F temperature bins with all five-axle trucks	103
Figure 5.39. Summation of violation with all other sensors vs. C2_BF and M2_BF	105
Figure 5.40. Summation of violation for base data limits utilizing absolute changes in strain with the 26 sensors vs. C2_BF	106
Figure 6.1. HS-20 trucks on a bridge	110
Figure 6.2. Flowchart of the automated step-by-step procedure of bridge load rating	112
Figure 6.3. Frequency histograms of axle spacing	114
Figure 6.4. Frequency histograms of gross vehicle weight	115
Figure 6.5. Maximum girder strains in different sensors of trucks of Subgroup No. 2	116
Figure 6.6. Flowchart of automated ambient traffic approach using Sampling Strategy C	118
Figure 6.7. Details of FE model of I-80 bridge	119
Figure 6.8. Sensors on interior girder cross section – positive moment region	121
Figure 6.9. Neutral axis determination based on sensor pair D4_BF and D4_TF	122
Figure 6.10. Axle and wheel configurations of dump trucks	124
Figure 6.11. Axle and wheel configuration of ambient traffic five-axle trucks	124
Figure 6.12. Comparisons of strain time histories between collected data and FE results using known trucks – Section D (1 ft = 0.305 m)	127
Figure 6.13. Comparisons of strain time histories between collected data and FE results using known trucks – Section G (1 ft = 0.305 m)	128
Figure 6.14. Frequency histograms of minimum rating factors using different sampling strategies	132
Figure 6.15. Comparisons of strain time histories between collected data and FE results using AAT approach – south-lane event and Section D (1 ft = 0.305 m)	134

Figure 6.16. Comparisons of strain time histories between collected data and FE results using AAT approach — north-lane event and Section D (1 ft = 0.305 m)	135
Figure 6.17. Comparisons of strain time histories between collected data and FE results using AAT approach — south-lane event and Section G (1 ft = 0.305 m)	136
Figure 6.18. Comparisons of strain time histories between collected data and FE results using AAT approach — north-lane event and Section G (1 ft = 0.305 m)	137
Figure 7.1. Current load rating process using SHM data	140
Figure 7.2. Relationship between flexural strength and moment of inertia	142
Figure 7.3. Relationship between capacity and moment of inertia of composite sections	143
Figure 7.4. Improved load rating process using SHM data	144
Figure 7.5. Monte Carlo simulation of composite I_n	146
Figure 7.6. Monte Carlo simulation of composite M_n	146
Figure 7.7. Relationship between M_n and I_n	147
Figure 7.8. Cross-sectional details	148
Figure 7.9. Rectangular tension coupon details	151
Figure 7.10. Typical applied load vs. average strain variation of a test specimen	151
Figure 7.11. Experimental setup and instrumentation plan, Specimen A	155
Figure 7.12. Experimental setup and instrumentation plan, Specimen B	157
Figure 7.13. Experimental setup and instrumentation plan, Specimen C and Specimen D	159
Figure 7.14. Effective width concept	160
Figure 7.15. Typical strain measurements at a cross section	163
Figure 7.16. Typical strain measurements at a cross section	164
Figure 7.17. Percent error vs. I_{exp}/I_n variation	166
Figure 7.18. Definition of PNA location	167
Figure 7.19. Variation of strain at each location at section 2 of Specimen A	170
Figure 7.20. Typical strain measurements at a cross section	170
Figure 7.21. Strain and stress distribution at section 2 of Specimen A	172
Figure 7.22. Strain and stress distribution at section 2 of Specimen B	174
Figure 7.23. Strain and stress distribution at section 2 of Specimen C	175
Figure 7.24. Strain and stress distribution at section 2 of Specimen D	176
Figure 7.25. Validation of proposed procedure with Specimen A	178
Figure 7.26. Validation of proposed procedure with Specimen B	179
Figure 7.27. Validation of proposed procedure with Specimen C and Specimen D	180
Figure 8.1. Causes of deterioration of a typical bridge	183
Figure 8.2. Statistical data of structurally deficient bridges in the US	184
Figure 8.3. Condition of each bridge component in the US in 2012	185
Figure 8.4. Statistical data of structurally deficient bridges in US	185
Figure 8.5. Frequency vs. number of inspections for bridges in Iowa and Wisconsin	189
Figure 8.6. Frequency vs. age group for bridges in Iowa and Wisconsin	191
Figure 8.7. Percentage vs. condition rating for bridges in Iowa and Wisconsin	193
Figure 8.8. Condition rating vs. age for bridges in Iowa and Wisconsin	195
Figure 8.9. CPM development process, possible future deck condition ratings	198
Figure 8.10. Possible future condition ratings using tree diagram	200
Figure 8.11. Schematic representation of actual and simplified rating histories	203
Figure 8.12. Sojourn time types	204
Figure 8.13. Actual and simplified rating histories of an actual bridge deck	204

Figure 8.14. Sojourn time of each bridge component for Iowa and Wisconsin bridges.....	206
Figure 8.15. Sojourn time type of Iowa deck condition ratings.....	208
Figure 8.16. Sojourn time type of Wisconsin deck condition ratings.....	209
Figure 8.17. Relative frequency histogram of C value for Iowa bridge decks	213
Figure 8.18. Sample condition rating history.....	215
Figure 8.19. Different filtering methods	216
Figure 8.20. Representation of CPM Method I for Iowa bridge deck	218
Figure 8.21. CPM validation example	219
Figure 8.22. CPM validation results for Iowa deck condition rating data.....	221
Figure 8.23. CPM validation results for Iowa superstructure condition rating data.....	222
Figure 8.24. CPM validation results for Iowa substructure condition rating data.....	223
Figure 8.25. CPM validation results for Wisconsin deck condition rating data	224
Figure 8.26. CPM validation results for Wisconsin superstructure condition rating data	225
Figure 8.27. CPM validation results for Wisconsin substructure condition rating data	226
Figure 8.28. Representation of DPM Method I for Iowa bridge deck	227
Figure 8.29. DPM validation example.....	228
Figure 8.30. DPM validation results for Iowa deck condition rating data.....	230
Figure 8.31. DPM validation results for Iowa superstructure condition rating data.....	231
Figure 8.32. DPM validation results for Iowa substructure condition rating data.....	232
Figure 8.33. DPM validation results for Wisconsin deck condition rating data.....	233
Figure 8.34. DPM validation results for Wisconsin superstructure condition rating data.....	234
Figure 8.35. DPM validation results for Wisconsin substructure condition rating data.....	235
Figure 9.1. Ranking index computed using bridge inventory and SHM data.....	238
Figure 9.2. SR and BCI of all 21 demonstration bridges.....	244

LIST OF TABLES

Table 5.1. Mean, standard deviation, UCL, LCL, and number of truck events for intervals of 10°F temperature bins (B2_BF).....	51
Table 5.2. Mean, standard deviation, UCL, LCL, and number of truck events for intervals of 10°F temperature bins (C2_BF).....	52
Table 5.3. Axle spacing range for all five-axle trucks and semi-trucks	53
Table 5.4. Statistical parameters for all five-axle trucks, semi-trucks, all five-axle trucks in 70°F–80°F temperature bin, and semi-trucks in 70°F–80°F temperature bin	58
Table 5.5. Sigma level as percent variation	60
Table 5.6. Summary of F_{shm} limits for a sensor pair B2_BF versus C2_BF	64
Table 5.7. F_{shm} limit method and nomenclature.....	65
Table 5.8. Summary of false and true indication rate for 70–80°F temperature bins with all five-axle trucks for damage level 1	69
Table 5.9. Summary of false and true indication rate for 30–40°F temperature bin with all five-axle trucks for damage level 2	74
Table 5.10. Summary of false and true indication rate for 70–72°F temperature bin with all five-axle trucks for damage level 1	78
Table 5.11. Summary of false and true indication rate for 36–38°F temperature bin with all five-axle trucks for damage level 2	84
Table 5.12. Summary of false and true indication rate for 70–80°F temperature bin with semi-trucks for damage level 1	88
Table 5.13. Summary of false and true indication rate for 30–40°F temperature bin with semi-trucks for damage level 2	94
Table 5.14. Summary of false and true indication rate 70–72°F temperature bin with semi-trucks for damage level 1	98
Table 5.15. Summary of false and true indication rate for 35–40°F temperature bins with all five-axle trucks.....	104
Table 5.16. Sensors with a strain range under and above 10 $\mu\epsilon$	105
Table 6.1. Truck characteristics related to bridge model calibration.....	113
Table 6.2. Subgroups of five-axle trucks with different axle spacing intervals	114
Table 6.3. Sampling strategies with different strain and truck weight spectrums	117
Table 6.4. Axle weight distribution of heavy trucks of Subgroup No. 2.....	117
Table 6.5. Parameter values and ranges of I-80 bridge.....	120
Table 6.6. Neutral axis determination at different girder cross sections	123
Table 6.7. Parameters of three-axle dump truck.....	124
Table 6.8. Parameters of ambient traffic five-axle trucks.....	125
Table 6.9. Crawl speed tests	125
Table 6.10. Calibration and load rating results using crawl speed dump trucks	126
Table 6.11. High speed dump truck and ambient traffic five-axle trucks.....	129
Table 6.12. Calibration and load rating results using high speed trucks	129
Table 6.13. Sampling of truck events and WIM trucks for bridge model calibration	130
Table 6.14. Events and ambient traffic five-axle trucks	131
Table 6.15. Calibration and load rating results using the AAT approach with different sampling strategies	131
Table 6.16. Parameters of selected five-axle trucks	133

Table 7.1. Statistical distribution parameters of material properties	145
Table 7.2. Statistical distribution parameters of section properties	145
Table 7.3. Nominal dimensions of specimens	149
Table 7.4. Nominal material properties	150
Table 7.5. Material test results, steel.....	152
Table 7.6. Material test results, concrete	153
Table 7.7. Measured material properties.....	153
Table 7.8. The I_n of specimens.....	162
Table 7.9. The I'_n of specimens	162
Table 7.10. Summary of the average strains at each section, Specimen A.....	164
Table 7.11. Summary of the average strains at each section, Specimen B.....	164
Table 7.12. Summary of the average strains at each section, Specimen C.....	165
Table 7.13. Summary of the average strains at each section, Specimen D.....	165
Table 7.14. The I_{exp} of the specimens	166
Table 7.15. The PNA, M_p , and M_n of composite specimens.....	168
Table 7.16. The PNA, M'_p , and M'_n of composite specimens.....	169
Table 7.17. The M_{exp} of composite specimens	177
Table 7.18. Comparison of moment of inertia values.....	177
Table 7.19. Comparison of flexural strength values	178
Table 8.1. Description of condition ratings for deck, superstructure, and substructure	187
Table 8.2. Summary of sojourn times.....	205
Table 8.3. Iowa deck condition rating, average sojourn time.....	210
Table 8.4. Iowa substructure condition rating, average sojourn time.....	210
Table 8.5. Iowa superstructure condition rating, average sojourn time.....	211
Table 8.6. Wisconsin deck condition rating, average sojourn time.....	211
Table 8.7. Wisconsin substructure condition rating, average sojourn time	211
Table 8.8. Wisconsin superstructure condition rating, average sojourn time.....	212
Table 8.9. CPM validation results for Iowa condition rating data.....	220
Table 8.10. CPM validation results for Wisconsin condition rating data.....	220
Table 8.11. DPM validation results for Iowa condition rating data.....	228
Table 8.12. DPM validation results for Wisconsin condition rating data.....	229
Table 9.1. Comparison of SR and BCI calculations	239
Table 9.2. SR and BCI of all 21 bridges	243
Table 9.3. Values of F_1 to F_7 used in SHMM computation for bridge FHWA#22380	244
Table 9.4. Ranking index with $\gamma_1, 6, 7 = 1, \gamma_2$ to $\gamma_4 = 2$, and $\gamma_5 = 0.2$	246
Table 9.5. SR and corresponding bridge age	246
Table 9.6. BCI and corresponding bridge age	246

ACKNOWLEDGMENTS

The research team would like to acknowledge the Federal Highway Administration for sponsoring this Transportation Pooled Fund study: TPF-5(219). The authors would like to thank members of the technical advisory committee for their contributions and the following state pooled fund department of transportation (DOT) partners for their support:

- Iowa DOT (lead state)
- California DOT (Caltrans)
- Illinois DOT (IDOT)
- Wisconsin DOT (WisDOT)

EXECUTIVE SUMMARY

Objectives

This project had three primary objectives, to develop the following:

- An automated structural health monitoring (SHM) system capable of detecting bridge damages and estimating the load ratings of bridges in real-time or near real-time
- Condition rating prediction models, using biennial bridge inspections in the National Bridge Inventory (NBI) database, to predict future condition ratings of bridges
- A bridge maintenance prioritization system that integrates SHM techniques into current bridge management practices

Background

Bridges constitute the most expensive assets, by mile, for transportation agencies around the US and the world. Most of the bridges in the US were constructed between the 1950s and 1970s. Consequently, an increasing number of bridges are getting old and requiring much more frequent inspection and repairs or rehabilitation to keep them safe and functional. With tight construction and maintenance budgets, bridge owners are faced with the difficult task of balancing the condition of their bridges with the cost of maintaining them.

Bridge maintenance strategies depend on information used to estimate future condition and remaining service lives of bridges. The purpose of future bridge-condition assessment is to determine when to undertake repairs or maintenance to keep bridge condition within acceptable limits. The estimation of residual or remaining life is an important input for budgeting and setting longer-term repair and maintenance priorities. To better manage bridge inventories, tools that can accurately predict the future condition of a bridge, as well as its remaining life (i.e., when a bridge will become substandard in terms of load carrying capacity, serviceability, and/or functionality), are required. Essential to estimating the future condition of structures is having an accurate understanding of the current condition of the structure.

Problem Statement

The desire of many departments of transportation (DOTs) is to augment their existing inspection process and maintenance system with a system that can objectively and more accurately quantify the state of bridge health in terms of condition and performance, aid in inspection and maintenance activities, and estimate the remaining life of their bridge inventory in real time.

Project Description

Strain-based bridge damage detection: The research team investigated a control chart-based damage detection algorithm, F_{shm} , by minimizing the variability due to temperature and truck

configuration. F_{shm} control charts were constructed with different combinations of strain data and statistics- and structure-based limits were established to reduce the false indication rate.

Estimating the load ratings of bridges: Using four steel-concrete composite sections, the research team tested whether there was a relationship between moment of inertia and flexural strength of composite sections. The idea, then, was to use the finite element model-calibrated moment of inertia from the current load rating process to get an improved estimate of flexural strength.

Condition rating prediction models: The research team developed two different types of future condition rating prediction models—using NBI database data and sojourn time types. The models were called the current practice model (CPM) and the deterioration prediction model (DPM). CPM is capable of simulating the effects of historical maintenance activities when predicting the future condition rating probabilities, whereas DPM does not consider the effects of historical maintenance activities when predicting the future condition rating probabilities.

Bridge maintenance prioritization system: The research team developed a method of calculating a ranking index by using an inventory index, such as NBI data, and an SHM modifier (SHMM). The SHMM uses seven parameters (load rating ratio, load rating rate of change, behavior change, service level stress rate of change, service level stress margin, expert opinion, and reduced uncertainty), with each given a weighting factor to provide owner agencies the opportunity to customize their approach.

Key Findings

- For improved damage detection, in order to obtain enough strain data for limits, increasing the temperature bin size is required. However, a higher temperature bin range also creates higher strain variability. Therefore, a suitable temperature bin size is an important factor in terms of the amount of strain data available for establishing limits and strain variability.
- To estimate load ratings, the result of the team's experiments indicated that the theory of strength of materials and the American Association of State Highway and Transportation Officials (AASHTO) guidelines, along with actual material properties (when available), can accurately predict the moment of inertia and flexural strength of a section. In the absence of actual material properties, a Monte Carlo simulation along with the moment of inertia from the calibrated load rating model may significantly improve the rating factor of a bridge.
- For condition rating prediction models, quantitative evaluation results show that sojourn time is an important parameter when predicting future condition ratings, whereas the age of the bridges does not play as an important role in predicting the future condition ratings of bridges. The predictions, however, were entirely dependent on the original historical data of the bridges, which are subjective.

- For the condition rating prediction models, the CPMs tended to converge to condition rating 6 on a scale of 0 to 9 within 15 years, whereas the DPMs tended to converge to condition rating 4 with 15 years. This suggested that conducting current maintenance activities helps to keep the nation’s bridges in at least satisfactory condition. However, not performing any maintenance could lead bridges to be structurally deficient within 15 years.
- For a bridge maintenance prioritization system, using SHM data as a “tuning” factor rather than the dominant factor is the most practical way to implement SHM in the short term due to the relatively limited availability of SHM systems, and may well be more practical over the long term as well.

Implementation Readiness and Benefits

For this project, the research team developed an automated SHM system that could detect bridge damage and estimate load ratings of bridges, and also developed models to predict future condition ratings of bridges. The SHM system and models were then used to develop a bridge maintenance prioritization system that can help DOTs and other bridge owners to augment their current bridge management practices.

CHAPTER 1. INTRODUCTION

1.1. Background

Bridges constitute the most expensive assets, by mile, for transportation agencies around the US and the world. Most of the bridges in the US were constructed between the 1950s and the 1970s. Consequently, an increasing number of bridges are getting old and requiring much more frequent inspections, repairs, or rehabilitations to keep them safe and functional. However, due to constrained construction and maintenance budgets, bridge owners are faced with the difficult task of balancing the condition of their bridges with the cost of maintaining them.

In 2005, the American Association of State Highway and Transportation Officials (AASHTO) Highway Subcommittee on Bridges and Structures developed a strategic plan for bridge engineering to meet the grand challenges (2005). According to The American Infrastructure Report Card of the American Society of Civil Engineers (ASCE 2017), as of 2016, out of 614,387 bridges in the US, approximately 245,755 bridges (4 out of 10) are older than 50 years; in most cases, the design life is 50 years. Also, it states that 56,007 bridges (1 out of 11) are considered as structurally deficient; yet, on average 188 million trips across structurally deficient bridges each day were recorded. Further, more than 83,557 bridges (1 out of 8) in the nation do not serve current traffic demand or meet current standards. Rehabilitation of these bridges could cost about \$123 billion.

1.1.1. Bridge Management Systems

Bridge maintenance strategies depend upon information used to estimate future condition and remaining life of bridges. The purpose of future bridge-condition assessment is to determine when to undertake repairs or maintenance to keep its condition within acceptable limits. Also, the estimation of residual or remaining life is an important input for budgeting and setting longer-term repairs and maintenance priorities. To better manage bridge inventories, tools that can accurately predict the future condition of a bridge, as well as its remaining life (i.e., when a bridge will become substandard in terms of load carrying capacity, serviceability, and/or functionality), are required. Essential to estimating the future condition of structures is having an accurate understanding of the current condition of the structure.

The AASHTO Manual for Bridge Evaluation (2015), used together with AASHTO's software PONTIS and BRIDGIT, comprise the bridge management system (BMS) used by many states in the US. A BMS accurately documents the current and future condition of bridges, and is required by the 1991 Intermodal Surface Transportation Efficiency Act (ISTEA) and the 1998 Transportation Equity Act for the 21st Century (TEA-21), for public safety. In addition, bridge owners are mandated by other bridge preservation areas that include inspection scheduling, cost analysis, and rehabilitation planning.

The Manual for Bridge Evaluation (AASHTO 2015) characterizes the condition of bridges across the US following highly prescribed processes and procedures. The components of a bridge

are visually inspected biennially and the standardized four condition states (good, fair, poor, and severe) are assigned to each of the relevant components. The condition states are used to subsequently determine bridge condition, appraisal, and sufficiency ratings. These ratings then become an important parameter in the bridge management approach typically used by each state. Although the bridge condition states reflect deterioration or damage, they do not quantify the structural deficiency of a bridge or its components.

An approach to predict the future condition of bridge components could be to use a “back of the envelope” linear model that assumes one drop in deck condition rating every 8 years and one drop in superstructure and substructure condition rating every 10 years. This approach has a significant limitation in that it does not quite capture the actual aging process, and it does not reflect any difference between individual bridges. Aging is a continuous accumulation of deleterious chemical and mechanical reactions (observed and unobservable) throughout the life of the bridge due to weather, service conditions (traffic, deicing, etc.), and their interactions (Harman 1981, Mishalani and Madanat 2002). The linear deterioration model does not account for the nonlinear behavior caused by the impact of traffic volume, weight, structure and material type, environmental factors, and interactions between these variables specific to any given bridge, and this might result in an unreliable prediction of a bridge’s future condition.

1.1.2. Structural Health Monitoring

The desire of many departments of transportation (DOTs) is to augment their existing inspection process and maintenance system with a system that can objectively and more accurately quantify the state of bridge health in terms of condition and performance, aid in inspection and maintenance activities, and estimate the remaining life of their bridge inventory in real time. As early as the 1980s, bridge engineers have had the vision for an intelligent infrastructure system (Aktan et al. 1998, Connor and McCarthy 2006, Connor and Santosuosso 2002) capable of the following:

1. Sensing its own load environment, its responses, and any ongoing damage and deterioration
2. Assessing its condition regarding capacity, performance needs, and the actual capacity being delivered
3. Determining if and when behavior thresholds are exceeded or compromised such that the structural capacity, traffic volume capacity, environmental limiting conditions, and other factors have exceeded predetermined criteria

The bridge owner is ideally alerted by a system when a diversion of traffic is required, when load posting is required to prevent accelerated deterioration, when repairs are needed, and when the bridge needs to be closed. To this end, it has been identified (FHWA 1993) that one of the key requirements for an effective infrastructure management system is the establishment of a structural health monitoring (SHM) system. An SHM system traditionally consists of a network of monitoring sensors, data acquisition, and communication hardware and software capable of carrying out bridge condition assessments in real-time and accurately and objectively predicting the health of the infrastructure components and systems. It is also held by many researchers (Okasha and Frangopol 2012, Catbas et al. 2007) and the Federal Highway Administration

(FHWA) Long-Term Bridge Performance (LTBP) program (Ghasemi et al. 2009) that the other important component is the establishment of indices or thresholds for the critical structural elements through, for instance, calibration of finite element analytical models that compute into the measured strains, stresses, forces, reactions, and boundary conditions. In this conceptualization, an SHM system serves as the tool that enables the bridge owner to understand and evaluate the interactions between environmental conditions, bridge boundary conditions, bridge component mechanical conditions, and the impact of damage and deterioration on the mechanical characteristics of the bridge elements.

1.1.3. Bridge Maintenance Prioritization Strategies

1.1.3.1. State of the Practice of Bridge Maintenance Prioritization

Corrective maintenance and preventive maintenance are the most common maintenance prioritization approaches utilized by bridge owners. Sometimes these two approaches are combined using engineering judgement. For example, the Iowa DOT conducts a district meeting annually. In this meeting, DOT maintenance personnel meet with district engineers, inspection crews, and maintenance crews to go through previously collected National Bridge Inventory (NBI) data and to supplement inspection documentation for each bridge that has known defects, deterioration, or other concerns. A maintenance decision is then made based on the data and the judgement of the professionals in the meeting. This approach may optimize the decision making to certain degree; however, the decision is still somewhat subjective because it relies upon qualitative data and opinions that may or may not have inherent biases.

Within the corrective maintenance framework, a bridge is operated until a defect appears. Then, a decision needs to be made to determine if the defect is critical or non-critical. Prompt action is needed for critical defects. This approach has been used by bridge owners for years in prioritizing maintenance activities. However, some defects have gotten so significant that they were very expensive to fix and/or had safety threatening conditions. This approach is sometimes criticized because it does not use maintenance funding in an optimized way. In other words, some (minor) maintenance should have been performed before severe damage can even occur.

Preventive maintenance includes periodic maintenance or maintenance based on condition prediction. This is fairly commonly used in the bridge community, and it involves looking at the bridge rating history and available bridge deterioration models to find an optimized time for maintenance activities, but before severe failures occur. Due to the limitations of currently available bridge deterioration models and the lack of quantitative data, accurately predicting the performance of a specific bridge is hard, if not impossible. Therefore, preventive maintenance is still used more commonly for preventing severe failure rather than for optimizing the maintenance activities. Even so, there is a cost associated with this approach. Generally, this strategy advises that maintenance be performed more often than is absolutely necessary and, as such, can lead to an over maintenance scenario.

1.1.3.2. Condition-Based Maintenance Approach

Condition-based maintenance (CBM) (Cadick and Traugott 2009, Ni and Wong 2012) is a maintenance strategy used to actively manage the condition of assets/equipment in order to perform maintenance only when it is needed and at the most opportune times. CBM is accomplished by integrating all available data to predict the impending failures of assets as well as to avoid costly maintenance activities. This process depends, largely, on the ability of the manager or managing algorithm to recognize undesirable operating conditions as measured by diagnostic monitoring systems. The process also allows an asset to continue operating in an undesirable yet safe condition while it is being monitored until maintenance can be scheduled and performed.

CBM can reduce maintenance costs, improve availability and reliability, and enhance the life span of the asset. This strategy has been widely used in the management of weapon systems, nuclear power plants, jet engines, marine engines, wind turbine generators, natural gas compression, and others (IAEA 2007). However, its application in bridge management is limited because current bridge inventory data, which are collected biennially through scheduled bridge inspection, are not sufficient to implement CBM.

With the development of SHM, more and more bridges are being continuously monitored. By integrating the real-time or near real-time bridge condition data collected by an SHM system into bridge inventory data, an SHM facilitated CBM (SHM-CBM) framework is possible and is more fully developed in this research.

1.1.4. Financial Justification of SHM Instrumentation

With SHM instrumentation in place, uncertainties associated with structural performance are reduced because bridge owners know the true performance of the structure in a real-time or near real-time fashion. This will lead to postponed bridge replacement, delayed maintenance activities, and prevented bridge collapse. Taking these benefits into consideration, it is not difficult to justify the cost of SHM instrumentation.

1.2. Objectives

This project had three primary objectives.

The first objective was to develop an automated SHM system capable of (1) detecting bridge damages and (2) estimating the load ratings of bridges in real-time or near real-time. The second objective was to develop condition rating prediction models to predict future condition ratings of bridges. The biennial bridge inspections in the NBI database were used in developing the condition rating prediction models. The third objective was to develop a bridge maintenance prioritization system that integrates SHM techniques into current bridge management practices.

Due to the somewhat limited availability of installed SHM systems, biennial bridge inspections in the NBI database must still play a notable role in the maintenance decision-making process with the SHM data functioning as a “tuner” to refine the maintenance priority up or down to a degree that is reasonable and can be controlled by the user when such data are available.

1.3. Report Organization

In this report, Chapter 2 reviews a sample of current SHM systems. Chapter 3 provides an overview of the hardware and software of an SHM system developed by the authors and becoming more widely adopted. Chapter 4 describes the truck detection method, which is a critical component of the SHM system. Chapter 5 focuses on the automated damage detection system. Chapter 6 describes the estimation of load ratings of bridges under ambient traffic conditions. Chapter 7 describes the extensive large-scale experiments conducted in the Iowa State University (ISU) Structural Engineering Research Laboratory to further improve the automated load rating process. Chapter 8 illustrates the development of future condition rating prediction models. Chapter 9 describes the design and implementation of the proposed SHM-CBM system. Chapter 10 summarizes this work and presents several concluding remarks.

CHAPTER 2. LITERATURE REVIEW

A brief literature review was conducted to investigate the different types of asset management systems currently available in different areas, including pavements, vehicle systems, tall buildings, and bridges. The current bridge management methodology of the Iowa DOT is discussed at the end of the literature review.

2.1. Pavement Management Systems

In pavement management systems (PMS), some owners use the pavement condition index (PCI) as the controlling factor for scheduling maintenance and repair activities. PCI is a number between 0 and 100, with 0 being the worst condition. For instance, a PCI of less than 60 means the pavement needs reconstruction while a PCI between 80 and 85 means the pavement is in very good condition (NYSDOT 2010). The PCI is a function of road surface distress such as cracking, ride quality, structural capacity, and friction. The predictive variables for pavement condition in regression and deterministic mechanistic algorithms used in PMS include traffic loading, climatic conditions, pavement structural properties, and past rate of pavement deterioration. These algorithms are in essence mathematical tools that predict the time or cumulative traffic to reach a failure criterion. This information is then used to plan and schedule maintenance and repair activities for pavement systems.

2.2. Aerospace and Other Vehicle Management Systems

In the aircraft industry, a fleet management system is termed the Integrated Vehicle Health Management (IVHM) system (Ikegami and Haugse 2001). The goal of IVHM is to assess the present fleet and to predict future vehicle condition. This information enhances operational decisions, supports corrective actions, and determines subsequent continued use of the aircraft (Benedettini et al. 2009). In this framework, IVHM consists of four main blocks, namely:

1. SHM systems to measure the state of the aircraft while in flight for damage-prone stress concentration areas, for unanticipated aerial events such as impacts, and for aging effects such as fatigue and cracking, to establish the current state of the fleet. Structural health measurement is primarily through the use of fiber optic sensors for state parameter metrics such as strain, temperature, pressure load, and aircraft components acceleration. Probabilistic models for the state parameters and failure models are also established at this stage (Xu and Xu 2013, Xu et al. 2013).
2. A prognostics and health management (PHM) block that uses the current stochastic state parameters together with damage growth characteristics to form failure probability models. This is followed by calibration of a model to produce a probabilistic prognosis of damage evolution in terms of damage versus time or number of cycles the aircraft is in use. The calibrated structural model also can be used to assess failure probabilities in areas not instrumented by sensors. If the failure probabilities established above are lower than the pre-set levels, the fleet of aircraft is kept in service. The processed structural damage parameters include strain time histories, power spectral densities, and root mean square (RMS) values of the state parameters. As fatigue is the biggest problem in aircraft, the processed data are

primarily used in designing repair patches with increased damping properties for installation on the aircraft body. These patches lead to reduced structural responses and, thus, extend the service life of the aircraft fleet.

3. Non-destructive inspections (NDI) are also used on aircraft while they are on the ground. When the probability of failure is higher than the pre-set levels, the fleet of aircraft is further subjected to NDI, and if needed, repairs are carried out at the aircraft maintenance facility.
4. The IVHM architecture finally includes an information technology (IT) block for communication of the obtained knowledge base to the flight crew, operations and maintenance personnel, regulatory agencies, and the original equipment manufacturers (OEM).

Today, IVHM also includes other types of vehicle systems such as cars, trucks, ships, trains, helicopters, submarines, tanks, etc. In this broader sense, it is meant, therefore, to be an advanced system capable of carrying out health monitoring, diagnosis, prognosis, and computation of reactive planning decision-making tools for corrective and preventive measures for the numerous components and subsystems such as, structural frame, engine performance, electronics, hydraulics, fuel systems, and electric power systems.

2.3. Tall Building Management Systems

The issues of importance in tall buildings are safety and comfort of the occupants. Tall buildings are normally designed using state-of-the art structural analyses coupled with wind tunnel testing on scaled models. Wind speed and direction are the primary parameters for wind tunnel prediction models. In this framework, the impetus for structural health monitoring is the need for establishing the accuracy and validity of the design methods. The results of the analyses must be in conformity with the monitored building performance (Kijewski-Correa and Kochly 2007, Kijewski-Correa and Pirnia 2007, Kijewski-Correa et al. 2013) as determined by sensors monitoring ground accelerations, damping, strains, deflections, gravity loads, and meteorological site conditions. From the SHM knowledge base, structural control, in terms of limiting states, is then established via the use of structural control devices such as active mass dampers (AMD), active variable stiffness (AVS) systems, hybrid mass dampers (HMD), and active gyroscopic stabilizers (AGS) (Kareem et al. 1999, Spencer and Nagarajaiah 2003).

2.4. Bridge Management Systems

2.4.1. Current Bridge Management Systems

There are roughly 21 bridge management systems in the world (Adey et al. 2010). These management systems are used for quantification of the following:

- Deterioration and performance indicators
- Formulation of corrective intervention strategies with respect to cost and time
- Changes following an intervention program

What all of these have in common is a lack of an integrated SHM system. Hence, they are all subject to criticism of being subjective. The general organizational structure of a BMS with an integrated SHM system is a self-contained entity comprising, in the minimum, of the following main features (Aktan et al. 1996):

- Personnel, consisting mainly of the scientific team, the technical team, and general staff
- The physical bridge
- Information technology
- Analytical division
- Decision-making wing
- Influence of the non-technical sector

All of the most advanced bridge management systems (e.g., PONTIS and BRIDGIT in the US; NYSDOT in New York; OBMS in Ontario, Canada; QBMS in Quebec, Canada; and KUBA in Germany), tend to use Markov probabilistic models based on linear transition probabilities that specify the likelihood that the condition of a bridge component will change from one state to another in a specified interval of time. They have been found to be very useful in predicting the percentage of bridges in any given deterioration state, and in estimating the expected condition of a bridge at some given future time.

In the US, PONTIS is the bridge management system used by many states. In PONTIS, a bridge is subdivided into many structural elements instead of just three components that have been the focus of historical NBI inspections (i.e., deck, superstructure, and substructure). Each element is evaluated separately and later combined at the project level to determine the best maintenance repair and rehabilitation, improvement, and replacement strategy for the bridge. PONTIS is a federally funded management system that uses probabilistic modeling techniques and optimization procedures coupled with the NBI database. The database is an accumulation of inventory, inspection, and supplemental data from traffic and bridge accident reports. All this data are fed into PONTIS to do the following:

1. Predict bridge deterioration for each bridge element
2. Find the most cost-effective maintenance, repair, and rehabilitation (MR&R) action to solve the deterioration problem
3. Quantify any necessary functional improvements in terms of user cost and convenience, and weigh them against the cost of MR&R
4. Select the most appropriate bridge improvement and replacement
5. Help in scheduling the work to be undertaken using state-based statistical Markov models and solution methods that predict future bridge conditions

However, none of the data in PONTIS comes from a structural health monitoring system. PONTIS is, therefore, a subjective tool.

2.4.2. Implementation of an SHM System in the BMS

The planned objectives for the introduction of an SHM system are well known (i.e., to provide objective quantitative data in real-time that can be used to assess structural damage and deterioration, structural capacity, and which can be synthesized through algorithms to aid bridge owners in making decisions regarding bridge closures, posting, and maintenance, repairs, and rehabilitation) (Rytter 1993). The actual process involves monitoring and capturing critical inputs and responses of a structural system. These system descriptors might include physical dimensional properties, strain levels, vibration properties, material properties, damping properties, and boundary conditions. Collectively, these inputs and responses can be used to understand the root causes of the problems as well as to track responses to predict the future behavior of a bridge. There is no one SHM system that fits all bridges. A setting or application has to be defined for an SHM plan. Each bridge setting normally pre-determines a unique set of parameters to be measured and monitored so that a bridge may be accurately and completely characterized for reliable simulation.

2.4.3. Current Bridge Management System of the Iowa DOT

According to the FHWA, bridges must be given a component condition rating and a bridge overall sufficiency rating in accordance with the Recording and Coding Guide for the Structure Inventory and Appraisal of the Nation's Bridges (FHWA 1995). A component condition rating is an integer number from 0 and 9, with 9 representing a component in excellent condition while a 0 rating is given to a failed bridge, i.e., out of service and beyond any corrective action. A bridge with a component condition rating of 5 or better is structurally adequate, requiring only cosmetic routine maintenance for minor section loss, cracking, spalling, or scour.

The Iowa DOT's BMS is based on the biennial visual inspection reports generated, and it is required to update the NBI database. These inspection reports, including other levels of inspections deemed necessary by the Iowa DOT, include detailed descriptions of the type and extent of deteriorations observed by inspectors using photographs, construction drawings, and sketches. Bridge issues requiring immediate attention are also noted in the reports by the inspectors.

The Iowa DOT conducts around 2,500 bridge inspections annually. These inspections are most commonly completed using Iowa DOT personnel. Once each bridge inspection is complete, together with the FHWA-required bridge inventory and operating rating by the Bridge Office, a Structure Inventory and Appraisal Sheet is prepared for FHWA biennial NBI reporting compliance. In addition, all bridge issues reported by inspectors as requiring immediate actions are reviewed by the Iowa DOT Maintenance Office. Based on the review, repair orders are issued to the district office with jurisdiction over the bridge. The DOT determines the type of repairs to be conducted, and whether the repairs are to be done in-house or through a contract.

Bridges requiring contract-based repairs are entered into a five-year program of repair and replacement overseen by the Iowa Transportation Commission (ITC), although the commission cannot preclude a bridge from repairs. Six times annually the Iowa DOT conducts meetings to

review and prioritize the bridges for repair and to determine the type of continued monitoring for those bridges that cannot be repaired with the current budget. A bridge repair ranking system has been developed by the Iowa DOT for funding purposes. The ranking is based on the average daily traffic (ADT) and a number of issues at the bridge reported by the inspector.

The Iowa DOT BMS is similar in many respects to what it was 25 years ago (Fanous et al. 1991). However, since 2014, the Iowa DOT has been developing a bridge element condition index classification as well as a modified sufficiency rating formula for bridge elements. This sufficiency rating is meant to help in the decision-making process when a large number of bridges are reported with varying element deterioration levels. One of the features the Iowa DOT is looking for in an SHM system, therefore, is the capability to help document the varying levels of deterioration in bridge elements.

2.4.4. SHM Framework for the Iowa DOT

The Iowa DOT, in conjunction with the Bridge Engineering Center (BEC) at ISU, has embarked on developing an SHM system to help collect on-site quantitative bridge measurements for use in its current bridge management system. The Iowa DOT conceptualization of an SHM is a system that would have the following characteristics:

1. Generates significant bridge performance parameters and their thresholds that may assist them in their current bridge management system. These parameters and thresholds, for the most part, will be dictated by or set in collaboration with the Iowa DOT.
2. Includes rate of change of performance parameters for comparison with other bridges in the system.
3. Allows users to query the system for specific bridge performance parameters at any time.
4. Helps in bridge life-cycle cost computations, e.g., life lost while a bridge is awaiting repairs, knowledge of preventable part of lost bridge life, annual loss of value of bridges in its inventory, etc.
5. Enables communications that go through personnel in the Iowa DOT Bridge Maintenance Office.

In a strain-based SHM system, such as the Bridge Engineering Condition Assessment System (BECAS) software developed at ISU (see Chapter 3), the Iowa DOT has indicated a desire for a system that, at a minimum, computes strain and load rating time histories, strain/stress cycle accumulation, strain comparisons between bridges, and remaining bridge life. The Iowa DOT has also expressed an interest in a system that can also monitor deck joints and quantify as a function of time deck reinforcement corrosion, bridge element condition states, and bridge element deterioration extent.

CHAPTER 3. BRIDGE ENGINEERING CONDITION ASSESSMENT SYSTEM

3.1. Introduction to the SHM System, BECAS

The BEC has developed structural health monitoring software called BECAS. The software eliminates the subjectivity of current inspection approaches; increases evaluation frequency from once every two years to continuously; virtually removes human error, bias, and limitations; and provides feedback that can be used to perform proactive, rather than reactive, preventive maintenance. This chapter provides an overview of the major components of BECAS including hardware and the software suite.

The BECAS hardware consists of off-the-shelf components integrated to form a network of state-of-the-art sensors, data collection equipment, data storage, and an N-tier data processing hub. There are three sensor types that make up every BECAS installation: resistance strain sensors, temperature sensors, and global positioning system (GPS) signal collectors. In addition, sensors of multiple types can be integrated into the system (tilt, deflection, corrosion, acceleration, etc.) depending upon any unique monitoring needs. The sensors are connected to an on-site data logger that has integrated filtering capabilities. With read speed capabilities that approach 1,000 Hz, the data logger has the ability to collect the data as needed (high speed data collection is needed for vehicle identification and classification). On-board filtering capabilities added to each system helps to ensure that measurement noise is minimized. To temporarily store, initially process, and then transfer the data to the main data processing hub, a mid-level desktop personal computer (PC) is connected to the data logger via wired Ethernet. An IP-based video camera is also installed at each BECAS site. This camera is set up to record (and temporarily store) a live video feed of the bridge (including traffic crossing the bridge).

One final key piece of the on-site hardware is an IP-based power switch. This power switch has multiple features that make it a useful part of the system. For example, the power switch allows remote users to power up or down individual system components from anywhere in the world. Second, in the event that the on-site system loses connection with the internet, the power switch will automatically reboot the on-site cellular modem until the system comes back on-line fully.

Once transferred from the bridge to the office, the data are stored on a networked location. Then, an N-tier system of computers automatically detects the presence of new data and processes them. To create redundancy in the system and to provide a lower-cost method of analyzing the data in real-time, a typical BECAS processing architecture consists of a workstation class PC (the parent) plus one or more lower-cost desktop PC(s) (the children). Additionally, since currently available computers have multiple cores (i.e., processing threads), the BECAS software described subsequently will parallel-process multiple files at once. Photographs of a typical field installation and a typical data processing cluster are given in Figure 3.1.

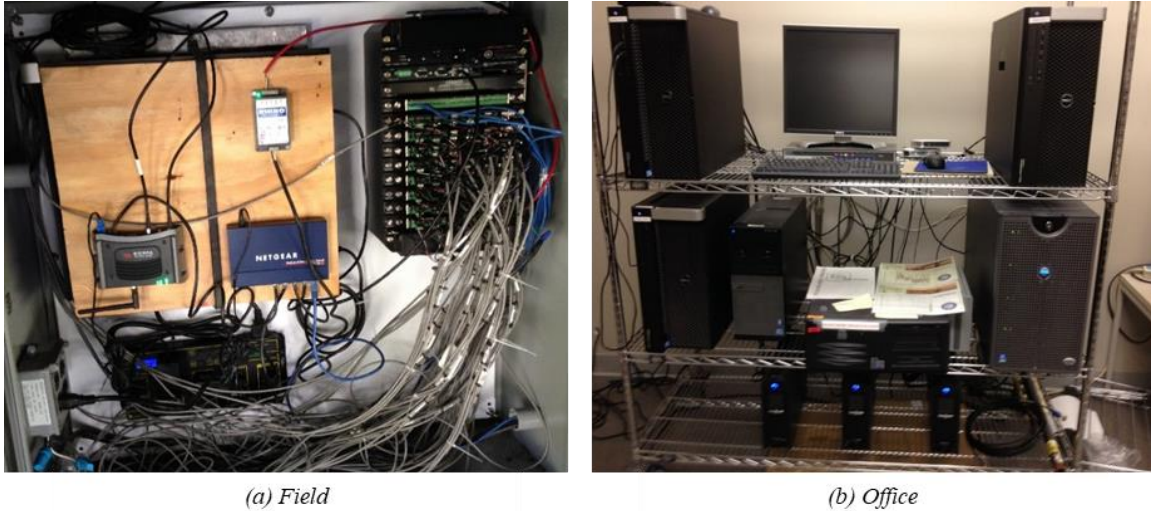


Figure 3.1. BECAS computer hardware arrangement

3.1.1. Bridge Description

The BEC installed the BECAS SHM system on several bridges in Iowa, including an I-80 bridge (Figure 3.2) used as a demonstration bridge to explain the aspects of the BECAS SHM system for this report.



Figure 3.2. I-80 bridge

The bridge was built in 1966, and it is 200 ft long, 40 ft wide, 15 degrees skewed to right eastbound and carries two lanes of I-80 eastbound traffic. It has a 7.5 in. thick cast-in-place

reinforced concrete deck, which is supported by five continuous steel girders (three W36 x 150 interior girders and two W36 x 136 exterior girders). The bridge consists of two 61 ft outer spans and a 78 ft middle span, where the girders are continuous over both piers and within the negative moment region. The exterior and interior girder flanges have cover plates with dimensions of 14 in. x 9/16 in. x 18.5 ft and 14 in. x 5/8 in. x 18.5 ft, respectively. The girders are spliced at locations 17.6 ft away from both piers. The spacing between the girders is 9.5 ft. The substructure consists of two end stub concrete abutments, and two intermediate open column concrete piers with cantilevers. Roller supports at both abutments and at the east pier and pinned support at the west pier were designed for the bridge.

3.1.2. Bridge Instrumentation

The SHM system developed for the I-80 bridge consists of 71 electrical resistance strain gauges installed on the steel girders as shown in Figure 3.3.

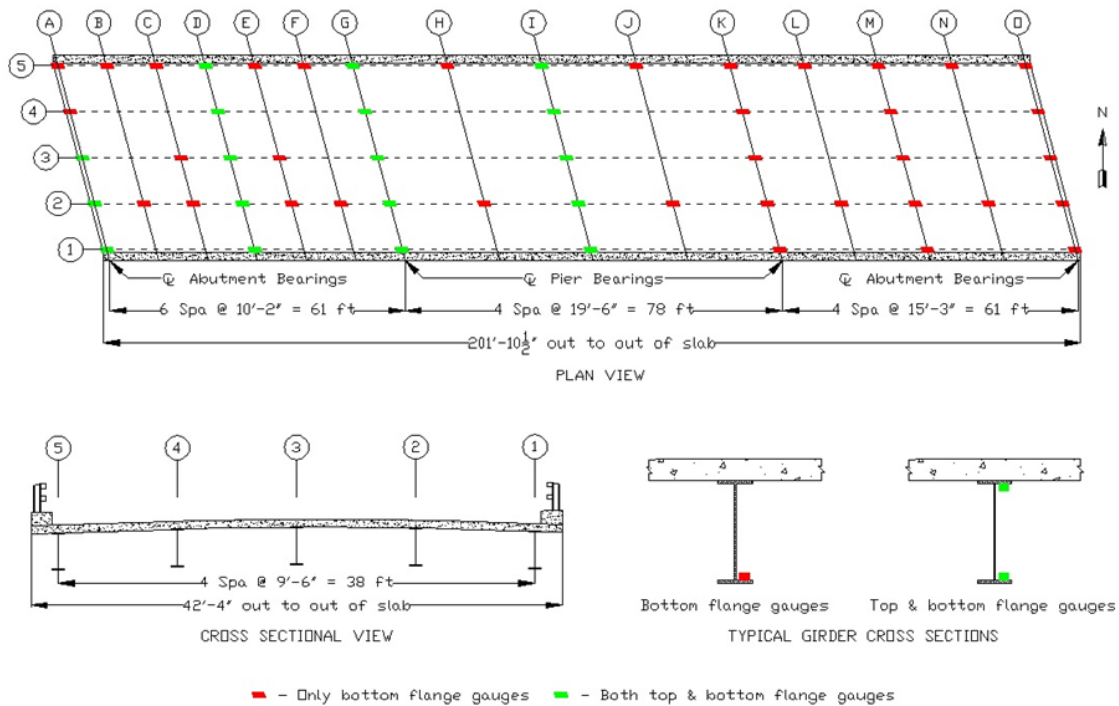


Figure 3.3. I-80 bridge instrumentation plan girder gauges

In Figure 3.3, the red disks represent 35 strain gauges installed on the top of the bottom flange of steel girders, whereas green disks represent total of 36 strain gauges installed on both the top of the bottom flange and the bottom of the top flange of the steel girders. The bridge cross sections with instrumentation were labeled from A to O and the girder lines were labeled from 1 to 5. The nomenclature for the sensor designation is the strain gauge location by cross section, girder line, and flange location. For instance, sensor designation B2_BF represents a sensor installed at the intersection of cross section B and girder line 2, and at the bottom flange (BF) of the girder, whereas sensor designation G1_TF represents a sensor installed at the intersection of cross

section G and girder line 1, and at the top flange (TF) of the girder. These strain gauges monitor the performance of the bridge.

The SHM system of the I-80 bridge also consists of eight electrical resistance strain gauges installed at the bottom of the concrete deck (Figure 3.4).

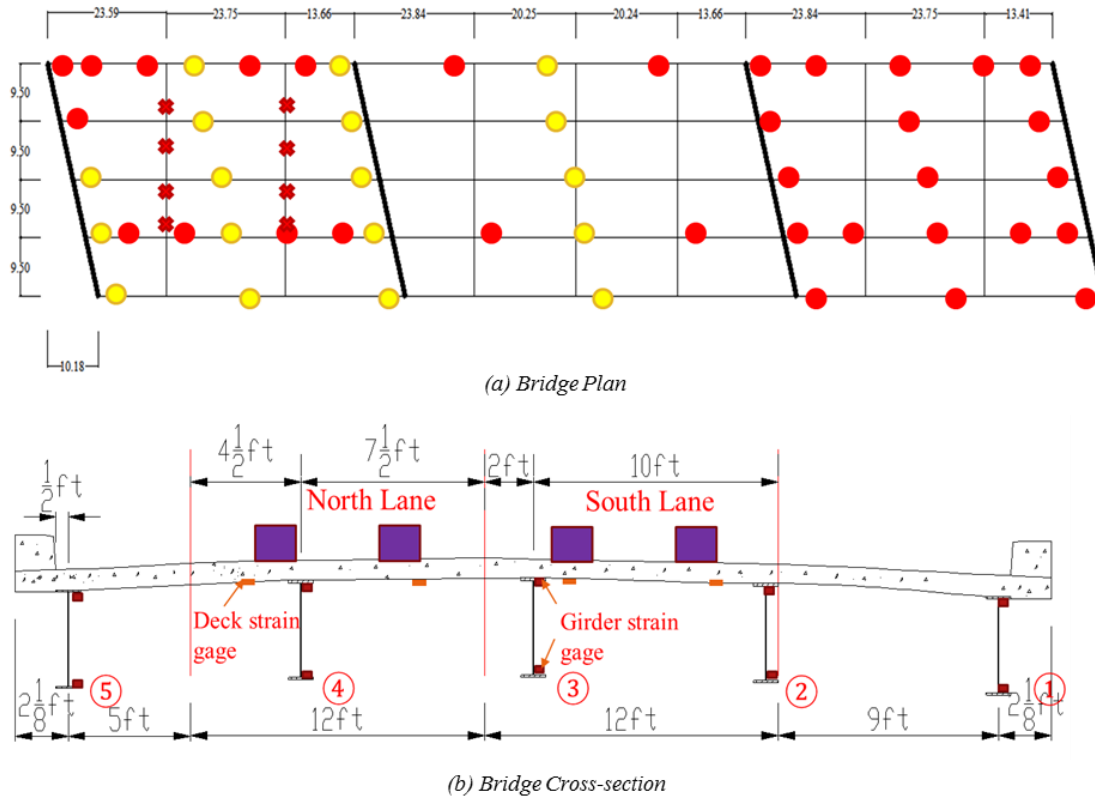


Figure 3.4. I-80 bridge instrumentation plan deck gauges

These strain gauges are in two rows of four in each and are located 23.59 ft and 47.34 ft from the northwest corner of the I-80 bridge. For each row of deck strain gauges, two gauges were installed on the south and north lanes, respectively. The deck strain gauges are used to identify vehicle travel lane, axle number and spacing, and vehicle speed. Additional details about demonstration bridges studied during the course of this project is shown in the Appendix.

3.2. BECAS Software Architecture

The primary monitoring metrics for BECAS are strain and temperature. The data loggers typically sample sensor strains and temperature at 250 Hz (every 0.004 seconds). It should be noted that other sensors used for other purposes, such as chloride infiltration, tilt, corrosion extent, acceleration, etc., might be integrated into BECAS at the request of the bridge owner or agency.

For bridge behavior changes, damage detection, and load rating computations, the quasi-static strain response of the bridge under single five-axle truck events are used. The use of quasi-static responses assumes that vehicle inertia loads and dynamic forces are negligibly small, and therefore, the vehicle axle loads on a bridge are a result of vehicle weight, geometry, and stiffness of the suspension components. These computations, therefore, require filtering of the collected raw strain data for the quasi-static strain response. This is accomplished by eliminating from the raw data the other strain components by zeroing the data and using a low-pass filter (Wipf et al. 2007, Lu et al. 2010) on the raw strain signal. The resulting quasi-static truck-strain events are further reduced to just the extrema strain values for bridge behavior assessment, culminating in bridge behavior change or damage detection and load rating. The following sections describe the key components of the BECAS software architecture.

3.2.1. BECAS Merge

Most BECAS installations require multiple data loggers to collect the amount and fidelity of data needed for the various downstream applications (described in the following sections). BECAS Merge creates time-sequenced data files with concatenated columns from multiple input files produced from multiple data sources. BECAS Merge performs initial data quality checking and repair associated with timestamping anomalies. Entries from multiple data sources are aligned to within 0.004 seconds or less. A screen shot of BECAS Merge during the merge process is shown in Figure 3.5.

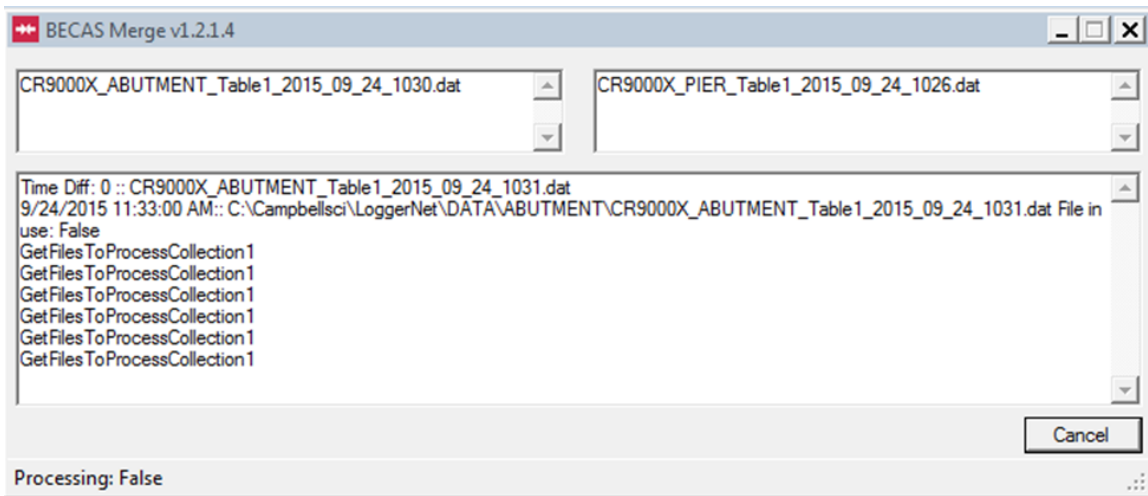


Figure 3.5. Screenshot of BECAS Merge

3.2.2. BECAS Distributor

The BECAS Distributor continuously monitors a specified data repository containing flat files (e.g., comma delimited text data stored in rows). Distributor moves a specific number of files from the repository to a defined number of subdirectories (clients). The BECAS Distributor continuously monitors these client folders to maintain the specific number of files. Once moved, the BECAS Processing Engine, operating on each of the clients (parent and children computers,)

process the data and prepare the results for BECAS Damage Detection and BECAS Load Rating. Each installation of BECAS Processing Engine has a series of checks and balances integrated such that the same files are not processed by multiple clients nor are results being simultaneously written to the same output files.

3.2.3. BECAS Processing Engine

The BECAS Damage Detection and load rating algorithms (BECAS Load Rating) require that the continuously collected data be manipulated prior to further processing to ensure high quality. The system utilizes a subset of live load events during the damage detection and load rating processes. Although the specific loadings are user configurable, it is most common to use five-axle semi-trucks. Also, to eliminate the impact of differences in vehicle suspension systems, it is desirable to use the predicted pseudo-static response of the bridge.

The BECAS Processing Engine checks the continuous data stream for anomalies and then analyzes the time-sequenced data and evaluates those data to determine if a catastrophic event has occurred. It then assesses the presence of user-specified truck traffic on the bridge. The potential events are evaluated for data consistency and for concurrency of multiple trucks on the bridge. Events that have passed integrity evaluations may then have macro-temperature effects removed, with resulting damage detection files produced.

After a user-specified number of trucks has been detected, BECAS Processing Engine passes the damage detection files to BECAS Damage Detection. Detected trucks then undergo further discrimination and discretization and strain time histories for trucks with specific user-specified characteristics, which are then passed to BECAS Load Rating. A screenshot of BECAS Processing Engine is shown in Figure 3.6.

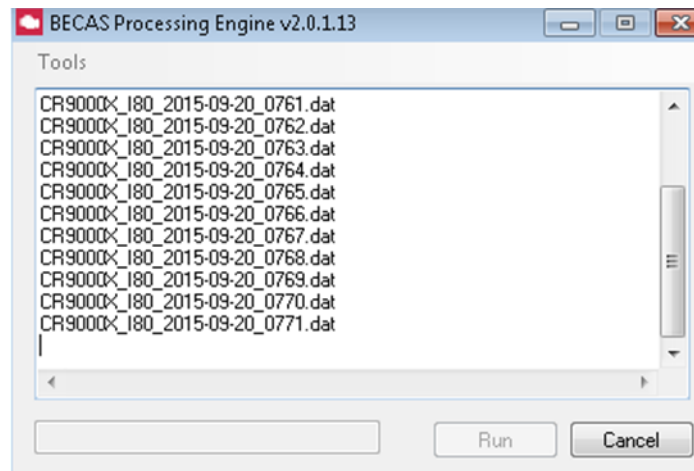


Figure 3.6. Screenshot of BECAS Processing Engine

3.2.4. BECAS Damage Detection

The key to the BECAS Damage Detection approach is the custom-developed and validated (both experimentally and analytically) data analytic approaches. Although length limitations prohibit an extremely detailed description of the approaches, the two damage detection approaches combine important aspects of structural engineering and statistics. More detail is presented in Chapter 5.

Loosely rooted in control theory, the damage detection approach uses comparisons between current behaviors and those established during training (using BECAS Training described below) to determine whether damage has occurred. If damage has been detected, the system then employs multiple approaches to determine the location and severity of the damage. BECAS Damage Detection applies user-specified settings established with BECAS Training to data obtained from the BECAS Processing Engine to detect changes in structural behavior and performance using a combination of statistical and/or structural tests following pre-defined rules. Outputs, including damage location and estimated damage levels, are output to individual files for each test and rule. End results are then packaged, and notification is sent to authorities. A screenshot of BECAS Damage Detection is shown in Figure 3.7.

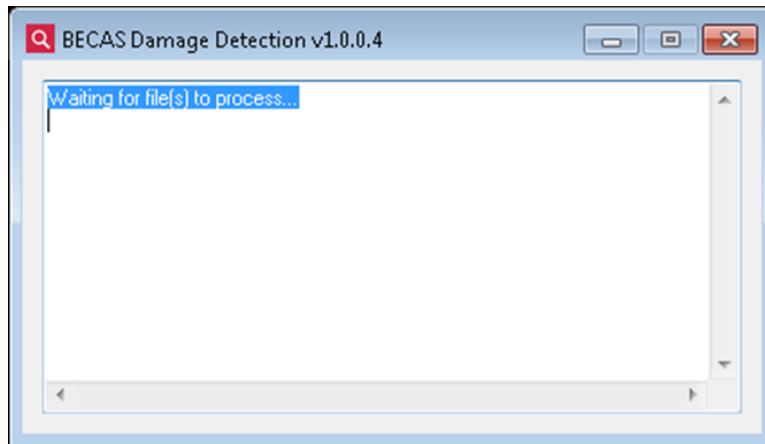


Figure 3.7. Screenshot of BECAS Damage Detection

3.2.5. BECAS Training

BECAS Training is used to initially set up parts of the system (BECAS Damage Detection). This training can be at least partially completed after less than one day of system operation in some instances. BECAS Training establishes control thresholds for BECAS Damage Detection utilizing baseline data sets. Control construction approaches can, based upon user specifications, create thresholds for two custom damage detection methods. Users may set various training parameters including training size, group size, step size, as well as select other options.

3.2.6. BECAS Load Rating

BECAS Load Rating (Figure 3.8) uses the measured response from partially known vehicles to calibrate a bridge-specific math model with geometrically/weight similar trucks selected from a specially created database.

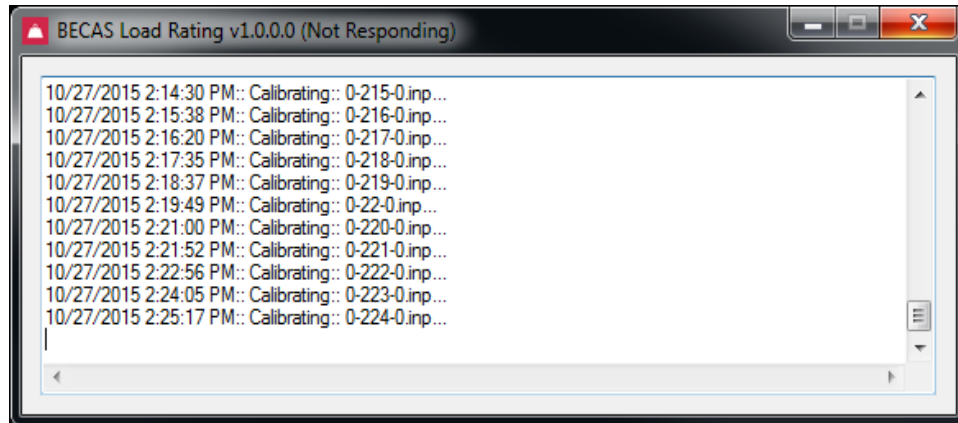


Figure 3.8. Screenshot of BECAS Load Rating

The calibrated math model is then used to calculate bridge capacity based upon user input parameters. If the estimated capacity is below a user-specified amount, a notification is sent to authorities.

Each of the applications described above has integrated communication outlets. For the most part, the system requires no routine user interaction or intervention. However, when BECAS determines that user interaction is needed, the system is configured to send out emails and/or texts to one or multiple people. When received, these communications are then quickly evaluated to determine if any immediate response is needed. For example, a live video camera feed might be evaluated to determine if a serious condition exists, or the recorded video feed can be replayed to determine what vehicle may have caused an overload to occur.

In addition to the on-demand communications created by the various BECAS applications, a concise report can be generated to summarize a period of monitoring. The form of these reports has been crafted to be similar to other bridge evaluation reports currently in use (i.e., National Bridge Inspection reports).

CHAPTER 4. TRUCK DETECTION METHODOLOGY OF SHM SYSTEM

4.1. Introduction

The bridge load rating and damage detection work (described in the following sections) primarily relies on truck events and associated bridge response detected using truck detection methodology, which is a critical component of the BECAS SHM system. In this chapter, the processes of the truck detection methodology including single-truck event detection, lane detection, and truck axle detection are presented. The approaches to zero out and filter the collected data related to the detected single-truck events are introduced, and the methodology is applied to a demonstration bridge and verified against the measured data.

4.2. Truck Detection Methodology

4.2.1. Single-Truck Event Detection Using Strain Rate Response

The truck detection method is developed based upon the previously developed SHM system to detect single-truck events within its associated travel lane, while other concurrent events with more than one truck simultaneously on the bridge are abandoned. The single-truck event represents the scenario that only a single truck travels on a single lane of a multi-lane bridge. The concurrence event represents the scenarios of side-by-side trucks and/or one-after-another trucks traveling across a multi-lane bridge simultaneously.

For instance, on a two-lane bridge, the desired single-lane events consist of Case #1, where a truck travels on Lane A, and Case #2, where a truck travels on Lane B, as shown in Figure 4.1.

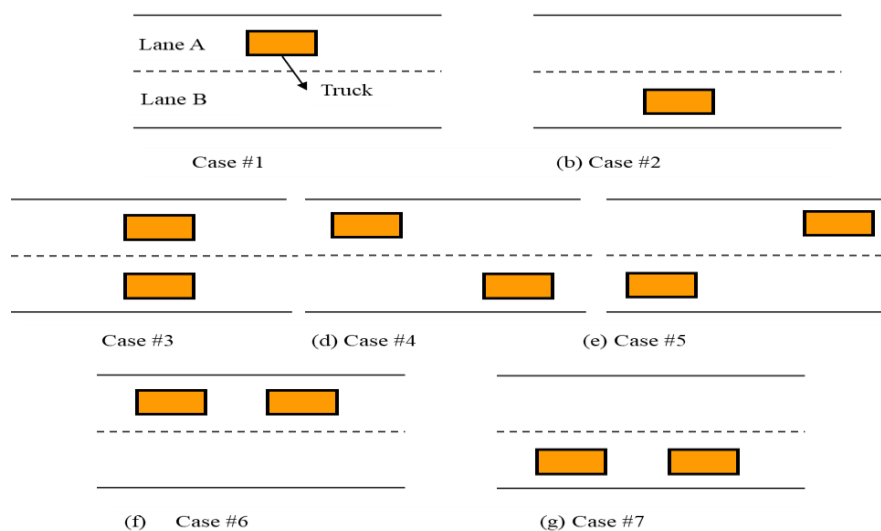


Figure 4.1. Scenarios of trucks traveling on a two-lane bridge

The side-by-side concurrent events include Cases #3, #4, and #5, where two trucks travel on Lane A and B side-by-side simultaneously, as shown in in Figure 4.1c, Figure 4.1d, and Figure 4.1e, respectively. The one-after-another concurrent events include Cases #6 and #7, where two trucks travel on Lane A or B one-after-another simultaneously, as shown in in Figure 4.1f and Figure 4.1g, respectively.

The single-lane events could be detected using the strains from strategically placed strain gauges on the concrete deck bottom of a bridge. When considering the ambient traffic, most trucks tend to travel and stay in the center of a lane. Accordingly, to detect trucks on each lane of a bridge, two gauges are placed under or close to two wheel lines of each truck, respectively (Section 3.1.2). The peaks of strain response due to a wheel line represent the axles of each truck as shown in Figure 4.2a.

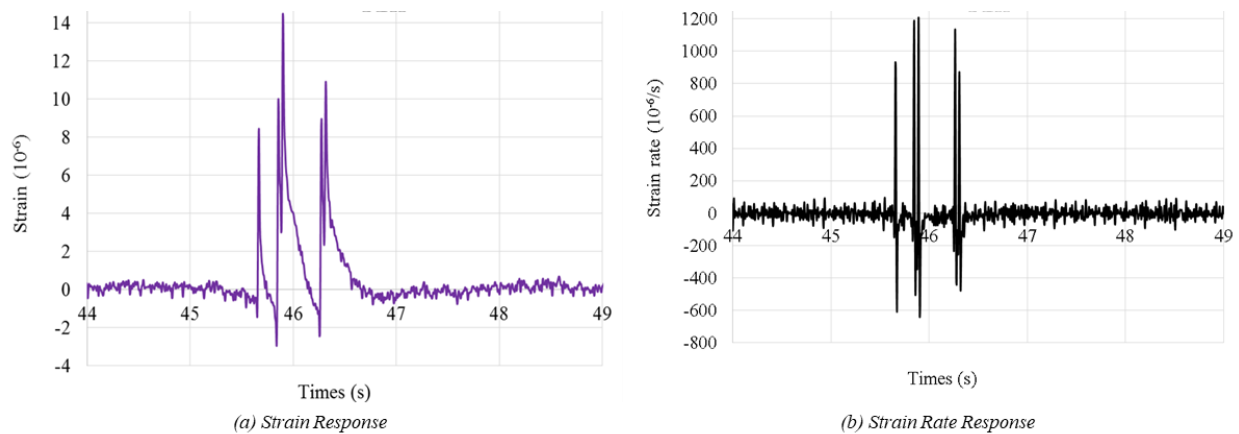


Figure 4.2. Deck strain response due to each wheel line

The strain values are relatively small and affected by the noise and global strain response. The strain rate response can clearly show and exploit the localized strain effects with the elimination of noise and global effects as shown in Figure 4.2b. Note that the peaks of strain rate response due to a wheel line also represent the axles of each truck.

Accordingly, strain rate response is utilized for the development of the truck detection methodology. The truck detection methodology consists of three important parts: (1) event detection – extract single-lane event, (2) lane detection – determine the lane that the truck travels on, and (3) axle detection – determine the number of axles of the detected trucks. Utilizing the proposed truck detection methodology, not only the single-truck events can be detected with the elimination of other events, but also the specific truck types also can be retained in the process. This method can be applied to bridges with different configurations, dimensions, and number of girders. For this project, the single-truck events with a five-axle truck are extracted from the SHM system to perform bridge load rating and damage detection for two reasons: (1) five-axle trucks have the largest truck population based on the weigh-in-motion (WIM) database, and (2) five-axle trucks generally induce large absolute strains in bridges with relatively small influence due to noises.

4.2.2. Procedure of Truck Event and Lane Detection

The fundamentals of truck event/lane detection are as follows:

- If no peak strains are detected in strain deck gauges, no event is found.
- If peak strains are detected in both strain gauges of a lane and no peak strains are detected in all the gauges of other lanes, a single-lane event is found on the bridge.
- If peak strains are detected only in one of the two strain gauges of a lane and no peak strains are detected in the gauges of other lanes, no single-lane event is found on the bridge.
- If peak strains are detected in the strain gauges of a lane and some peak strains are detected in the gauges of any other lanes, a concurrent event is found on the bridge.

Note that if the truck significantly deviates from the lane center on either side, strain peaks will possibly be detected only in the one of the two deck strain gauges in a lane. Such type of single-lane events are also eliminated from the event collection using the lane detection method.

A two-lane bridge shown in Figure 4.3 is taken as an example.

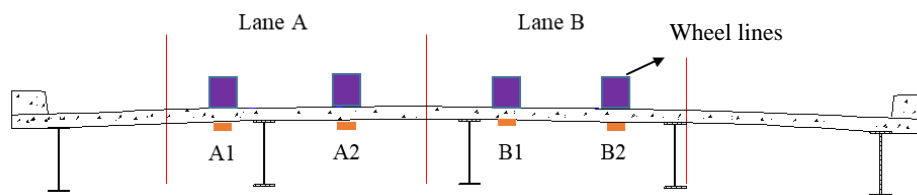


Figure 4.3. Deck sensors installed for a two-lane bridge

The algorithm of single-truck event detection is illustrated in the flowchart shown in Figure 4.4.

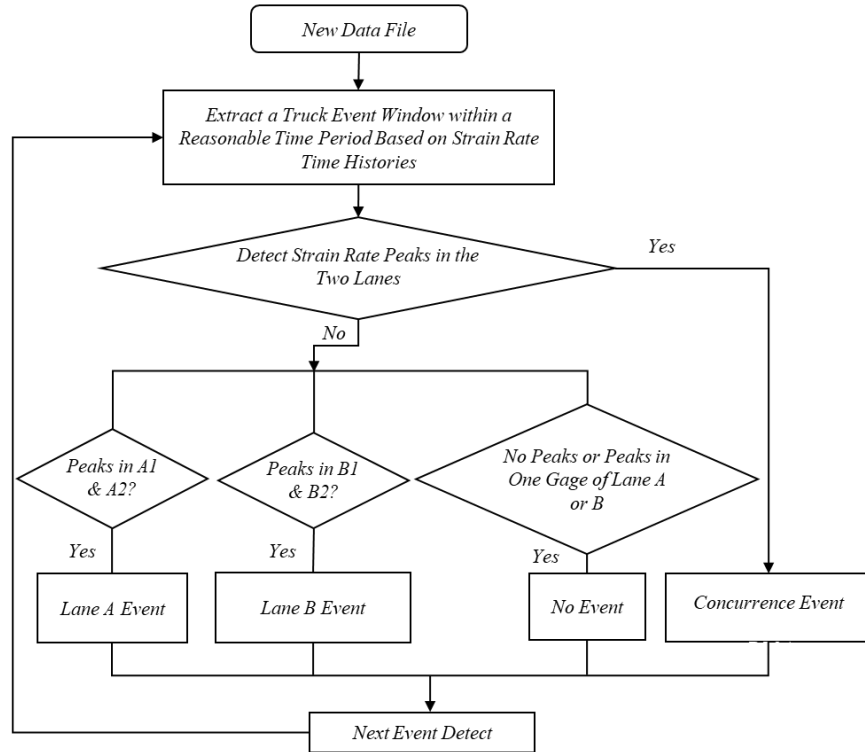


Figure 4.4. Algorithm of single-lane event detection of a two-lane bridge

The records collected by the SHM system are stored in large volumes of continuous one-minute data files. For each data file, a truck event window within a reasonable time period is extracted based on strain rate time histories. The peaks of strain rate response in Lane A (A1 and A2) and Lane B (B1 and B2) will be checked using a peak detection program. If the strain rate peaks are detected in both Lanes A and B, a concurrent truck event is deemed existing in the selected window. Otherwise, the process will be continued for the single-truck event detection. If peaks are detected only in gauges A1 and A2, a single-truck event is found in Lane A. If peaks are detected only in gauges B1 and B2, a single-truck event is found in Lane B. If no peak is detected or peaks are only detected in one gauge (A1 or A2) of Lane A or one gauge (B1 or B2) of Lane B, no event is found. Once the process of the truck detection in the selected window is finished, the process will continue through checking the next window until the end of each data file. Subsequently, the next data file will be loaded, and the same truck detection procedure will be implemented.

The truck event window is determined based on the required distances between the truck on the bridge and the truck off the bridge, which should be larger than the sum of the bridge length and the truck length for single-truck events. For concurrent events, the distance between the two trucks is less than the sum of the bridge length and the truck length for both side-by-side and one-after-another events as illustrated in Figure 4.5a and Figure 4.5b, respectively.

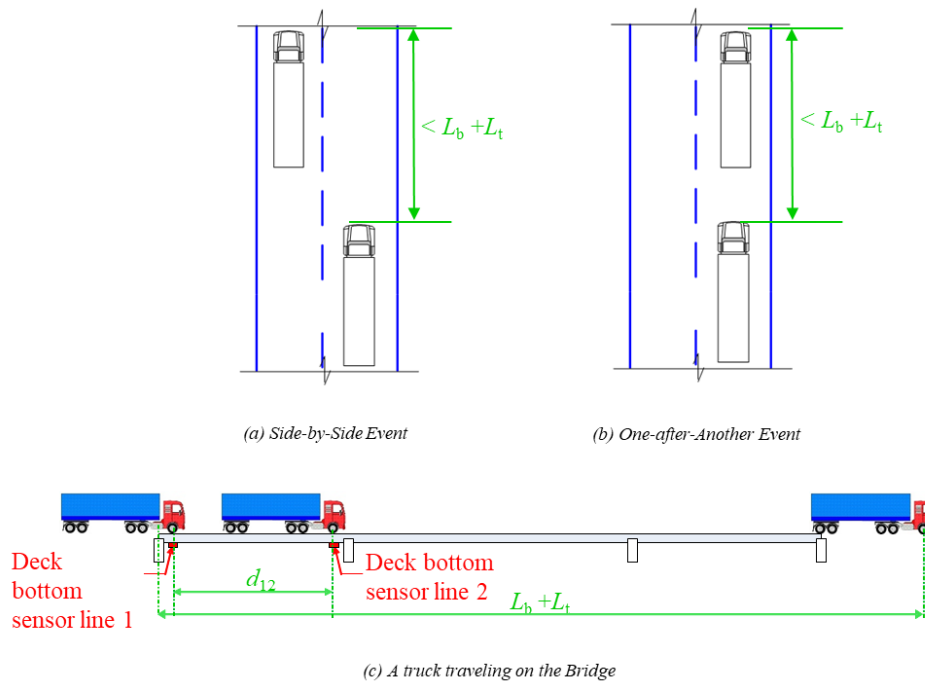


Figure 4.5. Trucks traveling on a bridge

According to Figure 4.5c, the time duration (t_T) for the truck to travel across a bridge can be expressed by equation (1).

$$t_T = (L_B + L_T)/V_T \quad (1)$$

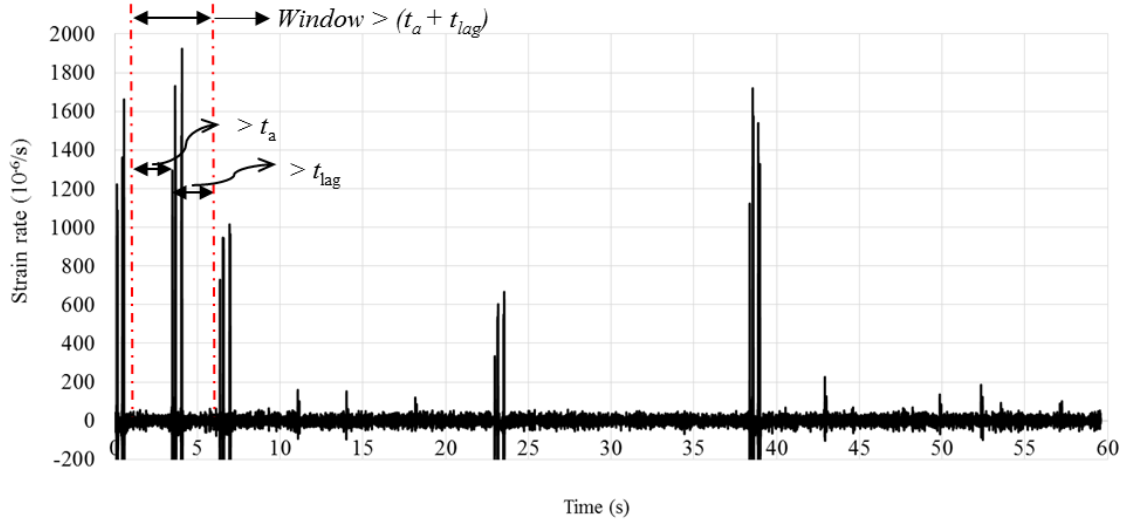
where,

L_B = bridge length

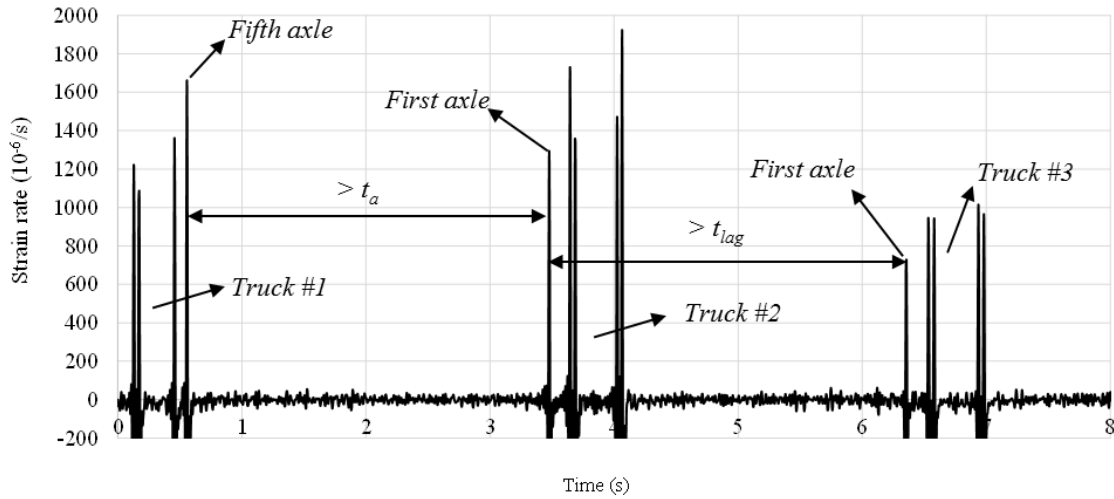
L_T = truck length

V_T = truck speed

A window is selected from a one-minute data file as illustrated in Figure 4.6a.



(a) One-minute Data File



(b) Three Trucks

Figure 4.6. Truck event window selection of strain rate response

Three trucks were detected in the eight seconds of the window and exaggerated details are shown in Figure 4.6b. If the second truck is a single-truck event, the first axle of the second truck advances the fifth axle of the first truck in a certain time (t_a), which can be derived by equation (2).

$$t_a = L_B/V_T \quad (2)$$

And the first axle of the second truck lags behind the fifth axle of the first truck in a certain time period (t_{lag}), which can be derived by equation (3).

$$t_{lag} = (L_B + L_T)/V_T \quad (3)$$

The total time period (t_{tot}) of the selected window should be equal to the sum of t_a and t_{lag} . For a bridge length of 200 ft, truck length of 80 ft, and truck speed of 80 ft/s (54.5 mi/h), the time periods are calculated as follows: $t_a = 200 \text{ ft}/80 \text{ ft/s} = 2.5 \text{ s}$, $t_{\text{lag}} = (200 + 80 \text{ ft})/80 \text{ ft/s} = 3.5 \text{ s}$, $t_{\text{tot}} = (2.5 + 3.5)\text{s} = 6.3 \text{ s}$.

4.2.3. Truck Axle Detection

Axle spacing and travel position can be detected using the strain rate response recorded by gauges in sensor lines 1 and 2 placed on the deck bottom, as illustrated in Figure 4.5c. The truck speed (V) can be determined by equation (4).

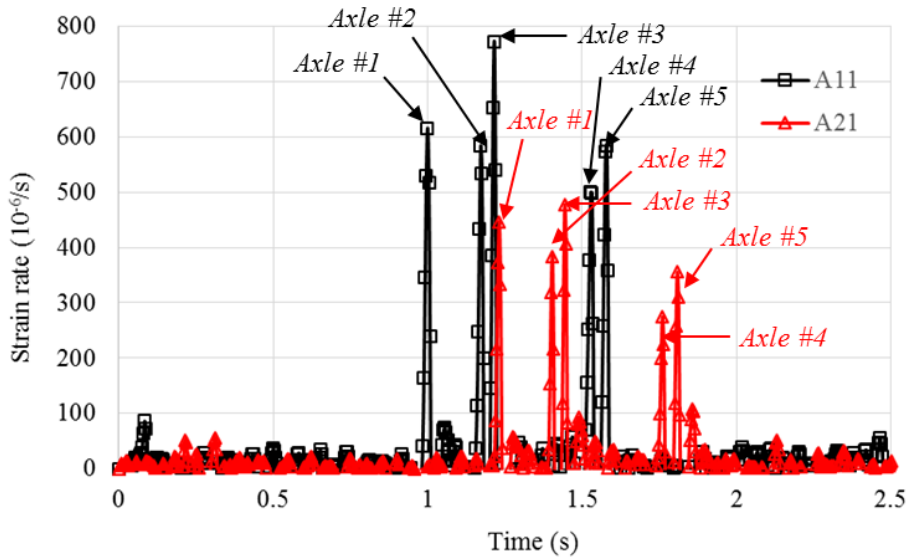
$$V = d_{12}/t_{12} \quad (4)$$

where,

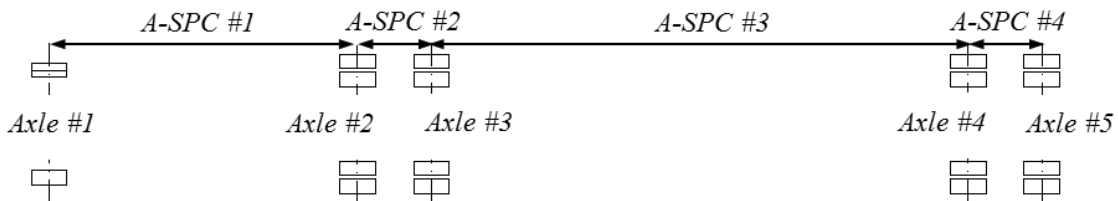
d_{12} = the distance between the two deck bottom sensor lines

t_{12} = the time duration that it takes for the truck to travel from sensor line 1 to sensor line 2

Two longitudinally aligned sensors, A11 and A21 (the first and second numbers in the subscript represent sensor line and gauge, respectively) are utilized for the illustration. Five peak strains, detected by the two sensors, represent the five axles of a truck, as shown in Figure 4.7a.



(a) Peak Strain Rates in Sensors A11 and A21



(b) Five-axle Truck Corresponding to Peak Strain Rates

Figure 4.7. Peak strains induced by a five-axle truck

Five truck speeds can be calculated by equation (4). Note that the values of the five speeds should be close if those peaks are induced by a single five-axle truck. With the calculated speed, the four-axle spacing of the truck (A-SPC #1, A-SPC #2, A-SPC #3, and A-SPC #4 as shown in Figure 4.7b) can then be determined as the product of the speed and timestamp differences between related peak strains in sensors A11 and A21. The travel position of the truck can be correlated with the girder and deck strain data using the truck speed, timestamps of deck peak strains, and locations of sensor lines.

4.2.4. Data Zeroing and Filtering

As mentioned previously, the raw strain data collected in the SHM system were stored in the database consisting of continuously stored one-minute data files. Each one-minute data file contains five strain components: (1) creep- and shrinkage-induced strain response, (2) temperature-induced strain response, (3) noise, (4) quasi-static strain response due to ambient traffic, and (5) dynamic strain response due to the ambient traffic and other dynamic loads such as wind. For this study, the damage detection and structural capacity evaluation are both based on the quasi-static bridge response due to single five-axle truck events, which is a portion of the

fourth strain component. Accordingly, the other four strain components should be excluded from the strain data collected for these truck events.

It is considered that the change of the strain response due to creep, shrinkage, and temperature change with a one-minute period are very small and can be neglected during the data processing, which was also discussed by Wipf et al. (2007) and Lu et al. (2010). However, the strain response due to due to creep, shrinkage, and temperature change, which is almost constant in each data file, needs to be eliminated. To zero the strain response for each one-minute data file, a constant baseline strain should be determined for each strain sensor as shown in Figure 4.8a.

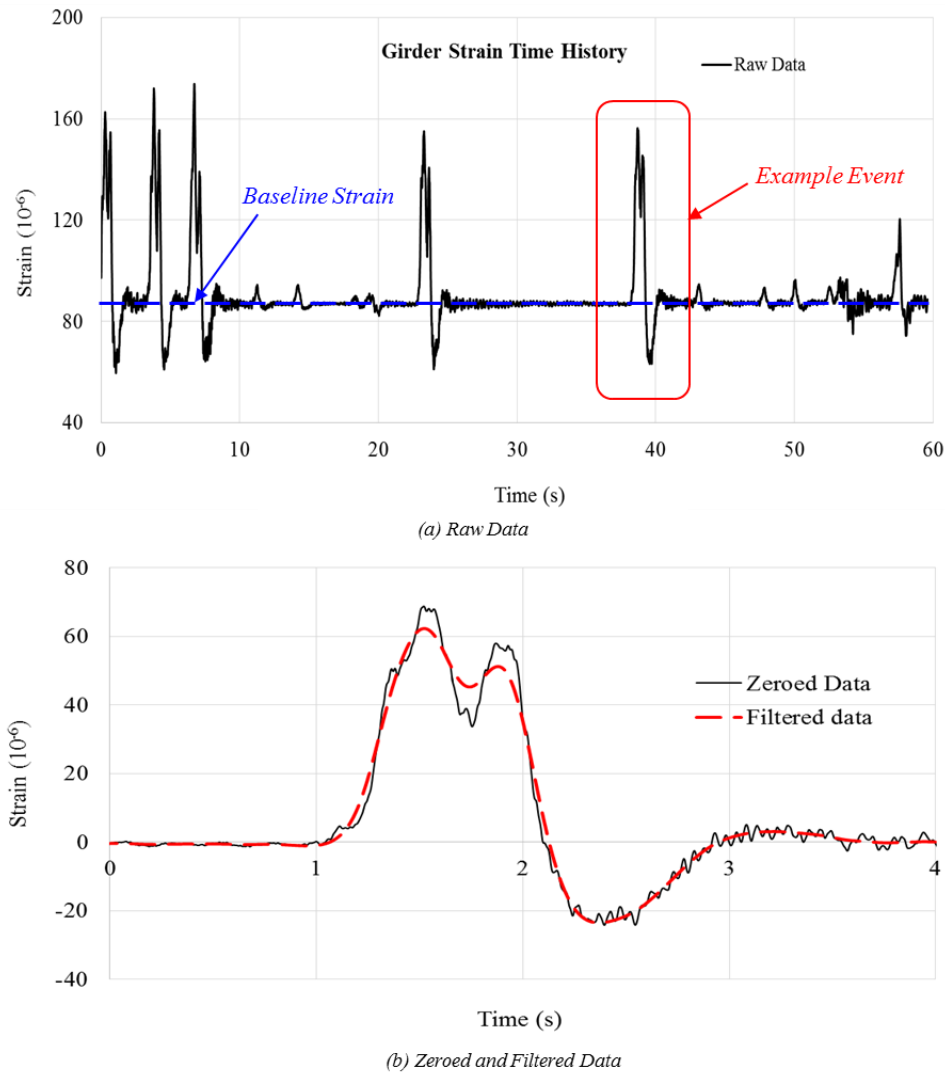


Figure 4.8. Raw, zeroed, and filtered data of a sensor for a five-axle truck event

The baseline strain for each sensor can be identified through searching the mode of the sensor data, which represents the value most frequently occurring in the one-minute data collection (Lu et al. 2010). The raw strain data of each sensor can then be zeroed with respect to the baseline

strain to eliminate the creep, shrinkage, and temperature induced strain components. An example of zeroed strain data of a sensor for a single-truck event is shown in Figure 4.8b.

Strain components (1) and (2) can be eliminated through the zeroing process. The remaining data still contains the unexpected strain components (3) and (5) due to the noise and structural dynamic effects and also should be excluded. Since the frequency contents of the strain response due to noise and dynamic effects are generally higher than those of the quasi-static bridge response, a low-pass digital filter can be designed and utilized to exclude the high-frequency contents. For this study, the low-pass Chebyshev filter is used to filter the raw data, removing the dynamic strain responses and the high-frequency noise components. Further, the zero-phase filter is utilized to avoid the phase shift during the data filtering process. A ripple of 0.5% for the low-pass Chebyshev filter, which is deemed a good option for digital filters (Smith 1997), is selected. To determine the cut-off frequency, the fast Fourier transform (FFT) should be used to derive the plot of the power spectral density (PSD) for different frequency components. For this study, one-hour data files (including 60-minute data files) are utilized to produce the PSD plot for each sensor. An example PSD plot for a one-hour data file is illustrated in Figure 4.9.

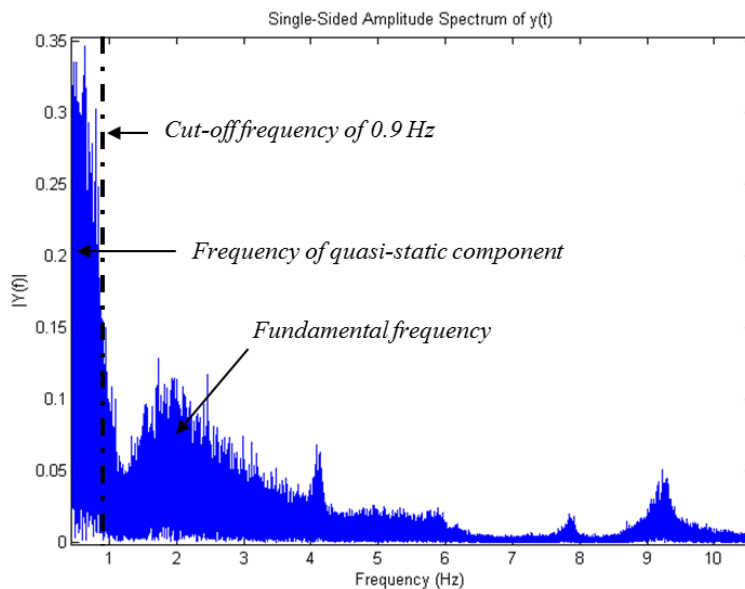


Figure 4.9. Peak strains induced by a five-axle truck

Figure 4.9 indicates that the quasi-static strain response has a relatively lower frequency content compared to the fundamental frequency of the bridge. The cut-off frequency should be determined to retain the frequency content of the quasi-static strain response, which is equal to 0.9 Hz for the demonstrated example as shown in Figure 4.9. The strain time history of the filtered data for the example truck event is illustrated in Figure 4.9. Figure 4.9 indicates that the majority of the dynamic effects are removed from the strain response. Since the PSD plots are different for different sensors, the cut-off frequency for each sensor should be determined based on its PSD plot accordingly.

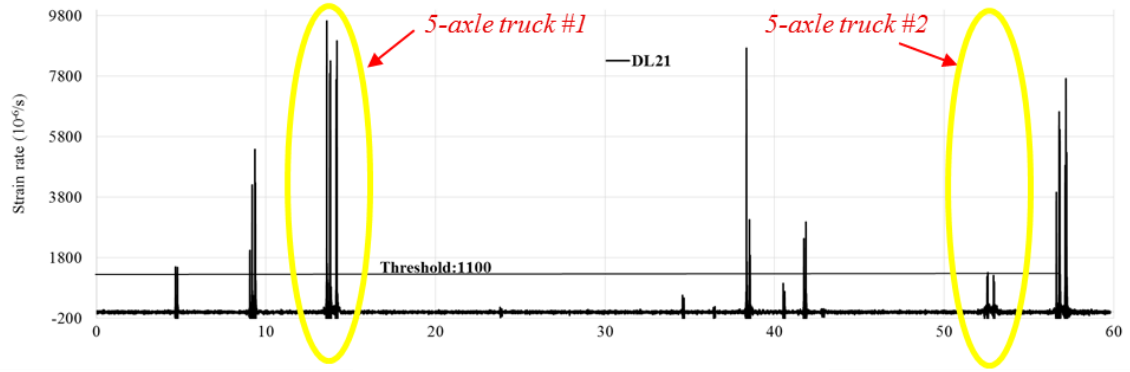
4.3. Validation of Truck Detection Approach

A camera was temporarily set up on the demonstration bridge and captured the traffic for 25 minutes. The videos and collected bridge response were utilized to validate the adequacy of the truck detection approach. The truck detection process is demonstrated herein using a one-minute data file. The file includes two single-truck events, five-axle trucks #1 and #2, as shown in Figure 4.10a and Figure 4.10b, respectively.

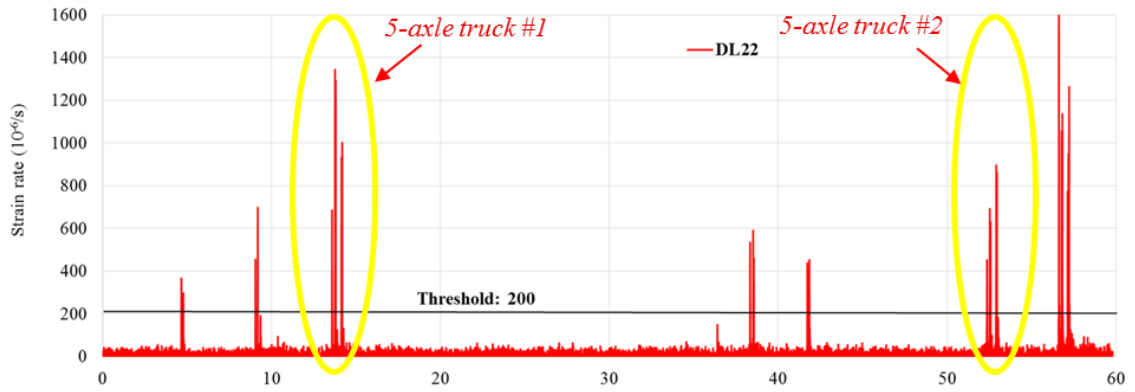


Figure 4.10. Two example trucks

Since the two deck sensor lines show similar results, sensor line 2 is selected as an illustration. As shown in Figure 4.11, strain rate response in the sensors DL21 and DL22 of the south lane indicates that the five-axle truck #1 was detected on the south lane.



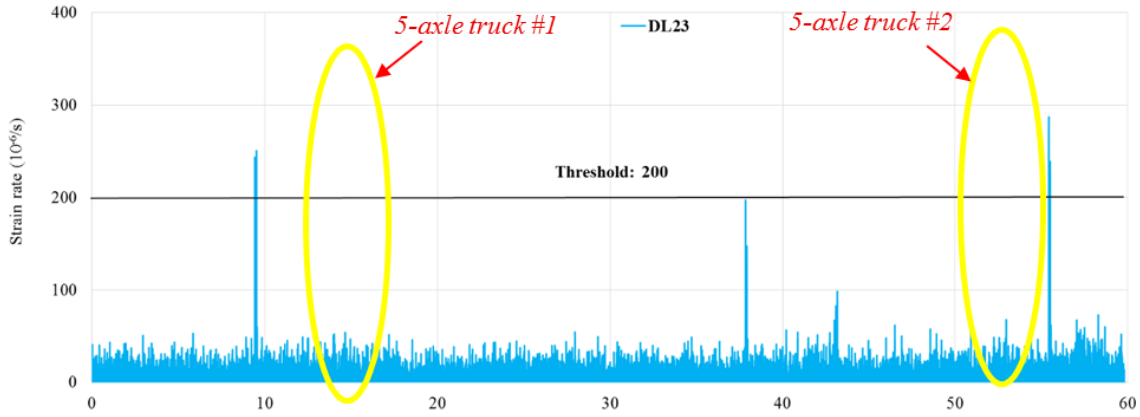
(a) Sensor DL21



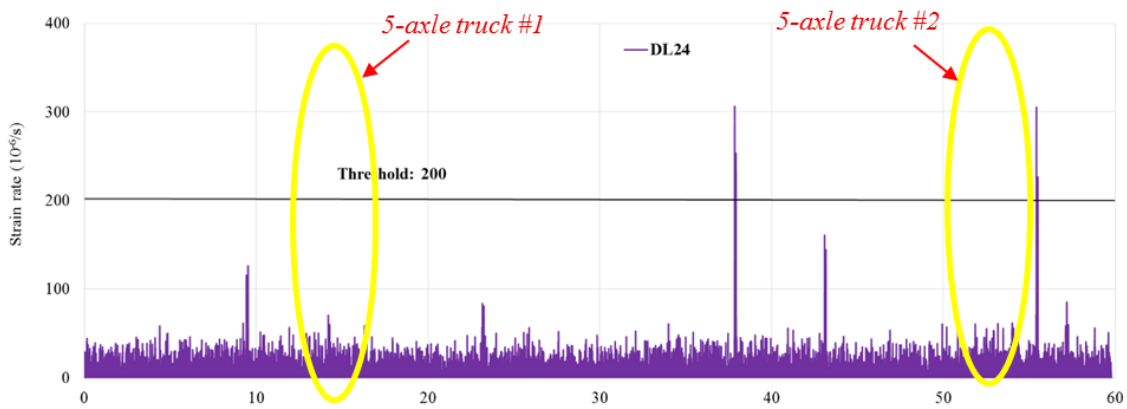
(b) Sensor DL22

Figure 4.11. Two deck sensors of south lane – sensor line 2

As shown in Figure 4.12, strain rate response in the sensors DL23 and DL24 of the north lane indicates that no truck was detected on the north lane.



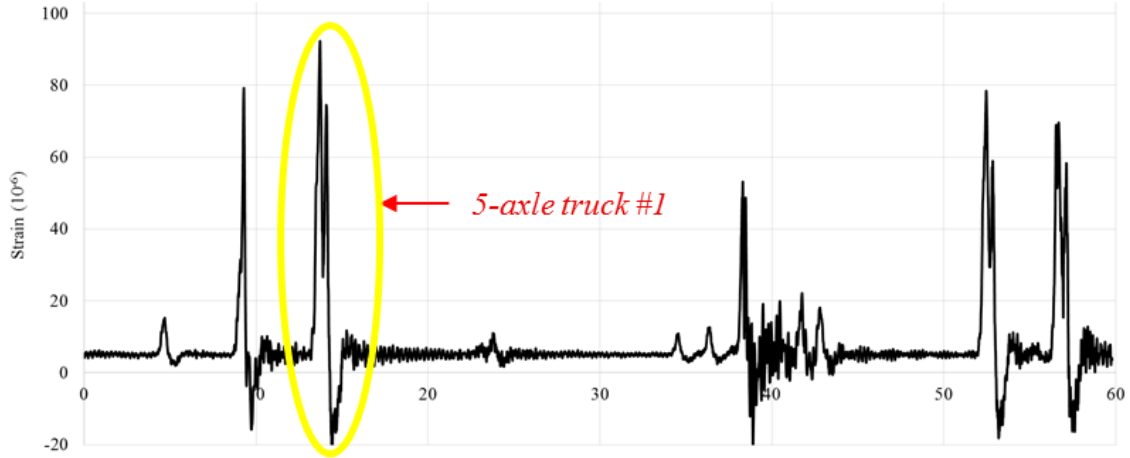
(a) Sensor DL23



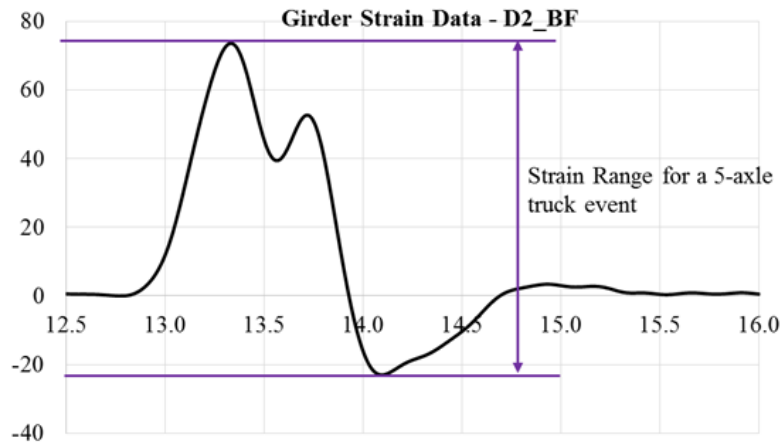
(b) Sensor DL24

Figure 4.12. Two deck sensors of north lane – sensor line 2

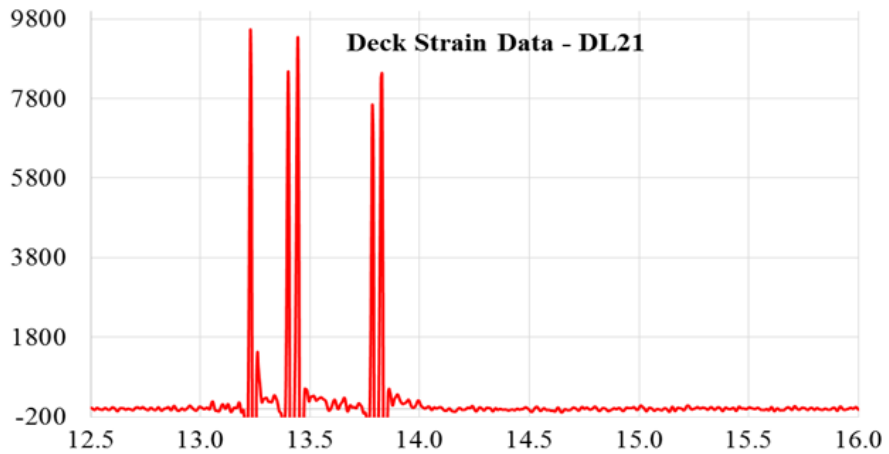
Five-axle truck #1 induced a single-truck event. However, the strain rate response in sensor DL21 due to truck #2 was below the threshold although the strain rate response in sensor DL22 was detected. This is due to the fact that five-axle truck #2 gradually changed lanes when it traveled across the bridge as shown in Figure 4.10b. Since there are no other trucks on the north lane, no strain rate response in sensors DL21 and DL22 was detected as truck #2 traveled across the bridge. Consequently, the single-truck events without lane changes were successfully detected using the truck detection approach. It should also be noted that the truck detection approach has been further validated using trucks in a total of 25 one-minute data files. Figure 4.13 shows the single-truck event due to five-axle truck #1.



(a) Raw Girder Strain Response – Sensor D2_BF



(b) Girder Strain Response – D2_BF



(c) Deck Strain Rate Response – DL21

Figure 4.13. Single-truck event due to five-axle truck #1

4.4. Summary and Conclusions

The fundamentals and procedures of the truck detection methodology for single-truck event detection, lane detection, and truck axle detection through the use of the SHM system were presented. The statistical and analytical processes needed to zero and filter the collected data from detected single-truck events were presented. The adequacy of the truck detection methodology was validated using collected data on an I-80 bridge instrumented with an SHM system.

CHAPTER 5. STRAIN-BASED BRIDGE DAMAGE DETECTION

5.1. Introduction

5.1.1. Background

US infrastructure continues to deteriorate, and bridge inspections continue to play a crucial part in ensuring the safety of all who cross over the bridges. SHM is becoming more prominent throughout the US, and it has been widely studied and investigated during the past two decades.

Concerns regarding the current structural condition of bridges has been raised due to recent catastrophes on bridges such as the I-35 bridge in Minneapolis, Minnesota in 2007 and de la Concorde Overpass in Quebec, Canada in 2006 (Mosavi Khandan Haghghi 2010). In the 2009 Bottom Line Report, AASHTO announced that 73,000 bridges in the US were structurally deficient in 2007. When viewed from this perspective, there are still a large number of bridges in the US that are in routine use without enough information regarding their current structural condition (AASHTO 2009).

In the initial stages of SHM, it has been shown that periodic visual inspections may not be as reliable as desired (Lu 2008). Many SHM systems have been proposed to improve methods to increase the overall safety of bridges. These developments have been, in part, driven by a desire to have continuous feedback on system performance. Departments of transportation are looking toward methods of measuring the structural integrity of highway bridges.

Since 2003, a strain-based damage detection algorithm for the US 30 bridge over the South Skunk River has been developed and studied by the BEC. For the first generation of the damage detection algorithm, a long-term monitoring system was developed with novel data management processes by including automated data zeroing, filtering, and extrema identification (Doornink 2006). Two important advancements were made to improve the detection capabilities and to remove user subjectivity for the second generation of the damage detection algorithm. First, a vehicle identification system was developed, and second, the algorithm named the cross-prediction method was quantified using traditional linear regression together with a statistical control chart by Lu (2008).

For the efficacy of the cross-prediction approaches, an experimental validation was conducted by constructing a sacrificial specimen. The specimen was mounted to an in-service bridge and exposed to ambient traffic loads to try to induce fatigue cracks (Phares et al. 2011). The results showed that the damage detection algorithm detects structural damage well. Unfortunately, a relatively high false indication rate was also observed. Therefore, the statistical F-test using orthogonal linear regression was proposed as a means to improve overall system performance (Phares et al. 2011).

A damage detection process based on statistical control charts, using continuous strain range data, was developed. Four strain-based damage detection methodologies: (1) one-truck event, (2)

truck events grouped by 10, (3) cross prediction, and (4) F-tests were investigated and compared using a control chart methodology. False indication and true indication rates were compared for damage detection ability (Phares 2001).

An objective of this research was to minimize strain range uncertainty on the damage detection algorithm. Influences of temperature and truck configuration were investigated to reduce the strain range variability as well as false indication rate. Additionally, a strain-based damage detection algorithm, F_{shm} method, was further advanced. Strain range data are filtered into temperature bins and axle spacing for all five-axle trucks and semi-trucks. The three F_{shm} limits on the damage detection method were investigated to evaluate reducing false indication rates. Six sigma, base data, and training data methods are introduced. Proposed thresholds on F_{shm} methods were further investigated and then analyzed in terms of false-indication.

5.2. Literature Review of Damage Detection Methods

Damage detection, as a part of an SHM system, is the means of determining if damage exists in the structure by evaluating changes in modal parameters, differences in strain, or other changes in behavior over time. Various damage detection algorithms have been proposed based on different mechanical principles. Sohn et al. (2004) classified damage detection into two categories: dynamic-based or static-based.

For dynamic-based damage detection algorithms, dynamic response parameters, such as natural frequencies, modal shape, and damping, are employed. There are attractive features to the dynamic-based damage detection approach, but it also has limitations. One limitation, for example, is that changes in dynamic properties occur due to the variation in excitation or environmental conditions. Also, there are sensitivity issues when using global dynamic parameters to detect local damages in a small structural response region. Furthermore, a dynamic-based approach may result in reductions in sensitivity due to redundancies associated with a highway bridge (Lu et al. 2007).

Autoregressive models (AR) fit to the measured acceleration-time histories were selected as the method for damage detection. Residuals, differences in quantity from AR model and observed measurements, are used as the damage detection feature (Fugate et al. 2001). Statistical control chart methodology was applied to this approach by employing the identification of model parameters to extract damage sensitive features such as natural frequencies, mode shape, and damping ratio from the response data (Kullaa 2003).

More recently, damage detection methods based on principal component analysis (PCA) were introduced and applied to vibration features under varying environmental and operational conditions. In the PCA method, environmental parameters, assumed as a linear effect on vibration features, were considered as embedded variables and a statistical indication of damage was identified using the residuals from the PCA prediction model (Yan et al. 2005). Another study focused on the effects of changing environmental conditions using factor analysis. The multivariate Shewhart-T control chart was introduced as the damage detection tool (Deraemaekera et al. 2008). To minimize the effect of environmental and operational factors on

the bridge's natural frequencies, static and dynamic regression models were developed for a concrete arch bridge and complemented by a PCA (Magalhaes et al. 2012). However, these studies were limited by relying on dynamic parameters.

Due to the limitations on dynamic-based damage detection, strain-based (non-dynamic) damage detection methods were introduced and then investigated by the BEC. A strain-based damage detection algorithm is beneficial because there is no requirement to convert to a different type of parameter (i.e., dynamic parameter) and also strain data can be used directly in the algorithm. Further details of strain-based damage detection methods are discussed in the next section.

5.3. Strain-Based Data for Identifying Damage

In 2007, a long-term SHM system for detecting damage autonomously using strain as the monitoring metric was developed (Doornink 2006). The demonstration bridge used during this development has three spans with two equal outer spans with a skew of 20 degrees. The superstructure consists of 2 continuous welded steel plate girders, 19 floor beams, and 2 stringers. A total of 40 fiber optic strain gauges were installed on the bridge to measure strain under ambient traffic loads. The complete monitoring system is more fully described in Doornink (2006), Lu (2008), and Phares et al. (2011).

5.3.1. Strain Data Identification

Raw strain data was collected and processed for data zeroing, filtering, and extrema identification. To remove short-term temperature effects, data zeroing was conducted by subtracting a constant temperature offset from data collected in small increments. After zeroing, data filtering was carried out to obtain a strain data set that represents the quasi-static response of the bridge under ambient traffic loads. The strain data from each vehicular event are then reduced to the maximum and minimum strain values.

Relationships between two strain sensors, target sensors (TSs), where damage might be expected, and non-target sensors (NTSs) were designated. The “training” process defined the normal behavior of the system with relationship limits for each sensor pair determined manually. Examples of matched data from two sensors with limits are shown in Figure 5.1.

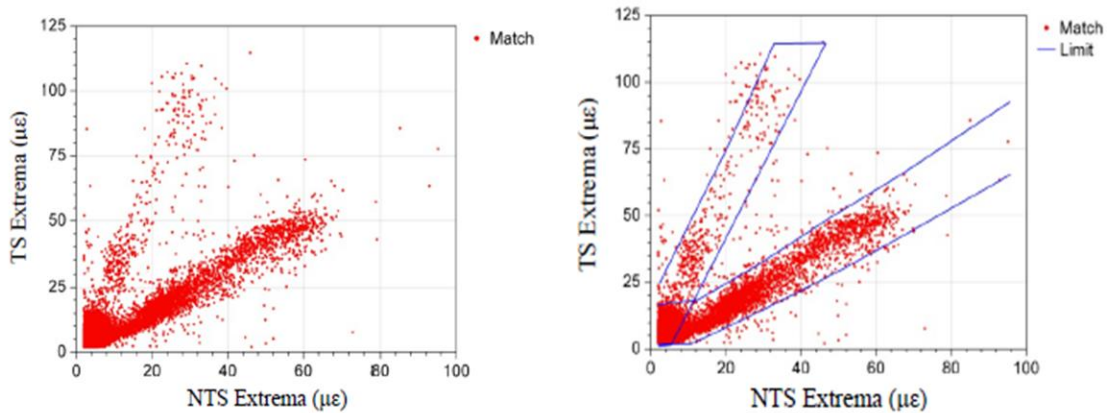


Figure 5.1. Example of matched data from two sensors with applied limits

Following training, during which the limits of normal behavior are defined, subsequent truck events would then be compared to the limits. A pass assessment defines a point within the limits and a fail assessment defines data outside of the limits.

5.3.2. Truck Parameter Identification

Vis (2007) developed a finite element (FE) model, which simulated damage, in “Evaluation of a Structural Health Monitoring System for Steel Girder Bridges.” It was shown in his work that natural variability exists due to truck parameters such as the number of axles and the transverse position of the truck (e.g., left lane or right lane). Vis indicates that removing this variability would likely enhance the ability to detect.

To deal with uncertainties identified by Vis, a second-generation damage detection algorithm was developed by Lu (2008) to improve the approach by including truck parameters such as the travel lane, number of axles, speed, axle spacing, and truck weight. The truck travel lane was determined by sensors installed on the girder closest to the vehicle travel lane. A truck axle detection algorithm utilized sensors placed on the bottom of the deck near the truck wheel line. Truck weight was categorized as either heavy or light.

The damage detection algorithm developed by Lu (2008) utilized strain data from only right-lane, five-axle heavy trucks. Lu also determined that the strain range (i.e., the difference between the maximum and minimum strain during the truck event) is more effective in damage detection than using both the maximum and minimum strains.

5.3.3. Cross Prediction Method

A linear regression model was developed to predict the relationship between each two sensor strain range pairs for multiple trucks (Lu 2008). The residual was defined as the difference between the measured strain range and the predicted strain range data as follows:

$$\text{Residual}(i, j) = \text{Measured Strain Range}(i, j) - \text{Predicted Strain Range}(i, j) \quad (5)$$

With the residual, an $n \times n$ residual matrix could be created for each truck event. The information was reduced to an n degree vector in which element i represented the residual for sensor i and was defined to be the combined-sum-residual equal to the sum of row i minus the sum of column i for each truck. An example of sample distributions for the combined-sum-residuals are shown in Figure 5.2.

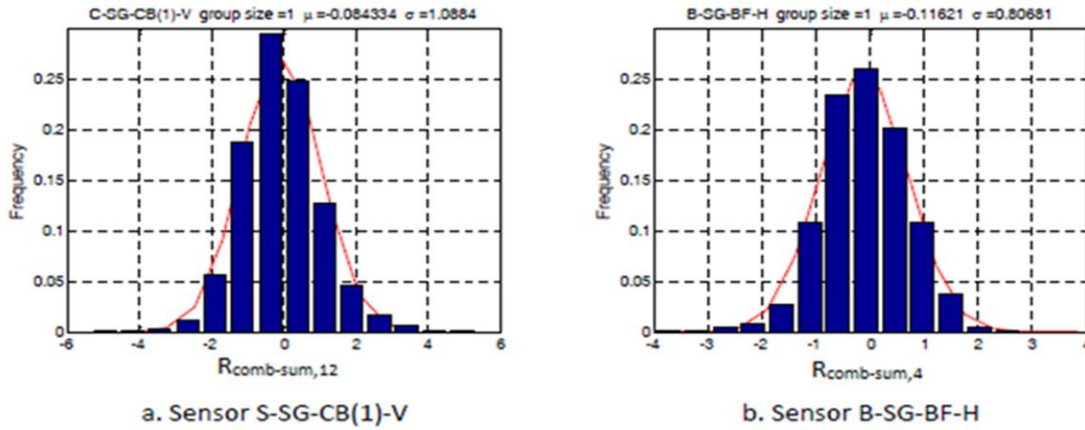


Figure 5.2. Example of sample distribution for the combined-sum-residuals

With the n degree vectors, one for each truck, resulting from the combined-sum residual, Shewhart \bar{x} control charts, typically used for process control, could be constructed as a strategically defined damage indicator for each sensor by plotting the residual values versus truck event.

Multiple events were grouped together to form one point on these charts and a group size of 10 consecutive trucks for each point was determined. Based on the observed normal distribution pattern in Figure 5.2, the upper control limits (UCL) and the lower control limits (LCL) were set as shown in equation (6).

$$\text{UCL} = \bar{R} + 3s \quad (6a)$$

$$\text{LCL} = \bar{R} - 3s \quad (6b)$$

Where \bar{R} and s are the mean and standard deviation of the combined-sum-residuals, respectively. A sample control chart (Lu 2008) is shown in Figure 5.3.

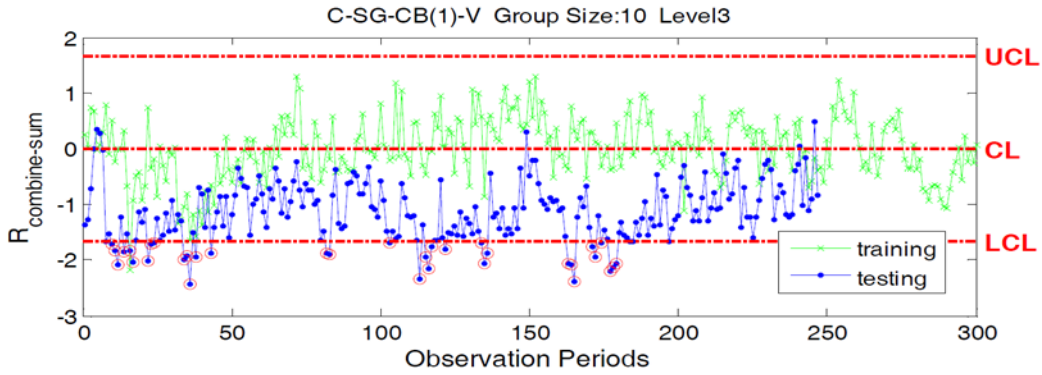


Figure 5.3. Sample control chart

An indication of possible structural damage was defined when points are out of limits on the control charts. To check the sensitivity of the damage detection approach, the probability of detection (POD), which equals the ratio of the number of detections to the total number of events, was investigated.

5.3.4. Experimental Validation

For validation of the cross-prediction damage-detection algorithm, a sacrificial specimen simulating the floor-beam web gap region was fabricated for the US 30 bridge (Phares et al. 2011). The specimen was integrated into the bridge in such a way that it responded to traffic loads but did not create a safety concern with the introduction of damage. The sacrificial specimen consisted of two web gaps connected by a steel plate. In this configuration, the sacrificial specimen simulated the double curvature bending occurring within the web gap regions. The sacrificial specimen and double curvature bending phenomena is shown in Figure 5.4.

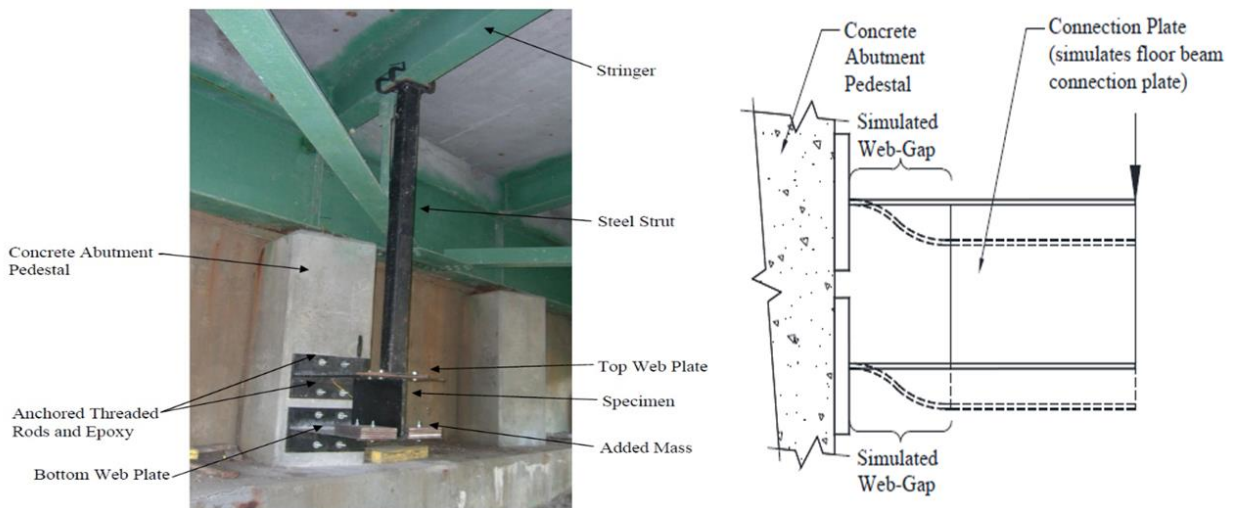


Figure 5.4. Typical installed sacrificial specimen and double curvature bending of sacrificial specimen

The cross-prediction damage detection methodology described in Section 5.3.3 was applied to the data obtained from the sacrificial specimens to evaluate its effectiveness in detecting damage. The methodology worked quite well, but results showed a relatively high false indication rate (Phares et al. 2011).

5.3.5. Orthogonal Regression and Statistical Evolution Approach

To reduce the relatively high false indication rate in the cross-prediction damage detection method, the use of an orthogonal linear regression and the statistical F-test concept were proposed and developed. The most common use of orthogonal linear regression is in comparing two measurement systems that have similar values (Carroll and Ruppert 1996). In other words, the y measurement variation and the x measurement variation are both the same. A traditional linear regression assumes that the x variable is fixed and the y variable is a function of x plus variation. Samples of standard linear regression and orthogonal linear regression are shown in Figure 5.5.

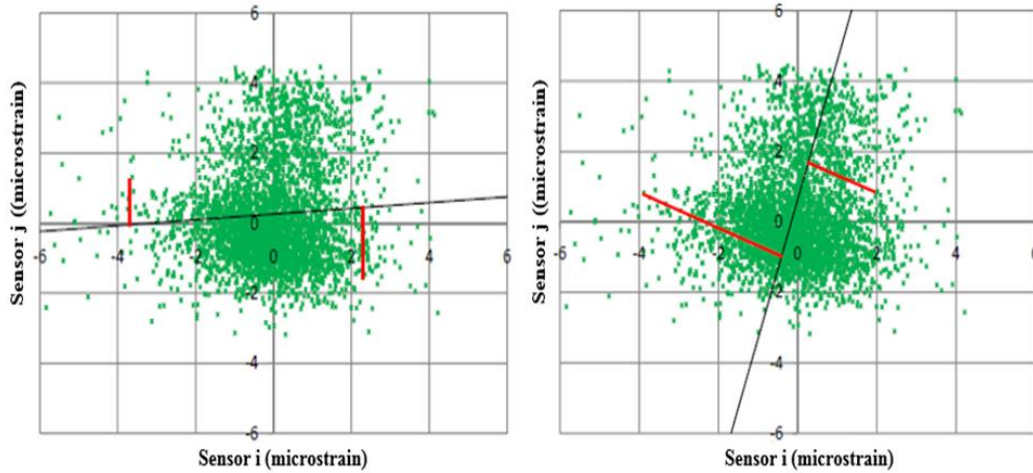


Figure 5.5. Sample standard linear regression and sample orthogonal linear regression

The vertical lines in the left figure represent the residuals in the y-direction and sloping lines in the right figure show the orthogonal residuals.

As with any linear regression, y and x are linearly related through the following:

$$y = mx + b \quad (7)$$

The equation for standard linear regression can be developed by minimizing the sum of the square of the residuals in the y direction, while the sum of the squares of the perpendicular residuals is minimized in orthogonal linear regression as shown in equation (8).

$$r_i = \frac{y_i - b - mx_i}{\sqrt{m^2 + 1}} \quad (8)$$

When the strain range data are in the first quadrant system, an orthogonal residual is defined. An example of an orthogonal line fit and an orthogonal residual are shown in Figure 5.6.

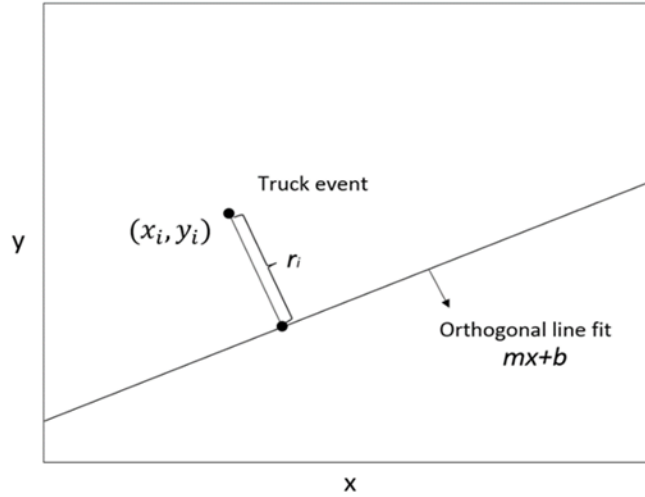


Figure 5.6. Example of an orthogonal line fit and an orthogonal residual

The sum of the squares of the perpendicular residuals r_i (SSR) from the data points to the regression line are given by the following:

$$SSR = \sum_{i=1}^n r_i^2 \quad (9)$$

Minimizing SSR results in (Carroll and Ruppert 1996, Fuller 1987) the following:

$$m = \frac{(S_x^2 - S_y^2 + \{(S_x^2 - S_y^2)^2 + [4S_{xy}]^2\}^{(1/2)})}{[2S_{xy}]}$$
(10)

$$b = \bar{y} - m\bar{x} \quad (11)$$

where S_x^2 and S_y^2 are the variance of the x and y data, respectively, and S_{xy} is the covariance of x and y that can be written $\gamma_{xy}S_xS_y$ in which γ_{xy} is the correlation coefficient.

5.3.6. Damage Detection Approach with F-Test

The F-test is typically used to compare two different data sets. Generally, the purpose of the F-test is to quantify the amount of model improvement with additional variables by comparing the sum of squares residual of a reduced and a full model with respect to each degree of freedom. The full model, the more complex model, which contains more variables than the reduced model is taken in Phares et al. (2011) to be as follows:

$$y = (\alpha_1 + \alpha_3x) + Z(\alpha_2 + \alpha_4x) \quad (12)$$

When Z is equal to zero, α_1 and α_3 are parameters from an orthogonal linear regression through the training data, and similarly, when Z is equal to one, α_1 plus α_2 and α_3 plus α_4 are the parameters from orthogonal linear regression through the post training data. The reduced model must be nested in the full model as follows:

$$y = \alpha_5 + \alpha_6 x \quad (13)$$

where, α_5 and α_6 are parameters from an orthogonal linear regression through all the data (training and post training). An example of orthogonal fit lines for the full and reduced model is shown in Figure 5.7.

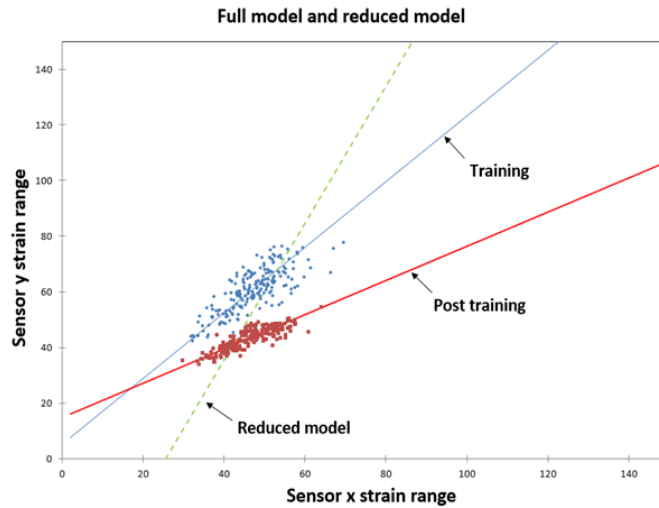


Figure 5.7. Orthogonal fit lines for the full and reduced models

With the full and reduced model, one must test the similarity hypothesis:

$$H_0 \text{ (Null hypothesis): } \alpha_2 = \alpha_4 = 0$$

$$H_A \text{ (Alternative hypothesis): } \alpha_2 \text{ or } \alpha_4 \neq 0$$

If H_0 is true, then the reduced model is statistically the same as the full model as graphically demonstrated in Figure 5.8a, and it can be concluded that there is no damage at those two sensor locations.

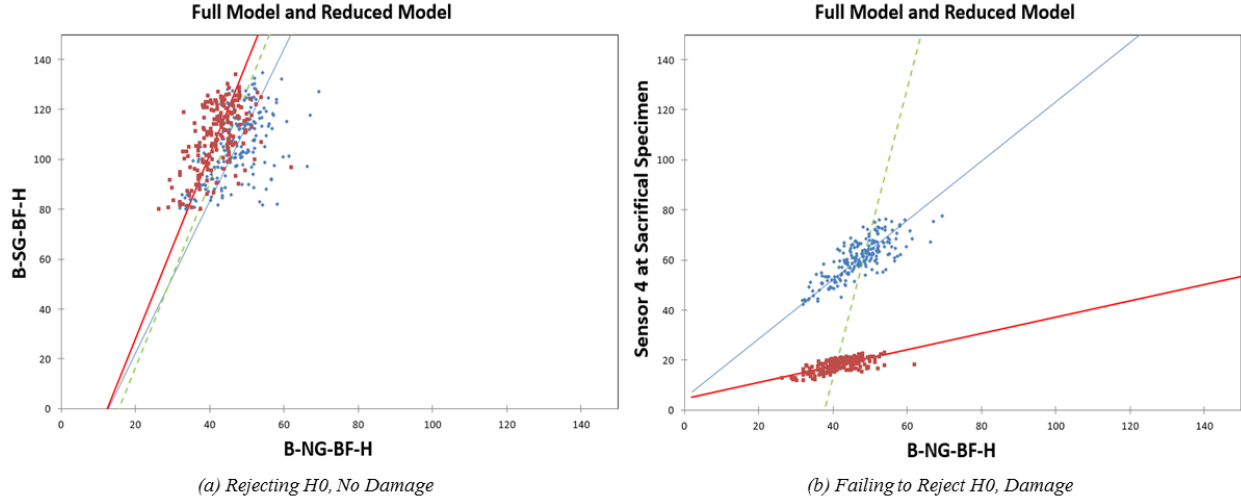


Figure 5.8. Graphical representation of the test of hypothesis

On the other hand, if H_0 is rejected, which is graphically illustrated in Figure 5.8b, the reduced model is significantly different from the full model and it may represent an indication of damage.

To quantify the test, the F-test is conducted with a null hypothesis ($\alpha_2 = \alpha_4 = 0$). In general, the F statistic is defined as follows:

$$F = \left(\frac{SSR_{\text{Reduced}} - SSR_{\text{Full}}}{df_{\text{Reduced}} - df_{\text{Full}}} \right) \div \left(\frac{SSR_{\text{Full}}}{df_{\text{Full}}} \right) \quad (14)$$

where SSR_{Reduced} is the sum of squares residual of reduced model and SSR_{Full} is the sum of squares residual of full model (training and post training) as given in equation (14). df_{Reduced} and df_{Full} are the degrees of freedom of the reduced and full models, respectively. For the case of the models in equations (15) and (16),

$$df_{\text{Reduced}} = n - 2 \text{ and } df_{\text{Full}} = n - 4 \quad (15)$$

because the reduced and full model has two terms and four terms in the model, respectively, and n represents the number of truck events, that is:

$$n = n_{\text{Training}} + n_{\text{Post-Training}} \quad (16)$$

Where, n_{Training} is number of trucks in the training data and $n_{\text{Post-Training}}$ is number of trucks in the post-training data set.

5.3.7. F-Test Control Chart Method

The statistical F-test was modified to the F_{shm} method to be used as a damage detection approach. The F-test has been further expanded to the F_{shm} approach to include control chart concepts such that condition can be tracked with time. A flow chart for the F_{shm} test control chart is shown in Figure 5.9.

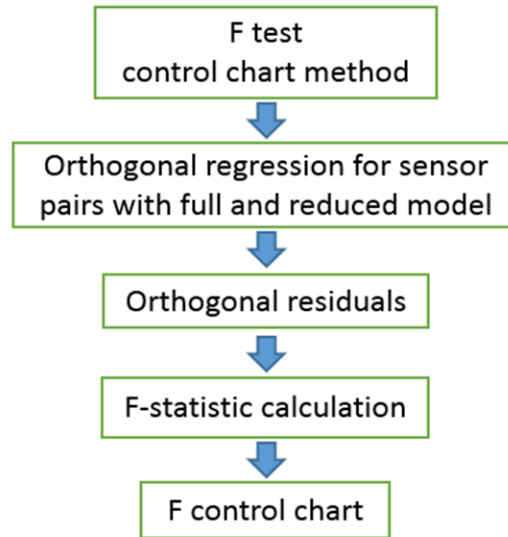


Figure 5.9. Flow chart for F-test control chart

As an initial step of constructing the F_{shm} control chart, the first 200 truck events recorded during training were designated as the baseline data and were the point of comparison for all subsequent evaluations. For truck events from 201 to 2,000, groups of 200 trucks were assigned by increasing 50 truck events for the next set of 200 data and then compared against the baseline data with the F-test equation. It enabled all of the F_{shm} values to have same sample size (200 from baseline data and another 200 for a comparison) and created a total 33 F_{shm} values. Collectively, this series of F_{shm} values were used to establish the means and standard deviations for all such evaluations made during the training period. The means and standard deviations then established the control chart limits for each sensor pair. An example of F_{shm} control chart is illustrated in Figure 5.10.

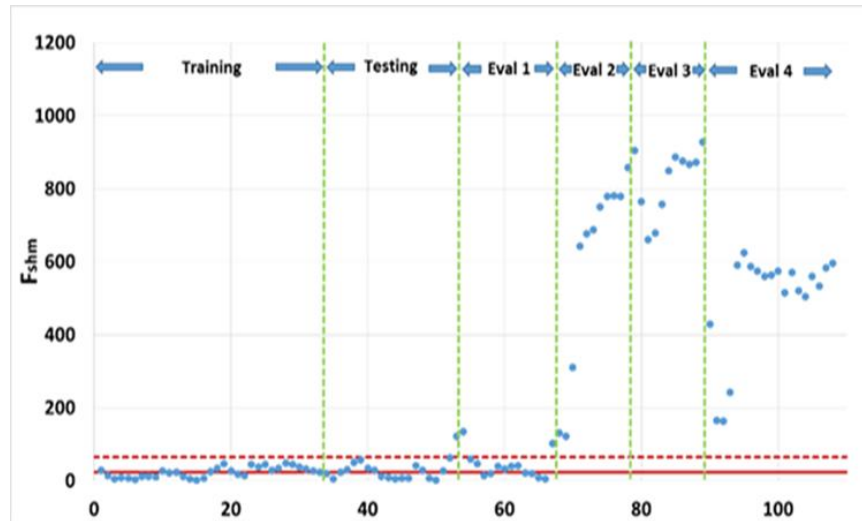


Figure 5.10. Example of F_{shm} control chart for web gap sensor 4 at sacrificial specimen vs. sensor in negative moment at bottom flange of north girder

For the F_{shm} damage detection approach, control charts were divided into three regions: training, testing, and evaluation. The first region was the training period, where strain range data were obtained from truck events from the presumed undamaged structure. Following the training period, the testing period typically included 1,000 truck events utilized to evaluate the efficacy of the training period. The evaluation period was for monitoring the bridge for changes in structural performance (e.g., possible damage).

The US 30 bridge project included additional tasks beyond the information provided earlier in this section. Some of those tasks included collecting ambient data after inducing three controlled cracks in the sacrificial specimen one test at a time. The evaluation region was subdivided into Evaluation 1, Evaluation 2, Evaluation 3, and Evaluation 4, representing varying levels of damage. For the sacrificial specimen, no damage was simulated during Evaluation 1. Crack sizes of 1.25 in., 1.50 in., and 1.75 in. were present during Evaluations 2, 3, and 4, respectively. The F_{shm} damage detection methodology was applied to cases of no damage and actual damage and evaluated with respect to damage detection capability with respect to true and false indications.

5.4. Demonstration Bridge on I-80 in Iowa

With reference to the I-80 bridge, the SHM system is described in terms of sensor installation. To obtain strain data, electrical resistance strain gauges were deployed. For sensor networking, two Cambell Scientific CR9000x data loggers, a desktop computer, network switch, router, and Sierra Wireless 4G cellular modem were installed as hardware components. The sensor networking system for the strain data acquisition system is schematically illustrated in Figure 5.11.

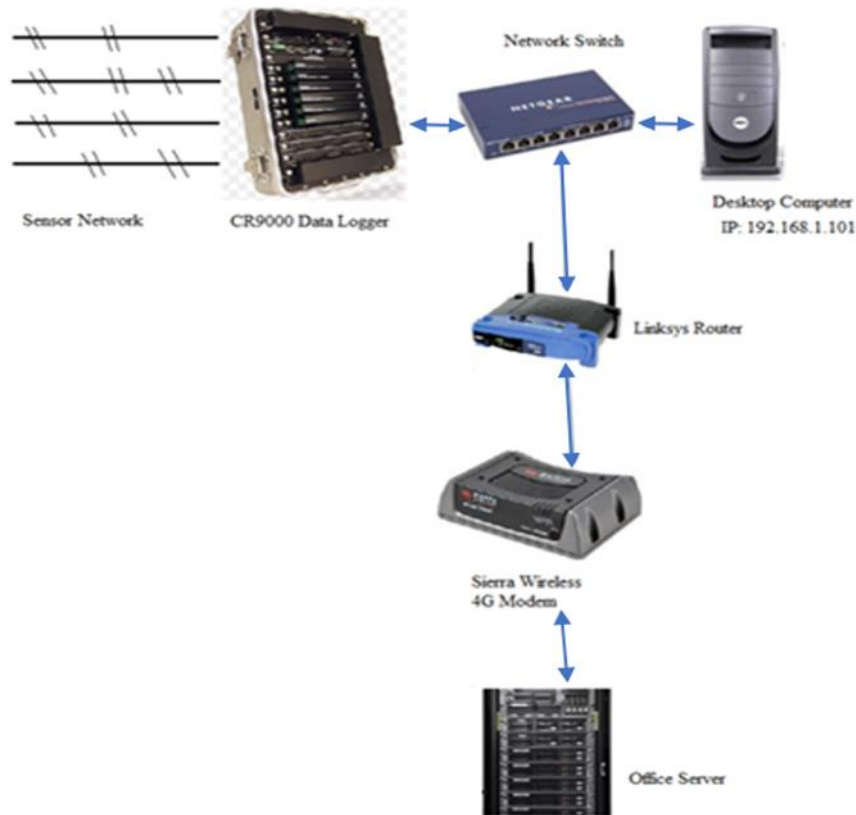


Figure 5.11. SHM system components

The data collected from the data logger are transferred to the desktop computer through a network switch. Before the data are sent to the router via the network switch, they are stored temporarily on the desktop computer. Lastly, the data was dispatched to the cellular modem, where they were transmitted to the office server via 4G cellular communication. DAT format files were obtained from the data files and they were collected every minute with a sampling rate of 250 Hz.

The I-80 bridge crosses the Sugar Creek located near a weigh station in Dallas County, Iowa (Figure 5.12).



Figure 5.12. I-80 bridge

The bridge has three spans; two end spans with spans of 61 ft and a center span of 78 ft. The bridge width is 38 ft, and a skew of 15 degrees. The bridge has a 7.5 in. thick concrete slab and steel girder W35 x 135 for exterior spans and W35 x 150 for the interior span.

5.4.1. Sensor Installation

A total 78 electrical resistance strain gauges including a deck gauge were strategically deployed at the I-80 bridge. The strain sensors at the deck were chosen to identify vehicle travel lane, axle number and spacing, and vehicle speed. The designation used to identify the sensors was by cross section and girder line-flange location. For instance, B2_BF represents a sensor installed at section B and girder line 2 and bottom flange (BF). The designation G1_TF identifies the sensor location at girder line 1 at cross section G and top flange (TF). Sensor layout for the I-80 bridge is illustrated in Figure 5.13 and dots indicate sensors.

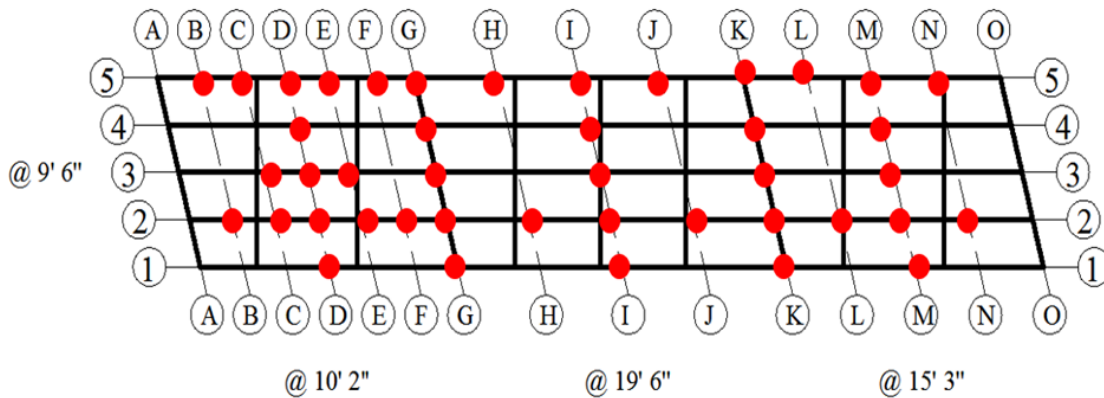


Figure 5.13. Sensor layout for I-80 bridge

5.4.2. Damage Simulation – Level 1 and Level 2

In this research work, two plates with C-clamps were attached to simulate damage. From a structural engineering perspective, strain reduction could be observed by changing stiffness (geometry of cross section at the lower flange). Two plates with clamps were installed between sensor locations for damage level 1 and at the sensor location for damage level 2. For damage level 1, two plates, which have dimensions 4 in. x 0.5 in. x 8 ft, with clamps were installed at the top side of the bottom flange on both sides of the web between C2 and D2 on May 5, 2014. The plates were moved to between C4 and D4 on July 2, 2014 and then removed on August 29, 2014. The cross section where the plates were added is shown in Figure 5.14.



Figure 5.14. Installation of two plates with C-clamps for damage level 1

For damage level 2, two plates that have the same dimensions as those for damage level 1 were attached at the underside of the bottom flange on March 4, 2015. In this damage situation, one plate was attached above the bottom flange and another one attached below the bottom flange. Two plates were located at sensor location C2. Figure 5.15 shows the installation of the two plates for damage level 2.



Figure 5.15. Installation of two plates with C-clamps for damage level 2

5.5. Potential Evolution of Damage Detection Approach

The potential evolution of F_{shm} damage detection approaches is investigated and discussed in this section. In the previous chapter, the high false indication rate for the control chart based F_{shm} method was believed to be because of strain range variability. This section discusses the improvements made to decrease the variability by studying the influence of temperature and truck configuration on strain range data. Strain data were sorted into temperature bins and axle spacing of trucks. Additionally, F-limits were established for the six sigma method, base data method, and training data method.

5.5.1. Influence of Temperature

Continuously collected strain range data at B2_BF (cross section B, girder line 2, and bottom flange) and temperature changes are graphically shown in Figure 5.16 at the same time periods from February 2014 to September 2014.

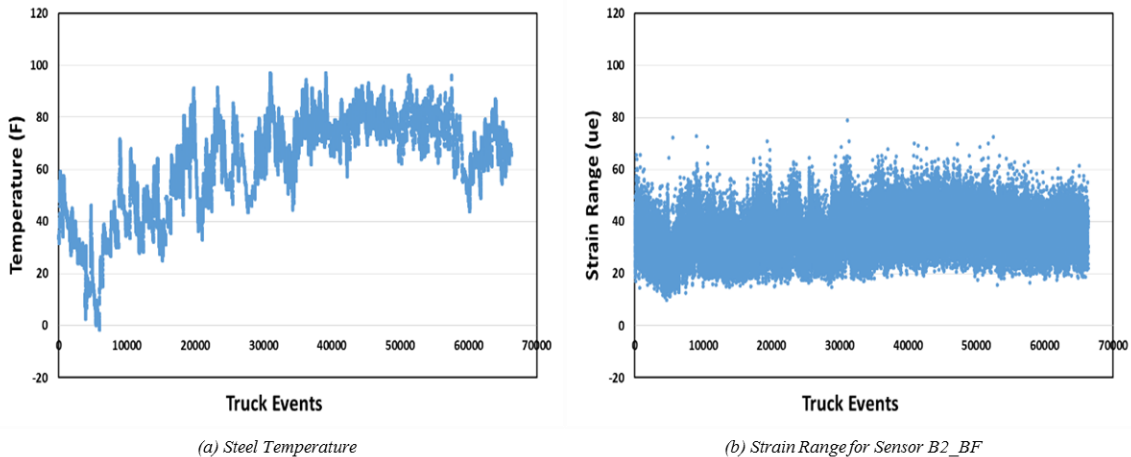


Figure 5.16. Temperature and strain range changes

Some strain range data seemed to vary as the temperature changed. To minimize strain range variability, it was essential to investigate the influence of temperature on the strain range.

For a better understanding the relationship between strain range variability and temperature, a moving average technique for strain range data was applied by taking groups of 200 truck events to obtain the mean strain value. Then, the 200 truck event was modified by shifting forward by one truck event. Both moving average strain range and temperature data are plotted in one graph in Figure 5.17.

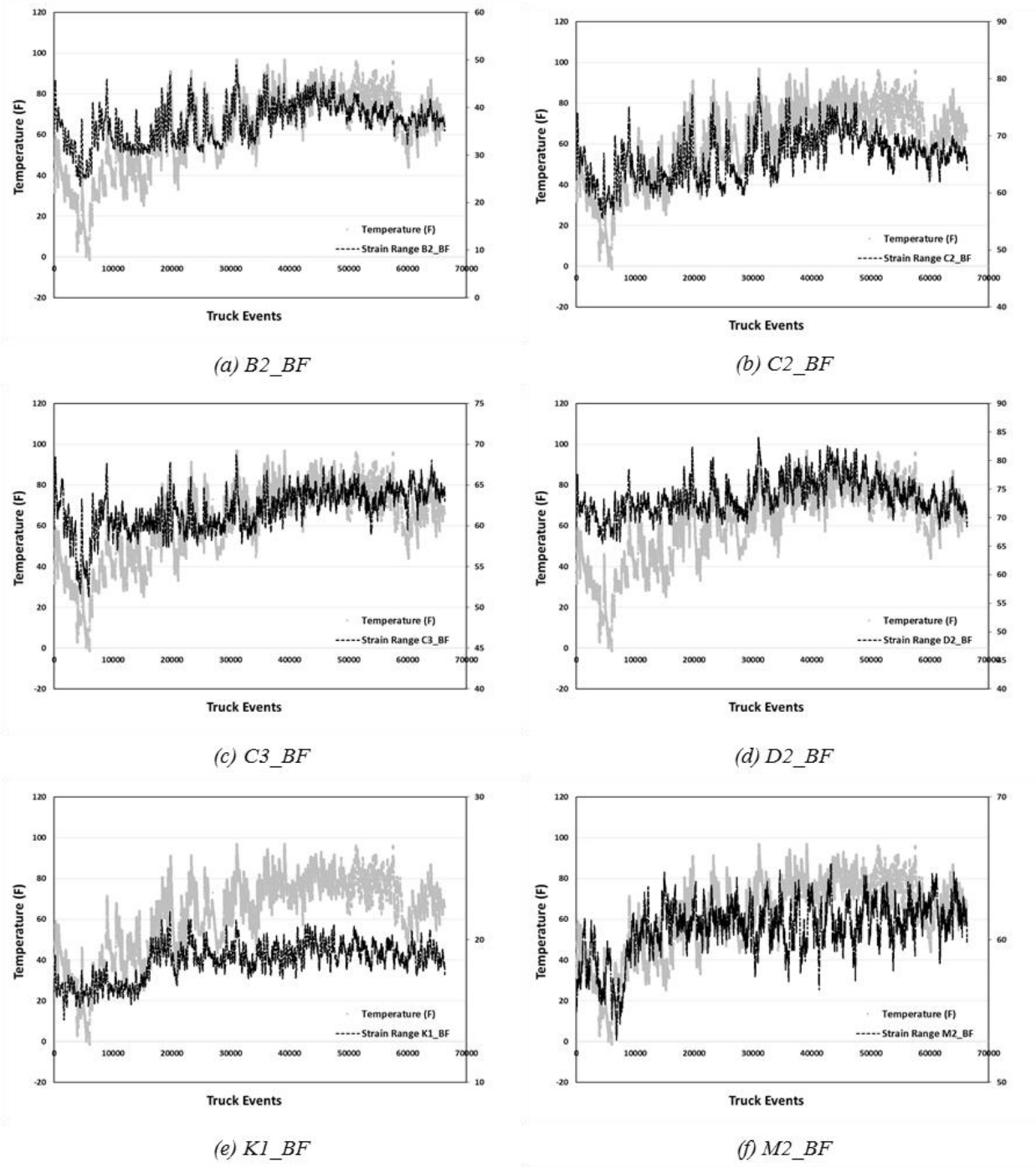


Figure 5.17. Temperature and strain range

The left y-axis shown in Figure 5.17 represents temperature in Fahrenheit, and the right y-axis represents the moving average strain data. The graphs show there is a strong correlation between the strain moving average and temperature for each sensor location.

To observe the relationship between strain range (y-axis) and temperature (x-axis) more closely, plots for B2_BF and C2_BF are shown in Figure 5.18.

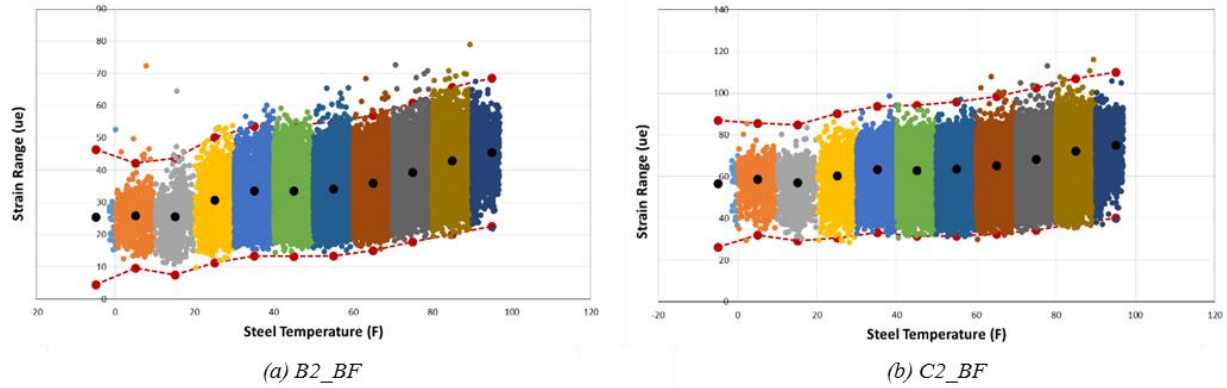


Figure 5.18. Relationship between strain range and temperature

Dots in the middle represent the mean value of each 10°F temperature bin, and the two dashed lines with dots show the mean plus and minus three standard deviations of each 10°F bin, called UCL (upper control limit) and LCL (lower control limit), respectively. For each temperature bin, the mean strain range increased as temperature increased, as well as for the standard deviation. Table 5.1 and Table 5.2 show the mean, standard deviation, UCL, LCL, and number of truck events for each 10°F temperature bin, respectively, for B2_BF and C2_BF. The standard deviations were reduced when the strain range data were separated into intervals of 10°F temperature bins.

Table 5.1. Mean, standard deviation, UCL, LCL, and number of truck events for intervals of 10°F temperature bins (B2_BF)

Temperature bins	Mean	Std. dev.	UCL	LCL	Truck events
-10-0	25.49	6.99	46.47	4.51	29
0-10	25.91	5.41	42.14	9.69	863
10-20	25.58	6.03	43.68	7.49	1,026
20-30	30.78	6.49	50.25	11.31	2,475
30-40	33.54	6.71	53.67	13.42	5,617
40-50	33.58	6.76	53.87	13.28	6,397
50-60	34.18	6.95	55.02	13.34	8,485
60-70	36.06	6.98	57.01	15.11	12,175
70-80	39.26	7.19	60.82	17.70	18,115
80-90	42.96	7.59	65.74	20.19	9,559
90-100	45.57	7.69	68.63	22.52	1,397
All	36.93	8.14	61.33	12.52	66,138

Table 5.2. Mean, standard deviation, UCL, LCL, and number of truck events for intervals of 10°F temperature bins (C2_BF)

Temperature bins	Mean	Std dev.	UCL	LCL	Truck events
-10-0	56.59	10.14	86.99	26.18	29
0-10	58.84	8.92	85.60	32.09	863
10-20	57.06	9.30	84.95	29.17	1,026
20-30	60.41	9.95	90.26	30.56	2,475
30-40	63.42	10.11	93.73	33.10	5,617
40-50	62.89	10.44	94.21	31.57	6,397
50-60	63.62	10.71	95.75	31.49	8,485
60-70	65.41	10.98	98.34	32.48	12,175
70-80	68.43	11.36	102.50	34.35	18,115
80-90	72.23	11.62	107.09	37.36	9,559
90-100	75.12	11.67	110.14	40.09	1,397
All	66.36	11.58	101.11	31.62	66,138

All strain range data for B2_BF were collected during 2014, the moving average for the mean and standard deviation are plotted in Figure 5.19a.

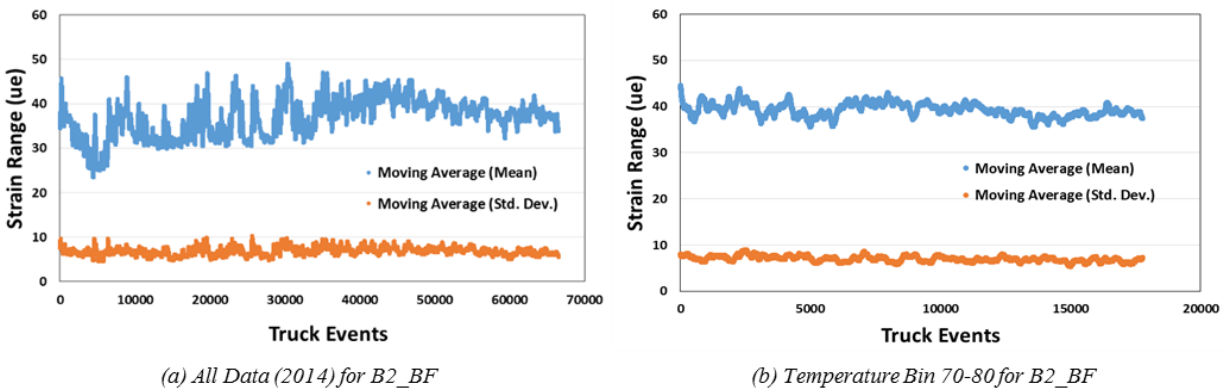


Figure 5.19. Moving average mean and standard deviation for all data and data in 70–80°F temperature bin for B2_BF

The moving average plot is created for the 70–80°F temperature bin strain data in Figure 5.19b, which shows the variation of strain range is reduced when strain range data are separated into the 70–80°F temperature bin.

The F_{shm} damage detection approach was improved by minimizing strain variability due to temperature, that is by sorting strain range data into temperature bins. The effects of temperature using different ranges of temperature bins is investigated in Section 5.6.

5.5.2. Influence of Truck Configuration

To further minimize strain range variability, the influence of truck configuration on the strain range was investigated. Strain range data was collected for five-axle trucks using the truck detection methodology from strain rate data collected at the I-80 demonstration bridge from sensors installed at the bottom of the deck. All five-axle trucks were further filtered into semi-trucks with a narrow axle spacing limit as shown in Table 5.3.

Table 5.3. Axle spacing range for all five-axle trucks and semi-trucks

Type of truck	Axle spacing range (ft)			
All five-axle trucks	7–25	3.5–6	25–40	3–12
Semi-trucks	15–20	4–6	30–35	4–6
Axle spacing #	1	2	3	4

In 2014, strain range data were collected for a total 66,138 truck events for all five-axle trucks, and the moving average for the mean and standard deviation and F_{shm} control chart for B2_BF and C2_BF are shown in Figure 5.20.

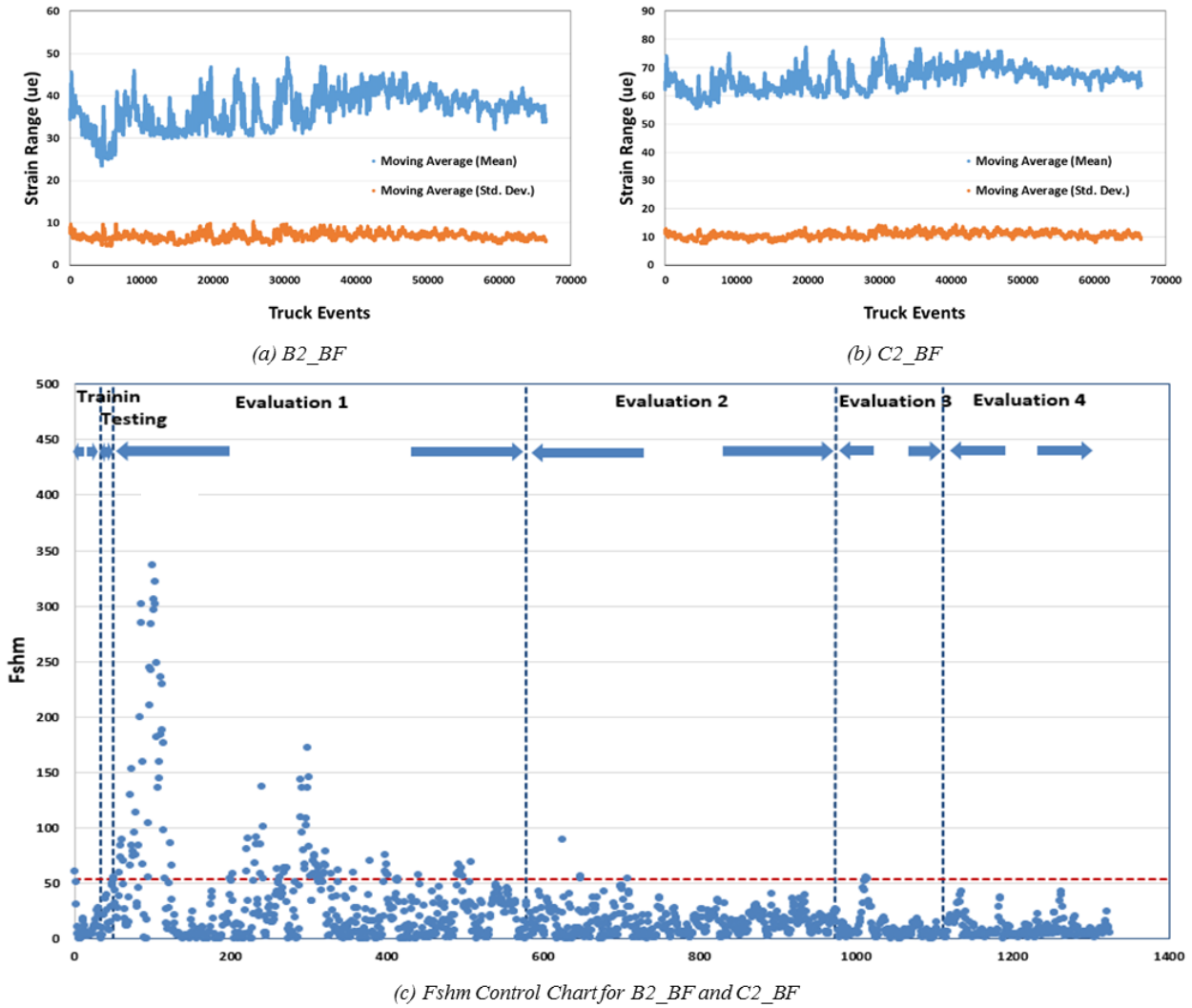


Figure 5.20. Moving average plots and F_{shm} control chart for B2_BF and C2_BF for all five-axle trucks

In moving average plots, the mean value of strain range value varies from 25 to 50 (ue) for B2_BF and 55 to 80 (ue) for C2_BF, respectively. High F_{shm} values are observed in the F_{shm} control chart due to the high variation of strain.

For semi-trucks, a total 24,715 trucks were selected by limiting axle spacing as in Table 5.3, and their moving average plots and F_{shm} control chart are shown in Figure 5.21.

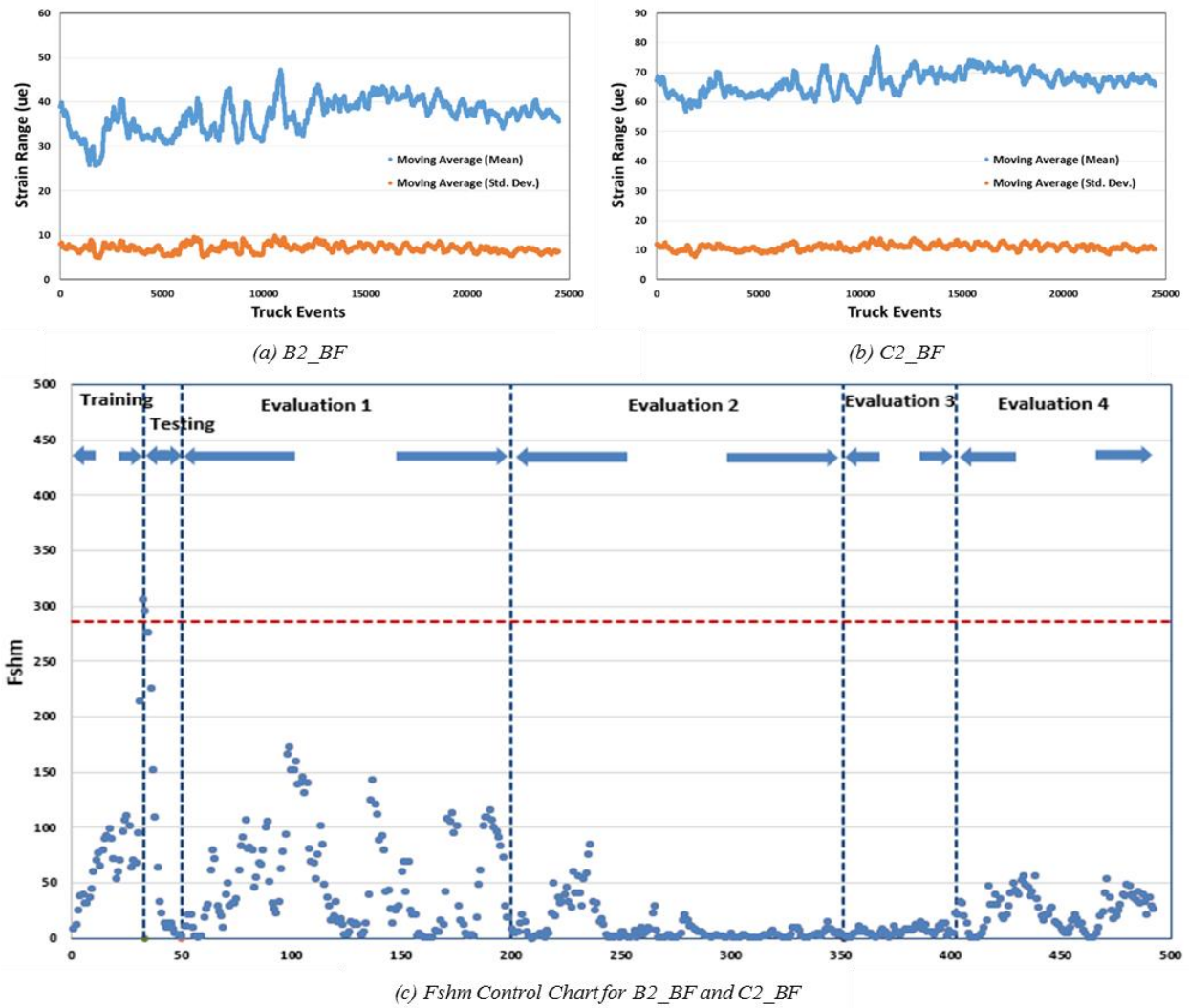


Figure 5.21. Moving average for mean and standard deviation of B2_BF and C2_BF for semi-trucks

The moving average for the mean and standard deviation also varies similar to all five-axle trucks. Also, the F_{shM} control chart shows high F_{shM} values. The high F_{shM} limit was established because of high F_{shM} values in the training region.

Strain data for semi-trucks are for the 70–80°F temperature bin. A total 6,948 truck events were selected by limiting to the 70–80°F temperature bin, and their moving average for mean and standard deviation are plotted in Figure 5.22.

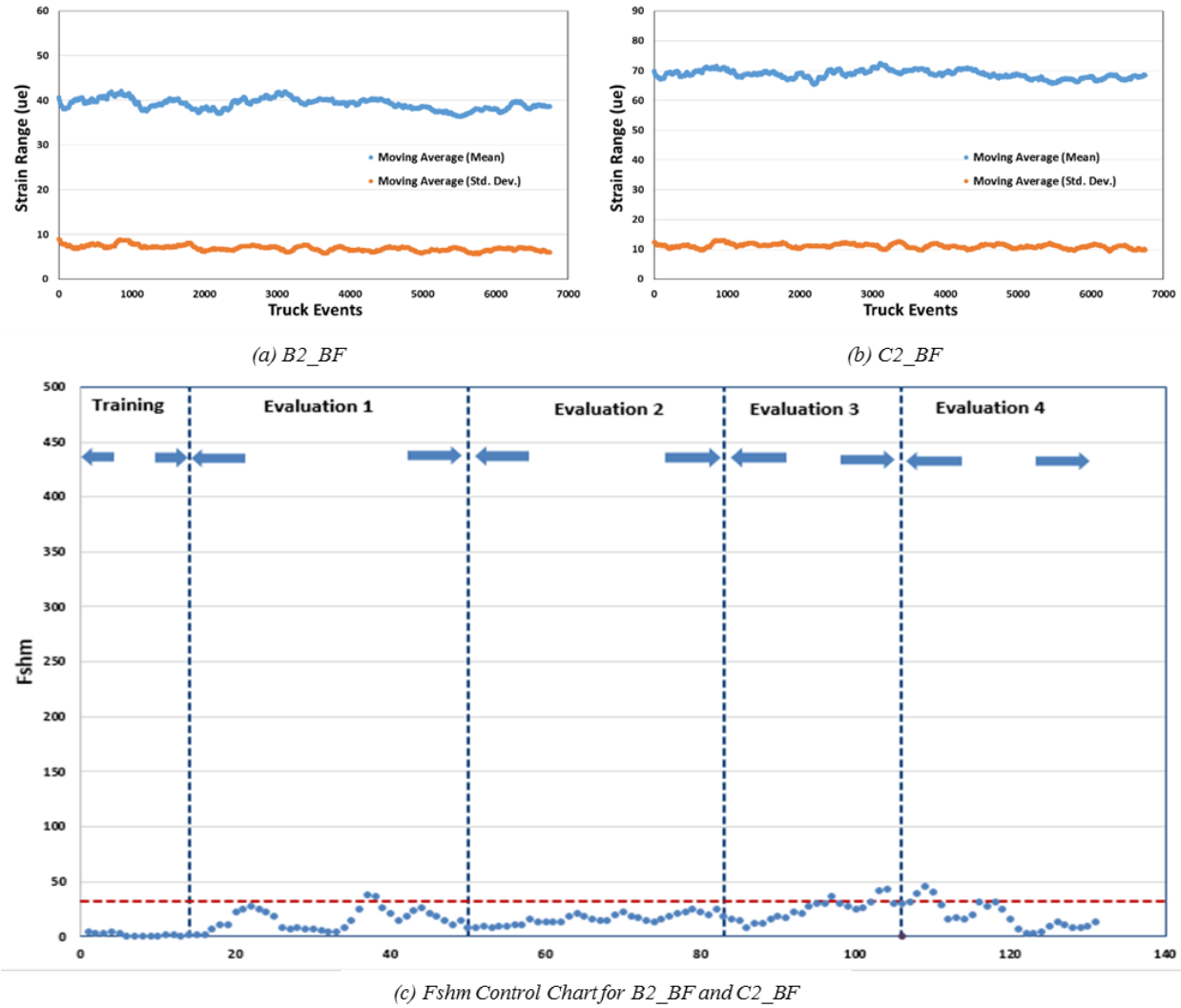


Figure 5.22. Moving average for mean and standard deviation of B2_BF and C2_BF for semi-trucks in 70–80°F temperature bin

The mean values for moving average are smoothed out for semi-trucks compared to all five-axle trucks. In the F_{shM} control chart, lower F_{shM} values are obtained with the less varied strain range data.

To observe strain variability, box plots were created for each sensor for all five-axle trucks, semi-trucks, all five-axle trucks in the 70–80°F temperature bin, and semi-trucks in the 70–80°F temperature bin. As can be seen in the box plot in Figure 5.23, minimum values are increased while maximum values are decreased.

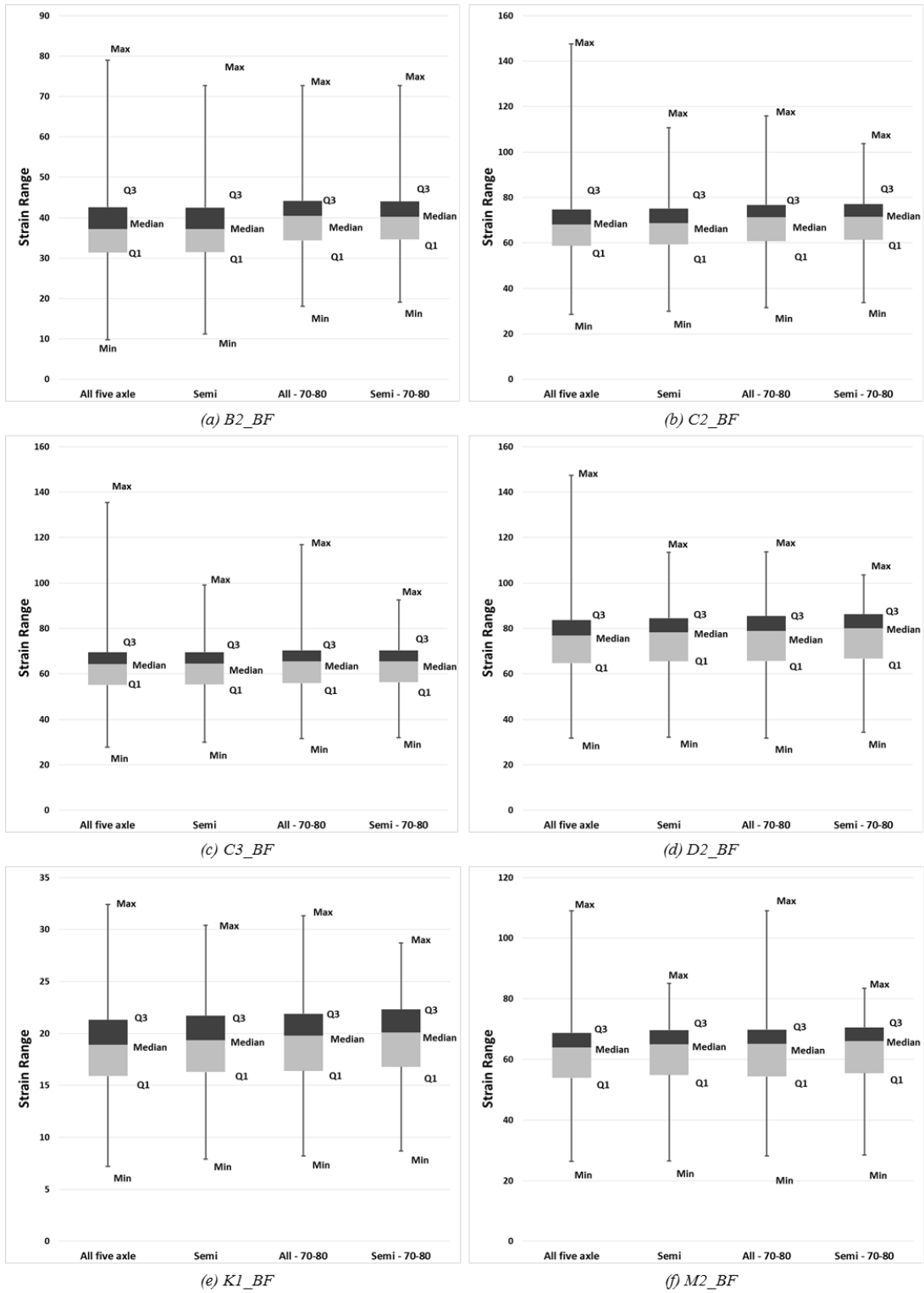


Figure 5.23. Box plots for all five-axle trucks, semi-trucks, all five-axle trucks in 70°F–80°F temperature bin, and semi-trucks in 70°F–80°F temperature bin

The entire length for the box plot is narrowed down from all five-axle truck to the semi-trucks and 70–80°F temperature bin. Minimum, quantile 1 (lower quartile, 25% of data less than this value), median, quantile 3 (upper quartile, 25% of data greater than this value), and maximum value are calculated and summarized in Table 5.4.

Table 5.4. Statistical parameters for all five-axle trucks, semi-trucks, all five-axle trucks in 70°F–80°F temperature bin, and semi-trucks in 70°F–80°F temperature bin

Sensors	Statistical parameters	All trucks	Semi-trucks	All 70°F–80°F	Semi 70°F–80°F
B2_BF	Minimum	9.8	11.3	18.1	17.1
	Quantile 3	31.4	31.5	34.4	34.6
	Median	37.2	37.2	40.5	40.3
	Quartile 1	42.6	42.5	44.2	44.0
	Maximum	78.9	72.7	72.7	72.7
C2_BF	Minimum	28.6	29.9	31.6	33.7
	Quantile 3	58.8	59.3	40.8	61.4
	Median	68.2	68.7	71.4	71.6
	Quartile 1	74.8	75.2	76.8	77.0
	Maximum	147.6	110.7	115.8	103.8
C3_BF	Minimum	27.8	30.0	31.5	31.9
	Quantile 3	55.1	55.5	55.9	56.3
	Median	64.3	64.5	65.5	65.5
	Quartile 1	69.5	69.6	70.4	70.4
	Maximum	135.3	99.2	116.9	92.52
D2_BF	Minimum	31.7	32.2	31.7	34.3
	Quantile 3	64.7	65.6	65.7	66.7
	Median	77.0	78.4	78.9	80.1
	Quartile 1	83.6	84.5	85.4	86.2
	Maximum	147.3	113.4	113.8	103.6
K1_BF	Minimum	7.2	7.9	8.2	8.7
	Quantile 3	15.9	16.3	16.4	16.8
	Median	18.9	19.3	19.8	20.1
	Quartile 1	21.3	21.7	21.9	22.3
	Maximum	32.4	30.4	31.3	28.7
M2_BF	Minimum	26.4	26.5	28.2	28.5
	Quantile 3	53.9	54.9	54.4	55.5
	Median	63.9	65.0	65.2	66.0
	Quartile 1	68.8	67.7	69.8	70.6
	Maximum	109.0	85.1	109.0	83.5
Number of truck events		66,138	24,715	17,955	6,948

5.5.3. F-Limit

In this section, F-limit setting methods such as the six sigma method, base data method, and training data method are investigated to reduce the false indication rate. The F-limit for the six sigma method is defined as mean value plus six times standard deviation using F_{shm} values during the training period (2,000 truck events and 33 F points). The base data method is developed only using 200 truck events. Another set of 200 truck event data is created by duplicating the base data and then increasing or decreasing 10% (or adding/subtracting a uniform strain amount) of strain range on a sensor. For the training data method, a total of 2,000 truck events are used and 1,800 corresponding data after the 200 base data are increased or decreased to establish a new F-limit.

5.5.4. Six Sigma Method

The concept of the six sigma approach was developed and proposed for process improvement by measuring and controlling variation for probabilistic design (Tennant 2001). To improve the quality of process output, the six sigma design method is applicable as a set of empirical and statistical quality management methods that minimize variability in a manufacturing process. It focuses on probabilistic analysis and optimization (Koch 2002).

Variation of performance in normal distribution for three sigma and six sigma design can be graphically shown by the mean plus or minus multiples of the standard deviation in Figure 5.24.

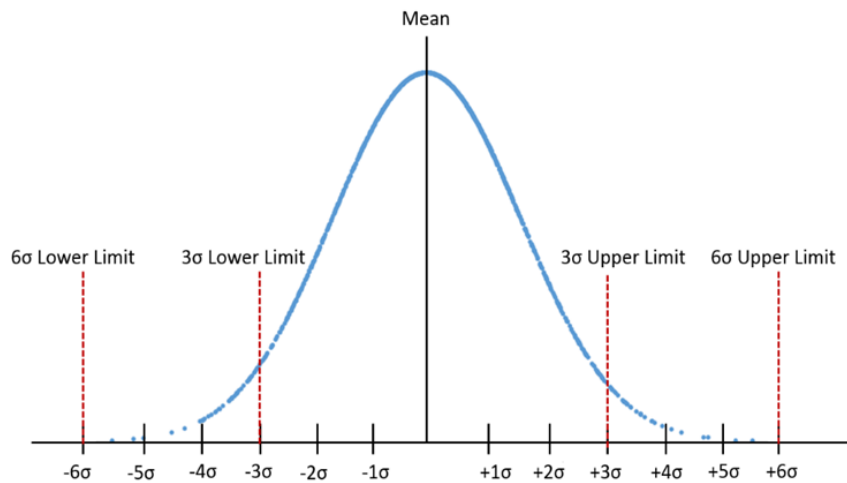


Figure 5.24. Normal distribution for 3σ and 6σ design

The area under the normal distribution curve, which depends on the sigma level, represents the probability of performance and summary of probability as percent variation as shown in Table 5.5.

Table 5.5. Sigma level as percent variation

Sigma level	Percent variation
$\pm 1\sigma$	68.26
$\pm 2\sigma$	95.46
$\pm 3\sigma$	99.73
$\pm 4\sigma$	99.9937
$\pm 5\sigma$	99.999943
$\pm 6\sigma$	99.9999998

In this study, the six sigma approach was applied to the statistical control chart method to reduce the false indication rate.

As discussed previously, F_{shm} limits were established using the mean plus three standard deviation from the F_{shm} output during training periods (2,000 truck events and 33 F_{shm} points). To reduce false indication rate, the six sigma (mean plus six standard deviation) approach was employed. An example of the F_{shm} control chart for the six sigma method is illustrated in Figure 5.25 with 70–80°F temperature bin data.

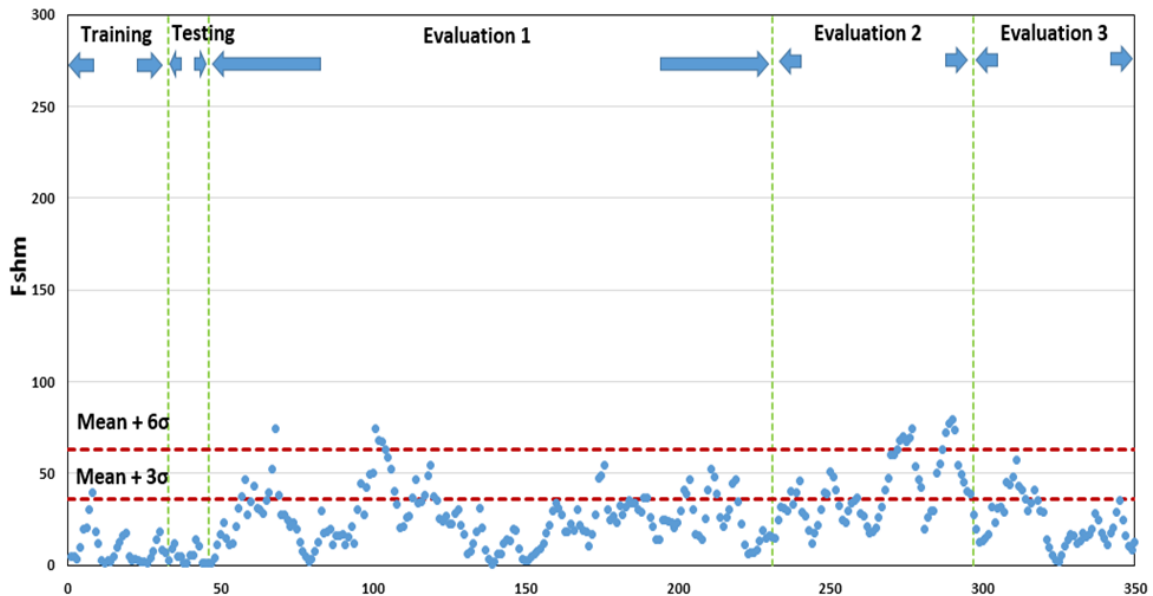


Figure 5.25. An example of 6σ method for F_{shm} damage detection approach

In the figure, the two horizontal dash lines show the limits for mean plus three sigma (36.24) and mean plus six sigma (62.95), and the vertical dash lines represent regions for training, testing, and evaluation. False indication and true indication with the six sigma limit are further studied in Section 5.6.

5.5.5. Base Data Method

The base data method was developed to establish a new F_{shm} limit by utilizing the 200 base strain range data. Although the previously proposed three sigma and six sigma methods are based on statistical theory, the base data limit method is based on identifying the structurally significant meaning of strain changes expressed by the statistical F_{shm} calculation. To calculate the F_{shm} limit, additional sets of 200 strain data are created by increasing and decreasing the strain range by 10% or absolute value of strain. The purpose of this process is to set a limit only, and the F_{shm} value should not be changed, as the true strain range data remains unchanged.

As an example, consider the scatter plots (x, y) in Figure 5.26, where 200 strain data pairs from the B2_BF and the C2_BF sensors are plotted.

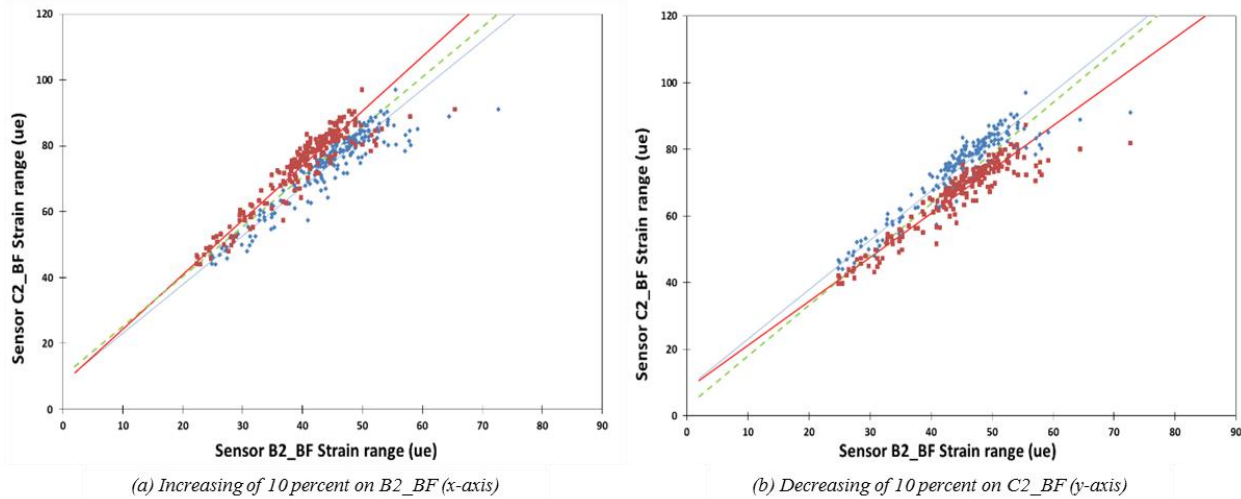


Figure 5.26. Examples of base data method

After decreasing the strain range at B2_BF in the x-axis, one F_{shm} limit 125, is calculated using the two data sets. Another F_{shm} limit, 151, is obtained by decreasing 10% of strain on C2_BF (y-axis).

Further F_{shm} limit establishment options were investigated by decreasing and increasing the B2_BF and C2_BF strain range by 10–20%, respectively. Figure 5.27 shows that if the same set of strain data is used, the F_{shm} value must be zero.

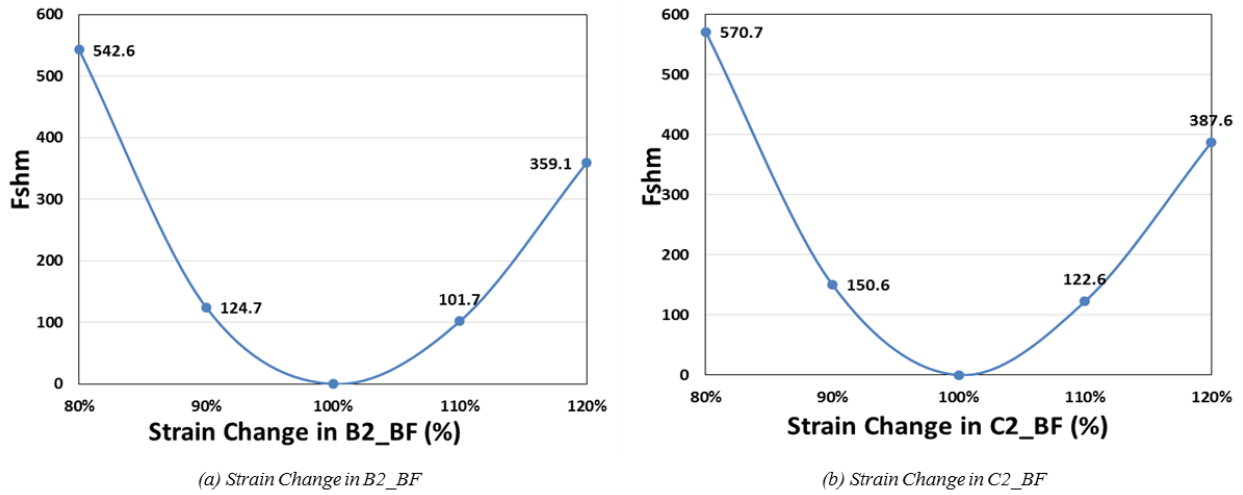


Figure 5.27. Examples of strain change in percent

A significant increase in the F_{sh_m} limit is observed when strain data changes by 20%.

F_{sh_m} limits created as above are applied to the F_{sh_m} control chart in Figure 5.28.

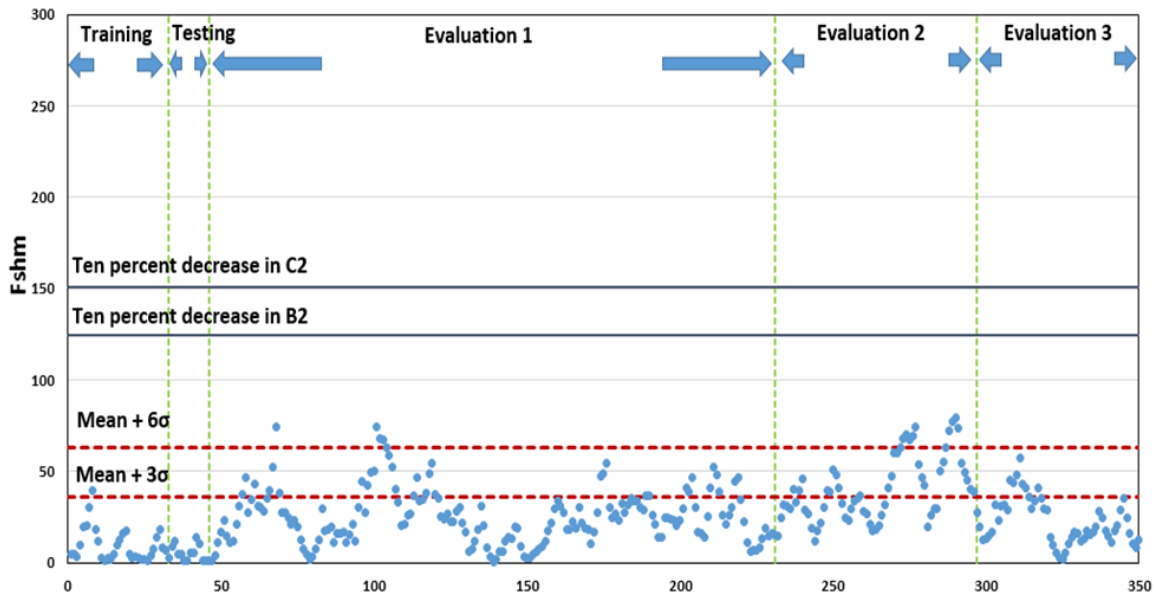


Figure 5.28. Examples of base data method for F_{sh_m} damage detection approach

For the sensor pair B2_BF and C2_BF, the F_{sh_m} limits associated with decreasing and increasing 10% of strain range are 125 and 151, respectively, and those are shown by two solid lines. By applying the base data method, the new F_{sh_m} limits are higher than those using the mean plus three sigma (36) and six sigma (63). Using the base data method is expected to minimize the false indication rate.

5.5.6. Training Data Method

Another F_{shm} limit establishment method, the training data method using the first 2,000 truck events is proposed in this section. In this method, 1,800 corresponding data after the 200 base data are increased and decreased at one sensor at a time to establish an F_{shm} limit. A total 33 F_{shm} values were created and the maximum F_{shm} value was selected as a new F_{shm} limit.

The F_{shm} control chart for sensor B2_BF versus C2_BF in the temperature bin 70–80°F is illustrated in Figure 5.29 with the new F_{shm} limits from applying the training data method.

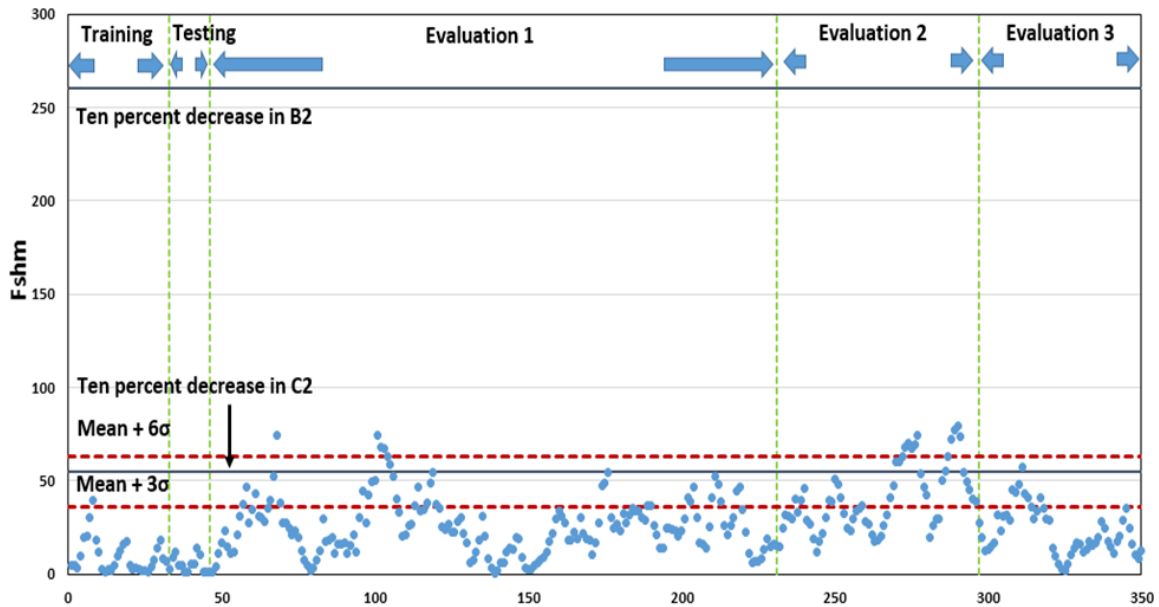


Figure 5.29. Examples of training data method for F_{shm} damage detection approach

The maximum values of F_{shm} , which are obtained by decreasing by 10% from 1,800 strain data in B2_BF and C2_BF, are 260 and 55, respectively, and are shown as two solid blue lines in the F_{shm} control chart above. The F_{shm} limits introduced and proposed are summarized in Table 5.6.

Table 5.6. Summary of F_{shm} limits for a sensor pair B2_BF versus C2_BF

F_{shm} limit method		F_{shm} value
3σ		36
6σ		63
Base data	10% decrease in B2_BF	124
	10% decrease in C2_BF	150
	10% increase in B2_BF	101
	10% increase in C2_BF	123
	10 $\mu\epsilon$ decrease in x	530
	10 $\mu\epsilon$ decrease in y	231
	10 $\mu\epsilon$ increase in x	530
	10 $\mu\epsilon$ increase in y	231
Training data	10% decrease in B2_BF	260
	10% decrease in C2_BF	55
	10% increase in B2_BF	103
	10% increase in C2_BF	322

5.6. Applications of Data to Evaluate Potential Damage

The overall application of the F_{shm} approach considering different sensor combinations of strain data are shown in Figure 5.30.

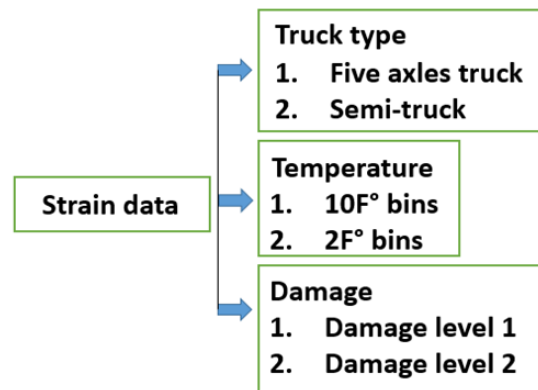


Figure 5.30. Combination of strain data

Potential damage evaluation is shown in the figure for combinations of strain data considering both the 2°F temperature bin and 10°F temperature bin and considering both five-axle trucks and semi-trucks. For example, the strain data are evaluated for five-axle trucks within the 10°F temperature bin and damage level 1. With the F_{shm} approach, the strain data is evaluated via sensor pairing. Fifteen sensor pairs are evaluated with six selected sensors including B2_BF, C2_BF, C3_BF, D2_BF, K1_BF, and M2_BF. Table 5.7 represents F_{shm} limit methods and nomenclature for the summary of false/true indication rate. For instance, B-Dx is the limit for the base data method with a 10% decrease in the x-axis.

Table 5.7. F_{shm} limit method and nomenclature

F_{shm} limit method		Nomenclature
3σ		
6σ		
Base data	10% decrease in x	B-Dx
	10% decrease in y	B-Dy
	10% increase in x	B-Ix
	10% increase in y	B-Iy
	10 $\mu\epsilon$ decrease in x	B-10Dx
	10 $\mu\epsilon$ decrease in y	B-10Dy
	10 $\mu\epsilon$ increase in x	B-10Ix
	10 $\mu\epsilon$ increase in y	B-10Iy
Training data	10% decrease in x	I-Dx
	10% decrease in y	I-Dy
	10% increase in x	I-Ix
	10% increase in y	I-Iy

As indicated in previous Section 5.5.3, the F_{shm} control chart is divided into training, testing, and evaluation. The training period is developed to define the normal operation of the system, and F_{shm} values in the training period are used to establish statistic-based limits named three sigma and six sigma. The testing period is utilized to evaluate the efficacy of the training period. For monitoring the bridge for change in structural performance, the evaluation period is subdivided into the following regions: Evaluation 1, Evaluation 2, and Evaluation 3.

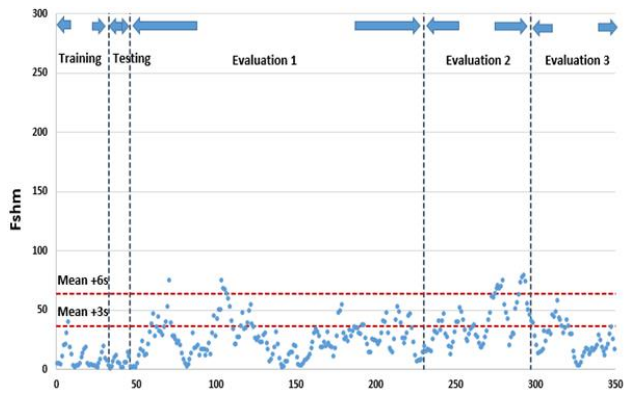
Evaluation 1 is the period when there was a change in stiffness between sensor C2 and D2 after adding two plates with C-clamps. (Details were discussed in Section 5.4.2.) Evaluation 2 begins after plates with clamps were moved to between C4 and D4. The two plates were removed in the Evaluation 3 period.

5.6.1. 10°F Temperature Bins and All Five-Axle Trucks

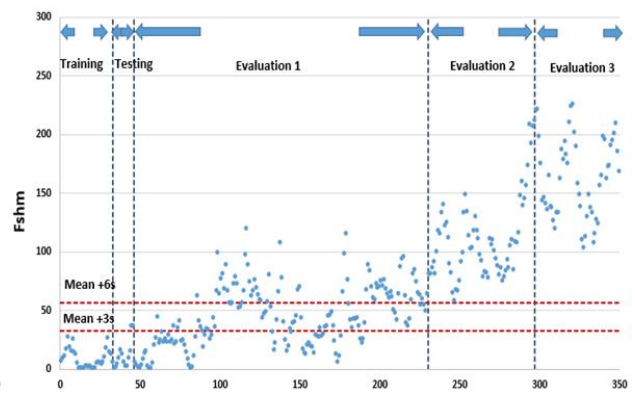
5.6.1.1. Damage Level 1

Since changes in stiffness were relatively small for damage level 1, it was anticipated that there would be no significant structural changes. Therefore, false indication rates were calculated for training, testing, and Evaluation 1, 2, and 3 regions.

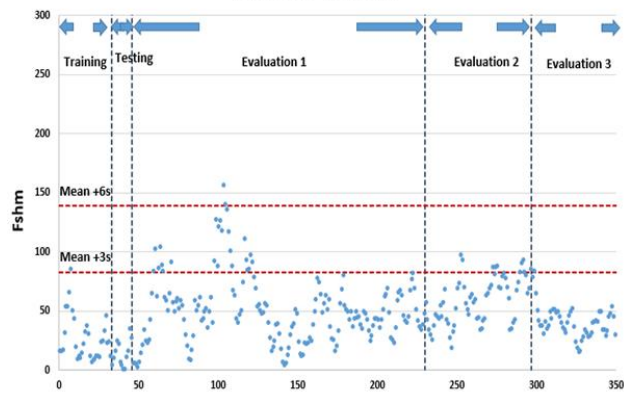
Figure 5.31 shows the F_{shm} control charts for the 70°F–80°F temperature bins with all five-axle trucks for damage level 1. The two horizontal dash lines represent statistics-based limits using three sigma and six sigma.



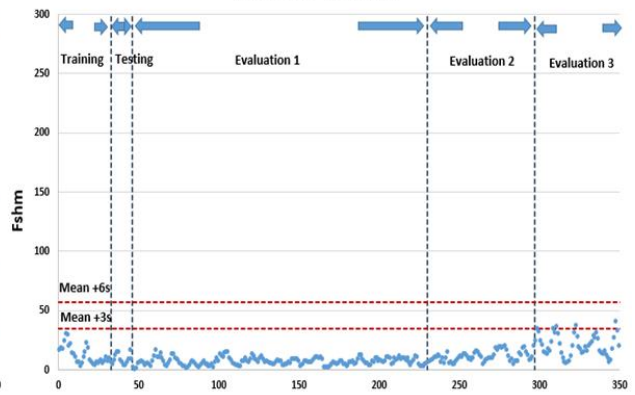
(a) $B2_BF$ vs. $C2_BF$



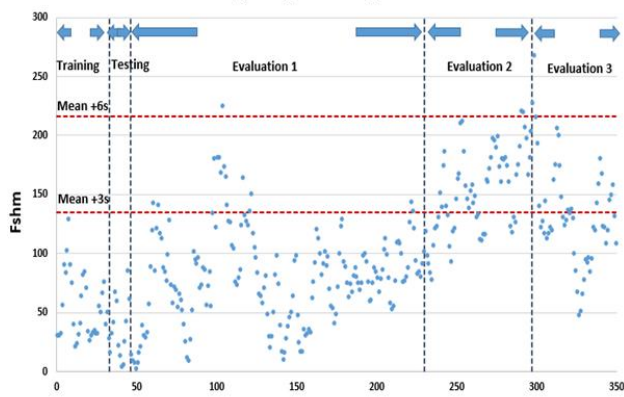
(b) $B2_BF$ vs. $C3_BF$



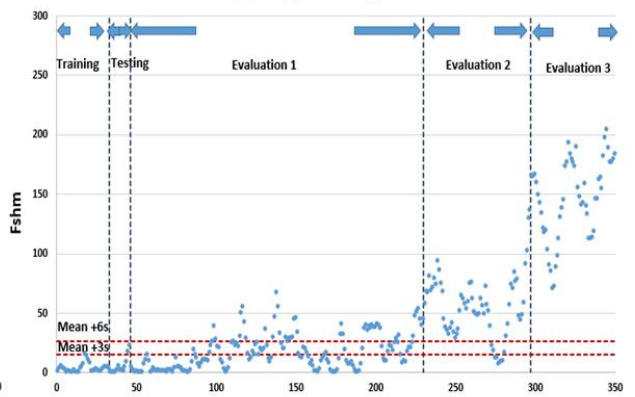
(c) $B2_BF$ vs. $D2_BF$



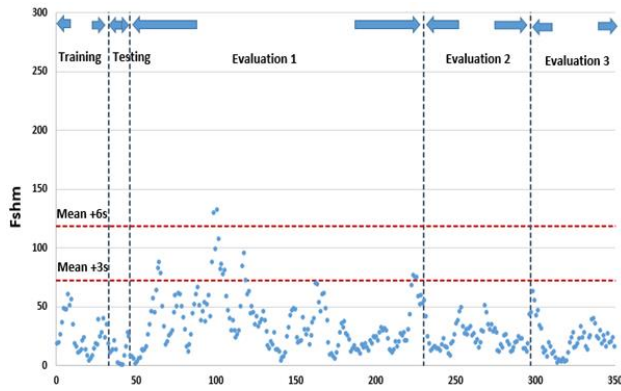
(d) $B2_BF$ vs. $K1_BF$



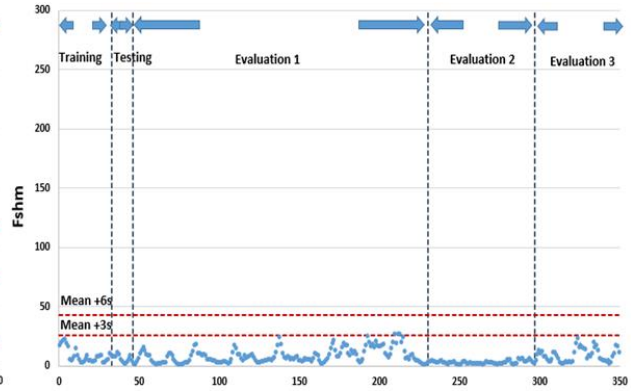
(e) $B2_BF$ vs. $M2_BF$



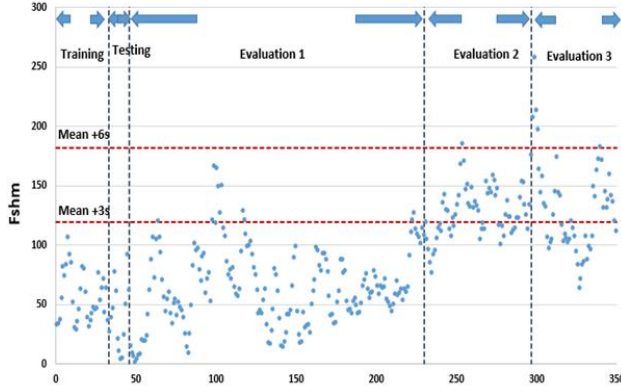
(f) $C2_BF$ vs. $C3_BF$



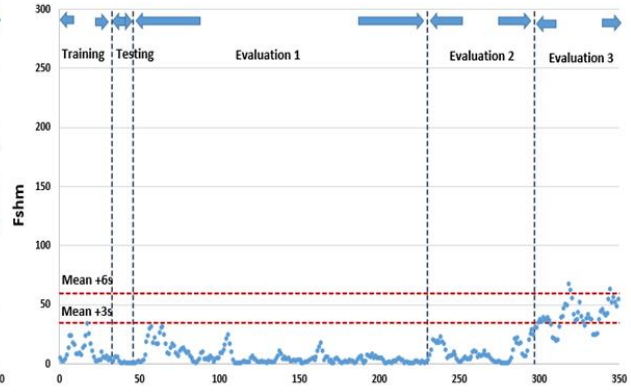
(g) $C2_BF$ vs. $D2_BF$



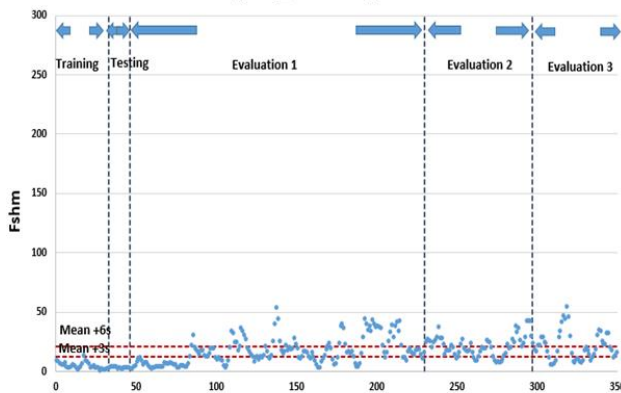
(h) $C2_BF$ vs. $K1_BF$



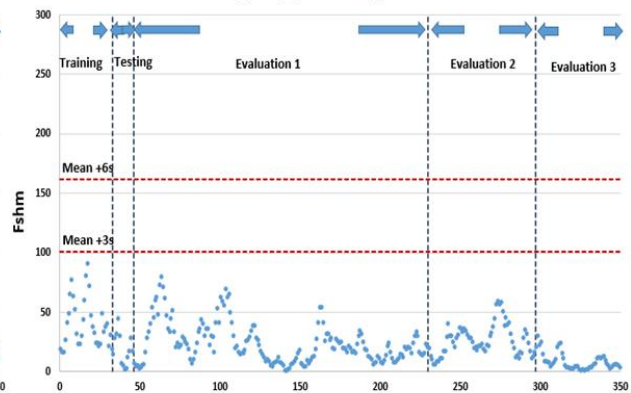
(i) $C2_BF$ vs. $M2_BF$



(j) $C3_BF$ vs. $D2_BF$



(k) $C3_BF$ vs. $K1_BF$



(l) $C3_BF$ vs. $M2_BF$

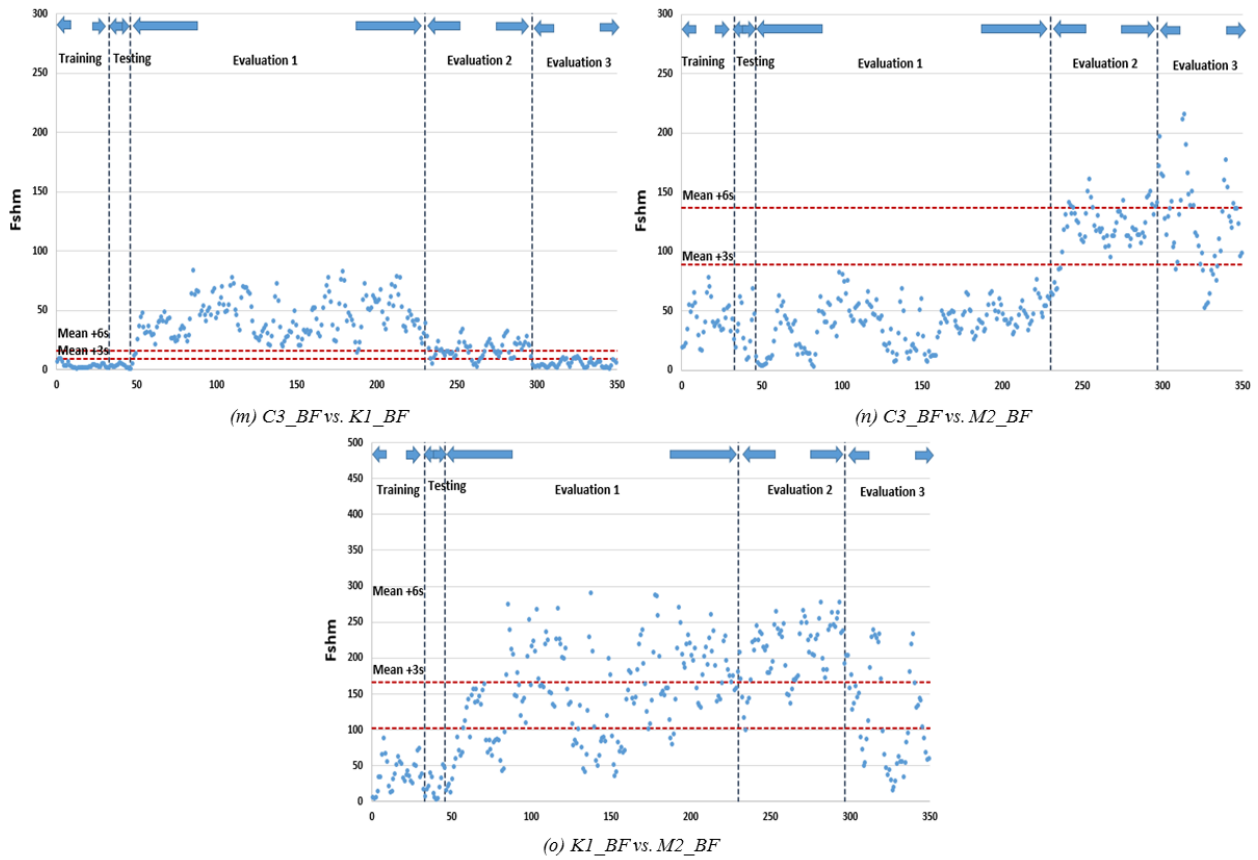


Figure 5.31. F_{shm} control charts for 70°F–80°F temperature bins with all five-axle trucks

A summary of false and true indication rates for statistics- and structure-based limit methods for selected sensor pairs are shown in Table 5.8.

Table 5.8. Summary of false and true indication rate for 70–80°F temperature bins with all five-axle trucks for damage level 1

Sensor pair	Period	Number of F_{shm}	Statistics-based		Structure-based								
			3σ	6σ	Base data method				Training data method				
					Dx	Dy	Ix	Iy	Dx	Dy	Ix	Iy	
B2_BF vs. C2_BF	T & T	46	2.2	0	0	0	0	0	0	0	0	0	0
	E 1	184	20.1	2.2	0	0	0	0	0	0	0	0	0
	E 2	67	47.8	13.4	0	0	0	0	0	0	0	0	0
	E 3	58	15.5	0	0	0	0	0	0	0	0	0	0
	Limit		37	67	125	151	101	122	259	129	102	321	
B2_BF vs. C3_BF	T & T	46	4.4	0	0	0	0	0	0	0	0	0	0
	E 1	184	63.0	35.3	1.6	0	7.6	2.2	0	0	1.6	0	0
	E 2	67	100	100	55.2	26.9	85.1	56.7	6.0	23.9	49.3	0	0
	E 3	58	100	100	100	89.7	100	100	25.9	87.9	98.3	0	0
	Limit		33	57	100	121	81	98	189	126	104	233	
B2_BF vs. D2_BF	T & T	46	2.2	0	2.2	2.2	2.2	2.2	0	13.0	15.2	0	0
	E 1	184	13.6	1.1	12.5	13.6	20.1	20.1	0	54.3	62.5	0	0
	E 2	67	11.9	0	11.9	11.9	40.3	40.1	0	68.7	79.1	0	0
	E 3	58	1.7	0	0	1.7	3.4	3.4	0	32.8	41.4	0	0
	Limit		83	139	84	83	67	67	305	44	40	316	
B2_BF vs. K1_BF	T & T	46	0	0	0	0	0	4.3	0	0	0	0	0
	E 1	184	0	0	0	0	0	0	0	0	0	0	0
	E 2	67	0	0	0	0	0	0	0	0	0	0	0
	E 3	58	5.2	0	10.3	0	0	25.9	0	8.6	36.2	0	0
	Limit		34	57	32	46	26	37	110	33	23	141	
B2_BF vs. M2_BF	T & T	46	0	0	43.5	39.1	54.3	47.8	0	37.3	78.3	0	0
	E 1	184	8.2	0.5	81.0	78.3	84.2	81.5	0	94.0	89.1	0	0
	E 2	67	64.2	3.0	100	100	100	100	0	100	100	0	0
	E 3	58	39.7	3.4	100	96.6	100	100	0	100	100	0	0
	Limit		134	216	46	51	37	41	309	16	29	318	
C2_BF vs. C3_BF	T & T	46	0	0	0	0	0	0	0	0	0	0	0
	E 1	184	9.2	1.1	0	0	0	0	0	0	0	0	0
	E 2	67	0	0	0	0	0	0	0	0	0	0	0
	E 3	58	0	0	0	0	0	0	0	0	0	0	0
	Limit		72	118	416	352	339	288	690	220	233	619	
C2_BF vs. D2_BF	T & T	46	0	0	0	0	0	0	0	0	0	0	0
	E 1	184	1.6	0	0	0	0	0	0	0	0	0	0
	E 2	67	0	0	0	0	0	0	0	0	0	0	0
	E 3	58	0	0	0	0	0	0	0	0	0	0	0
	Limit		25.5	42.9	68	70	56	57	169	67	72	173	
C2_BF vs. K1_BF	T & T	46	0	0	2.2	2.2	17.4	15.2	0	91.3	93.5	0	0
	E 1	184	6.0	0	16.3	15.2	29.3	28.3	0	89.7	92.9	0	0
	E 2	67	62.7	1.5	92.5	92.5	98.5	98.5	0	100	100	0	0
	E 3	58	53.4	6.9	84.5	82.8	96.6	96.6	0	100	100	0	0
	Limit		119	182	98	99	79	80	389	23	17	394	
C3_BF vs. M2_BF	T & T	46	0	0	0	0	0	0	0	0	0	0	0
	E 1	184	0	0	0	0	0	0	0	0	0	0	0
	E 2	67	0	0	0	0	0	0	0	0	0	0	0
	E 3	58	75.7	5.2	0	0	0	0	0	0	0	0	0
	Limit		35	59	130	105	106	85	263	80	93	222	

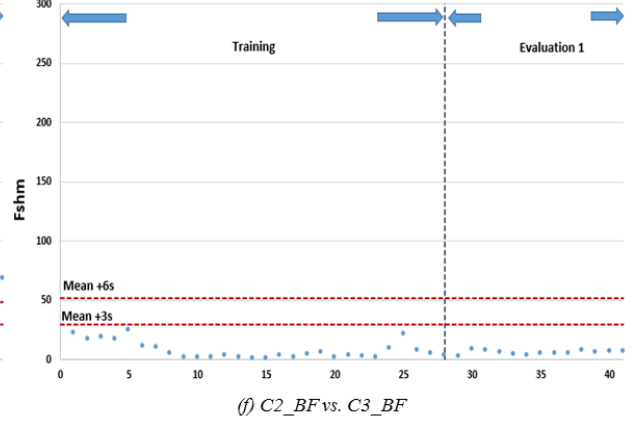
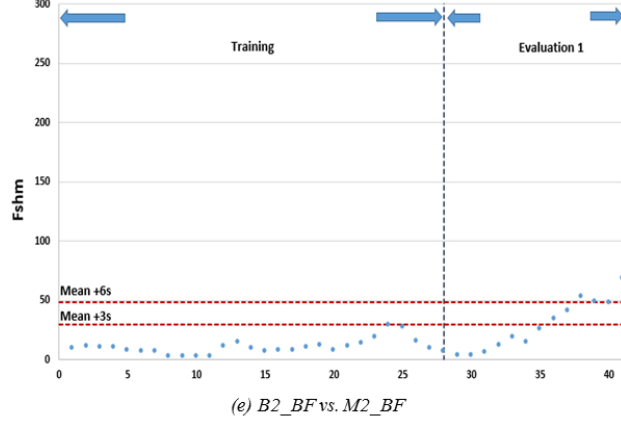
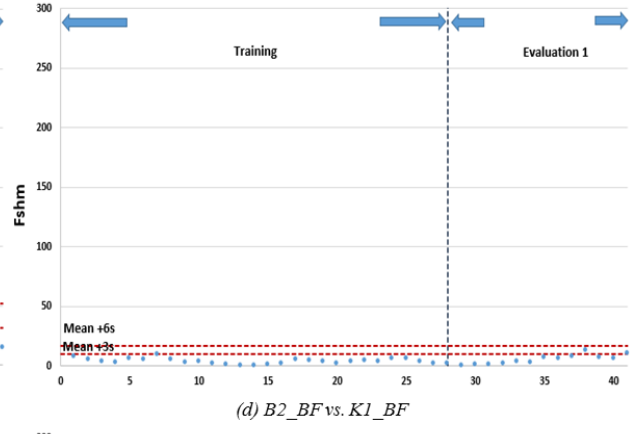
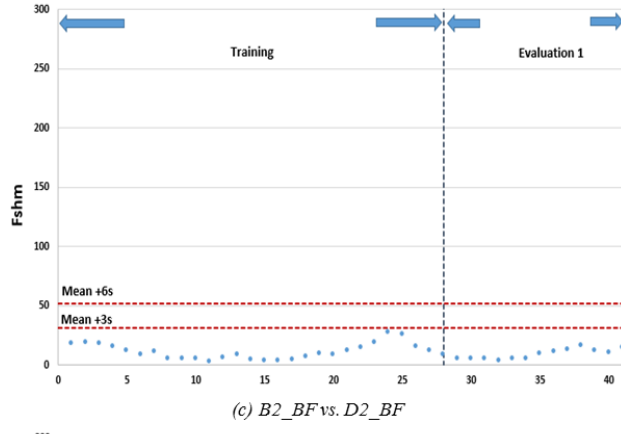
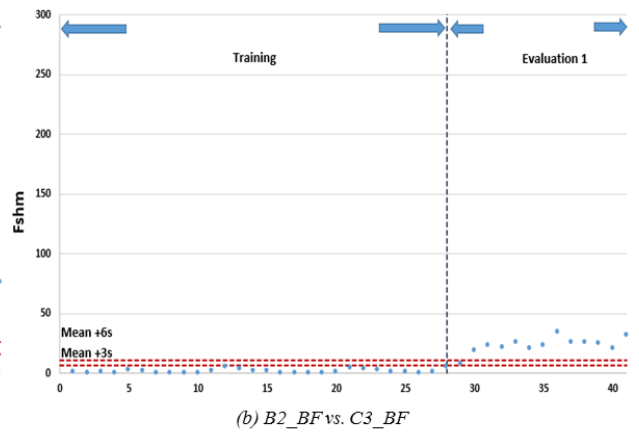
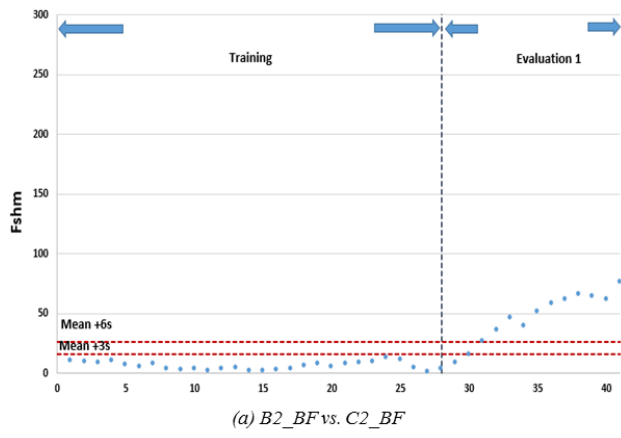
Sensor pair	Period	Number of F_{shm}	Statistics-based		Structure-based								
			3σ	6σ	Base data method				Training data method				
					Dx	Dy	Ix	Iy	Dx	Dy	Ix	Iy	
C3_BF vs. D2_BF	T & T	46	2.2	0	0	0	0	0	0	0	0	0	0
	E 1	184	53.8	25.0	14.7		3.3	17.9	14.1	0	3.3	17.9	
	E 2	67	79.1	46.3	10.4	4.5	28.4	10.4	0	4.5	28.4	10.4	
	E 3	58	74.1	41.4	17.2	8.6	27.6	13.7	0	8.6	27.6	13.8	
	Limit		13	21	31	40	25	32	76	47	43	85	
C3_BF vs. K1_BF	T & T	46	2.2	0	0	0	0	0	0	0	0	0	
	E 1	184	53.8	25.0	14.7	3.3	17.9	14.1	0	3.3	17.9	14.1	
	E 2	67	79.1	46.3	10.4	4.5	28.4	10.4	0	4.5	28.4	10.4	
	E 3	58	74.1	41.4	17.2	8.6	27.6	13.7	0	8.6	27.6	13.8	
	Limit		13	21	31	40	25	32	76	47	43	85	
C3_BF vs. M2_BF	T & T	46	0	0	10.9	13.0	17.4	17.4	0	69.6	69.6	0	
	E 1	184	0	0	2.7	2.7	8.7	9.2	0	44.0	44.0	0	
	E 2	67	0	0	0	0	6.0	6.0	0	55.2	55.2	0	
	E 3	58	0	0	0	0	0	0	0	8.6	8.6	0	
	Limit		101	162	64	63	51	50	303	21	21	287	
D2_BF vs. K1_BF	T & T	46	0	0	0	0	0	0	0	0	0	0	
	E 1	184	98.9	97.3	0	0	0	0	0	0	0	0	
	E 2	67	82.1	49.3	0	0	0	0	0	0	0	0	
	E 3	58	5.2	0	0	0	0	0	0	0	0	0	
	Limit		9	16	101	109	84	90	187	181	170	181	
D2_BF vs. M2_BF	T & T	46	0	0	0	0	0	0	0	2.2	32.6	0	
	E 1	184	0	0	0	0	0	0	0	1.1	30.1	0	
	E 2	67	89.6	17.9	23.9	1.5	80.6	35.8	0	92.5	100	0	
	E 3	58	81.0	34.5	41.4	20.7	62.1	46.6	0	91.4	100	0	
	Limit		89.2	136.7	132	157	107	127	430	77	48	440	
K1_BF vs. M2_BF	T & T	46	0	0	0	0	0	0	0	0	2.2	0	
	E 1	184	70.7	37.0	65.2	59.2	70.1	67.4	0	70.7	83.7	0	
	E 2	67	98.5	86.6	97.0	95.5	98.5	98.5	0	98.5	100	0	
	E 3	58	50	24.1	43.1	37.9	48.3	46.6	0	50.0	62.1	0	
	Limit		102	167	129	137	106	113	400	101	77	353	

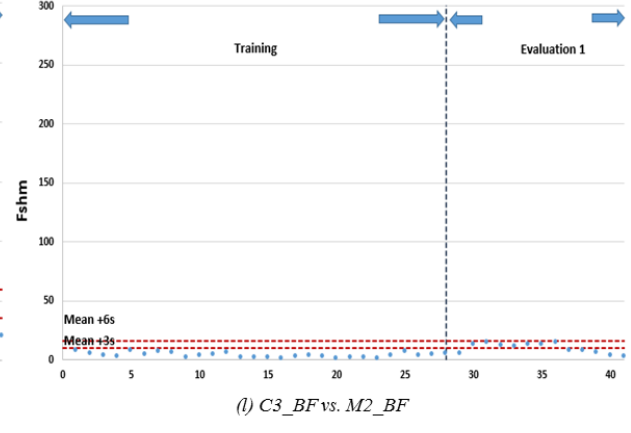
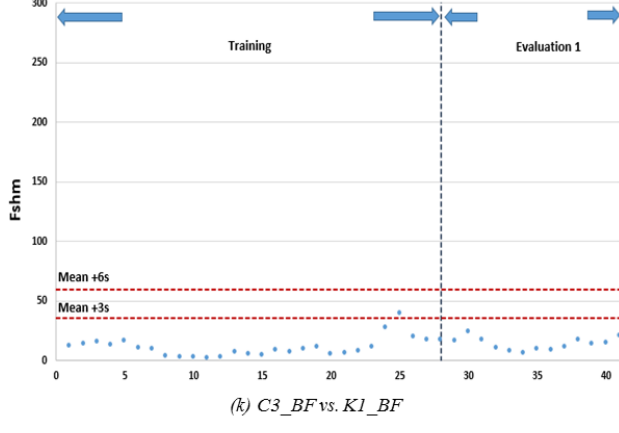
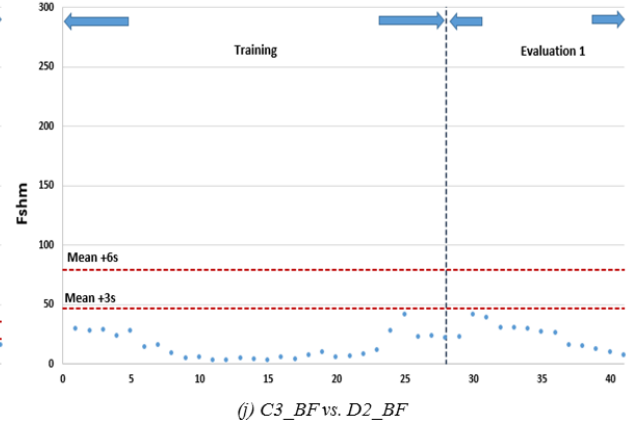
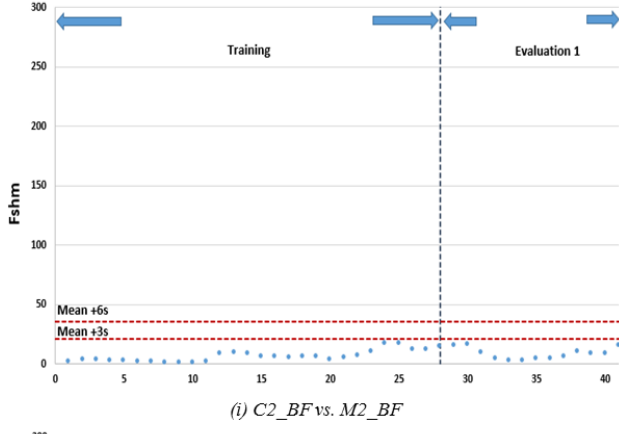
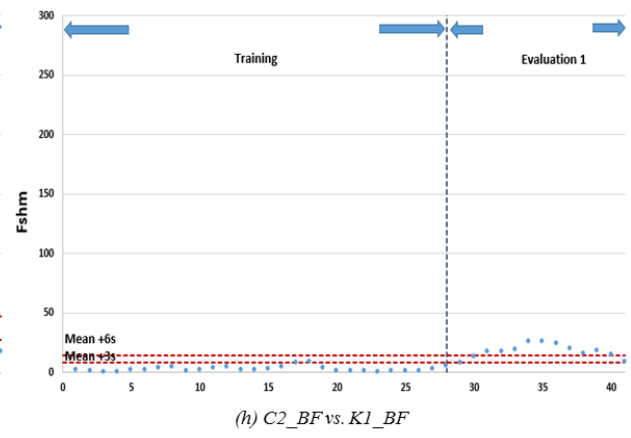
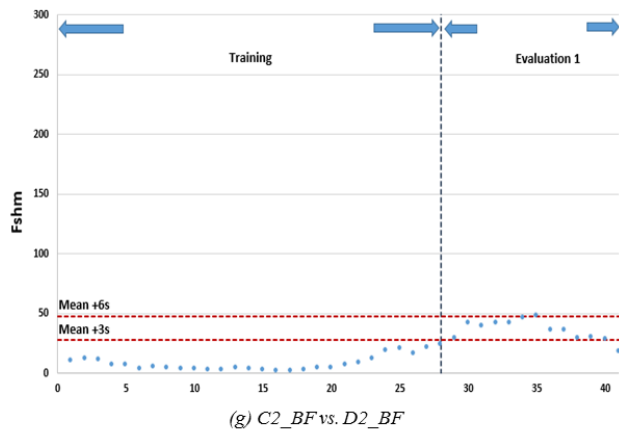
In general, a higher false indication rate was observed with statistics-based limits. It was observed that the false indication rate is minimized when a higher limit is achieved from the structure-based limit method. Among the structure-based limit methods, the highest limits were found using Dx or Dy training data methods.

5.6.1.2. Damage Level 2

As discussed in Section 5.4.2, two plates were clamped at sensor location C2 for the damage level 2. F_{shm} control charts were divided into two regions: training and Evaluation 1.

False indications were obtained in the training period and true indications were observed in the Evaluation 1 period. For damage level 2, F_{shm} control charts for the 30–40°F temperature bin with all five-axle trucks are shown in Figure 5.32.





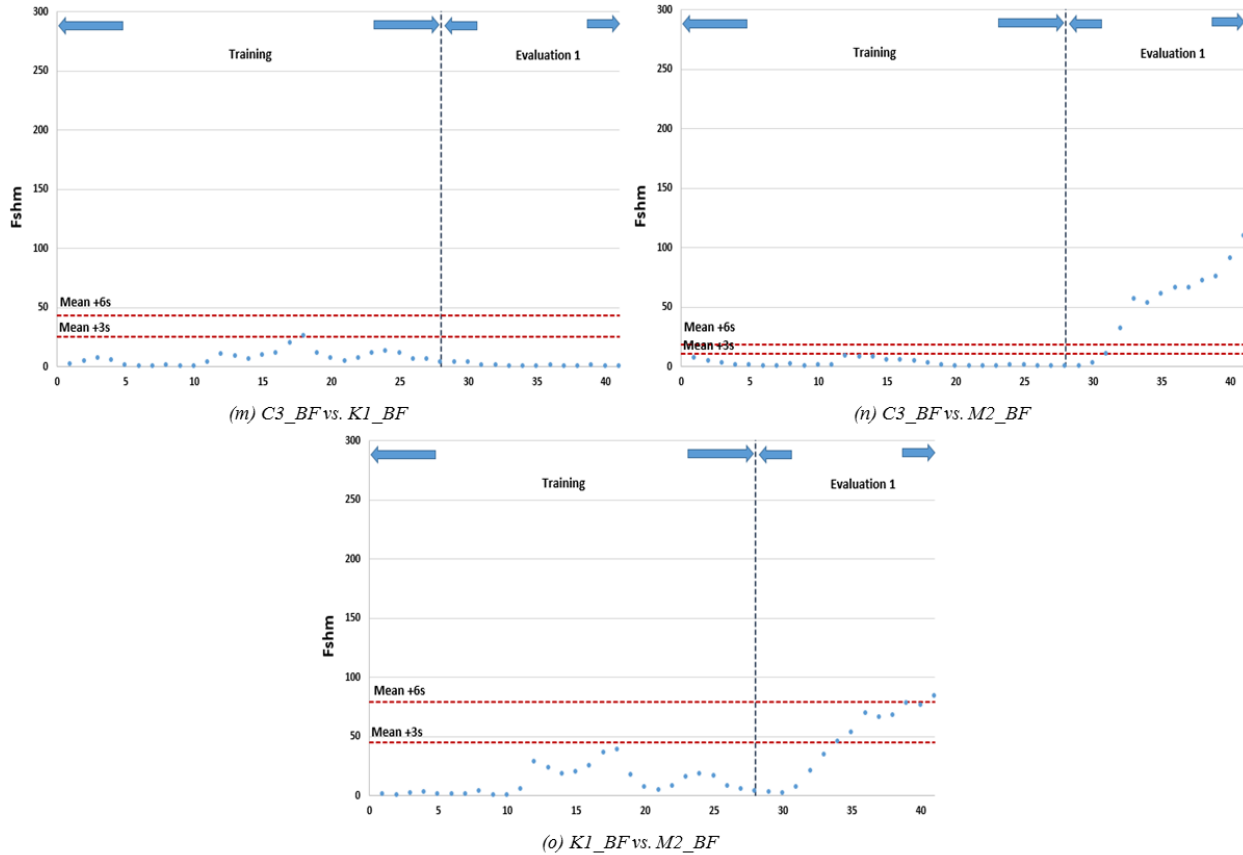


Figure 5.32. F_{shm} control charts for 30°F–40°F temperature bin with all five-axle trucks

For damage level 2, only base data limits were developed due to the amount of strain data.

In Evaluation 1 period, a low true indication rate was obtained at the sensor pair with $C2_BF$ versus a near sensor of $C2_BF$ such as $B2_BF$ and $D2_BF$. This was because there are similar structural behaviors at sensors deployed closely. For damage level 2 with a 10°F temperature bin, higher true indication rates were achieved with statistics-based limits. A summary of false and true indication rate (%) for statistics- and structure-based limit methods are shown in Table 5.9.

Table 5.9. Summary of false and true indication rate for 30–40°F temperature bin with all five-axle trucks for damage level 2

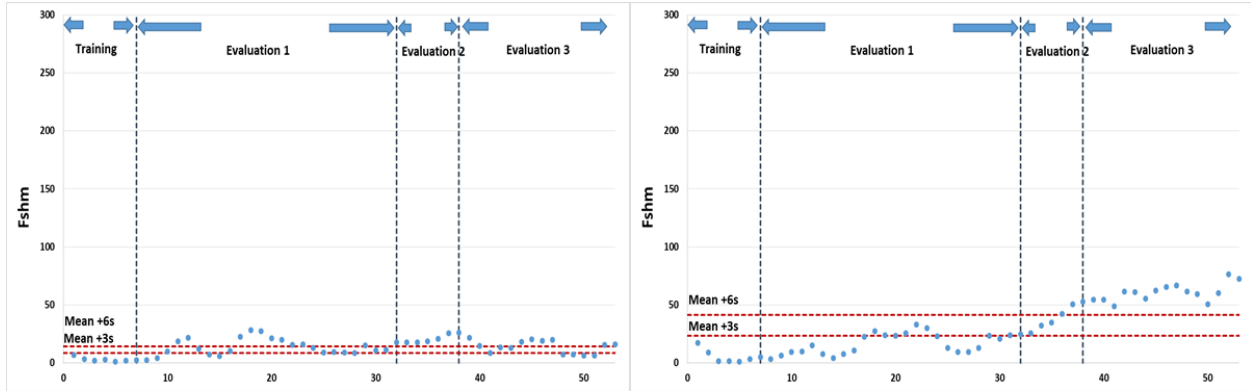
Sensor pair	Period	Number of F_{shm}	Statistics-based		Structure-based			
			3σ	6σ	Base data method			
					Dx	Dy	Ix	Iy
B2_BF vs. C2_BF	T	28	0	0	0	0	0	0
	E 1	13	84.6	84.6	0	0	0	0
	Limit		16	26	165	202	135	165
B2_BF vs. C3_BF	T	28	7.1	3.6	0	0	0	0
	E 1	13	84.6	84.6	0	0	0	0
	Limit		6.3	11.0	104	110	85	90
B2_BF vs. D2_BF	T	28	0	0	0	0	0	0
	E 1	13	0	0	0	0	0	0
	Limit		31	52	73	76	60	62
B2_BF vs. K1_BF	T	28	0	0	0	0	0	0
	E 1	13	7.7	0	0	0	0	0
	Limit		10	17	52	69	42	57
B2_BF vs. M2_BF	T	28	0	0	0	0	0	0
	E 1	13	46.2	7.7	7.7	73.7	30.8	7.7
	Limit		29	48	59	67	48	54
C2_BF vs. C3_BF	T	28	0	0	0	0	0	0
	E 1	13	0	0	0	0	0	0
	Limit		30	52	246	219	201	179
C2_BF vs. D2_BF	T	28	7.1	0	0	0	0	0
	E 1	13	76.9	7.7	0	0	0	0
	Limit		28	47	206	190	168	155
C2_BF vs. K1_BF	T	28	3.6	0	0	0	0	0
	E 1	13	84.6	76.9	0	0	0	0
	Limit		9	15	112	112	93	92
C2_BF vs. M2_BF	T	28	0	0	0	0	0	0
	E 1	13	0	0	0	0	0	0
	Limit		21	36	113	117	91	94
C3_BF vs. D2_BF	T	28	0	0	0	0	0	0
	E 1	13	0	0	0	0	0	0
	Limit		47	79	95	97	77	78
C3_BF vs. K1_BF	T	28	3.6	0	0	0	0	0
	E 1	13	46.2	0	0	0	0	0
	Limit		10	16	41	55	34	45
C3_BF vs. M2_BF	T	28	3.6	0	0	0	0	0
	E 1	13	0	0	0	0	0	0
	Limit		35	60	65	76	52	61
D2_BF vs. K1_BF	T	28	3.6	0	0	0	0	0
	E 1	13	0	0	0	0	0	0
	Limit		25	43	223	218	184	178
D2_BF vs. M2_BF	T	28	0	0	0	0	0	0
	E 1	13	77.0	77.0	0	0	0	0
	Limit		10	19	246	271	201	221
K1_BF vs. M2_BF	T	28	0	0	0	0	0	0
	E 1	13	61.5	7.7	0	0	0	0
	Limit		45	79	190	205	156	169

5.6.2. 2°F Temperature Bins and All Five-Axle Trucks

5.6.2.1. Damage Level 1

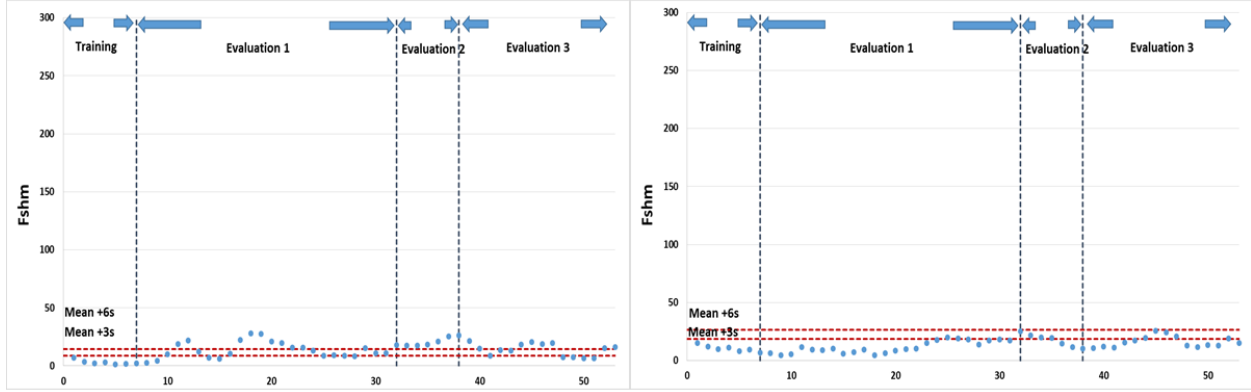
In this section, F_{shm} control charts were constructed for 2°F temperature bins (i.e., 70°F–72°F). The control charts were divided into training and evaluation. The evaluation periods were subdivided into the following regions: Evaluation 1, Evaluation 2, and Evaluation 3.

Since there was a relatively small damage level, the false indication rate is considered for training and Evaluation 1, 2, and 3 region. Figure 5.33 shows F_{shm} control charts for the 70°F–72°F temperature bin with all five-axle trucks.



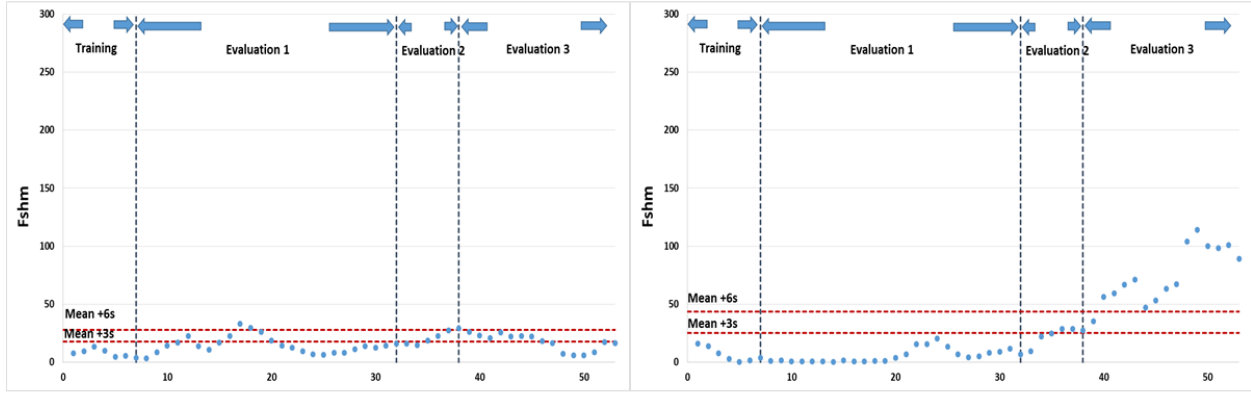
(a) $B2_BF$ vs. $C2_BF$

(b) $B2_BF$ vs. $C3_BF$



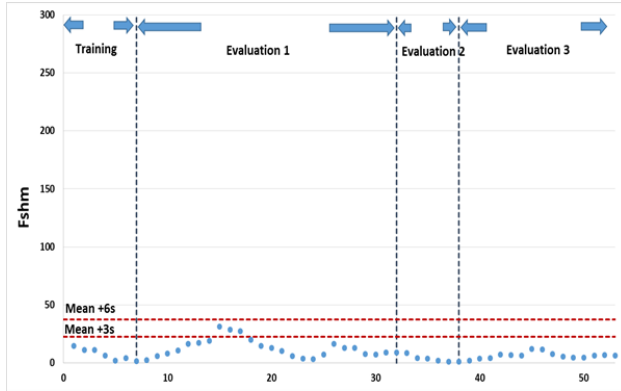
(c) $B2_BF$ vs. $D2_BF$

(d) $B2_BF$ vs. $K1_BF$

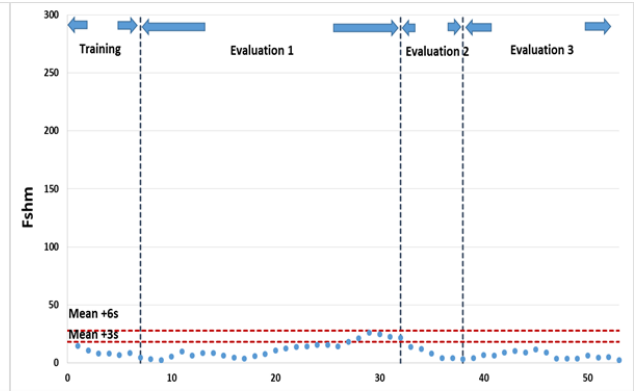


(e) $B2_BF$ vs. $M2_BF$

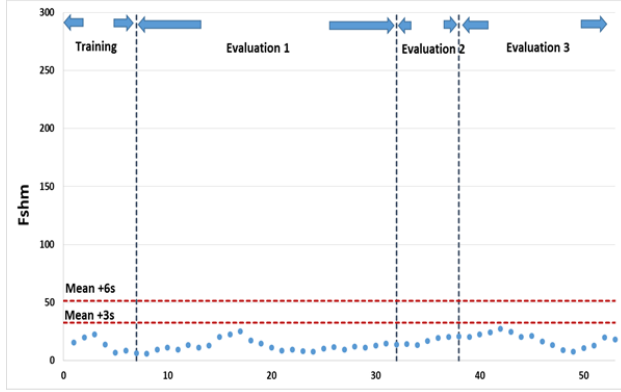
(f) $C2_BF$ vs. $C3_BF$



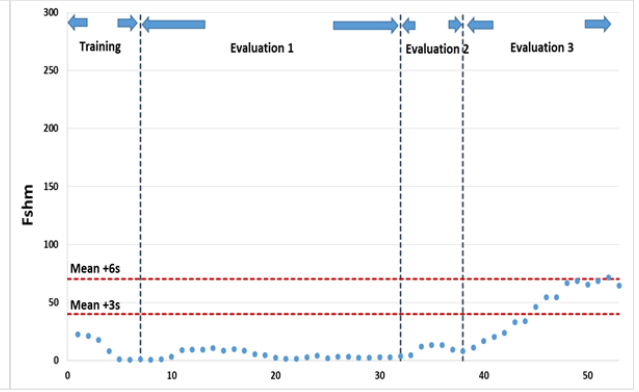
(g) $C2_BF$ vs. $D2_BF$



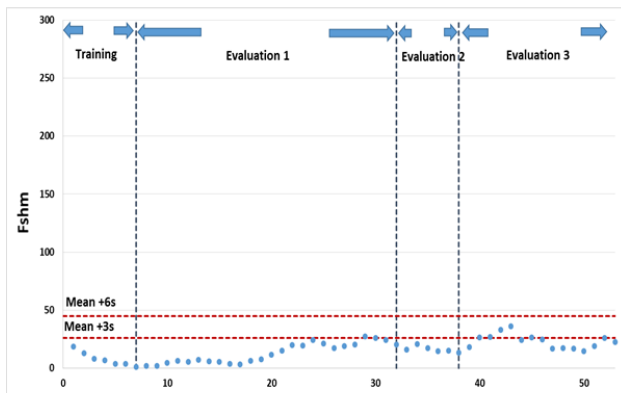
(h) $C2_BF$ vs. $K1_BF$



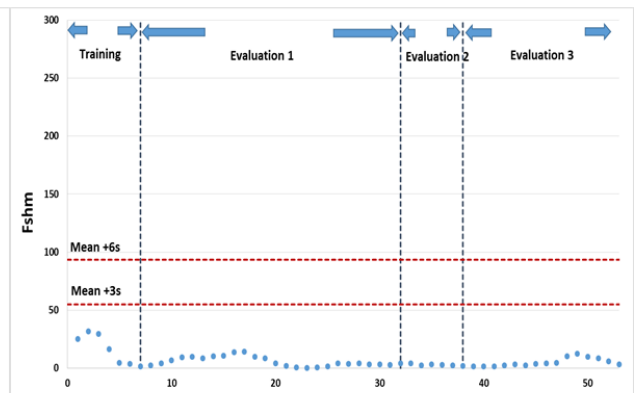
(i) $C2_BF$ vs. $M2_BF$



(j) $C3_BF$ vs. $D2_BF$



(k) $C3_BF$ vs. $K1_BF$



(l) $C3_BF$ vs. $M2_BF$

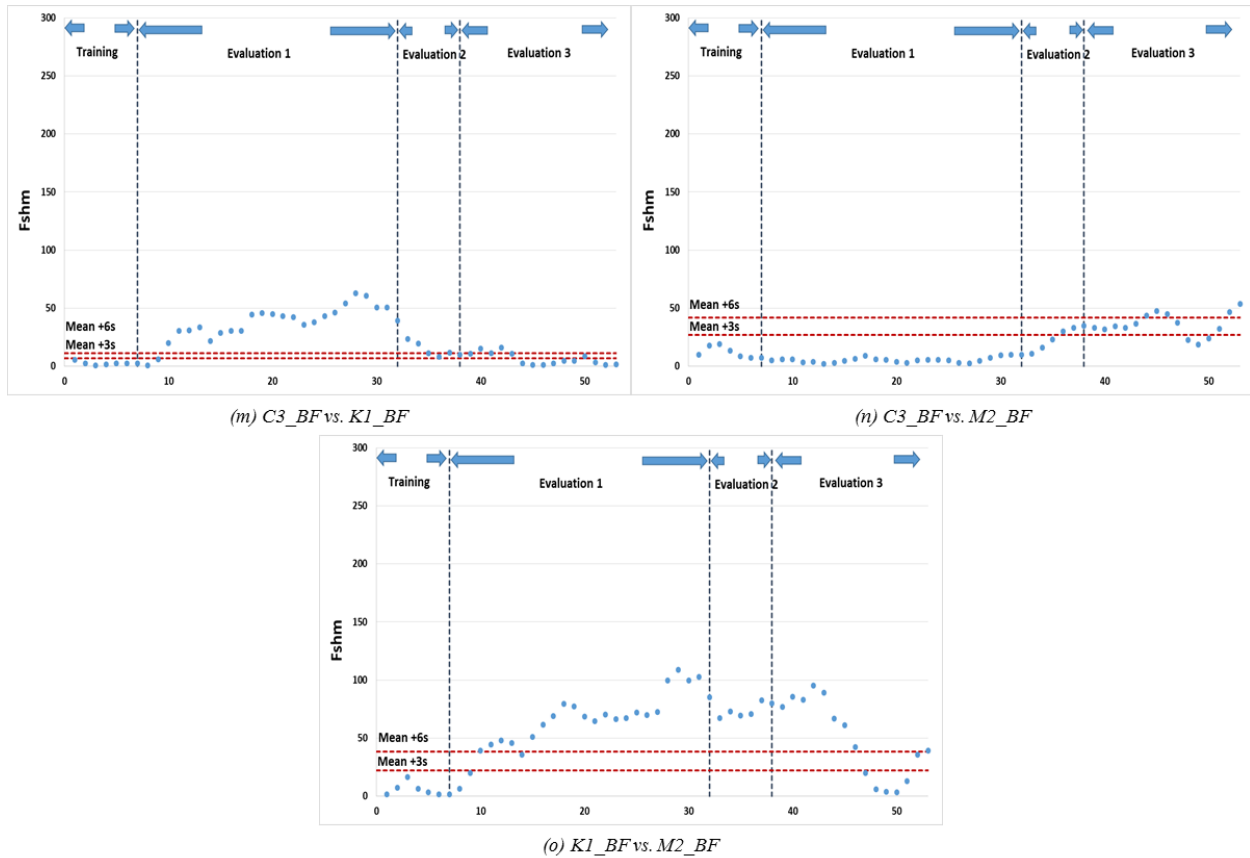


Figure 5.33. F_{shm} control charts for 70°F–72°F temperature bin with all five-axle trucks

A summary of false indication rates for statistics- and structure-based limit methods for selected sensor pairs is given in Table 5.10.

Table 5.10. Summary of false and true indication rate for 70–72°F temperature bin with all five-axle trucks for damage level 1

Sensor pair	Period	Number of F_{shm}	Statistics-based		Structure-based			
			3σ	6σ	Base data method			
					Dx	Dy	Ix	Iy
B2_BF vs. C2_BF	T	7	0	0	0	0	0	0
	E 1	25	80.0	44.0	0	0	0	0
	E 2	6	100	100	0	0	0	0
	E 3	15	73.3	53.3	0	0	0	0
	Limit		9	14	82	118	67	96
B2_BF vs. C3_BF	T	7	0	0	0	0	0	0
	E 1	25	32.0	0	0	0	0	0
	E 2	6	100	50.0	0	0	33.3	0
	E 3	15	100	100	33.3	0	93.3	6.7
	Limit		23	41	62	94	50	76

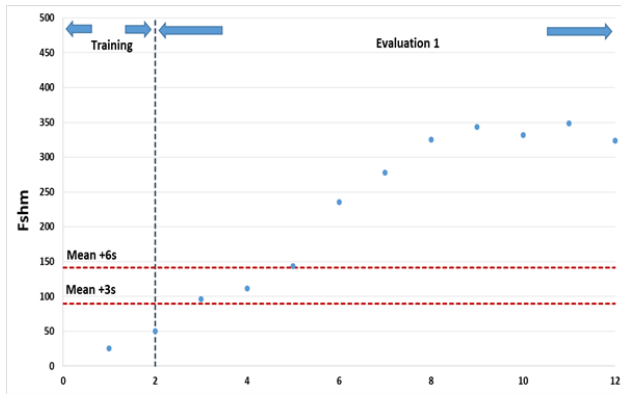
Sensor pair	Period	Number of F_{shm}	Statistics-based		Structure-based			
			3σ	6σ	Base data method			
					Dx	Dy	Ix	Iy
B2_BF vs. D2_BF	T	7	0	0	0	0	0	0
	E 1	25	60.0	28	0	0	12	0
	E 2	6	83.3	0	0	0	0	0
	E 3	15	20.0	0	0	0	0	0
	Limit		15	23	41	53	34	42
B2_BF vs. K1_BF	T	7	0	0	0	0	14.3	0
	E 1	25	12.0	0	32.0	0	36.0	0
	E 2	6	50.0	0	50.0	0	66.7	0
	E 3	15	33.3	0	40.0	0	53.3	0
	Limit		18	26	17	33	14	27
B2_BF vs. M2_BF	T	7	0	0	0	0	0	0
	E 1	25	24.0	8.0	24.0	12.0	36.0	20.0
	E 2	6	66.7	16.7	66.7	33.3	83.3	50.0
	E 3	15	53.3	0	53.3	13.3	73.3	46.7
	Limit		18	28	18	24	15	19
C2_BF vs. C3_BF	T	7	0	0	0	0	0	0
	E 1	25	0	0	0	0	0	0
	E 2	6	50.0	0	0	0	0	0
	E 3	15	100	93.3	0	0	0	0
	Limit		25	44	211	225	173	184
C2_BF vs. D2_BF	T	7	0	0	0	0	0	0
	E 1	25	12.0	0	0	0	0	0
	E 2	6	0	0	0	0	0	0
	E 3	15	0	0	0	0	0	0
	Limit		22	37	201	193	164	157
C2_BF vs. K1_BF	T	7	0	0	0	0	0	0
	E 1	25	20.0	0	0	0	0	0
	E 2	6	0	0	0	0	0	0
	E 3	15	0	0	0	0	0	0
	Limit		18	28	49	55	50	45
C3_BF vs. M2_BF	T	7	0	0	0	0	0	0
	E 1	25	0	0	0	0	0	0
	E 2	6	0	0	0	0	0	0
	E 3	15	0	0	0	0	0	0
	Limit		33	52	45	51	36	41
C3_BF vs. D2_BF	T	7	0	0	0	0	0	0
	E 1	25	0	0	0	0	0	0
	E 2	6	0	0	0	0	0	0
	E 3	15	60.0	6.7	0	0	0	0
	Limit		40	70	107	94	87	76
C3_BF vs. K1_BF	T	7	0	0	0	0	0	0
	E 1	25	0	0	0	0	16.0	0
	E 2	6	0	0	0	0	0	0
	E 3	15	33.3	0	13.3	6.7	53.3	13.3
	Limit		26	45	29	36	24	30
C3_BF vs. M2_BF	T	7	0	0	0	0	0	0
	E 1	25	0	0	0	0	0	0
	E 2	6	0	0	0	0	0	0
	E 3	15	0	0	0	0	0	0
	Limit		55	94	40	41	32	32

Sensor pair	Period	Number of F_{shm}	Statistics-based		Structure-based			
			3σ	6σ	Base data method			
					Dx	Dy	Ix	Iy
D2_BF vs. K1_BF	T	7	0	0	0	0	0	0
	E 1	25	92.0	92.0	0	0	0	0
	E 2	6	100	50.0	0	0	0	0
	E 3	15	40	13.3	0	0	0	0
	Limit		7	11	98	100	81	82
D2_BF vs. M2_BF	T	7	0	0	0	0	0	0
	E 1	25	0	0	0	0	0	0
	E 2	6	50.0	0	0	0	0	0
	E 3	15	80.0	33.3	0	0	0	0
	Limit		27	42	93	107	75	87
K1_BF vs. M2_BF	T	7	0	0	0	0	0	0
	E 1	25	92.0	88.0	8.0	4.0	20.0	16.0
	E 2	6	100	100	0	0	16.7	0
	E 3	15	66.7	60.0	0	0	26.7	13.3
	Limit		22	38	100	107	82	88

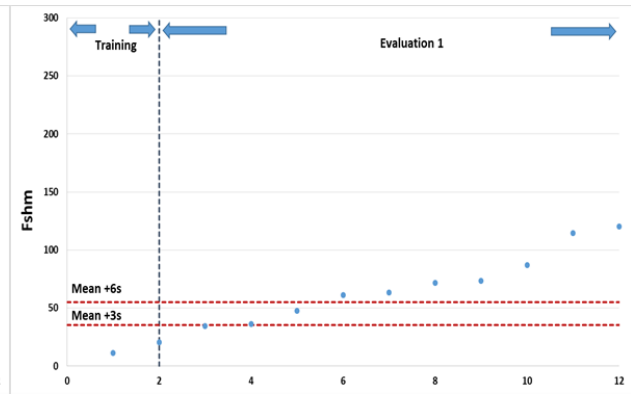
For most cases, the false indication rate decreased when structure-based limits were applied. Only the base data method was applied because fewer than 2,000 trucks were obtained for the training data.

5.6.2.2. Damage Level 2

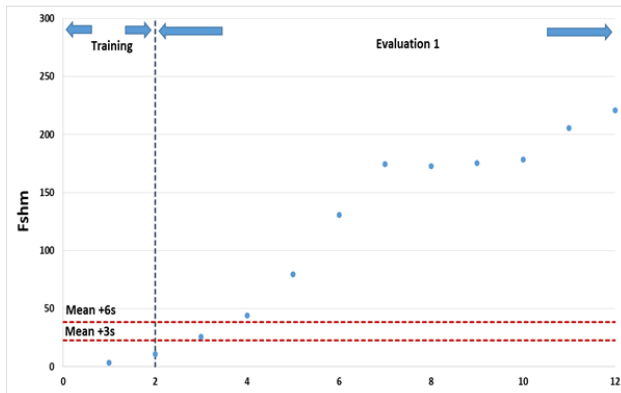
For the damage level 2 with the 2°F temperature bin control chart, the strain data within 36–38°F was selected. The F_{shm} control chart had only two regions: training and Evaluation 1. False and true indications were obtained in the training period and Evaluation 1 period, respectively. The F_{shm} control charts for 36°F–38°F temperature bins with all five-axle trucks is shown in Figure 5.34.



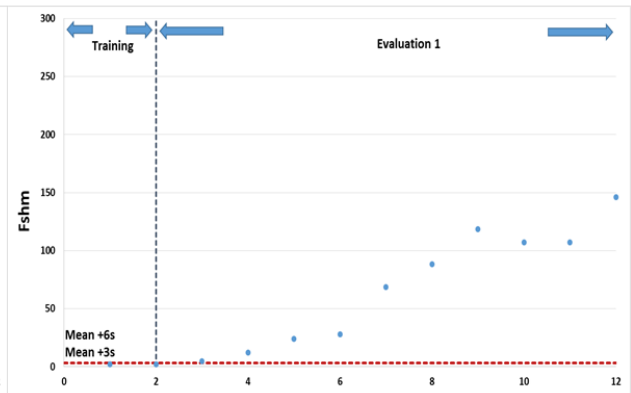
(a) $B2_BF$ vs. $C2_BF$



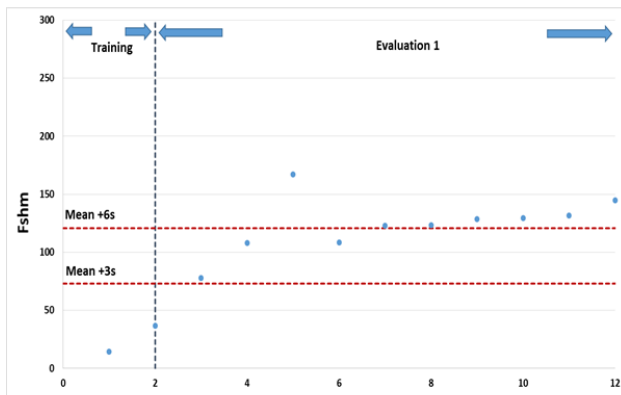
(b) $B2_BF$ vs. $C3_BF$



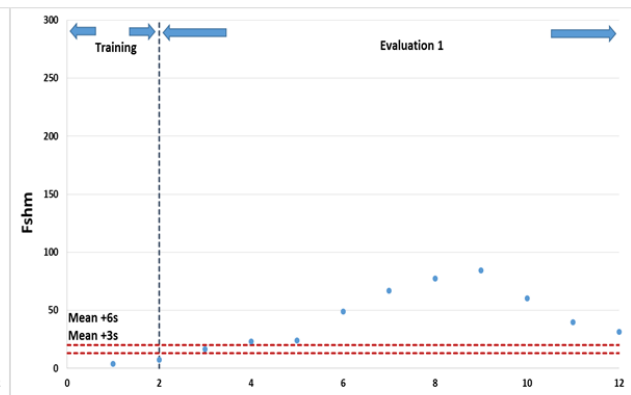
(c) $B2_BF$ vs. $D2_BF$



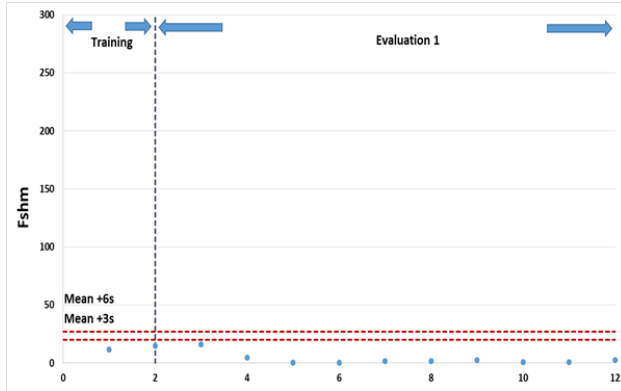
(d) $B2_BF$ vs. $K1_BF$



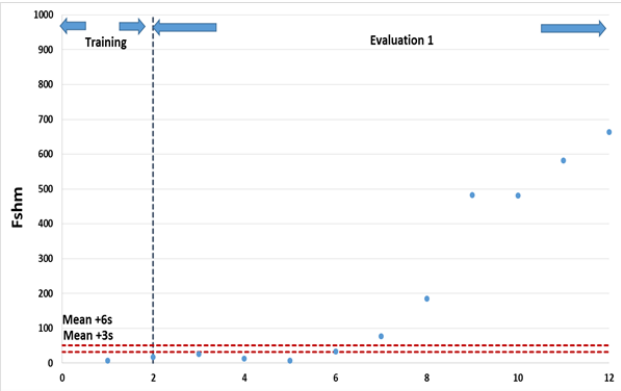
(e) $B2_BF$ vs. $M2_BF$



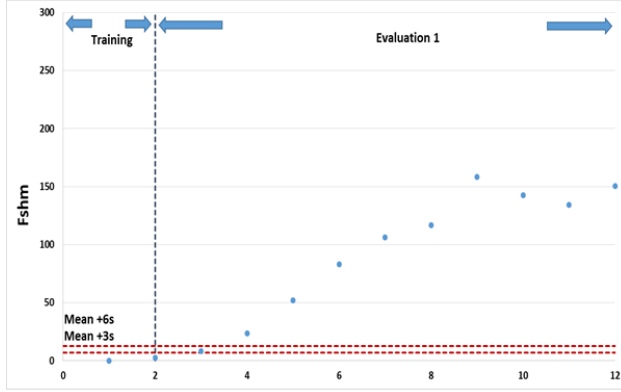
(f) $C2_BF$ vs. $C3_BF$



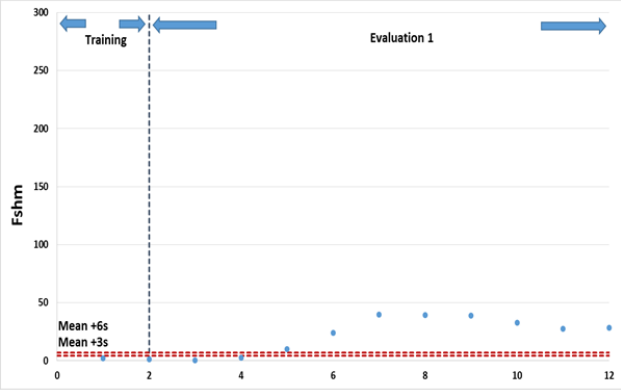
(g) $C2_BF$ vs. $D2_BF$



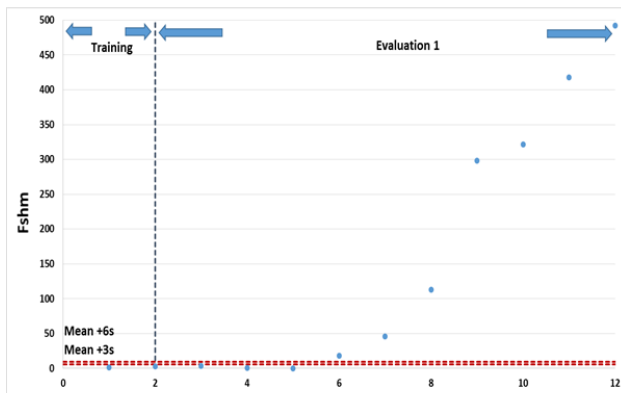
(h) $C2_BF$ vs. $K1_BF$



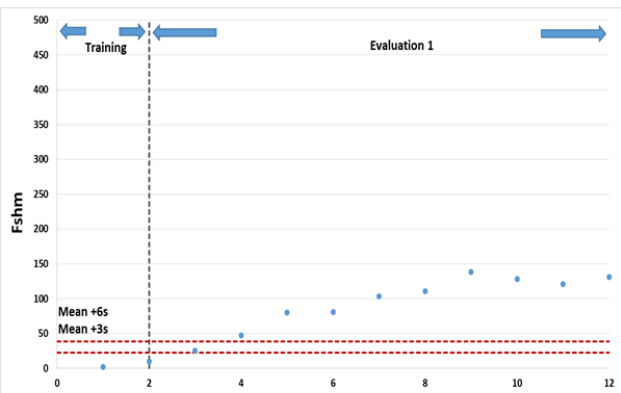
(i) $C2_BF$ vs. $M2_BF$



(j) $C3_BF$ vs. $D2_BF$



(k) $C3_BF$ vs. $K1_BF$



(l) $C3_BF$ vs. $M2_BF$

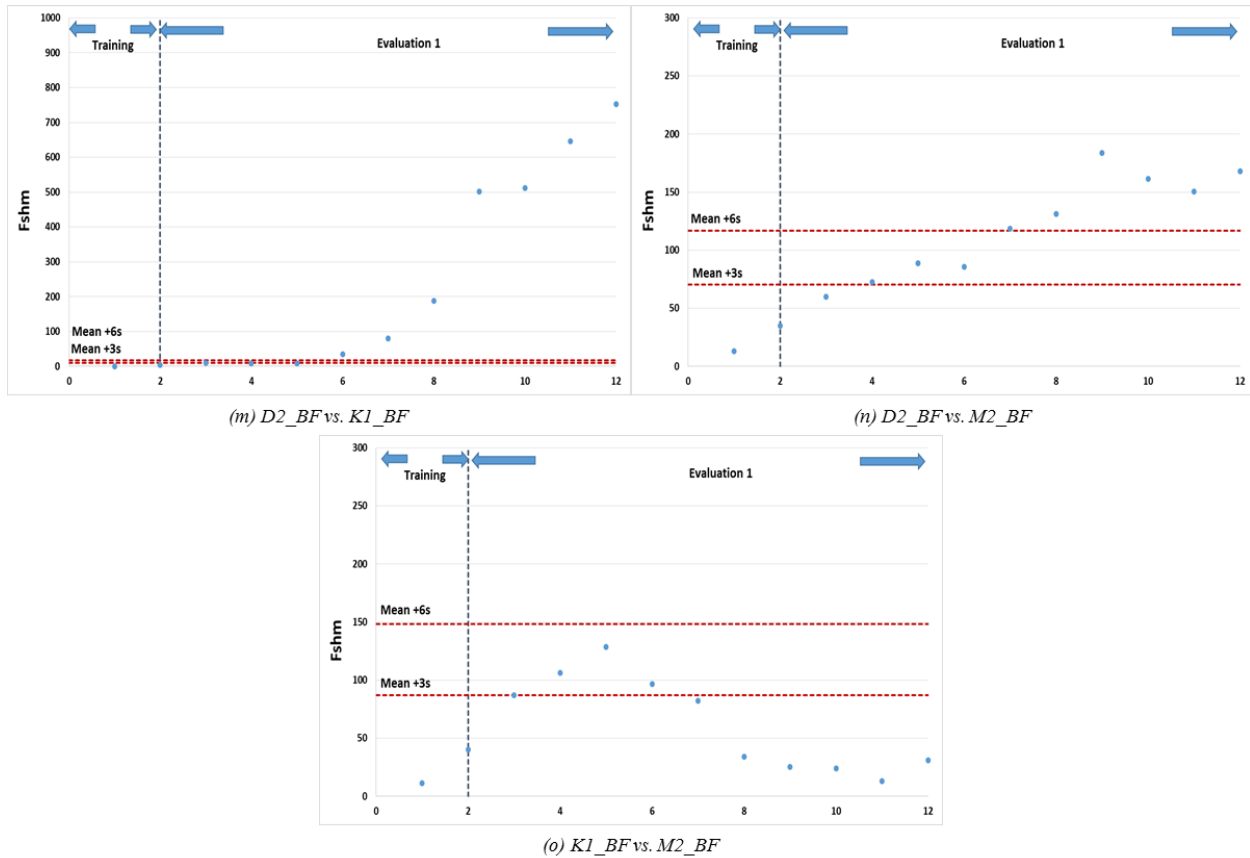


Figure 5.34. F_{shm} control charts for 36°F–38°F temperature bin with all five-axle trucks

Due to a lack of strain data, the limits for the training data method (requiring 2,000 truck events from training) were not developed.

As mentioned in Section 5.6.1, for the sensor pair C2_BF versus D2_BF, a low true indication rate was achieved even though there were changes in stiffness at C2_BF. This was because there were similar changes in stiffness for sensors, which were deployed close together at the same girder line. For damage level 2, with a 2°F temperature bin, only two F_{shm} points were considered to set a statistics-based limit. A high true indication rate was achieved with both statistics-based limits and structure-based limits. A summary of false and true indication rate for statistics- and structure-based methods is shown in Table 5.11.

Table 5.11. Summary of false and true indication rate for 36–38°F temperature bin with all five-axle trucks for damage level 2

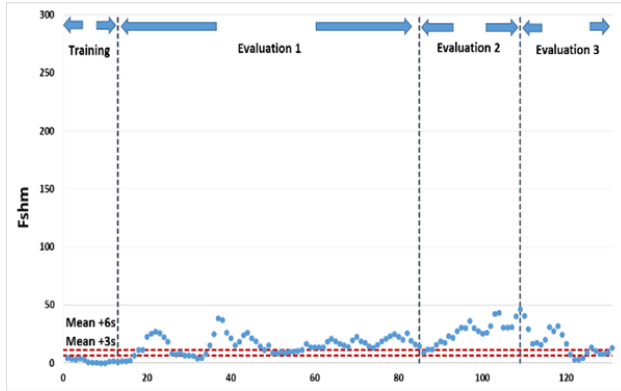
Sensor pair	Period	Number of F_{shm}	Statistics-based		Structure-based			
			3σ	6σ	Base data method			
					Dx	Dy	Ix	Iy
B2_BF vs. C2_BF	T	2	0	0	0	0	0	0
	E 1	10	100	80	70	70	80	80
	Limit		90	141	151	161	123	131
B2_BF vs. C3_BF	T	2	0	0	0	0	0	0
	E 1	10	90	70	20	0	20	0
	Limit		36	55	109	132	89	107
B2_BF vs. D2_BF	T	2	0	0	0	0	0	0
	E 1	10	100	90	70	80	80	80
	Limit		23	38	91	74	75	60
B2_BF vs. K1_BF	T	2	0	0	0	0	0	0
	E 1	10	100	100	60	60	60	60
	Limit		3	4	50	54	40	44
B2_BF vs. M2_BF	T	2	0	0	0	0	0	0
	E 1	10	100	70	100	100	100	100
	Limit		73	121	74	63	60	51
C2_BF vs. C3_BF	T	2	0	0	0	0	0	0
	E 1	10	100	90	0	0	0	0
	Limit		13	20	232	272	189	221
C2_BF vs. D2_BF	T	2	0	0	0	0	0	0
	E 1	10	0	0	0	0	0	0
	Limit		20	27	397	321	324	262
C2_BF vs. K1_BF	T	2	0	0	0	0	0	0
	E 1	10	70	60	50	50	50	50
	Limit		31	51	112	100	92	82
C2_BF vs. M2_BF	T	2	0	0	0	0	0	0
	E 1	10	100	90	40	50	50	60
	Limit		7	12	132	114	107	93
C3_BF vs. D2_BF	T	2	0	0	0	0	0	0
	E 1	10	80	80	0	0	0	0
	Limit		4	7	157	105	128	85
C3_BF vs. K1_BF	T	2	0	0	0	0	0	0
	E 1	10	70	70	50	50	60	60
	Limit		6	10	52	49	43	40
C3_BF vs. M2_BF	T	2	0	0	0	0	0	0
	E 1	10	100	90	40	60	60	80
	Limit		22	39	115	84	93	68
D2_BF vs. K1_BF	T	20	0	0	0	0	0	0
	E 1	10	80	70	50	50	50	50
	Limit		10	17	151	154	125	126
D2_BF vs. M2_BF	T	2	0	0	0	0	0	0
	E 1	10	90	60	40	30	50	50
	Limit		70	117	146	158	119	128
K1_BF vs. M2_BF	T	2	0	0	0	0	0	0
	E 1	10	30	0	20	20	40	40
	Limit		87	148	103	101	85	83

5.6.3. *10°F Temperature Bins and Semi-Trucks*

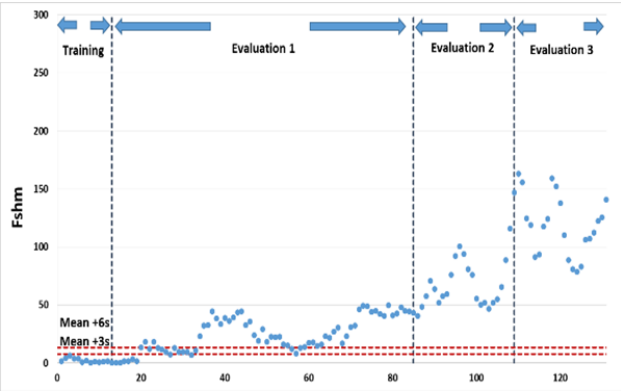
5.6.3.1. Damage Level 1

F_{shm} control charts with semi-trucks are constructed for the 10°F temperature bin. (i.e., 70°F–80°F) The control charts are divided into training and evaluation. The evaluation period is subdivided into the following periods: Evaluation 1, Evaluation 2, and Evaluation 3.

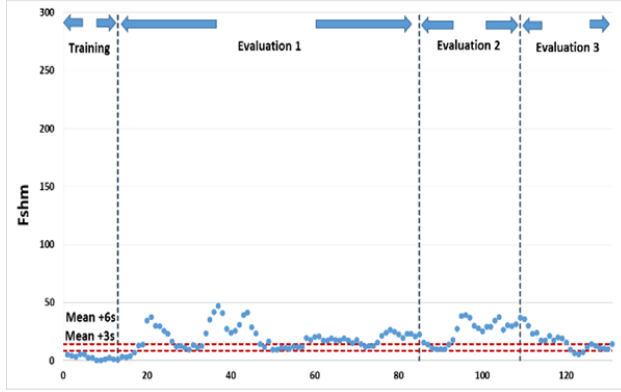
Since there is a relatively small damage level, the false indication rate is considered for training and Evaluation 1, 2, and 3 period. Figure 5.35 shows F_{shm} control charts for the 70°F–80°F temperature bin with all semi-trucks.



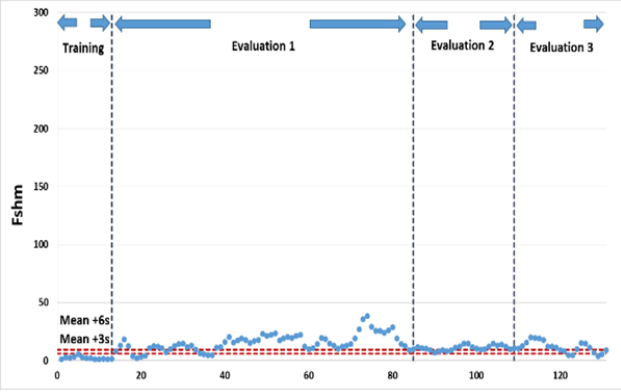
(a) $B2_BF$ vs. $C2_BF$



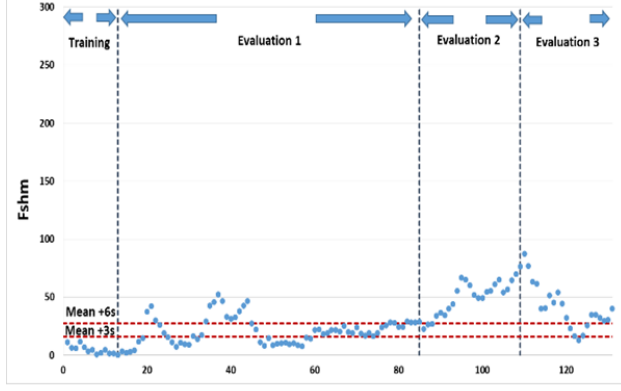
(b) $B2_BF$ vs. $C3_BF$



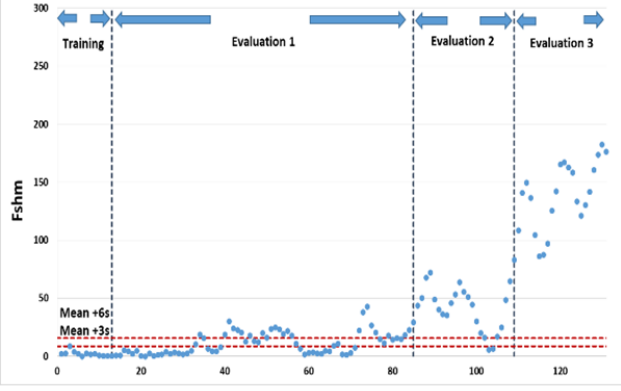
(c) $B2_BF$ vs. $D2_BF$



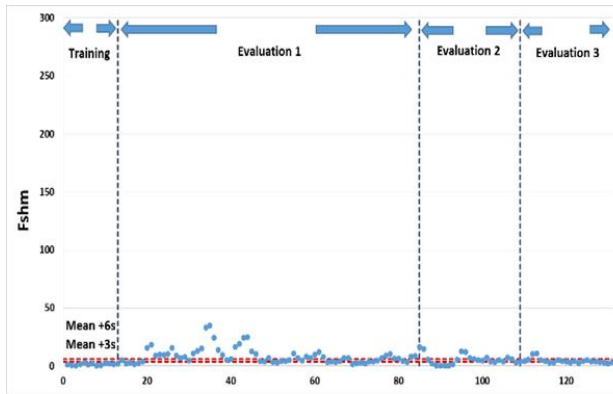
(d) $B2_BF$ vs. $K1_BF$



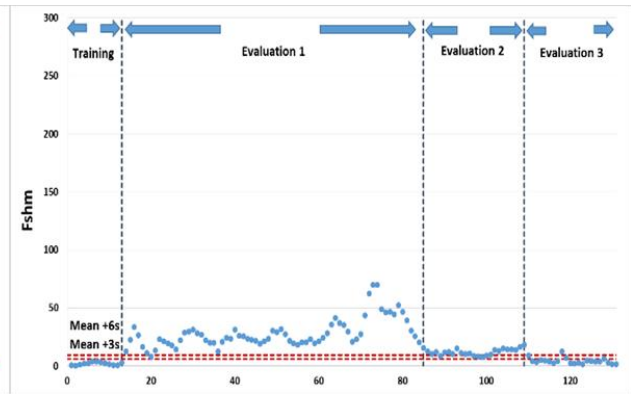
(e) $B2_BF$ vs. $M2_BF$



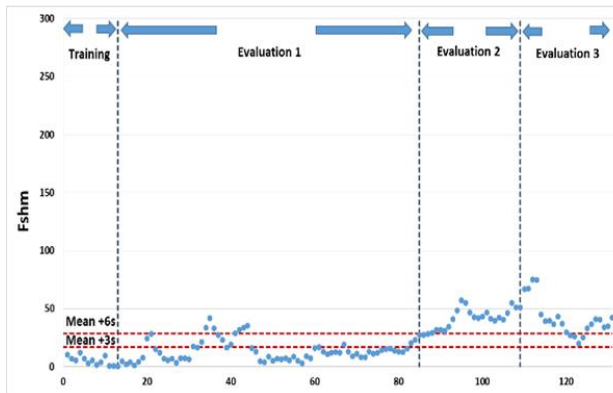
(f) $C2_BF$ vs. $C3_BF$



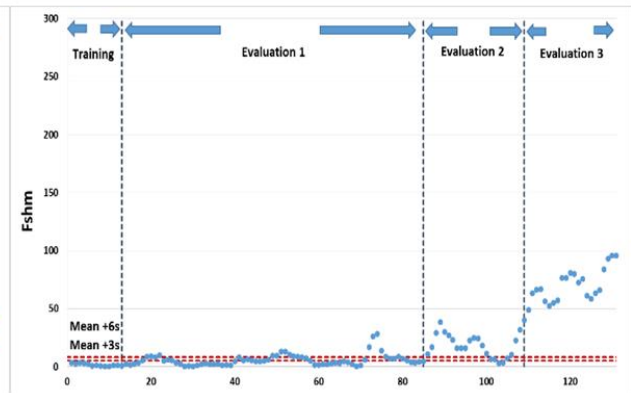
(g) $C2_BF$ vs. $D2_BF$



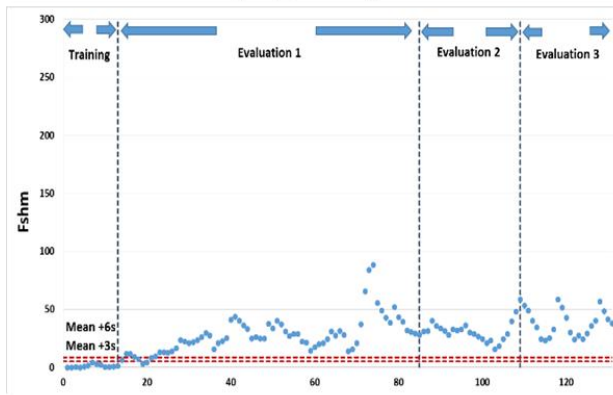
(h) $C2_BF$ vs. $K1_BF$



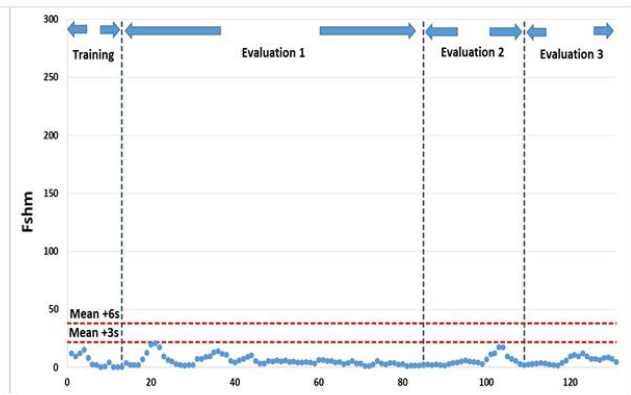
(i) $C2_BF$ vs. $M2_BF$



(j) $C3_BF$ vs. $D2_BF$



(k) $C3_BF$ vs. $K1_BF$



(l) $C3_BF$ vs. $M2_BF$

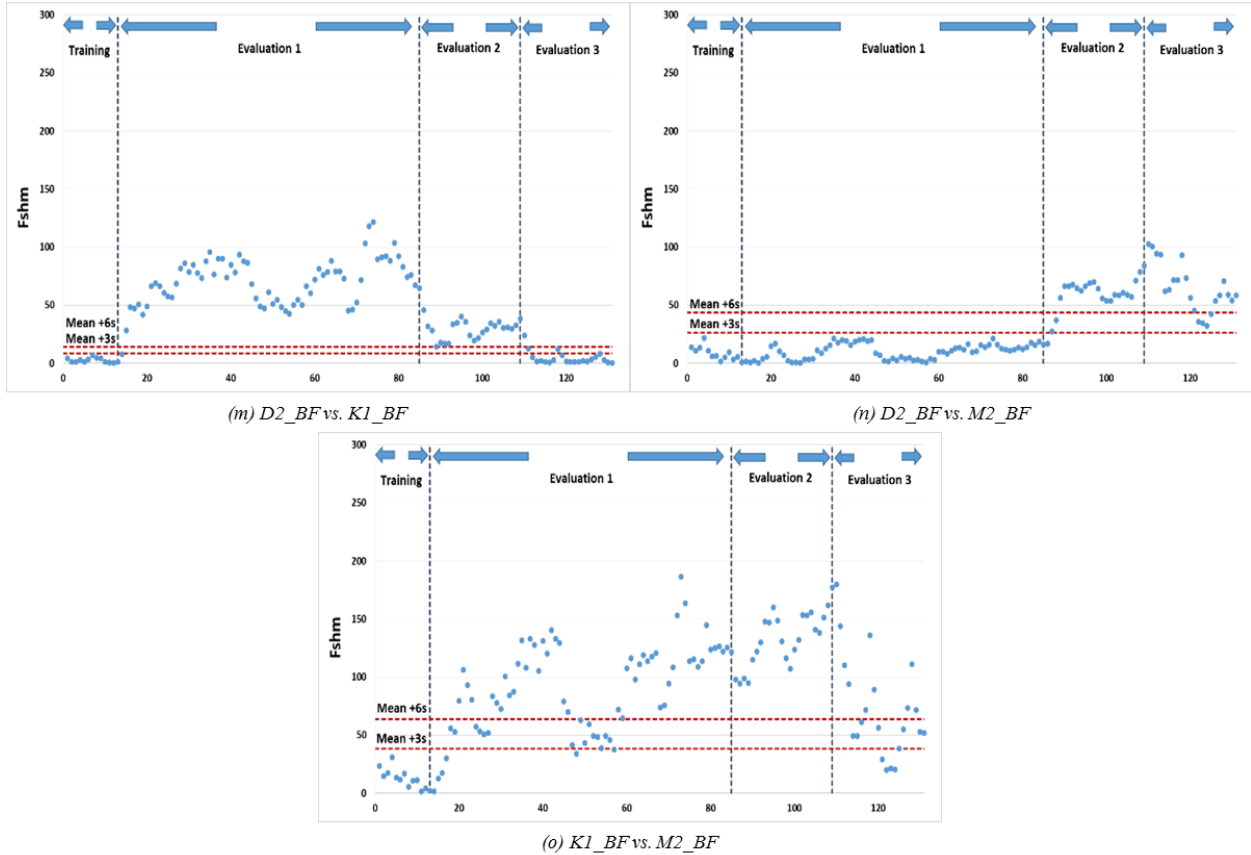


Figure 5.35. F_{sh_m} control charts for 70°F–80°F temperature bin with semi-trucks

A summary of false indication rates for statistics- and structure-based limit methods for selected sensor pairs appears in Table 5.12.

Table 5.12. Summary of false and true indication rate for 70–80°F temperature bin with semi-trucks for damage level 1

Sensor pair	Period	Number of F_{sh_m}	Statistics-based		Structure-based			
			3σ	6σ	Base data method			
					Dx	Dy	Ix	Iy
B2_BF vs. C2_BF	T	13	0	0	0	0	0	0
	E 1	72	90.3	70.8	0	0	0	0
	E 2	24	100	95.8	0	0	0	0
	E 3	22	86.4	59.1	0	0	0	0
	Limit		6	11	92	130	75	106
B2_BF vs. C3_BF	T	13	0	0	0	0	0	0
	E 1	72	88.9	72.2	0	0	0	0
	E 2	24	100	100	37.5	8.3	50.0	25.0
	E 3	22	100	100	100	63.6	100	86.4
	Limit		8	14	73	108	60	88

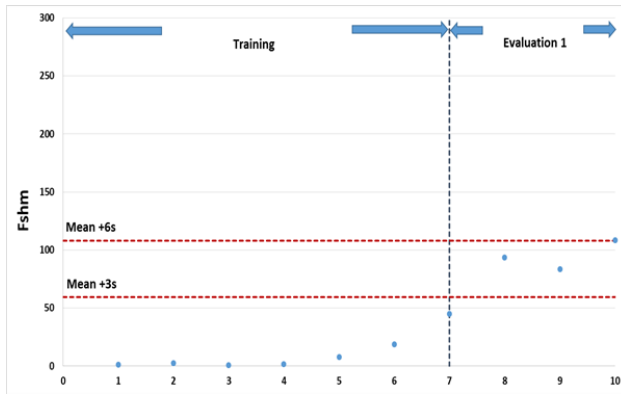
Sensor pair	Period	Number of F_{shm}	Statistics-based		Structure-based			
			3σ	6σ	Base data method			
					Dx	Dy	Ix	Iy
B2_BF vs. D2_BF	T	13	0	0	0	0	0	0
	E 1	72	94.4	62.5	0	0	1.4	0
	E 2	24	100	75.0	0	0	0	0
	E 3	22	86.4	54.5	0	0	0	0
	Limit		9	14	57	70	47	57
B2_BF vs. K1_BF	T	13	0	0	0	0	0	0
	E 1	72	90.3	83.3	4.2	0	13.9	0
	E 2	24	100	70.8	0	0	0	0
	E 3	22	81.8	63.6	0	0	0	0
	Limit		6	10	29	47	23	39
B2_BF vs. M2_BF	T	13	0	0	0	0	0	0
	E 1	72	63.9	29.2	29.2	9.7	41.7	18.1
	E 2	24	100	87.5	91.7	75.0	100	87.5
	E 3	22	95.5	77.3	77.3	50.0	86.4	72.7
	Limit		16	27	27	38	22	30
C2_BF vs. C3_BF	T	13	0	0	0	0	0	0
	E 1	72	51.4	34.7	0	0	0	0
	E 2	24	91.7	91.7	0	0	0	0
	E 3	22	100	100	0	0	0	0
	Limit		9	16	229	240	187	196
C2_BF vs. D2_BF	T	13	0	0	0	0	0	0
	E 1	72	79.2	58.3	0	0	0	0
	E 2	24	62.5	29.2	0	0	0	0
	E 3	22	59.1	9.1	0	0	0	0
	Limit		4	6	332	301	271	246
C2_BF vs. K1_BF	T	13	0	0	0	0	0	0
	E 1	72	100	98.6	0	0	0	0
	E 2	24	100	79.2	0	0	0	0
	E 3	22	18.2	4.5	0	0	0	0
	Limit		6	10	86	87	71	71
C3_BF vs. M2_BF	T	13	0	0	0	0	0	0
	E 1	72	26.4	8.3	0	0	0	0
	E 2	24	100	91.7	0	0	0	0
	E 3	22	100	81.8	0	0	18.2	13.6
	Limit		17	29	77	82	62	67
C3_BF vs. D2_BF	T	13	0	0	0	0	0	0
	E 1	72	47.2	23.6	0	0	0	0
	E 2	24	91.7	79.2	0	0	0	0
	E 3	22	100	100	0	0	0	0
	Limit		5	8	139	119	113	97
C3_BF vs. K1_BF	T	13	0	0	0	0	0	0
	E 1	72	97.2	93.1	8.3	6.9	19.4	12.5
	E 2	24	100	100	8.3	4.2	16.7	8.3
	E 3	22	100	100	27.3	18.2	45.5	31.8
	Limit		5	9	46	51	38	42
C3_BF vs. M2_BF	T	13	0	0	0	0	0	0
	E 1	72	0	0	0	0	0	0
	E 2	24	0	0	0	0	0	0
	E 3	22	0	0	0	0	0	0
	Limit		22	38	61	61	49	49

Sensor pair	Period	Number of F_{shm}	Statistics-based		Structure-based			
			3σ	6σ	Base data method			
					Dx	Dy	Ix	Iy
D2_BF vs. K1_BF	T	13	0	0	0	0	0	0
	E 1	72	98.6	98.6	0	0	0	0
	E 2	24	100	95.8	0	0	0	0
	E 3	22	13.6	4.5	0	0	0	0
	Limit		9	15	154	158	127	129
D2_BF vs. M2_BF	T	13	0	0	0	0	0	0
	E 1	72	0	0	0	0	0	0
	E 2	24	95.8	87.5	0	0	0	0
	E 3	22	100	81.8	0	0	0	0
	Limit		26	44	136	158	111	129
K1_BF vs. M2_BF	T	13	0	0	0	0	0	0
	E 1	72	91.7	70.8	29.2	19.4	50	47.2
	E 2	24	100	100	70.8	62.5	91.7	83.3
	E 3	22	81.8	45.5	13.6	13.6	22.7	22.7
	Limit		38	64	117	124	96	102

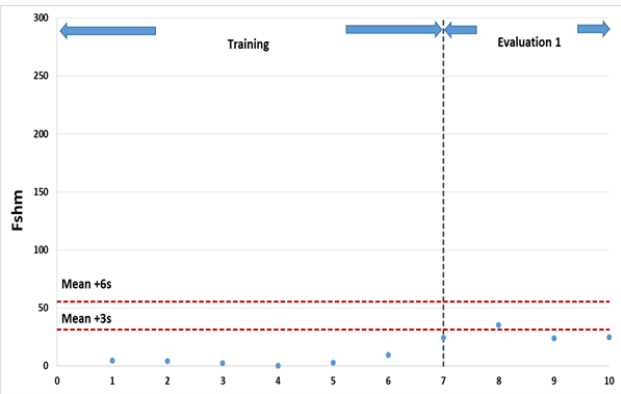
For most cases, the false indication rate decreased when structure-based limits were applied. Only the base data method was developed due to the lack of sufficient strain data.

5.6.3.2. Damage Level 2

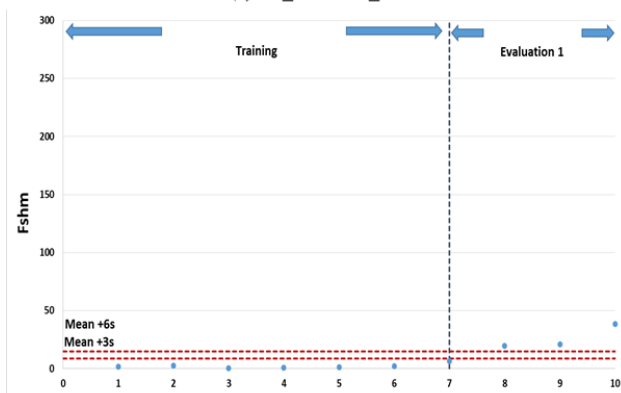
For damage level 2 with semi-trucks in the 10°F temperature bin, the strain data within 30°F–40°F was chosen for the control charts. F_{shm} control charts were developed with two periods: training and Evaluation 1. False and true indications were obtained in the training period and Evaluation 1 period, respectively. F_{shm} control charts for 30°F–40°F temperature bins with semi-trucks are shown in Figure 5.36.



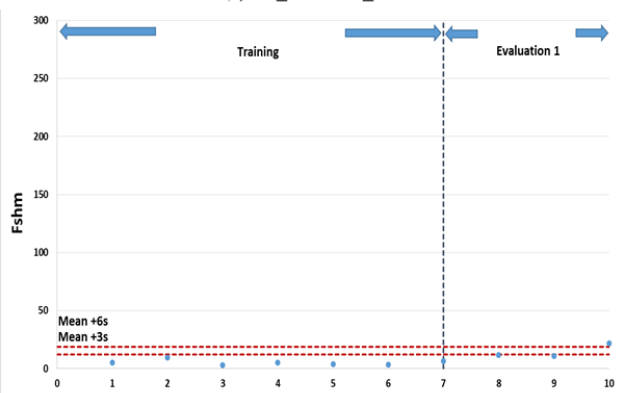
(a) $B2_BF$ vs. $C2_BF$



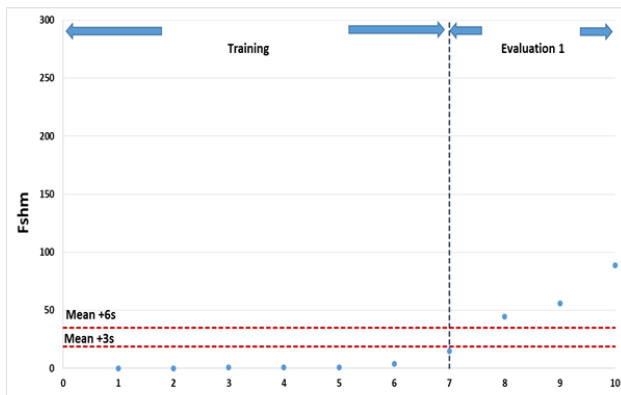
(b) $B2_BF$ vs. $C3_BF$



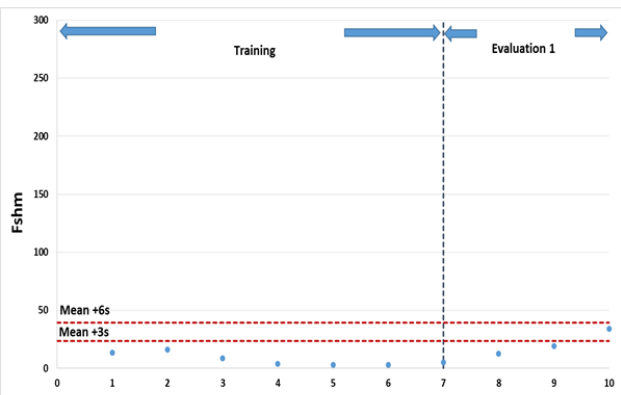
(c) $B2_BF$ vs. $D2_BF$



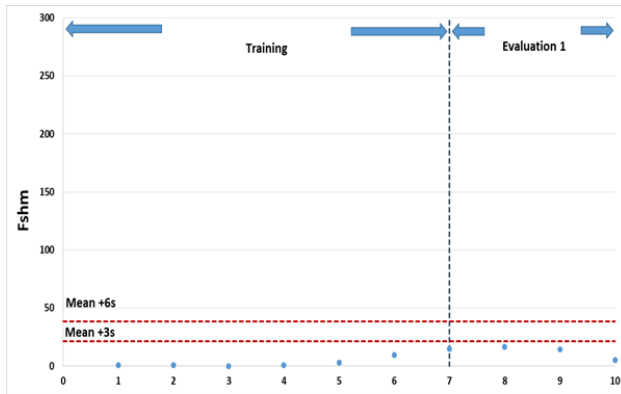
(d) $B2_BF$ vs. $K1_BF$



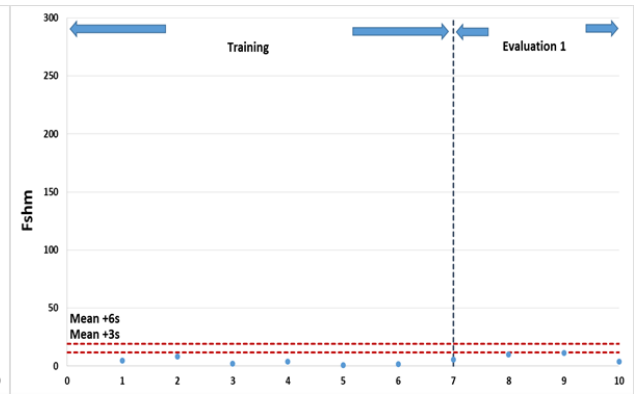
(e) $B2_BF$ vs. $M2_BF$



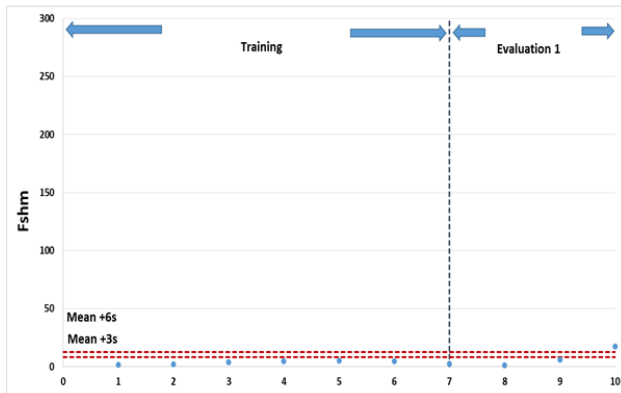
(f) $C2_BF$ vs. $C3_BF$



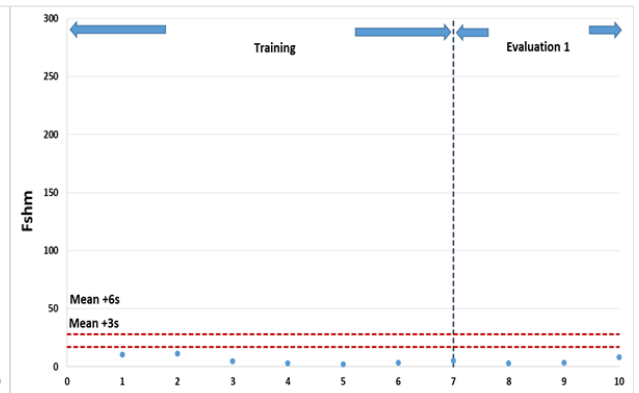
(g) C2_BF vs. D2_BF



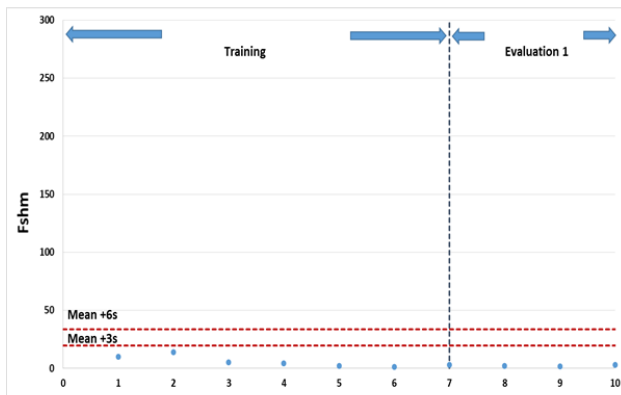
(h) C2_BF vs. K1_BF



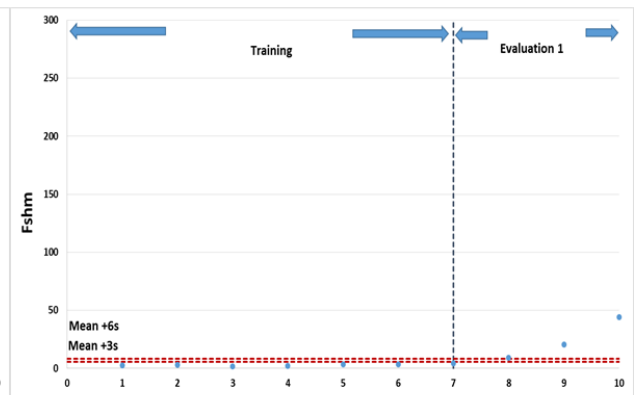
(i) C2_BF vs. M2_BF



(j) C3_BF vs. D2_BF



(k) C3_BF vs. K1_BF



(l) C3_BF vs. M2_BF

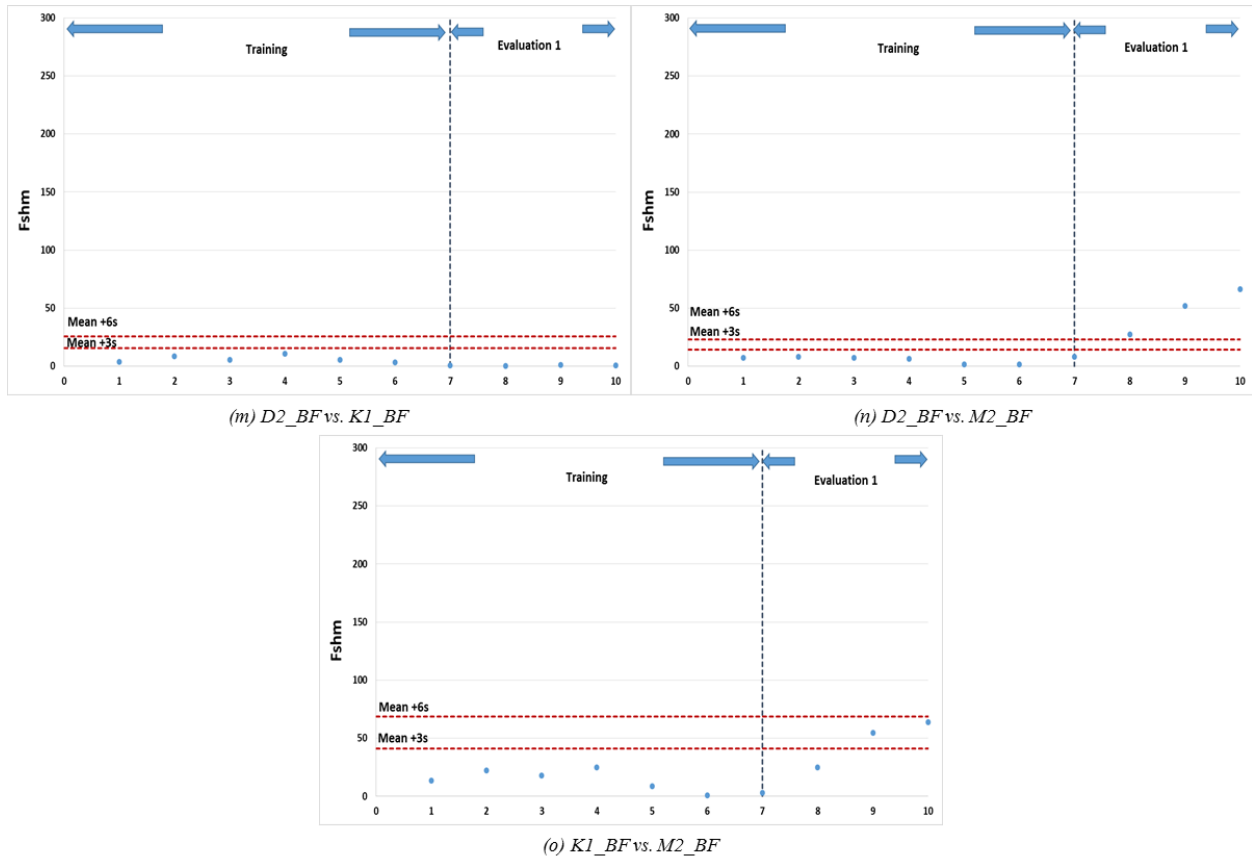


Figure 5.36. F_{shm} control charts for 30°F–40°F temperature bin with semi-trucks

With the statistics-based limits, the F_{shm} method detected damages well by achieving a higher true indication rate except sensor pairs that were deployed close to C2_BF. In most cases, true indication rate decreased with base data limits. A summary of false indication rates for statistics- and structure-based limit methods for selected sensor pairs appears in Table 5.13.

Table 5.13. Summary of false and true indication rate for 30–40°F temperature bin with semi-trucks for damage level 2

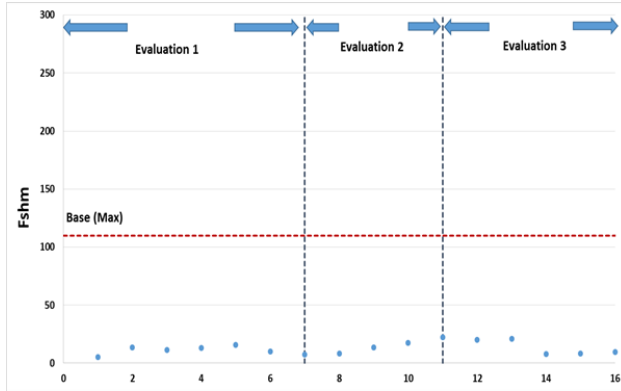
Sensor pair	Period	Number of F_{shm}	Statistics-based		Structure-based			
			3σ	6σ	Base data method			
					Dx	Dy	Ix	Iy
B2_BF vs. C2_BF	T	7	0	0	0	0	0	0
	E 1	3	100	33.3	0	0	0	0
	Limit		60	108	161	180	132	147
B2_BF vs. C3_BF	T	7	0	0	0	0	0	0
	E 1	3	33.3	0	0	0	0	0
	Limit		31	56	114	113	93	92
B2_BF vs. D2_BF	T	7	0	0	0	0	0	0
	E 1	3	100	100	0	0	0	0
	Limit		9	15	75	64	61	52
B2_BF vs. K1_BF	T	7	0	0	0	0	0	0
	E 1	3	33.	33.3	0	0	0	0
	Limit		12	19	49	59	40	48
B2_BF vs. M2_BF	T	7	0	0	0	0	0	0
	E 1	3	100	100	33.3	33.3	66.7	66.7
	Limit		19	35	66	63	53	51
C2_BF vs. C3_BF	T	7	0	0	0	0	0	0
	E 1	3	33.3	0	0	0	0	0
	Limit		24	39	226	204	184	166
C2_BF vs. D2_BF	T	7	0	0	0	0	0	0
	E 1	3	0	0	0	0	0	0
	Limit		21	39	212	177	173	144
C2_BF vs. K1_BF	T	7	0	0	0	0	0	0
	E 1	3	0	0	0	0	0	0
	Limit		12	19	119	115	98	94
C2_BF vs. M2_BF	T	7	0	0	0	0	0	0
	E 1	3	33.3	33.3	0	0	0	0
	Limit		8	13	137	128	111	104
C3_BF vs. D2_BF	T	7	0	0	0	0	0	0
	E 1	3	0	0	0	0	0	0
	Limit		17	28	96	87	78	70
C3_BF vs. K1_BF	T	7	0	0	0	0	0	0
	E 1	3	0	0	0	0	0	0
	Limit		20	34	44	55	36	45
C3_BF vs. M2_BF	T	7	0	0	0	0	0	0
	E 1	3	100	100	0	0	0	0
	Limit		6	8	75	78	60	63
D2_BF vs. K1_BF	T	7	0	0	0	0	0	0
	E 1	3	0	0	0	0	0	0
	Limit		15	25	242	252	200	206
D2_BF vs. M2_BF	T	7	0	0	0	0	0	0
	E 1	3	100	100	0	0	0	0
	Limit		16	23	225	249	183	203
K1_BF vs. M2_BF	T	7	0	0	0	0	0	
	E 1	3	66.7	0	0	0	0	0
	Limit		41	69	185	188	151	155

5.6.4. 2°F Temperature Bins and Semi-Trucks

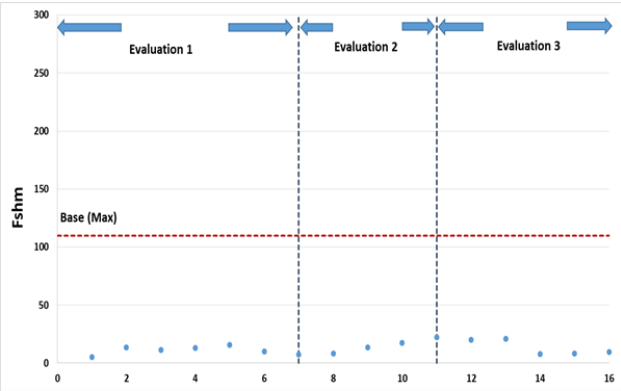
5.6.4.1. Damage Level 1

In this section, F_{shm} control charts are constructed for a 2°F temperature bin with semi-trucks (i.e., 70°F–72°F). Only 200 trucks as the base data were used for F_{shm} control charts. The control charts were constructed with three evaluation periods. The evaluation periods are subdivided into the following regions: Evaluation 1, Evaluation 2, and Evaluation 3. Due to the amount of data, only the structural-based base data method limits were established.

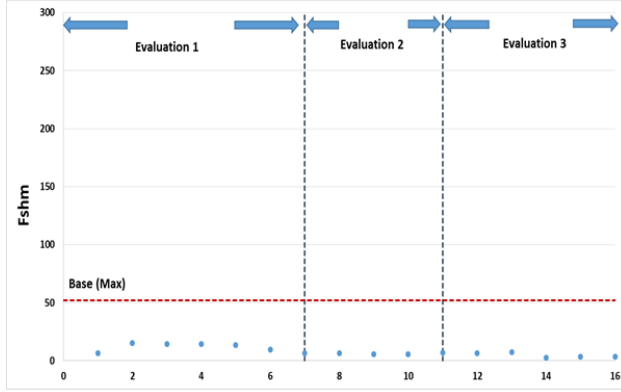
A relatively small change in stiffness was detected when the two plates between the two sensors were added. The false indication rate is considered for all evaluation regions. Figure 5.37 shows F_{shm} control charts for the 70°F–72°F temperature bin with semi-trucks.



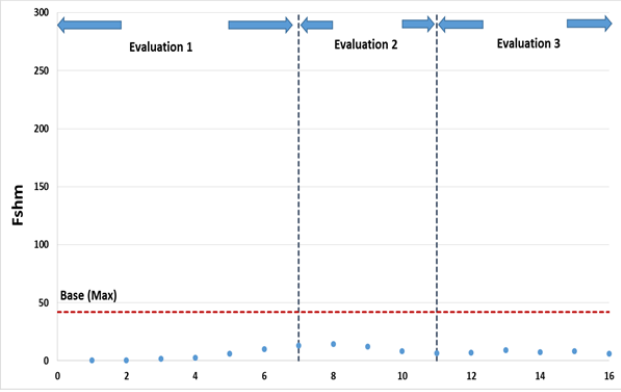
(a) $B2_BF$ vs. $C2_BF$



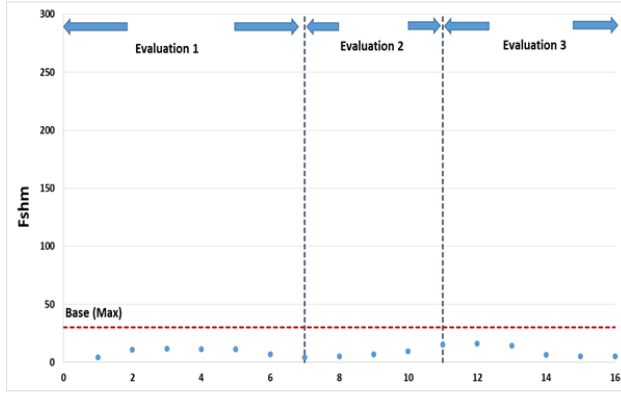
(b) $B2_BF$ vs. $C3_BF$



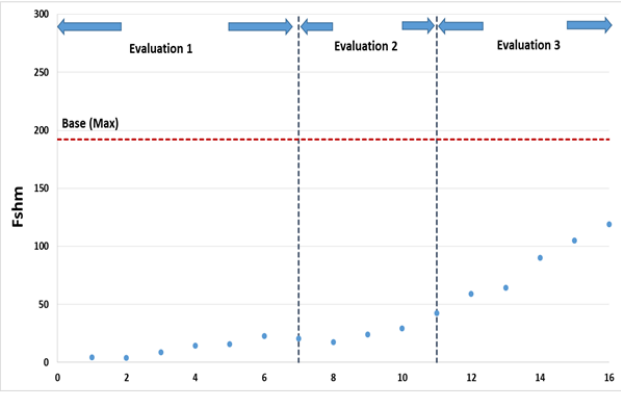
(c) $B2_BF$ vs. $D2_BF$



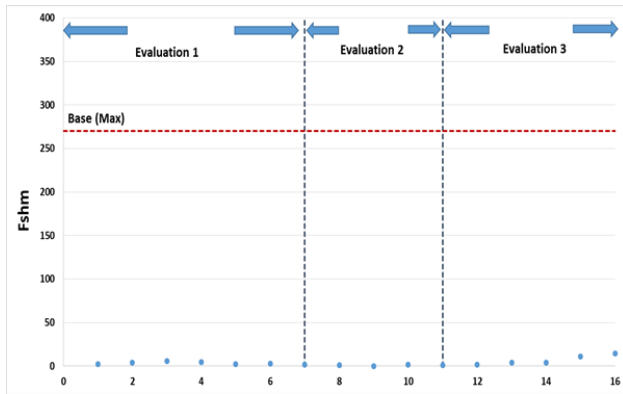
(d) $B2_BF$ vs. $K1_BF$



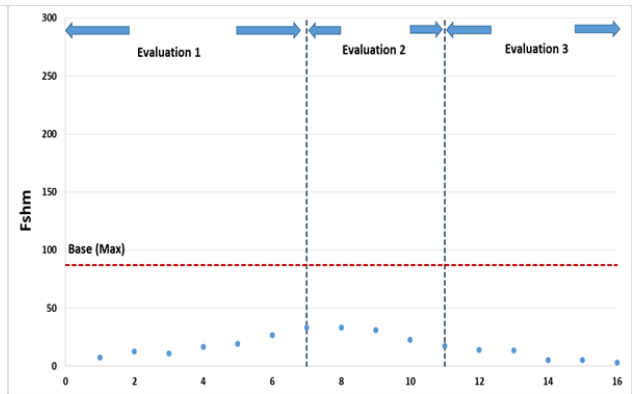
(e) $B2_BF$ vs. $M2_BF$



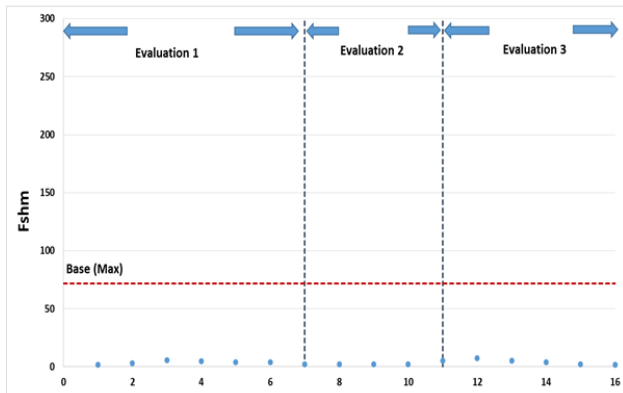
(f) $C2_BF$ vs. $C3_BF$



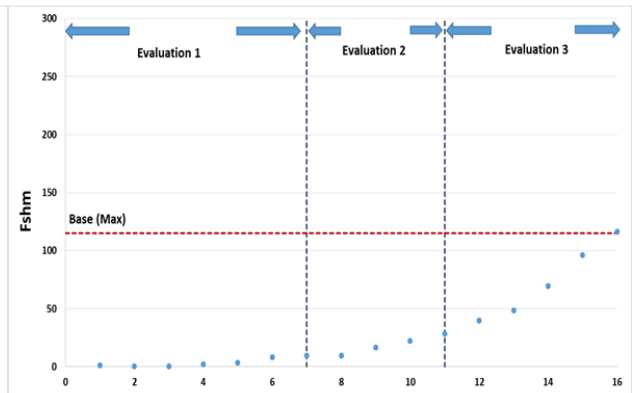
(g) $C2_BF$ vs. $D2_BF$



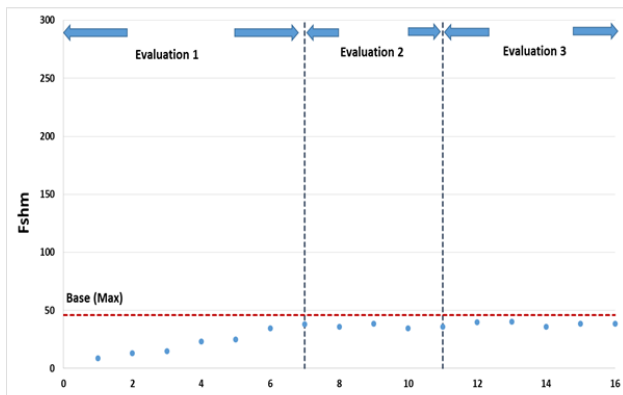
(h) $C2_BF$ vs. $K1_BF$



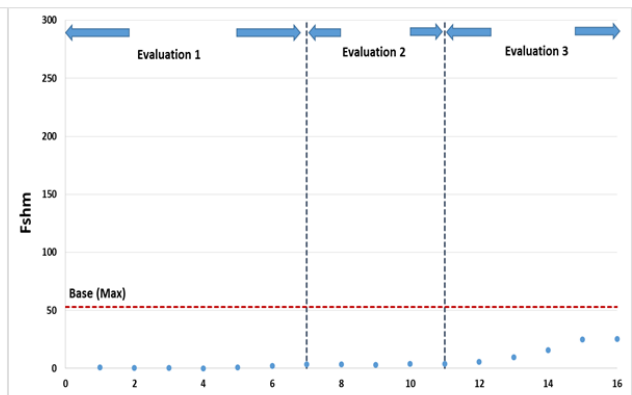
(i) $C2_BF$ vs. $M2_BF$



(j) $C3_BF$ vs. $D2_BF$



(k) $C3_BF$ vs. $K1_BF$



(l) $C3_BF$ vs. $M2_BF$

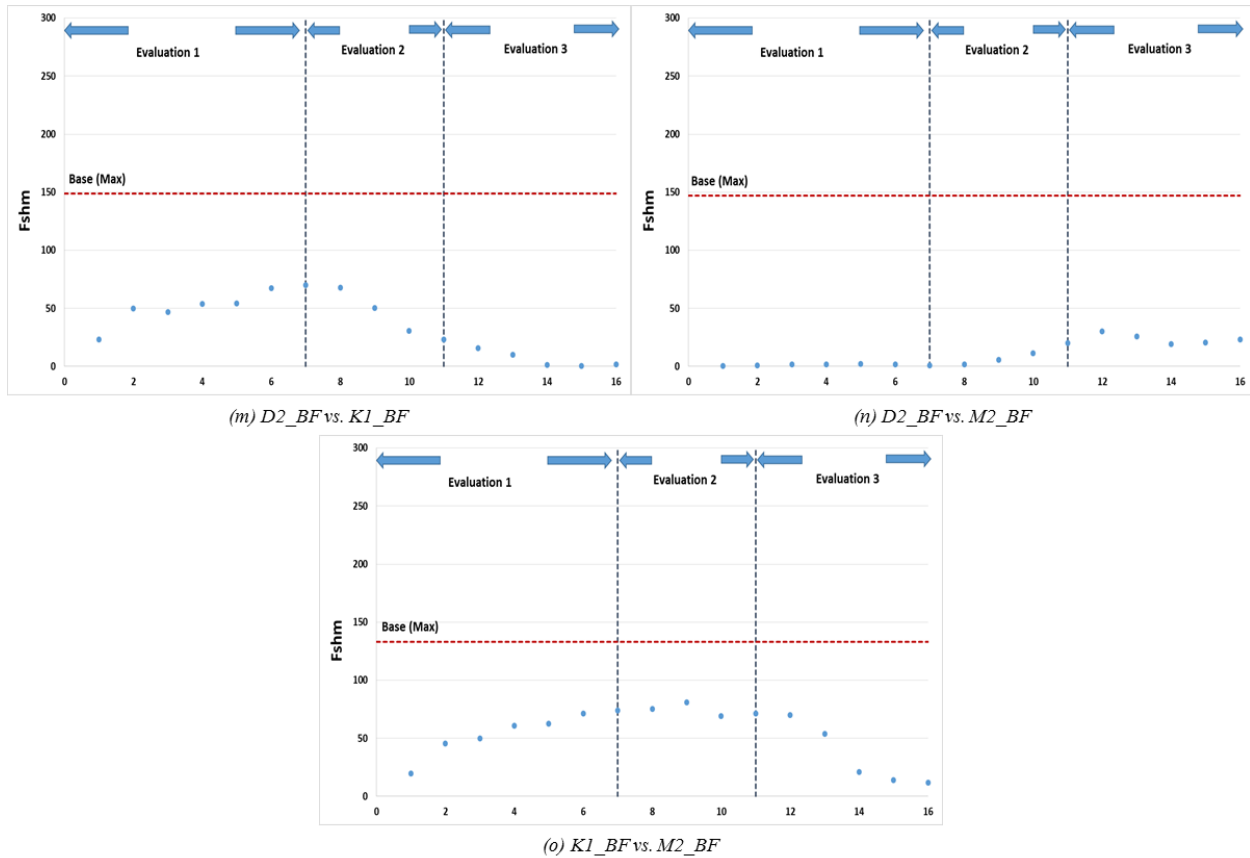


Figure 5.37. F_{sh_m} control charts for 70°F–72°F temperature bin with semi-trucks

Note that for damage level 2, with a 2°F temperature bin and semi-trucks, there was a limitation in developing an F_{sh_m} control chart due to the lack of strain data. (Only 181 truck events were obtained in total.)

A summary of false indication rates for structure-based limit methods (base data method) for selected sensor pairs are given in Table 5.14. A low false indication rate was achieved when the maximum limit was used from the base data limit method.

Table 5.14. Summary of false and true indication rate 70–72°F temperature bin with semi-trucks for damage level 1

Sensor pair	Period	Number of F_{sh_m}	Structure-based Base data method			
			Dx	Dy	Ix	Iy
B2_BF vs. C2_BF	E 1	7	0	0	0	0
	E 2	4	0	0	0	0
	E 3	5	0	0	0	0
	Limit		79	110	64	89
B2_BF vs. C3_BF	E 1	7	0	0	0	0
	E 2	4	25.0	0	25.0	0
	E 3	5	100	20	100	100
	Limit		61	90	50	72

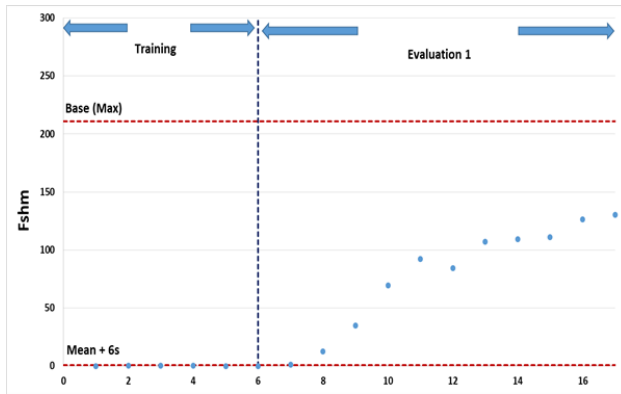
Sensor pair	Period	Number of F_{shm}	Structure-based			
			Base data method			
			Dx	Dy	Ix	Iy
B2_BF vs. C2_BF	E 1	7	0	0	0	0
	E 2	4	0	0	0	0
	E 3	5	0	0	0	0
	Limit		79	110	64	89
B2_BF vs. D2_BF	E 1	7	0	0	0	0
	E 2	4	0	0	0	0
	E 3	5	0	0	0	0
	Limit		46	52	38	42
B2_BF vs. K1_BF	E 1	7	0	0	0	0
	E 2	4	0	0	0	0
	E 3	5	0	0	0	0
	Limit		26	42	21	32
B2_BF vs. M2_BF	E 1	7	0	0	0	0
	E 2	4	0	0	0	0
	E 3	5	0	0	0	0
	Limit		25	30	20	23
C2_BF vs. C3_BF	E 1	7	0	0	0	0
	E 2	4	0	0	0	0
	E 3	5	0	0	0	0
	Limit		182	192	148	156
C2_BF vs. D2_BF	E 1	7	0	0	0	0
	E 2	4	0	0	0	0
	E 3	5	0	0	0	0
	Limit		270	232	220	189
C2_BF vs. K1_BF	E 1	7	0	0	0	0
	E 2	4	0	0	0	0
	E 3	5	0	0	0	0
	Limit		87	85	71	69
C3_BF vs. M2_BF	E 1	7	0	0	0	0
	E 2	4	0	0	0	0
	E 3	5	0	0	0	0
	Limit		72	72	58	58
C3_BF vs. D2_BF	E 1	7	0	0	0	0
	E 2	4	0	0	0	0
	E 3	5	20.0	40.0	40.0	40.0
	Limit		115	91	94	74
C3_BF vs. K1_BF	E 1	7	0	0	28.6	14.3
	E 2	4	0	0	100	25.0
	E 3	5	0	0	100	80.0
	Limit		42	46	34	37
C3_BF vs. M2_BF	E 1	7	0	0	0	0
	E 2	4	0	0	0	0
	E 3	5	0	0	0	0
	Limit		53	48	42	39
D2_BF vs. K1_BF	E 1	7	0	0	0	0
	E 2	4	0	0	0	0
	E 3	5	0	0	0	0
	Limit		144	149	119	122
D2_BF vs. M2_BF	E 1	7	0	0	0	0
	E 2	4	0	0	0	0

Sensor pair	Period	Number of F_{shm}	Structure-based			
			Base data method			
			Dx	Dy	Ix	Iy
B2_BF vs. C2_BF	E 1	7	0	0	0	0
	E 2	4	0	0	0	0
	E 3	5	0	0	0	0
	Limit		79	110	64	89
	E 3	5	0	0	0	0
	Limit		127	147	103	120
K1_BF vs. M2_BF	E 1	7	0	0	0	0
	E 2	4	0	0	0	0
	E 3	5	0	0	0	0
	Limit		126	133	103	109

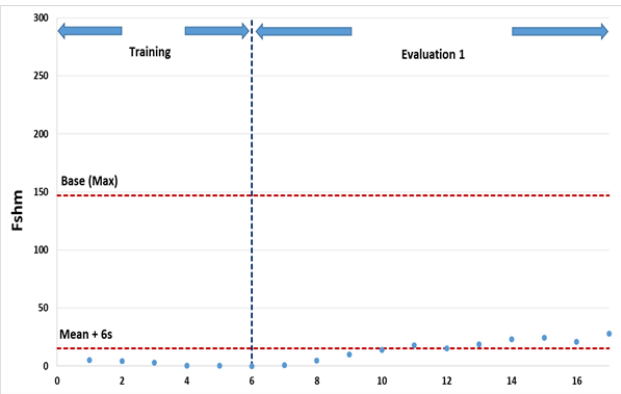
5.6.5. Recommendations

5.6.5.1. 5°F Temperature Bin and All Five-Axle Trucks

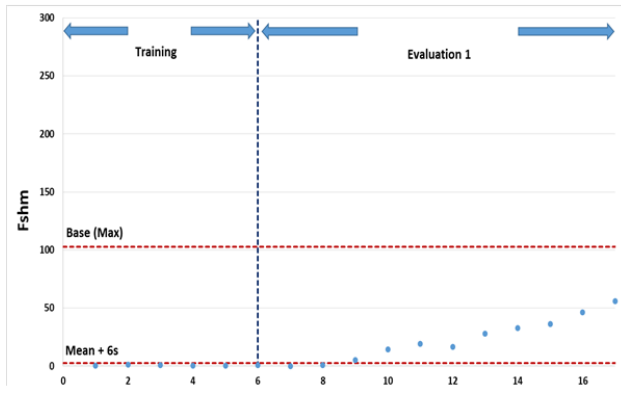
In this section, F_{shm} control charts were constructed only with a temperature bin range of 35°F–40°F and with all five-axle trucks as the part of the recommendation of damage detection categories. Two limits were selected: (1) statistics-based – six sigma and (2) structure-based – base data method (maximum). F_{shm} in the training period was used to establish the six sigma limit and the maximum number of limits from base data method were used. False indication rate was calculated in the training region, and Evaluation 1 region was established for true indication rate. With the six sigma limit, no false indications were observed while a high true indication rate was achieved. F_{shm} control charts for the 35°F–40°F temperature bin with all five-axle trucks are shown in Figure 5.38, and the summary of results of false and true indication are tabulated in Table 5.15.



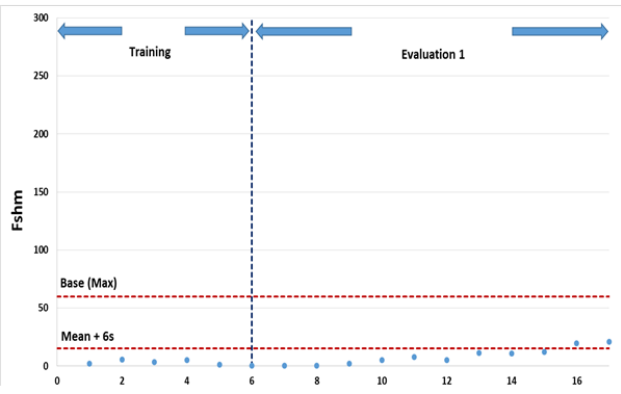
(a) $B2_BF$ vs. $C2_BF$



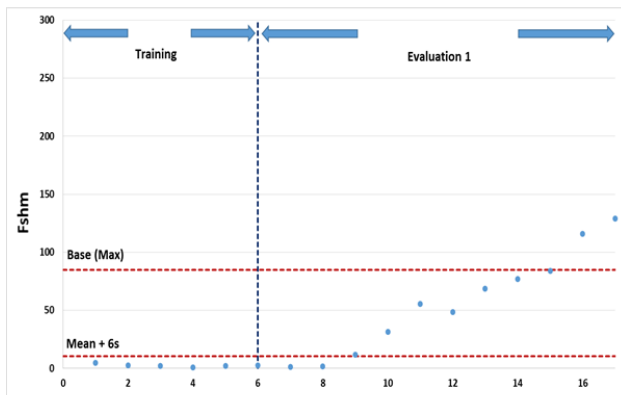
(b) $B2_BF$ vs. $C3_BF$



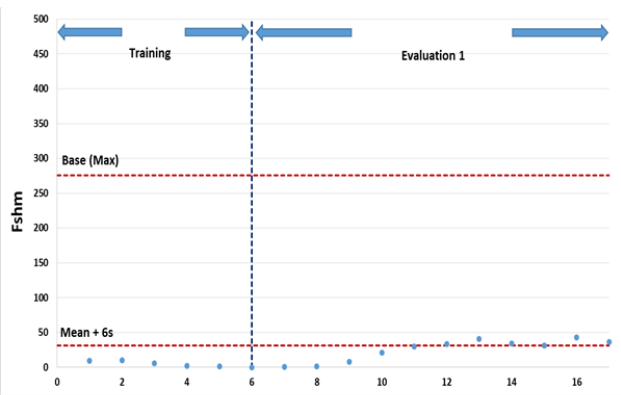
(c) $B2_BF$ vs. $D2_BF$



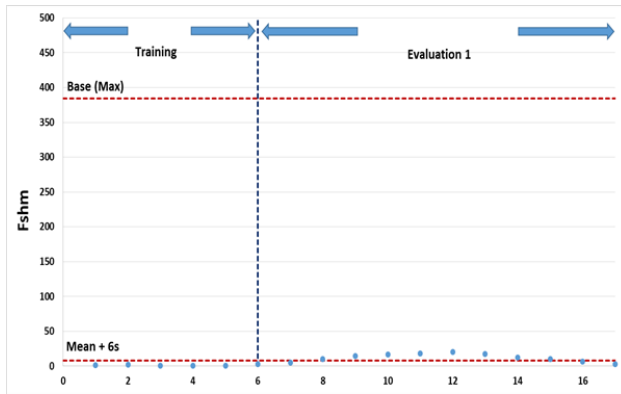
(d) $B2_BF$ vs. $K1_BF$



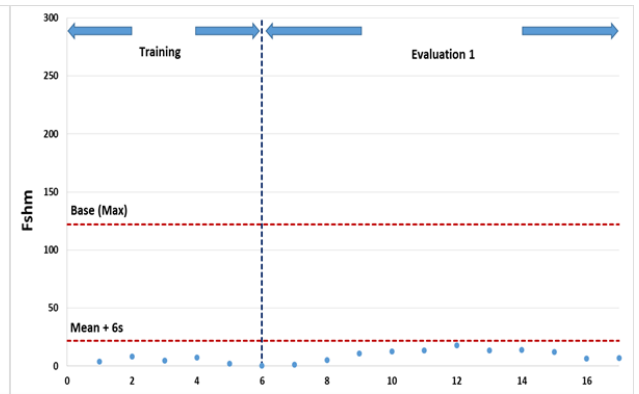
(e) $B2_BF$ vs. $M2_BF$



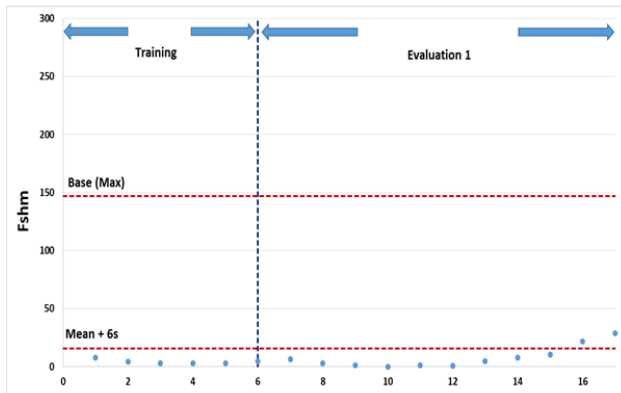
(f) $C2_BF$ vs. $C3_BF$



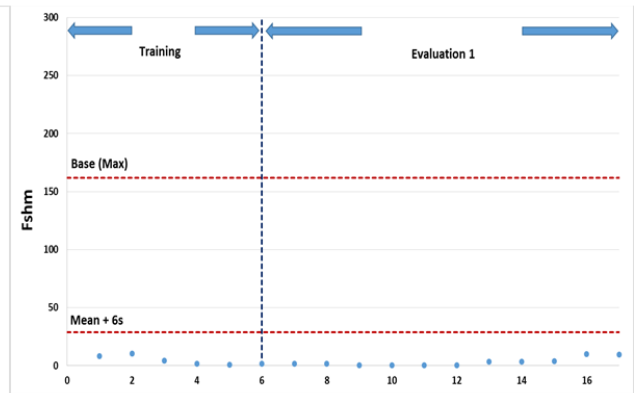
(g) $C2_BF$ vs. $D2_BF$



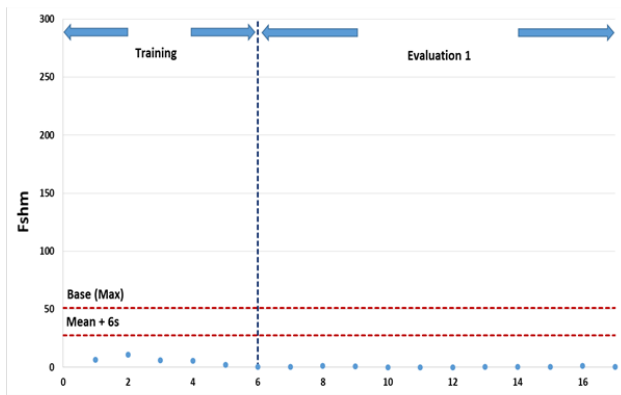
(h) $C2_BF$ vs. $K1_BF$



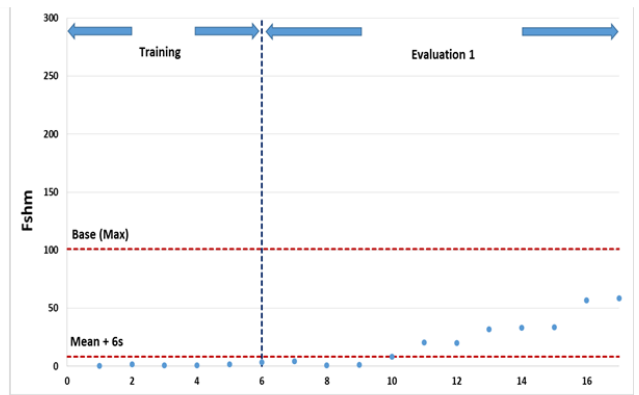
(i) $C2_BF$ vs. $M2_BF$



(j) $C3_BF$ vs. $D2_BF$



(k) $C3_BF$ vs. $K1_BF$



(l) $C3_BF$ vs. $M2_BF$

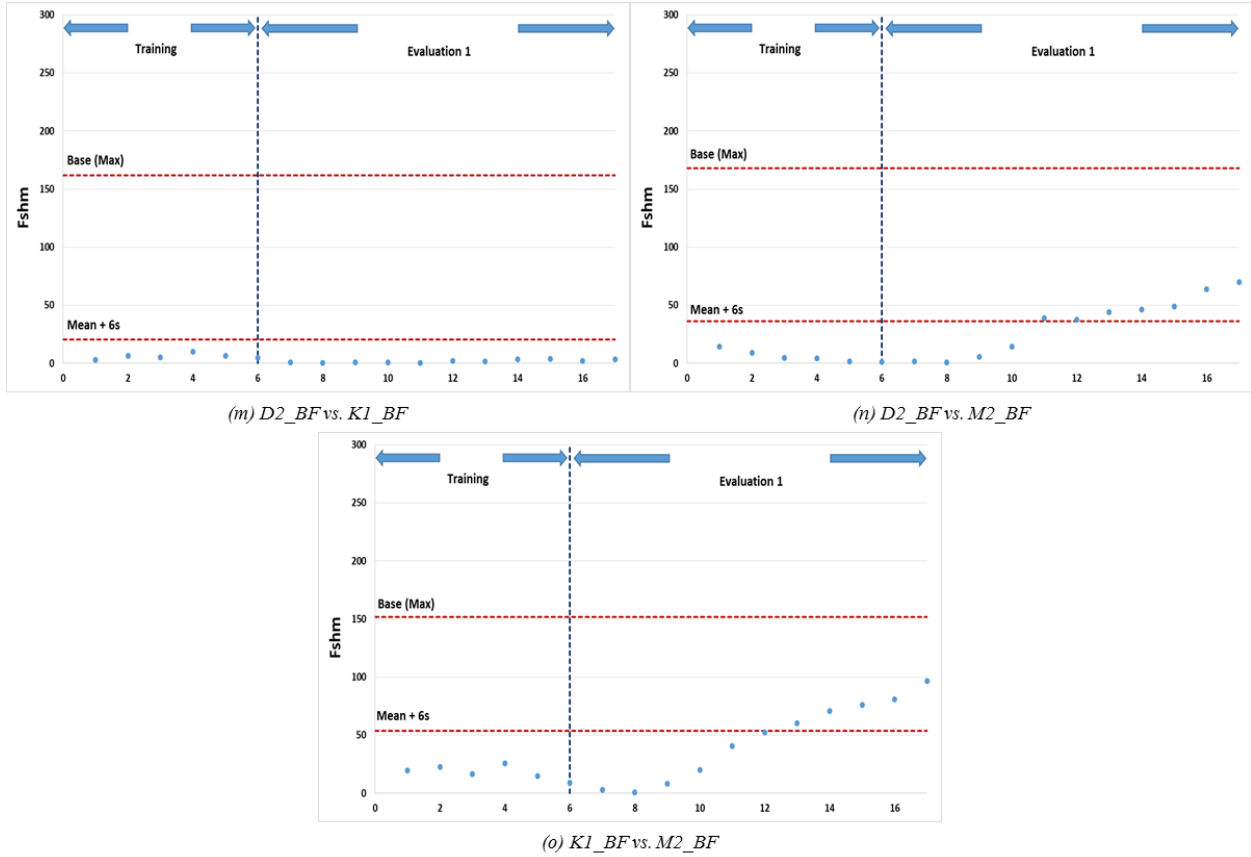


Figure 5.38. F_{sh_m} control chart for 35°F–40°F temperature bins with all five-axle trucks

Table 5.15. Summary of false and true indication rate for 35–40°F temperature bins with all five-axle trucks

Sensor pair	Period	Number of F_{shm}	Statistics-based		Structure-based			
			3σ	6σ	Base data method			
					Dx	Dy	Ix	Iy
B2_BF vs. C2_BF	T	6	0	0	0	0	0	0
	E 1	11	100	100	0	0	0	0
	Limit		1	1	206	211	168	173
B2_BF vs. C3_BF	T	6	0	0	0	0	0	0
	E 1	11	81.8	63.6	0	0	0	0
	Limit		9	15	137	147	111	120
B2_BF vs. D2_BF	T	6	0	0	0	0	0	0
	E 1	11	81.8	81.8	0	0	0	0
	Limit		2	3	103	80	84	65
B2_BF vs. K1_BF	T	6	0	0	0	0	0	0
	E 1	11	45.5	18.2	0	0	0	0
	Limit		9	15	60	60	48	49
B2_BF vs. M2_BF	T	6	0	0	0	0	0	0
	E 1	11	81.8	81.8	18.2	45.5	36.4	54.5
	Limit		6	10	85	66	69	53
C2_BF vs. C3_BF	T	6	0	0	0	0	0	0
	E 1	11	72.7	45.5	0	0	0	0
	Limit		18	31	254	276	206	225
C2_BF vs. D2_BF	T	6	0	0	0	0	0	0
	E 1	11	90.9	72.7	0	0	0	0
	Limit		5	8	384	315	314	257
C2_BF vs. K1_BF	T	6	0	0	0	0	0	0
	E 1	11	36.4	0	0	0	0	0
	Limit		13	22	122	106	101	87
C2_BF vs. M2_BF	T	6	0	0	0	0	0	0
	E 1	11	27.3	18.2	0	0	0	0
	Limit		10	16	147	121	119	98

Further, the summation of violations with all other sensors versus C2_BF and M2_BF are shown in Figure 5.39.

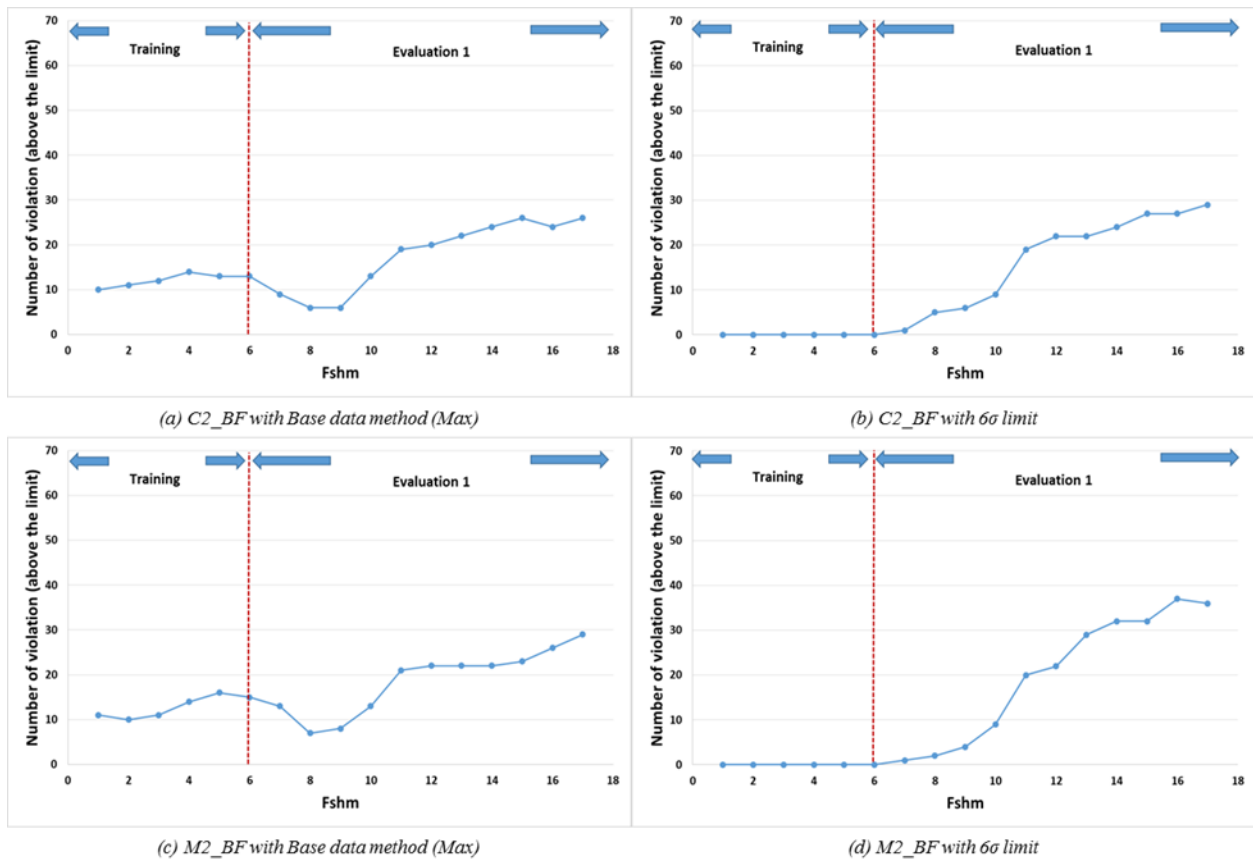


Figure 5.39. Summation of violation with all other sensors vs. C2_BF and M2_BF

The maximum number of violations is 68. With the maximum limit from the base data method, violations were observed in the training region while there were no violations with six sigma limits in both C2_BF and M2_BF.

In addition, the base data limits were further developed by applying absolute strain changes. For strain changes of plus or minus $10 \mu\epsilon$, sensors that have a strain range under $10 \mu\epsilon$ were eliminated to avoid a negative value of strain range. There were 26 sensors that have a strain range above $10 \mu\epsilon$, and the list of sensors is presented in Table 5.16.

Table 5.16. Sensors with a strain range under and above $10 \mu\epsilon$

	Sensors have strain range under $10 \mu\epsilon$	Sensors have strain range above $10 \mu\epsilon$
Sensors	A1_BF, A2_BF, A4_BF, A5_BF, A1_TF, A2_TF, A3_TF, B5_BF, C5_BF, D5_BF, D1_TF, D2_TF, D3_TF, D4_TF, D5_TF, E5_BF, F5_BF, G1_BF, G4_BF, G5_BF, G1_TF, G2_TF, G3_TF, G4_TF, G5_TF, H5_BF, I5_BF, J5_BF, K1_BF, K4_BF, K5_BF, I1_TF, I2_TF, I3_TF, I4_TF, I5_TF, L5_BF, M5_BF, N5_BF, O1_BF, O2_BF, O3_BF, O4_BF, O5_BF	B2_BF, C2_BF, C3_BF, D1_BF, D2_BF, D3_BF, D4_BF, E2_BF, E3_BF, F2_BF, G2_BF, G3_BF, H2_BF, I1_BF, I2_BF, I3_BF, I4_BF, K2_BF, K3_BF, J2_BF, L2_BF, M1_BF, M2_BF, M3_BF, M4_BF, N2_BF
Total	44	26

Figure 5.40 shows summation of violations for base data limits utilizing absolute changes in strain such as ± 10 , ± 5 , ± 3 , ± 2 , and ± 1 with the 26 sensors versus C2_BF.

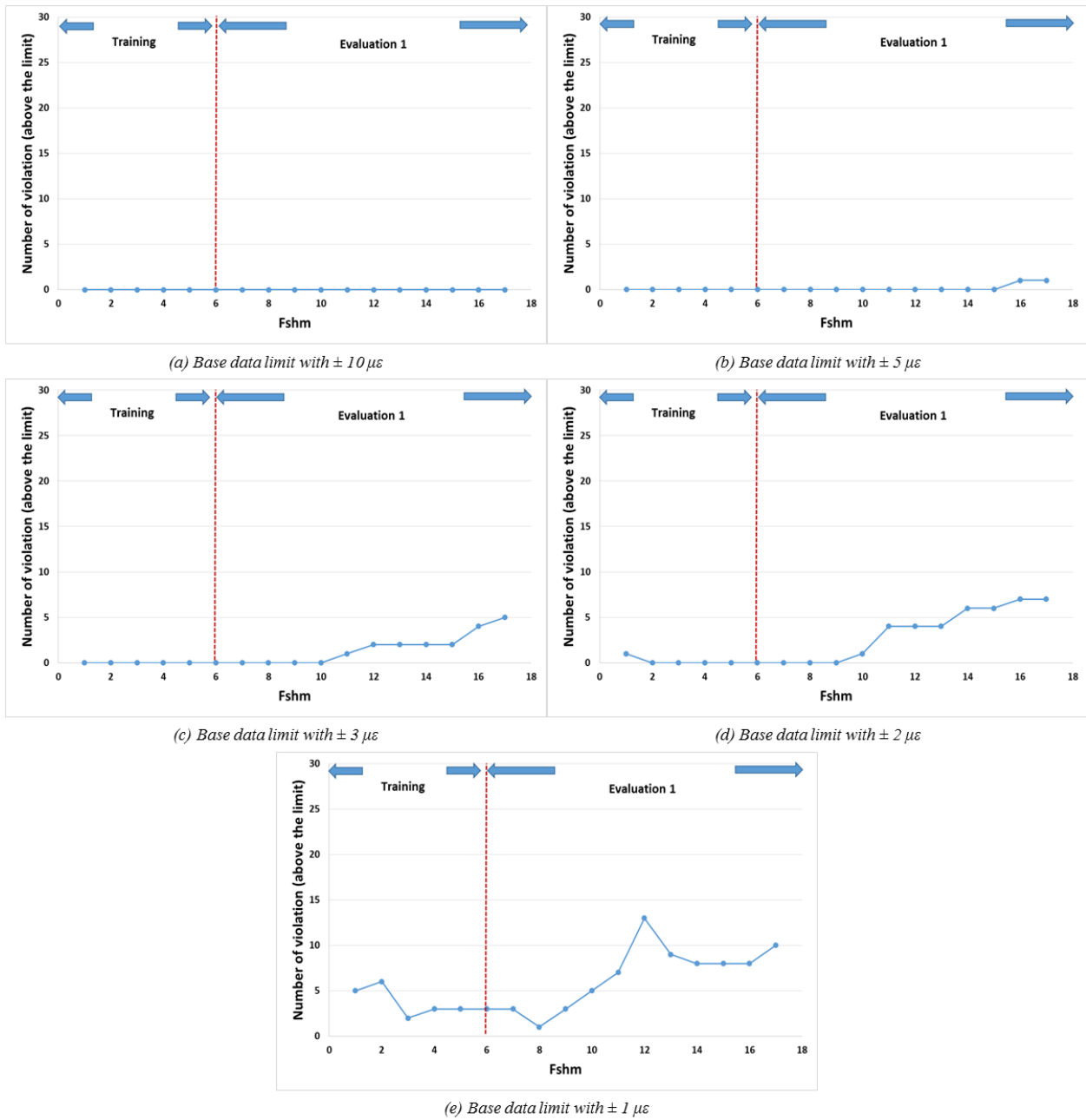


Figure 5.40. Summation of violation for base data limits utilizing absolute changes in strain with the 26 sensors vs. C2_BF

In terms of false and true indication rate that represents the ability of the damage detection algorithm, the strain data set for 35°F–40°F temperature bins with all five-axle truck is recommended with six sigma limit or base data limit with $\pm 3 \mu\epsilon$.

5.7. Summary and Conclusions

In this research, a control chart-based damage detection algorithm, F_{shm} , was investigated by minimizing the variability due to temperature and truck configuration. F_{shm} control charts were constructed with different combinations of strain data and limits both statistics- and structure-based were established to reduce the false indication rate. False and true indication rates for each combination of strain data were summarized in table format.

For damage level 1, changes in stiffness were relatively small and there were no significant structural changes. False indication rates were calculated for training, testing, and Evaluation 1, 2, and 3 regions. For all five-axle trucks with a 70°F–80°F temperature bin, a higher false indication rate was observed with a statistics-based limit and the false indication rate was minimized when a higher limit was achieved from the structure-based limit method. For a 70°F–72°F temperate bin, false indication rates were further decreased by applying structure-based limits. For semi-trucks with damage level 1 and a 70°F–80°F temperature bin, false indication rates in all evaluation regions were also decreased with structure-based limits. With a 2° temperature bin, 70°F–72°F, only structure-based limits (base data method) were established.

For all five-axle trucks with damage level 2 and a 30°F–40°F temperature bin, during the Evaluation 1 period, a low true indication rate was obtained at the sensor pair with C2_BF versus a near sensor of C2_BF, such as B2_BF and D2_BF. This was because there were similar structural behaviors at sensors deployed closely for damage level 2. This phenomenon was also observed with a 2° temperature bin, 36°F–38°F. A high true indication rate was achieved in both statistics-based limits and structure-based limits. For semi-trucks with damage level 2 and a 30°F–40°F degree temperature bin, the F_{shm} method detected damages well by achieving a higher true indication rate with the statistics-based limits except sensor pairs that were deployed close together with C2_BF. True indication rate was decreased with base data limits in most cases. For damage level 2 with a 2°F temperature bin and semi-trucks, there was a limitation in developing an F_{shm} control chart due to the lack of strain data.

As the part of recommendation of damage detection categories, F_{shm} control charts were constructed with a temperature bin of 35°F–40°F and all five-axle trucks by applying two selected limits: (1) six sigma and (2) base data (maximum). With the six sigma limit, no false indications were observed while a high true indication rate was achieved. Further, the summation of violations with all other sensors versus C2_BF and M2_BF were investigated. The results showed that violations were observed in the training region with the maximum limit from the base data method while there were no violations with the six sigma limits in both C2_BF and M2_BF. The base data limits were further developed by applying absolute strain changes. For strain changes in plus or minus 10 $\mu\epsilon$, sensors that had a strain range under 10 $\mu\epsilon$ were eliminated to avoid a negative value of strain range. There were 26 sensors that had a strain range above 10 $\mu\epsilon$ and a summation of violations for base data limits utilizing absolute changes in strain such as ± 10 , ± 5 , ± 3 , ± 2 , and ± 1 versus C2_BF. In terms of false and true indication rate, which represents the ability of the damage detection algorithm, the strain data set for the 35°F–40°F temperature bin with all five-axle trucks is recommended with six sigma limit or base data limit from $\pm 3 \mu\epsilon$.

In addition, it was found that there was a limitation in establishing limits in both statistics- and structure-based methods due to a lack of truck events during the training region. To obtain enough strain data for limits, increasing the temperature bin size is required. However, a higher temperature bin range also creates higher strain variability. Therefore, note that suitable temperature bin size is an important factor in terms of the amount of strain data available for establishing limits and strain variability.

CHAPTER 6. LOAD RATING FACTOR DETERMINATION USING AMBIENT TRAFFIC

In this chapter, an automated ambient traffic (AAT) approach is introduced to achieve continuous load rating of bridges under ambient traffic utilizing the BECAS SHM system. The first section describes the AAT approach in terms of bridge model calibration and load rating, process automation, and sampling strategies. The second section introduces the configurations and the FE modeling of the demonstration bridge, the I-80 bridge. The third section presents the load rating of the I-80 bridge using the traditional known truck (TKT) approach to provide a basis for comparison with the AAT approach. The fourth section presents the load rating results of the I-80 bridge using the AAT approach compared to those obtained using the TKT approach. The last section gives the summary and conclusions of this chapter.

6.1. Automated Ambient Traffic Approach

6.1.1. Bridge Model Calibration and Load Rating

The BEC currently performs bridge load rating using a set of commercially available software applications (Bridge Diagnostics Inc. 2003), including WinGen, which is used for bridge model generation and load test simulation, and WinSac, which is used for structural analysis, model calibration, and load rating computation. For the calibration problems, WinSac provides algorithms for making direct numeric comparisons between measured and computed strains. The bridge parameters are calibrated through a process of minimizing the difference between the measured and computed strains using a least squares approach. Four different statistical values, absolute error (AE), percent error (PE), scale error (SE), and correlation coefficient (CC), are used to describe the model's ability to represent the actual structure and can be determined by equations (17), (18), (19), and (20), respectively.

$$AE = \sum |\varepsilon_R - \varepsilon_C| \quad (17)$$

$$PE = \frac{\sum (\varepsilon_R - \varepsilon_C)^2}{\sum \varepsilon_R^2} \quad (18)$$

$$SE = \frac{\sum \max |\varepsilon_R - \varepsilon_C|_{\text{gauge}}}{\sum |\varepsilon_R|_{\text{gauge}}} \quad (19)$$

$$CC = \frac{\sum (\varepsilon_R - \mu_{\varepsilon_R})(\varepsilon_C - \mu_{\varepsilon_C})}{\sum \sqrt{(\varepsilon_R - \mu_{\varepsilon_R})^2 (\varepsilon_C - \mu_{\varepsilon_C})^2}} \quad (20)$$

where, ε_R is measured strain, ε_C is strain calculated using the FE model, $\max |\varepsilon_R - \varepsilon_C|_{\text{gauge}}$ is maximum absolute strain differences between measured and calculated strains in each gauge, $|\varepsilon_R|_{\text{gauge}}$ is maximum absolute strain in each gauge, μ_{ε_R} is average recorded strain in each gauge, μ_{ε_C} is average calculated strain in each gauge.

The bridge FE model, incorporated with the calibrated bridge parameters, is used to perform a load rating using WinSac. The inventory load rating is performed for the bridge and the load rating factor. The rating factor (RF) is calculated using the load factor rating (LFR) method per AASHTO Standard Specifications (AASHTO1996), and given in equation (21).

$$RF = \frac{C - A_1 D}{A_2 L(1 + I)} \quad (21)$$

where,

C = the capacity of the member

D = the dead load effect on the member

L = the live load effect on the member

A₁ = the factor for dead load, equals 1.3

A₂ = the factor for the live load, equals 2.17 for inventory level

I = the impact factor for live load effect (maximum 0.3), which can be expressed as (AASHTO 1996) in equation (22).

$$I = \frac{15}{L + 38} \quad (22)$$

where,

L = length in meters of the portion of the span that is loaded to produce the maximum stress in the member

The live loads applied to the load rating bridge model are the AASHTO HS-20 trucks. The demonstration I-80 bridge was designed for two traffic lanes. The most critical loading condition is when two trucks are transversely placed with the adjacent wheel lines at the spacing of 4 ft as shown in Figure 6.1.

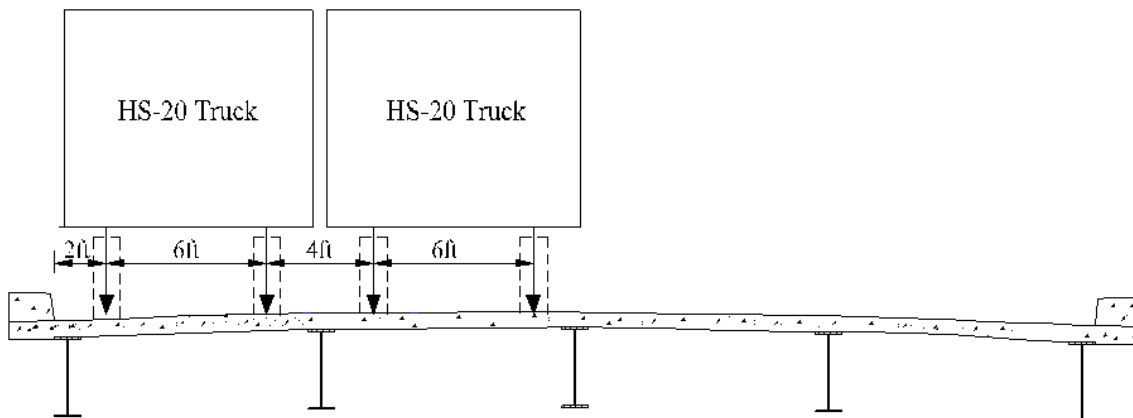


Figure 6.1. HS-20 trucks on a bridge

The loading cases with different transverse positions should be taken into account for the two trucks traveling across the bridge. The extreme situation is when the outer wheel line of the outer

truck is located at 2 ft away from the bridge parapet (AASHTO 1996) as shown in Figure 6.1. The dead loads consist of self-weights of the superstructure components including steel girders, stringers, floor beams, concrete deck, and parapets. Girders are the major bridge members for resisting dead and live loads, and their negative and positive flexural capacity at the negative and positive moment regions, respectively, are calculated for bridge load rating based on AASHTO Standard Specifications (AASHTO 1996). Load envelopes are calculated for the girders such that the rating factors are computed for all the finite element girder elements. The lowest rating factor of the girder elements are taken as the rating factor of the bridge.

6.1.2. Process Automation

The strain-based SHM system was developed by BEC to remotely monitor the bridge response under ambient traffic. This SHM system is adopted to assess the load carrying capacity of bridges utilizing the aforementioned techniques of bridge model calibration and load rating. However, the calibration and load rating process requires a certain amount of manual operations for each step. For instance, the bridge model is manually updated through the incorporation of the strain responses, truck parameters and calibrated bridge parameters using WinGen. The bridge model is manually calibrated and load rated executing WinSac. For efficiency and increased adoption, manual operations need to be automated due to the fact that manual operations may unintentionally produce operative errors and are not efficient for achieving many runs of calibration and load rating taking into account the uncertainties of bridge and loading conditions.

Accordingly, an AAT approach was further developed such that the process could automatically operate without user intervention. The automated step-by-step procedure of this approach is illustrated in the flowchart shown in Figure 6.2.

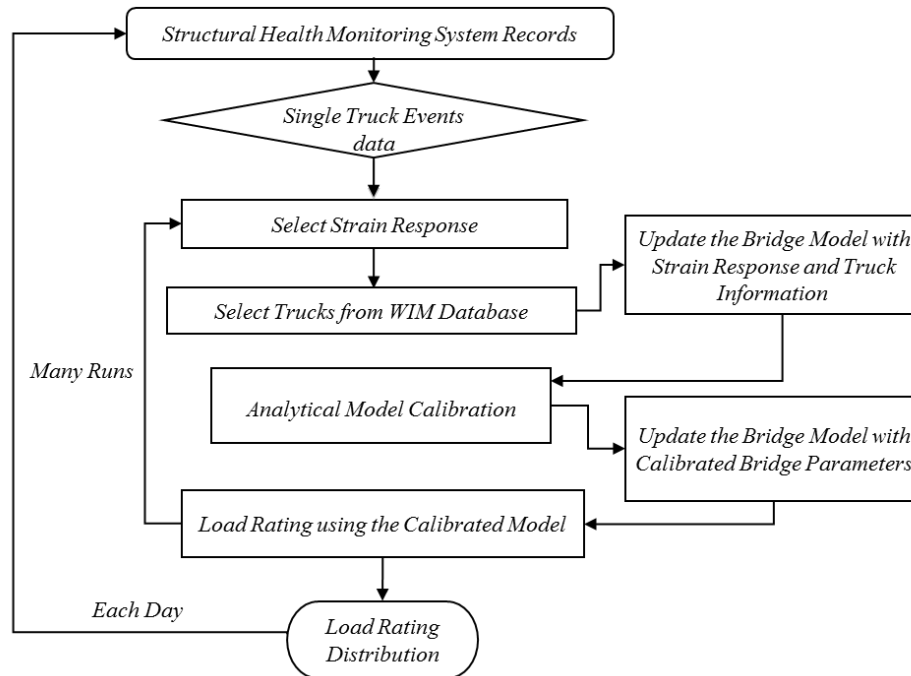


Figure 6.2. Flowchart of the automated step-by-step procedure of bridge load rating

As shown in Figure 6.2, the quasi-static bridge response of single-truck events detected using the SHM system are utilized for bridge model calibration. A batch of strain response of a truck event collected by the girder strain sensors is first selected. Based on the available information of the truck for the single-truck event, a truck is randomly selected from the weigh-in-motion (WIM) database with appropriate selection criteria. With the incorporation of the strain response and truck parameters into the bridge model, the bridge model is calibrated following the calibration approach. Once the parameters of the bridge model are calibrated, the updated bridge model is utilized to perform bridge load rating following the bridge load rating process. The operations within the flowchart are achieved using a custom-developed program that essentially replaces the graphical user interface with text-based manipulations. For instance, the bridge finite element model is updated by revising the WinGen output file of the model, and the computations for calibration and load rating are performed by calling the analytical routine (i.e., WinSac). During operation, the application is automatically initiated at the end of each day to complete the bridge model calibration and load rating as shown in Figure 6.2.

6.1.3. Sampling Strategies

The accuracy of the truck characteristics has an influence on the results of bridge model calibration. As listed in Table 6.1, the truck speed, axle spacing, travel lane, and travel position can be accurately determined from the SHM system using the truck detection approach described previously (See Chapter 4).

Table 6.1. Truck characteristics related to bridge model calibration

Known	Truck speed	Axle spacing	Travel lane	Travel position
Partially unknown	Gross vehicle weight	Axle weights	Transverse position	

However, gross vehicle weight, axle weights, and transverse position are not accurately known since no specific measurement is implemented to directly collect their values. In this study, the uncertainties of these parameter values are taken into account through the engineering judgement and sampling trucks from the WIM database. In an engineering sense, the magnitudes of truck parameters are correlated to those of bridge girder strains. For instance, a single-truck event with larger strain response in the girders is certainly related to a heavier truck. On the other hand, due to the influences of axle spacing, transverse position, and axle weights, the largest strain response is not always induced by the heaviest truck. Thus, such uncertainties can be further accounted through sampling heavier trucks from the WIM database for the bridge model calibration of each single-truck event.

As illustrated in the flowchart shown in Figure 6.2, for a single-truck event, one truck and one batch of strain time histories were used for each run of calibration and load rating. However, in order to take into account the uncertainties of the truck parameters, many runs of calibration and load rating were needed through the selection of different truck events collected from the SHM system and different trucks from the WIM database. In other words, either one batch or several batches of strain time histories can be sampled from the SHM system per day, and either one truck or several trucks corresponding to each batch of strain time histories can be sampled from the WIM database. Namely, an appropriate sampling strategy should be determined so as to properly select strain response from the SHM system database and select trucks from the WIM database. Further, the variation of the calibrated bridge parameters and the load rating results reflects the uncertainties of the truck parameters. As an illustration, the sampling strategies utilized for the I-80 bridge demonstration are presented in the following section.

The WIM database, collected at the Dallas County and Jasper County weigh stations on I-80 in Iowa during 2009–2011, was utilized to account for the uncertainties of the gross vehicle weight and axle weights of each detected truck. The WIM database has a total of 190,259 five-axle trucks. Figure 6.3 shows frequency histograms of axle spacing based on the WIM database, which indicate that the common ranges for axle spacing #1, #2, #3, and #4 are 10–22 ft, 4–5 ft, 25–40 ft, and 4–5 ft, respectively.

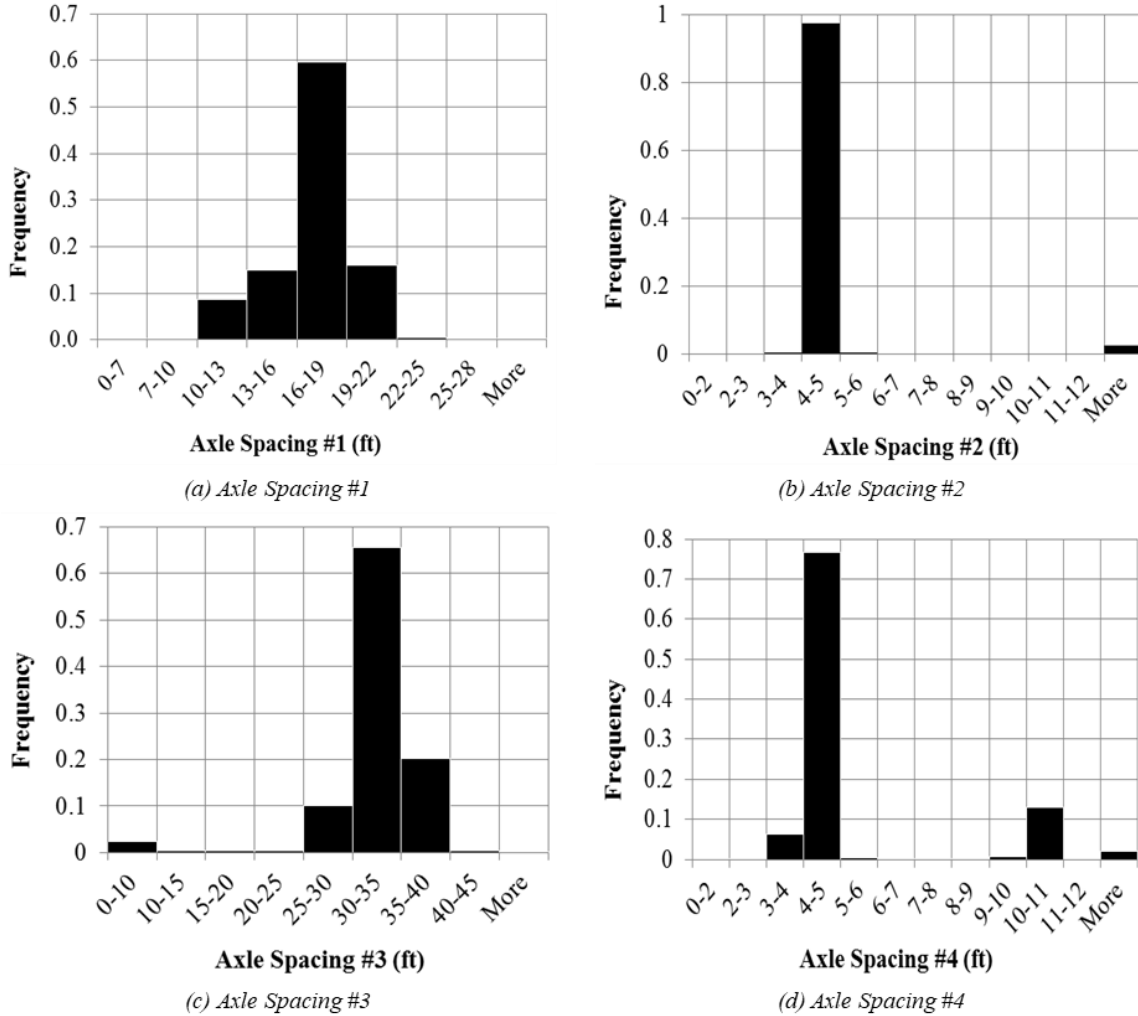


Figure 6.3. Frequency histograms of axle spacing

For reducing the uncertainties of truck parameters, it was reasonable to select five-axle trucks with axle spacing with smaller ranges for bridge model calibration. Note that such selection should be implemented both to select single-truck events from the SHM system and to select associated trucks from the WIM database. Based on Figure 6.3, two subgroups of five-axle trucks with respect to different axle spacing intervals were sorted for determining the sampling strategies as shown in Table 6.2.

Table 6.2. Subgroups of five-axle trucks with different axle spacing intervals

Subgroup	Axle spacing #1 (ft)	Axle spacing #2 (ft)	Axle spacing #3 (ft)	Axle spacing #4 (ft)
No. 1	10–22	4–5	25–40	4–5
No. 2	16–19	4–5	30–35	4–5

The frequency histograms of gross vehicle weight for Subgroups No. 1 and No. 2 are shown in Figure 6.4a and Figure 6.4b, respectively.

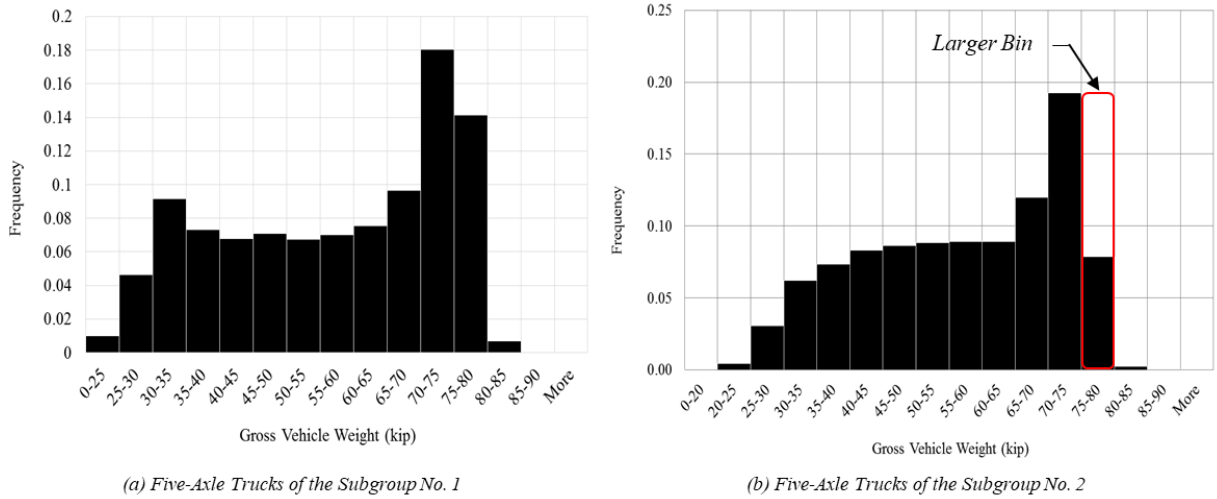
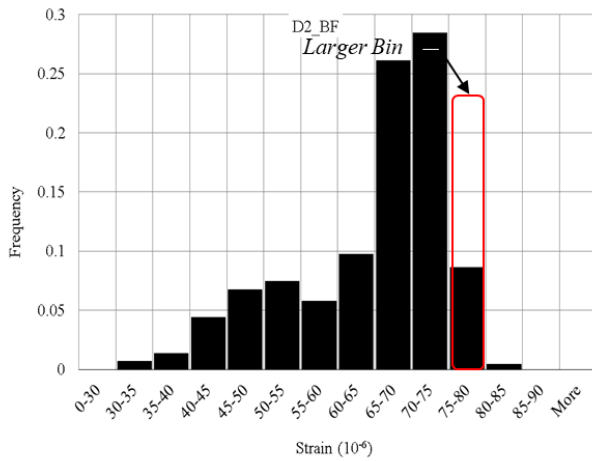


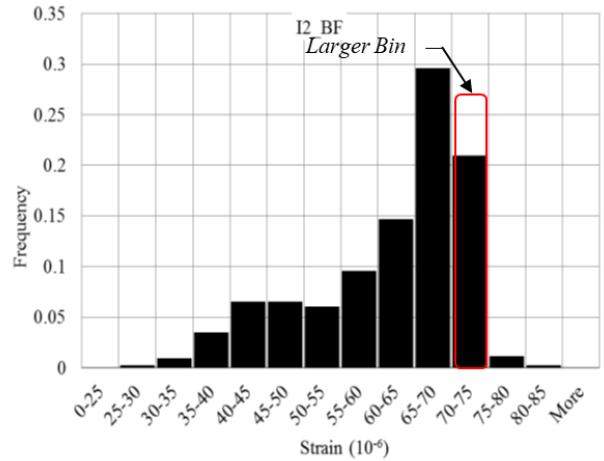
Figure 6.4. Frequency histograms of gross vehicle weight

Figure 6.4 indicates that the two frequency histograms have a similar pattern although the trucks were sorted utilizing different axle spacing ranges.

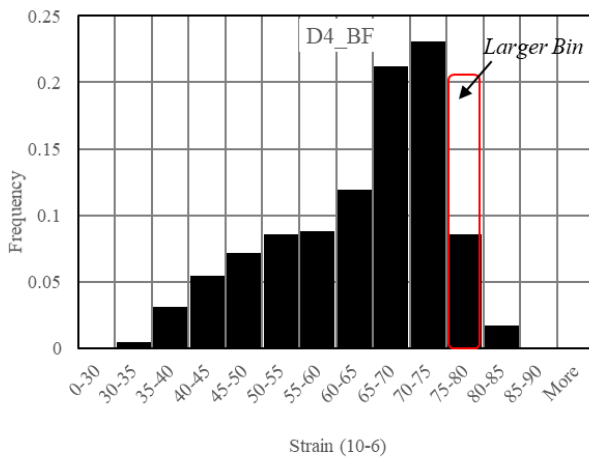
For comparison purposes, the frequency histogram for peak girder strains in sensors D2_BF at the first mid-span and sensor I2_BF at the center mid-span, based on the 2,310 five-axle truck south-lane events detected in the SHM system, are shown in Figure 6.5a and Figure 6.5b, respectively.



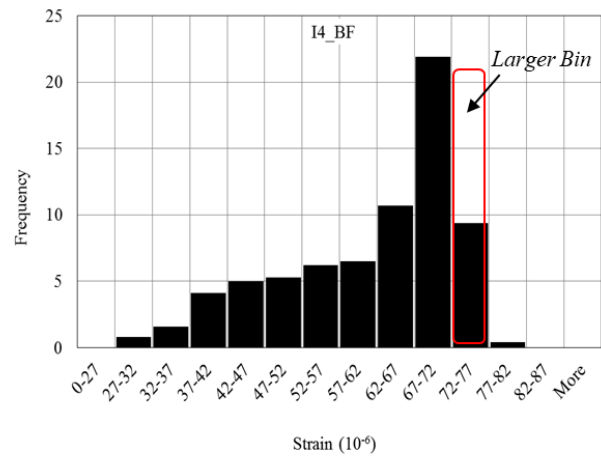
(a) Maximum Strain in Sensor D2_BF – South Lane Events



(b) Maximum Strain in Sensor I2_BF – South Lane Events



(c) Maximum Strain in Sensor D4_BF – North Lane Events



(d) Maximum Strain in Sensor I4_BF – North Lane Events

Figure 6.5. Maximum girder strains in different sensors of trucks of Subgroup No. 2

The frequency histogram for peak girder strains in sensors D4_BF at the first mid-span and sensor I4_BF at the center mid-span, based on the 2,247 five-axle truck north-lane events detected in the SHM system, are shown in Figure 6.5c and Figure 6.5d, respectively. As indicated in Figure 6.4b and Figure 6.5, the distributions of detected peak girder strains were correlated well with the distribution of truck weights in the WIM database.

Due to the similarities of the distributions of peak girder strains and truck weights, three sampling strategies were developed to account for the uncertainties of gross vehicle weight and axle weights as tabulated in Table 6.3.

Table 6.3. Sampling strategies with different strain and truck weight spectrums

Sampling strategy	South-lane events			North-lane events		
	WIM truck weight (kip)	D2_BF (10 ⁻⁶)	I2_BF (10 ⁻⁶)	WIM truck weight (kip)	D4_BF (10 ⁻⁶)	I4_BF (10 ⁻⁶)
A	20–80	30–80	25–75	N/A	N/A	N/A
	N/A	N/A	N/A	20–80	30–80	27–77
B	75–80	75–80	70–75	N/A	N/A	N/A
	N/A	N/A	N/A	75–80	75–80	72–77
C	75–80	75–80	70–75	75–80	75–80	72–77

For Sampling Strategy A, the available truck weight spectrum of Subgroup No. 2 and the available girder strain spectrums were utilized as listed in Table 6.3 and illustrated in Figure 6.4b and Figure 6.5. Either south- or north-lane events were utilized for bridge model calibration. Accordingly, for the Sampling Strategy B, a spectrum of larger truck weight of Subgroup No. 2 and a spectrum of larger girder strain were utilized as listed in Table 6.3 and illustrated in Figure 6.4b and Figure 6.5. Either south- or north-lane events were utilized for bridge model calibration. For the Sampling Strategy C, the same sampling approaches were utilized but both south- and north-lane events were utilized for bridge model calibration.

Table 6.4 indicates that the heavy trucks of Subgroup No. 2 have fewer variations of gross vehicle weight, axle weights and axle weight distribution along five axles.

Table 6.4. Axle weight distribution of heavy trucks of Subgroup No. 2

Truck selection		Gross (kips)	A-WT#1 (kips)	A-WT#2 (kips)	A-WT#3 (kips)	A-WT#4 (kips)	A-WT#5 (kips)	R ₁₂	R ₂₃	R ₃₄	R ₄₅
Subgroup No. 2	Avg	57.02	10.39	12.12	11.97	11.19	11.34	0.94	1.01	1.15	0.99
	Std dev	14.80	0.91	3.42	3.35	4.15	4.17	0.32	0.05	0.31	0.08
Heavy trucks of Subgroup No. 2	Avg	76.64	11.10	16.49	16.25	16.33	16.47	0.67	1.02	1.00	0.99
	Std dev	1.19	0.83	0.66	0.66	0.80	0.80	0.06	0.04	0.07	0.06

Note: R₁₂ — Ratio of A-WT#1 to A-WT#2; R₂₃ — Ratio of A-WT#2 to A-WT#3; R₃₄ — Ratio of A-WT#3 to A-WT#4; R₄₅ — Ratio of A-WT#4 to A-WT#5

The mean value of the axle weight #1 equals 0.67, while the mean values of axle weights #2 to #5 approximate 1.0, and the standard deviations of the ratios of weights between the different axles are less than 0.06.

To further illustrate the steps of strain response and truck sampling, the Sampling Strategy C was incorporated into the flowchart of the bridge model calibration and load rating as shown in Figure 6.6.

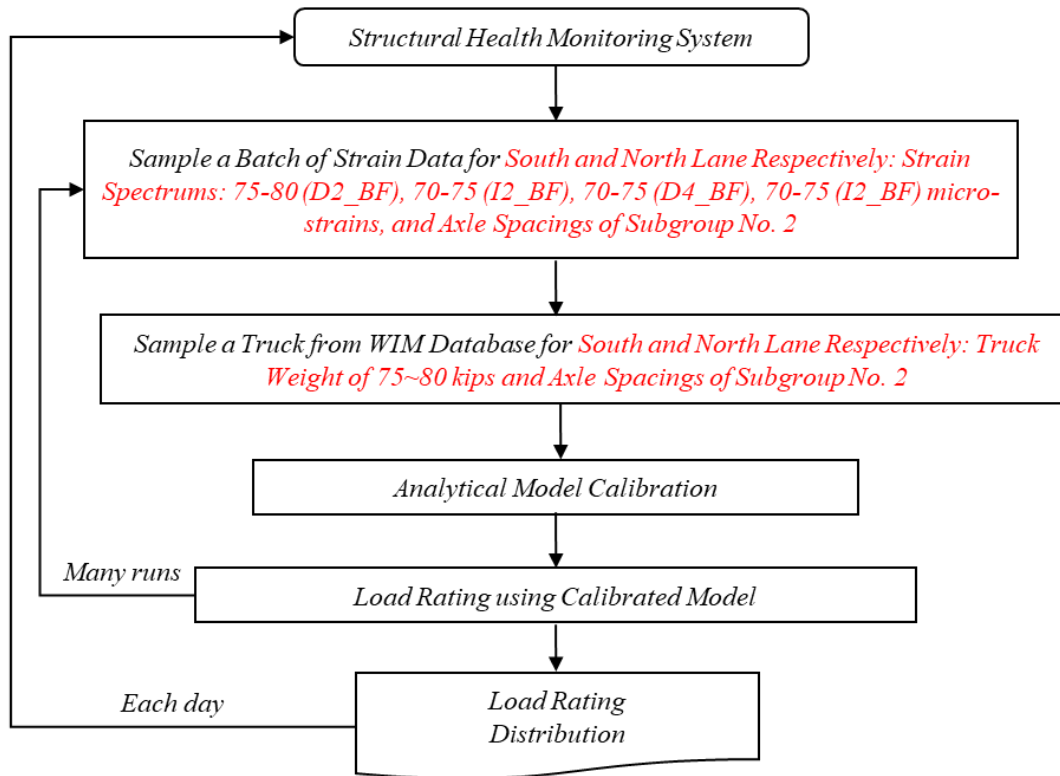
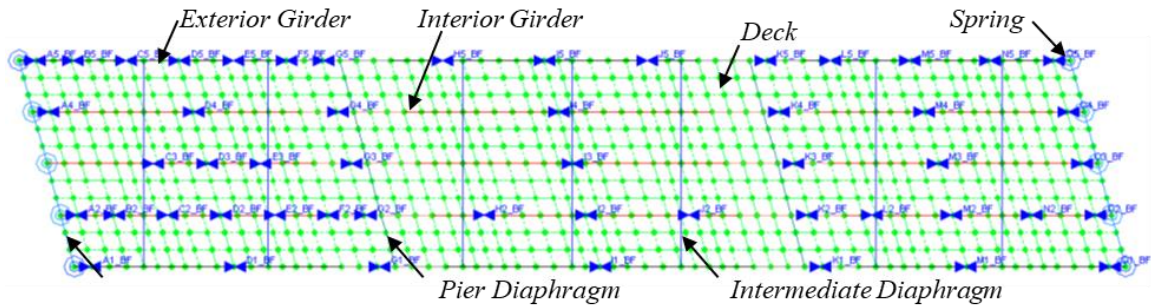


Figure 6.6. Flowchart of automated ambient traffic approach using Sampling Strategy C

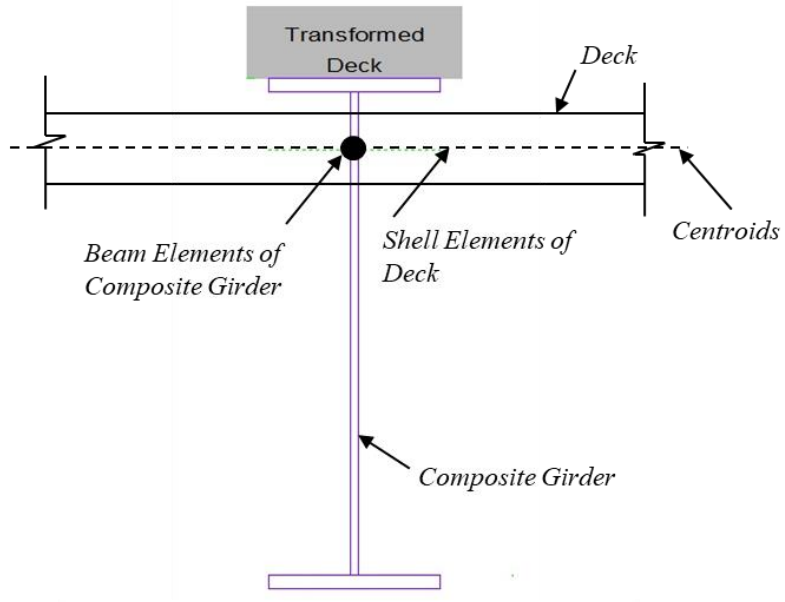
Each sampling strategy was intended to select strain responses and trucks for a certain quantity of bridge model calibration. For each calibration, a batch of strain time histories was randomly selected based on the spectrum of the peak girder strain, and a truck was randomly selected based on the spectrum of gross vehicle weight along with the axle spacing related to the selected batch. A batch of strain time histories represents girder strain responses induced by one five-axle truck event. Further, due to the precision of the axle detection approach, the values of the detected axle spacing ± 0.8 ft were used as one of the criteria to select trucks (i.e., truck parameters) from the WIM database. To take into account uncertainties of the transverse position of the truck, it was assumed for the proposed approach that the truck traveled in the center of the lane ± 1.5 ft following a uniform distribution.

6.2. FE Modeling of a Demonstration I-80 Bridge

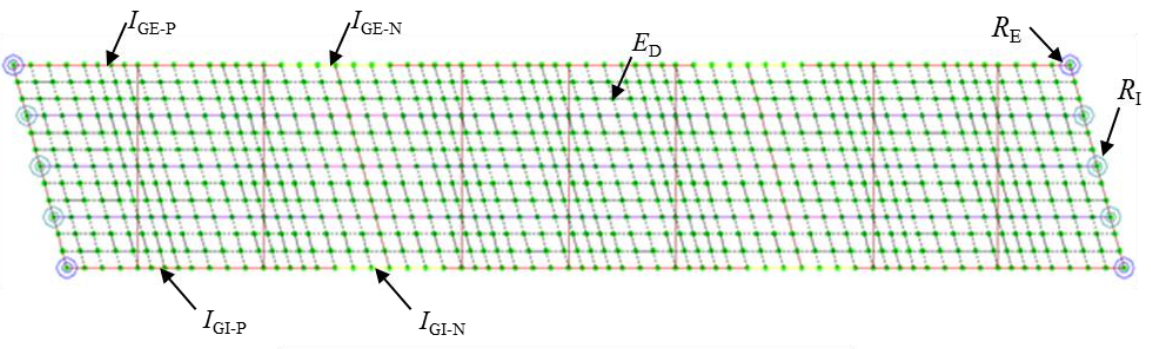
The FE model of the I-80 bridge was established as shown in Figure 6.7a.



(a) Bridge Model and Sensors



(b) Modeling of Girder and Deck



(c) Optimized Bridge Parameters

Figure 6.7. Details of FE model of I-80 bridge

The girders and diaphragms were modeled using two-node beam elements, which had three translational and three rotational degrees of freedom at each node. The deck was modeled using four-node quadrilateral shell elements, which had three translational and three rotational degrees of freedom at each node and only incorporated bending behavior (ignoring tension membrane

behavior). The restraint to girders at the abutment supports was modeled using spring elements. As shown in Figure 6.7b, the beam elements of girders shared the common nodes with the deck shell elements at the centroid locations. The composite section of the girder incorporating the transformed deck was utilized for the section properties of each beam element. The diaphragms only share the common nodes with the girder elements at the connection locations. Linear elastic material models were used for the concrete and steel.

To calibrate the established FE model, a set of bridge parameters significantly correlated to the bridge response was selected for the model optimization process. The common bridge parameters consisted of moments of inertia of girders and diaphragms, the elastic modulus of the deck, and spring constants at supports. The seven bridge parameters for the I-80 bridge to be calibrated were (1) moments inertia of exterior girder cross sections in the positive moment region (I_{GE-P}), (2) moment inertia of exterior girder cross sections in the negative moment region near piers (I_{GE-N}), (3) moment inertia of interior girder cross sections in the positive moment region (I_{GI-P}), (4) moment inertia of interior girder cross sections in the negative moment region near piers (I_{GI-N}), (5) modulus of elasticity of deck (E_D), (6) spring constant for exterior girders (R_E), and (7) spring constant for interior girders (R_I).

Various values and calibration ranges are tabulated in Table 6.5.

Table 6.5. Parameter values and ranges of I-80 bridge

Parameter	Non-composite plan value	Composite plan value	Lower limit	Upper limit
I_{GE-P} , in ⁴	7680	28677	5760	35846
I_{GE-N} , in ⁴	12791	33899	9594	42374
I_{GI-P} , in ⁴	8895	24926	6671	31158
I_{GI-N} , in ⁴	14761	35737	11071	44672
R_E , kips-in./rad	1000	1000	0	9000
R_I , kips-in./rad	1000	1000	0	9000
E_D , ksi	3834	3834	2876	4793

The initial values of the elastic modulus of the deck were set as plan values, and upper and lower limits were set as 25% higher and 25% lower than the plan values, respectively. The initial values of the girders were set as plan values considering fully composite actions with deck and railings. The upper and lower limits of the moments of inertia of the girders were set as 25% higher than plan values considering fully composite action and 25% lower than plan values considering non-composite action, respectively. The spring constants for both interior and exterior girders at abutments accounting for support restraint were set to have an initial value of 1,000 kip-in/rad, the lower limit of 0 kip-in/rad, and the upper limit of 9,000 kip-in/rad. It should be noted that the end restraint needs to be well evaluated because bridge load rating will be over-estimated if taking into account the unintentional support restraint provided by the abutments

(Chajes et al. 1997). Strains in a total of 52 strain sensors at different locations of girder bottom flanges as shown in Figure 6.7a were utilized for the parameter optimization process. As described previously, the parameters were calibrated through minimization of the discrepancy of the calculated and measured strain values.

The reliability of calibrated moments of inertia were significantly correlated with the accuracy of the centroid position of the girder cross sections. To realistically evaluate the centroid positions for different types of girder cross sections, the strain response in the top and bottom gauges was utilized to derive the neutral axis location. Take the cross section of the interior girder in the positive moment region as an example (Figure 6.8).

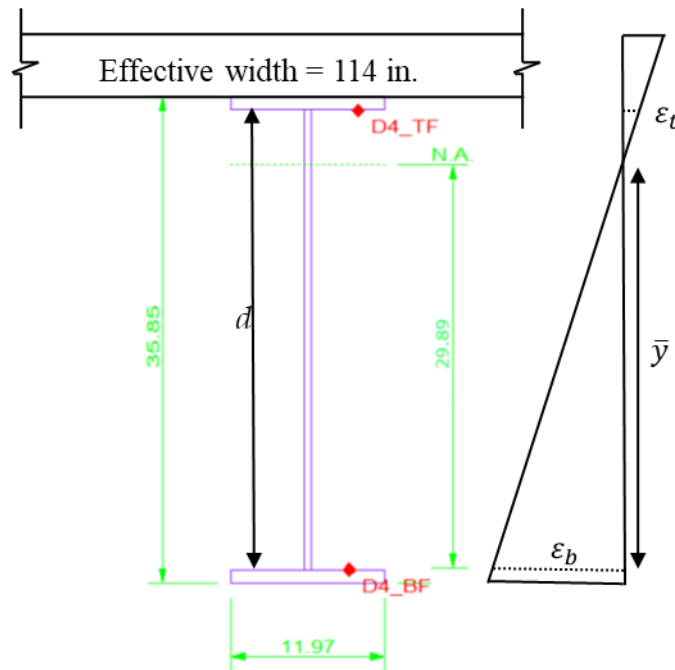
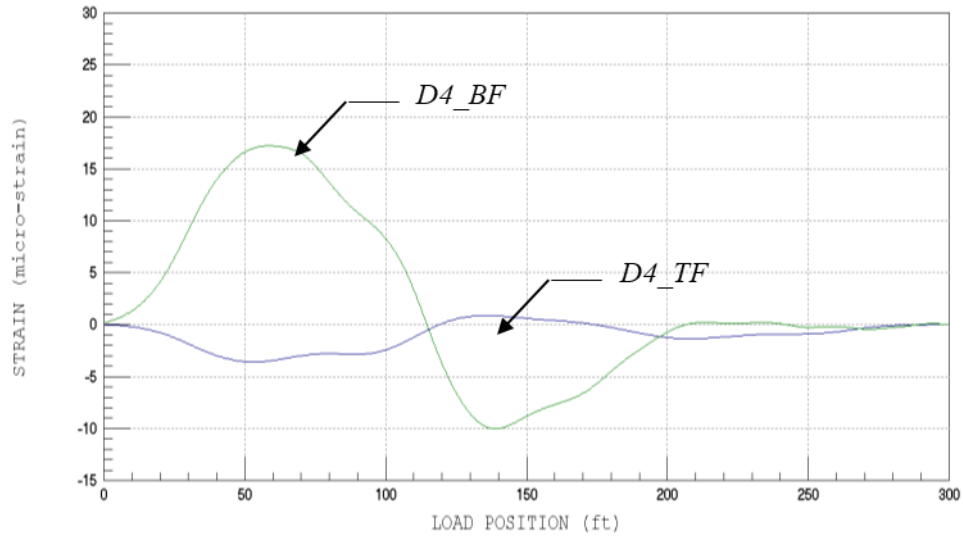
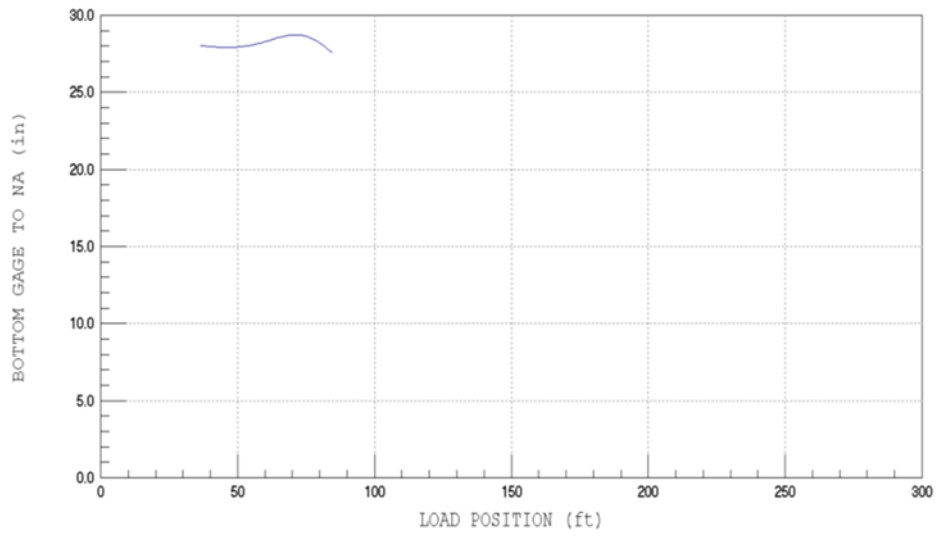


Figure 6.8. Sensors on interior girder cross section – positive moment region

As shown in Figure 6.8, the effective width of the deck is equal to the girder spacing, 114 in. The transformed deck section was derived using the stiffness ratio between the girder steel and deck concrete. Based on the composite girder section properties, the centroid position of the girder cross section was calculated to be 29.89 in. away from the bottom gauge location. The gauges, D2_BF and D2_TF, mounted on the bottom and top flanges of the steel girder, are shown in Figure 6.8, and the distance between D2_BF and D2_TF is 33.96 in. The strain response in D2_BF and D2_TF is shown in Figure 6.9a (positive in tension).



(a) Strain response of Sensor Pair D4_BF and D4_TF



(b) Neutral Axis Location

Figure 6.9. Neutral axis determination based on sensor pair D4_BF and D4_TF

Based on mechanics of materials, the strain profile is illustrated in Figure 6.8 and the neutral axis location can be derived using equation (23).

$$\bar{y} = \frac{\varepsilon_b}{\varepsilon_b + \varepsilon_t} d \quad (23)$$

where,

\bar{y} = neutral axis location relative to the bottom gauge location

ε_b = strain in the bottom gauge

ε_t = strain in the top gauge

d = the distance between the two gauges

Since the small strains in gauges are not reliable, the minimum delta strain, which is defined as the minimum strain difference between the top and bottom gauges, was utilized to pick the strain response for the calculation neutral axis location. For the sensor pair D2_BF and D2_TF, the minimum delta strain was set to 15 $\mu\epsilon$. The calculated neutral axis location for this sensor pair is plotted in Figure 6.9b, and has the mean of 28.22 in. and standard deviation of 0.311 in.

Likewise, the neutral axis locations in exterior girders in positive moment region, exterior girders in negative moment region, and interior girders in negative moment region were also calculated as tabulated in Table 6.6.

Table 6.6. Neutral axis determination at different girder cross sections

Girder cross sections	N.A. based on section properties (in.)	N.A. based on strain response			
		Base gauges	Mean (in.)	Standard deviation (in.)	Minimum delta strain (10^{-6})
Exterior girders in positive moment region	35.04	D5_BF & D5_TF	30.53	0.382	3.5
Exterior girders in negative moment region	33.90	G5_BF & G5_TF	31.33	0.183	3.5
Interior girders in positive moment region	29.89	D4_BF & D4_TF	28.22	0.311	15
Interior girders in negative moment region	26.75	G4_BF & G4_TF	27.41	0.496	13

Note: Neutral Axis (N.A.) Location — Relative to the bottom gauge location; Minimum Delta Strain — Minimum strain difference between the top and bottom gauges

The calculated neutral axis locations are generally different from those determined using the hand calculations based on section properties. Accordingly, the calculated means of neutral axis locations were imported into the FE model as the centroids of the cross sections of the beam elements for girders.

6.3. Load Rating Using Traditional Known Truck Approach

Bridge model calibration and load rating using the TKT approach were performed to provide information to validate the adequacy of the AAT approach. For the TKT approach, the strain response collected from field tests using trucks with known parameters were utilized for bridge model calibration. Two types of field testing were conducted: (1) crawl speed tests and (2) high speed tests. For the crawl speed tests, a three-axle dump truck was employed as the control truck. For the high-speed tests, the three-axle dump truck and ambient traffic five-axle trucks weighed

at the WIM station nearby were employed as the control trucks. The axle and wheel configurations of the three-axle dump truck are illustrated in Figure 6.10 and the axle spacing, axle weights and the total weight of the truck are summarized in Table 6.7.

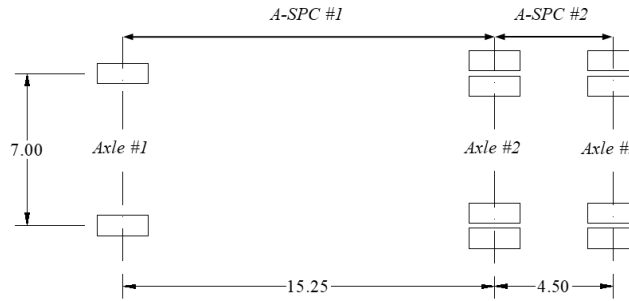


Figure 6.10. Axle and wheel configurations of dump trucks

Table 6.7. Parameters of three-axle dump truck

Truck type	A-SPC #1, ft	A-SPC #2, ft	A-WT #1, kips	A-WT #2, kips	A-WT #3, kips	GVW, kips
Dump truck	15.25	4.50	15.5	16.2	16.2	47.9

The axle and wheel configurations of the four five-axle trucks are illustrated in Figure 6.11 and the axle spacing, axle weights and the total weight of the trucks are summarized in Table 6.8.

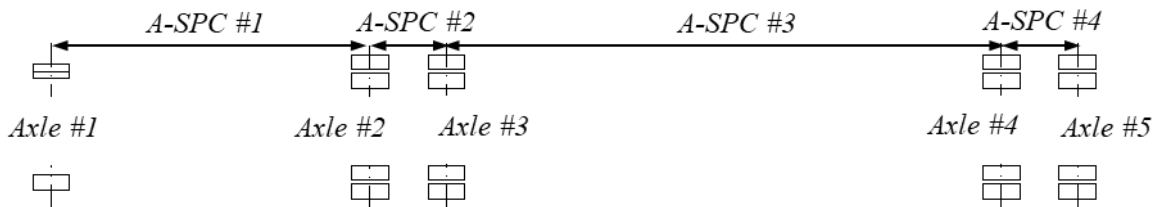


Figure 6.11. Axle and wheel configuration of ambient traffic five-axle trucks

Table 6.8. Parameters of ambient traffic five-axle trucks

Truck type	A-SPC #1, ft	A-SPC #2, ft	A-SPC #3, ft	A-SPC #4, ft	A-WT #1, kip	A-WT #2, kip	A-WT #3, kip	A-WT #4, kip	A-WT #5, kip	GVW, kip
Five-axle truck A	17.92	4.58	35.52	4.17	11.52	16.3	16.3	17.2	17.2	78.52
Five-axle truck B	17.5	4.69	34.5	4.3	10.8	16.35	16.35	16.64	16.64	76.78
Five-axle truck C	17.69	4.45	31.35	4.95	11.9	9.04	9.04	8.56	8.56	47.1
Five-axle truck D	16.99	3.97	32.59	4.07	11.26	15.08	15.08	16.16	16.16	73.74

Since the truck loading had little dynamic effect on the bridge during the crawl speed tests, the results, obtained from the bridge model calibration and load rating utilizing the collected data in these tests, will be taken as the benchmark results and further used to verify the other results obtained using other types of data or the AAT approach. It should be noted that the strain data were still filtered to fully eliminate the dynamic and noise effects. During the crawl speed tests, the south lane was closed, and the trucks were traveling with different transverse positions in the south lane at crawl speed. Only the test data, which were not affected by the ambient traffic, were utilized for bridge model calibration. The truck speeds and transverse positions of the five tests utilized for calibration are summarized in Table 6.9.

Table 6.9. Crawl speed tests

Test ID	Truck type	Speed, ft/s	Travel lane	Transverse position, ft
CT1	Dump truck	6.5	South	18.5
CT2	Dump truck	6.6	South	18.5
CT3	Dump truck	6.8	South	16.2
CT4	Dump truck	5.8	South	16.2
CT5	Dump truck	6.5	South	18.6

Five runs of bridge model calibration and load rating were performed utilizing the five tests as shown in Table 6.10.

Table 6.10. Calibration and load rating results using crawl speed dump trucks

Test ID	I_{GE-P} , in ⁴	I_{GE-N} , in ⁴	I_{GI-P} , in ⁴	I_{GI-N} , in ⁴	R_E , kips-in./rad	R_I , kips-in./rad	E_D , ksi	AE, 10 ⁻⁶	PE	SE	CC	Min. rating factor
CT1	32770	36450	23550	33430	437.5	7000	5400	3868	5.9%	6.4%	0.9778	1.65
CT2	32770	37260	23450	34230	437.5	7000	5400	4506	6.4%	6.8%	0.9737	1.65
CT3	30870	37250	24930	34050	5736	7000	5400	4629	4.8%	9.1%	0.9776	1.66
CT4	30110	37870	24200	33280	2122	7000	5400	4461	4.8%	8.6%	0.9779	1.64
CT5	32770	36620	23250	33900	437.5	7000	5400	5869	5.8%	8.0%	0.9735	1.65
Mean	31858	37090	23876	33778	1834	7000	5400	4667	5.5%	7.8%	0.9761	1.65
Std Dev	1277	569	688	407	2300	0	0	734	0.7%	1.2%	0.0023	0.01

Note: AE – Absolute error; PE – Percent error; SE – Scale error; CC – Correlation coefficient; 1 in.⁴ = 416,231 mm⁴; 1 ksi = 6.895 MPa

The final values of optimized parameters for each bridge model calibration are shown in Table 6.10. Among the five calibrations utilizing the data from the five crawl speed tests, the variations of the seven optimized parameters are small and indicate the robustness of the calibration process. The statistical values illustrating the accuracy of each calibration are also shown in Table 6.10. Small errors (including percent error and scale error) and correlation coefficients larger than 0.97, were generally found. Note that only the load carrying capacities of girders were evaluated because the strain responses in these components were utilized for bridge model calibration. During the calibration process, strain influence lines calculated using FE modeling were also visually compared with the experimental values. An example of this visual comparison of sensors at Section D and Section G for Test CT1 are shown in Figure 6.12 and Figure 6.13, respectively.

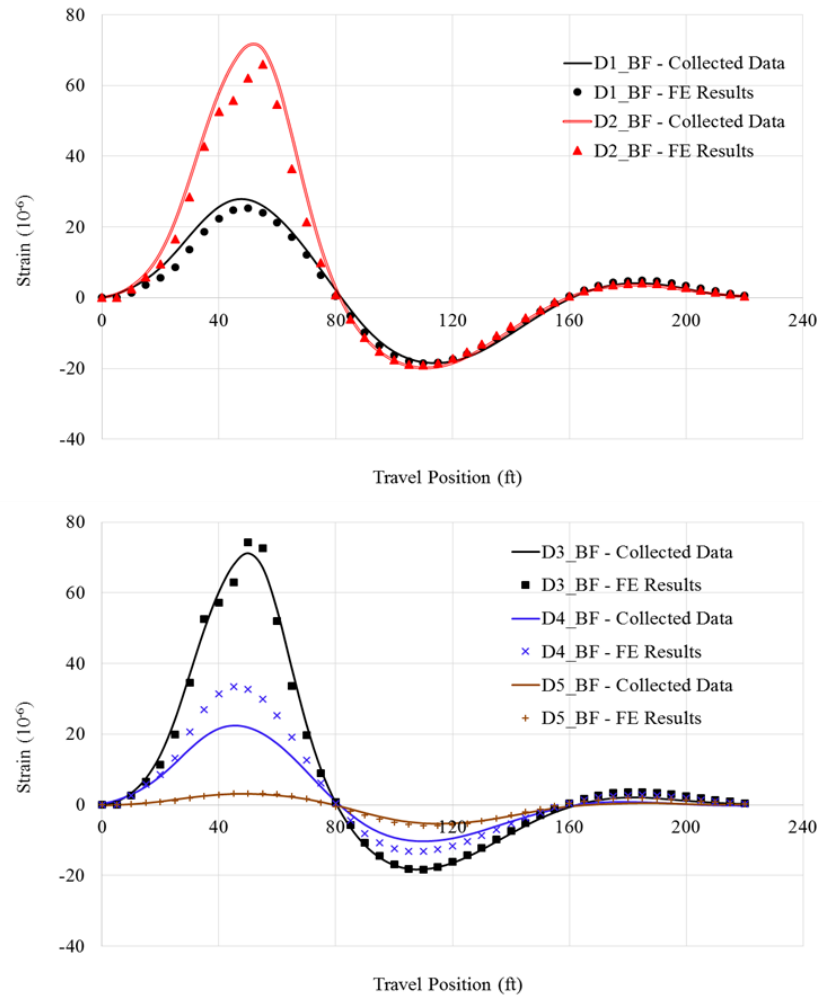


Figure 6.12. Comparisons of strain time histories between collected data and FE results using known trucks – Section D (1 ft = 0.305 m)

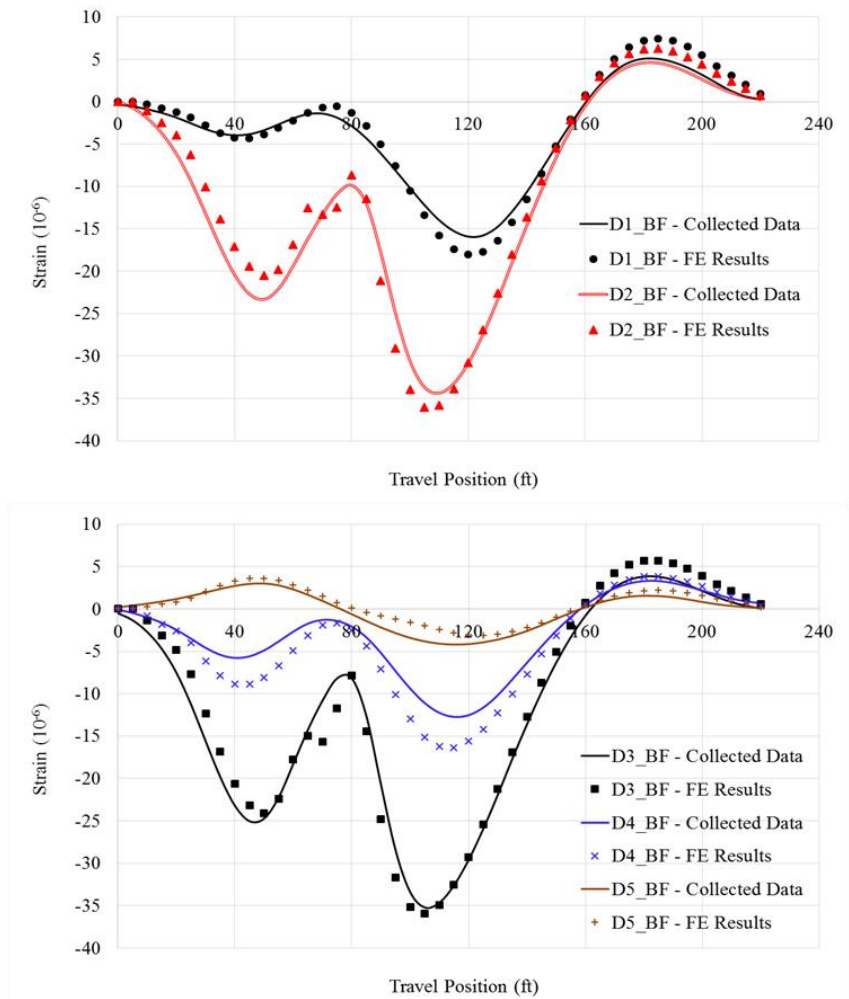


Figure 6.13. Comparisons of strain time histories between collected data and FE results using known trucks – Section G (1 ft = 0.305 m)

The minimum rating factors are shown in Table 6.10. The strength capacity (C) of components are not changed when performing the bridge model calibration. The rating factor as calculated by equation (21) is dependent on the effects of distributed dead load and live load to each component. Therefore, the rating factors can be well determined using different model calibrations as shown in Table 6.10. The mean and standard deviation of the bridge parameters, statistical values, and minimum rating factors are also calculated in Table 6.10.

For high speed tests, the dump truck was traveling across the bridge in the north and south lanes two times, respectively, at high speed and the four five-axle trucks were individually traveling across the bridge in either north or south lane at high speed as shown in Table 6.11.

Table 6.11. High speed dump truck and ambient traffic five-axle trucks

Test ID	Truck type	Speed, ft/s	Travel lane	Transverse position, ft
HT1	Dump truck	100.6	South	17.5
HT2	Dump truck	108.0	South	18.5
HT3	Dump truck	101.6	North	30.5
HT4	Dump truck	102.3	North	30.0
AT1	Five-axle truck A	104.2	South	17.5
AT2	Five-axle truck B	97.7	South	18.0
AT3	Five-axle truck C	103.7	North	32.0
AT4	Five-axle truck D	100.6	North	30.5

Only the test data that were not affected by the ambient traffic were used during model calibration, and the strain data were filtered to eliminate the dynamic and noise effects. The truck types, speeds, travel lanes, and transverse positions of the eight tests utilized for calibration are summarized in Table 6.11. It should be noted that the trucks attempted to travel in the center of each travel lane and the transverse positions were visually estimated during testing.

Eight runs of bridge model calibration and load rating were performed utilizing the eight tests as shown in Table 6.12.

Table 6.12. Calibration and load rating results using high speed trucks

Test ID	I _{GE-P} , in ⁴	I _{GE-N} , in ⁴	I _{GL-P} , in ⁴	I _{GL-N} , in ⁴	R _E , kips-in./rad	R _I , kips-in./rad	E _D , ksi	AE, 10 ⁻⁶	PE	SE	CC	Min. rating factor
HT1	24870	31390	24830	33180	437.5	7000	5400	6352	7%	8%	0.9635	1.70
HT2	25690	28120	23600	34080	437.5	7000	5400	5535	9%	7%	0.9577	1.66
HT3	28910	34820	21580	36020	7000	7000	5400	5188	9%	7%	0.9593	1.63
HT4	28220	34080	21490	35530	7000	7000	5400	5524	10%	7%	0.9574	1.63
AT1	22280	27760	27120	33990	7000	7000	5400	9180	9%	10%	0.9535	1.66
AT2	28510	35140	26710	36320	7000	7000	5400	9688	11%	11%	0.9461	1.72
AT3	29230	36950	27660	35210	7000	7000	5400	5867	9%	16%	0.9604	1.71
AT4	28440	35300	24880	36330	7000	7000	5400	6955	7%	11%	0.9688	1.66
HT1 & HT3	27950	33850	23110	34240	7000	7000	5400	10703	8%	4%	0.9614	1.67
HT2 & HT4	26780	32170	23350	34190	7000	7000	5400	11945	10%	4%	0.9506	1.67
AT1 & AT3	28180	34890	25930	36510	7000	7000	5400	9279	9%	12%	0.9540	1.72
AT2 & AT4	27540	34210	26560	34220	7000	7000	5400	9279	9%	12%	0.9540	1.67
Mean of crawl speed tests	31858	37090	23876	33778	1834	7000	5400	4667	5.5%	7.8%	0.9761	1.65

It was found that the calibration results were improved when both a south-lane test and a north-lane test were utilized for a run of bridge model calibration. This is due to fact that high strain response in the girders near both lanes were utilized for calibration. Accordingly, four extra runs of bridge model calibration and load rating were performed utilizing the south- and north-lane

test data simultaneously for each run as shown in Table 6.12. The final values of optimized parameters for each calibration using high speed test data are shown in Table 6.12. Among the eight calibrations utilizing eight tests, the variations of the seven optimized parameters are relatively larger compared to the results using crawl speed tests. This is probably due to the fact that the transverse positions were visually estimated and the dynamic effects were not fully eliminated using the low-pass filter. However, when the two lanes' data were utilized for one calibration, the optimized parameter values were improved compared to the means of the results using crawl speed tests as shown in Table 6.12. This is the reason that two lanes' data are utilized for each bridge model calibration using the AAT approach with Sampling Strategy C.

For all the calibrations using high speed test data, the interior girder moments of inertia are better calibrated compared to the exterior girder moments of inertia. This is due to the fact that the higher strains generally occurred in the interior girders. The statistical values illustrating the accuracy of each calibration are also shown in Table 6.12. Relatively small errors (including percent error and scale error) and correlation coefficients larger than 0.95 were generally found. The rating factors determined using the calibrated models based on high speed tests are slightly higher than those calculated based on crawl speed tests as shown in Table 6.12.

6.4. Load Rating Using Automated Ambient Traffic Approach

The details of sampling of truck events and WIM trucks for bridge model calibration are shown in Table 6.13.

Table 6.13. Sampling of truck events and WIM trucks for bridge model calibration

Sampling strategy	Event No.	Travel lane	Transverse position (ft)	Strain bin (10^{-6})		Amount of WIM trucks	WIM truck weight bin (kips)
Strategy A	1	South lane	17–20	30–80 (D2_BF)	25–75 (I2_BF)	100	20–80
Strategy B	2	South lane	17–20	75–80 (D2_BF)	70–75 (I2_BF)	100	75–80
	3	North lane	29–32	75–80 (D4_BF)	72–77 (I4_BF)	100	75–80
Strategy C	2 & 3	South & north lanes	17–20 & 29–32	75–80 (D2_BF) & 75–80 (D4_BF)	70–75 (I2_BF) & 72–77 (I4_BF)	100 & 100	75–80 & 75–80

For each sampling strategy, 100 runs of calibration and load rating were performed. One demonstration using south-lane events was presented for Sampling Strategy A, two demonstrations using south- and north-lane events, respectively, were presented for Sampling Strategy B, and one demonstration using both the south- and north-lane events was presented for Sampling Strategy C for comparison purposes as shown in Table 6.13. The final selected truck events and associated truck characteristics are summarized in Table 6.14.

Table 6.14. Events and ambient traffic five-axle trucks

Event No.	Peak strain 1	Peak strain 2	Truck No.	Speed, ft/s	A-SPC #1, ft	A-SPC #2, ft	A-SPC #3, ft	A-SPC #4, ft
1	69.8 (D2_BF)	70.3 (I2_BF)	Five-axle Truck 1	104.2	18.83	4.58	34.58	4.5
2	77.6 (D2_BF)	71.2 (I2_BF)	Five-axle Truck 2	104.2	16.15	4.58	34.17	4.17
3	77.43 (D4_BF)	72.1 (I4_BF)	Five-axle Truck 3	102.4	16.79	4.5	31.15	4.09

Calibration and load rating results obtained using the AAT approach through different sampling strategies are summarized and compared with those determined using the TKT approach shown in Table 6.15.

Table 6.15. Calibration and load rating results using the AAT approach with different sampling strategies

Calibration and load rating approach			I _{GE-P} , in ⁴	I _{GE-N} , in ⁴	I _{GI-P} , in ⁴	I _{GI-N} , in ⁴	R _E , kips-in./rad	R _I , kips-in./rad	E _D , ksi	AE, 10 ⁻⁶	PE	SE	CC	Min. rating factor	
AAT approach	Strategy A	Event 1	Mean	11411	13326	21616	26013	1321	8776	4624	11727	13.2%	12.2%	0.9311	1.49
			STVD	3788	3619	4564	6835	1762	226	938	2311	5.9%	1.1%	0.0323	0.17
	Strategy B	Event 1	Mean	15655	18528	25465	34943	5694	8500	5524	9393	9.0%	11.7%	0.9546	1.45
			STVD	3569	3591	919	734	1114	0	177	582	0.9%	0.8%	0.0049	0.10
		Event 2	Mean	31299	38440	21653	33329	6859	8500	5850	7415	7.2%	8.9%	0.9694	1.57
			STVD	3892	4842	1848	2085	0	0	0	397	1.0%	0.3%	0.0016	0.06
	Strategy C	Event 1 & 2	Mean	30222	36782	22334	33852	6859	8500	5850	17207	9.0%	5.2%	0.9575	1.60
			STVD	4160	5595	1161	940	0	0	0	853	1.0%	0.4%	0.0042	0.06
TKT approach			Mean	31858	37090	23876	33778	1834	7000	5400	4667	5.5%	7.8%	0.9761	1.65
			STVD	1277	569	688	407	2300	0	0	734	0.7%	1.2%	0.0023	0.01

Note: STVD - Standard Deviation; 1 in.⁴ = 416,231 mm⁴; 1 ksi = 6.895 MPa.

As before, only the load carrying capacities of girders were considered. The means and the standard deviations of converged parameter values, statistical values, and minimum rating factors were calculated for 100 runs of calibration and load rating using each sampling strategy (see Table 6.15). As indicated in Table 6.15, Sampling Strategy C is the best of three strategies while Sampling Strategy B is better than Sampling Strategy A. When using Sampling Strategy C, the means and standard deviations of errors are relatively smaller, and the correlations are larger than 0.95. The means and standard deviations of the statistical values and minimum rating factors are comparable to those obtained using known trucks. The mean values of bridge parameters using Sampling Strategy C are in agreement with the results using the TKT approach, although some dispersions of bridge parameter values are found especially for the exterior girder moments of inertia as shown in Table 6.15. Larger discrepancy of the bridge parameter values, statistical values, and rating factors were obtained using strategies B and C compared to strategy A.

Figure 6.14 shows that a wide spread of the minimum rating factor (ranging from 1.2 to 1.9) is found using Sampling Strategy A, a smaller spread of the minimum rating factor ranging from 1.3 to 1.7 is obtained using Sampling Strategy B, and the smallest spread of the minimum rating factor ranging from 1.5 to 1.7 is obtained using Sampling Strategy C, which is closest to the result obtained using the TKT approach.

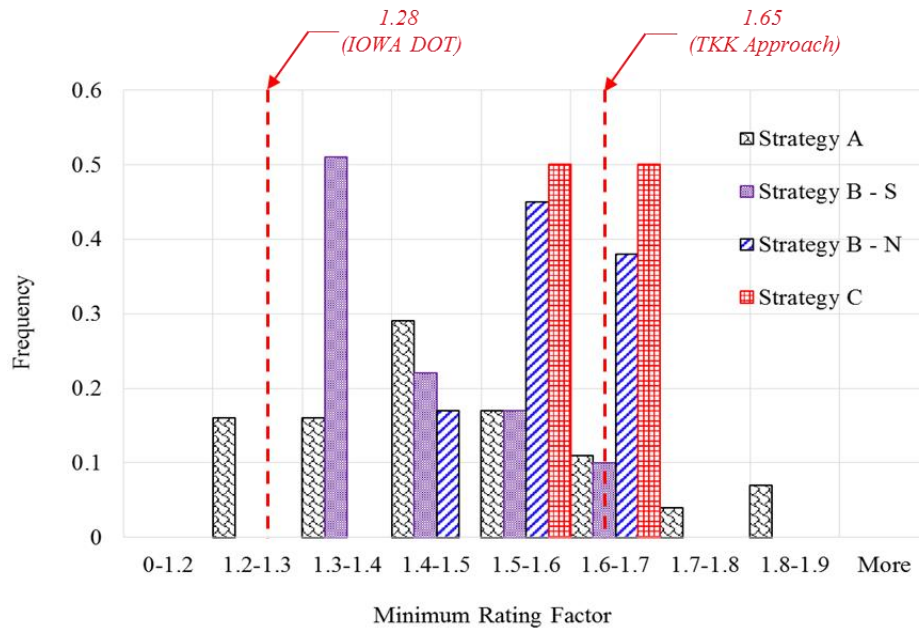


Figure 6.14. Frequency histograms of minimum rating factors using different sampling strategies

Sampling Strategy C is recommended for automated bridge load rating determination using ambient traffic. The mean, the standard deviation, and the range of the minimum rating factor using Sampling Strategy C is 1.60, 0.06, and 1.5–1.7, respectively. The Iowa DOT currently performs bridge load rating using the LARS Bridge software (Bentley Systems, Inc.), which uses a single line girder method and is not capable of modeling lateral load distribution effects. A minimum rating factor of 1.28 is obtained using LARS Bridge (Bentley Systems Inc.), which is much lower than the mean of 1.60 using Sampling Strategy C. This indicates that an average increase in rating factor of 25% was obtained when the bridge models were established, calibrated, and load rated.

One of the 100 calibrations using Sampling Strategy C that had a percent error of 8.4%, scale error of 5.3%, and correlation coefficient of 0.9596 is taken as an example to illustrate the results. The trucks randomly selected for this calibration from the WIM database are shown in Table 6.16.

Table 6.16. Parameters of selected five-axle trucks

Trucks	A-SPC #1, ft	A-SPC #2, ft	A-SPC #3, ft	A-SPC #4, ft	A-WT #1, kip	A-WT #2, kip	A-WT #3, kip	A-WT #4, kip	A-WT #5, kip	GVW, kip
Five-axle truck 1	16.2	4.3	33.5	4.1	10.31	17.4	16.9	16.45	16.45	77.51
Five-axle truck 2	17	4.5	31.9	4.1	10.97	15.83	17.07	16.5	16.59	76.96

The strain time histories calculated using FE modeling are in agreement with those from test data, as shown in Figure 6.15 and Figure 6.16 for sections D of south and north lanes, respectively, and Figure 6.17 and Figure 6.18 for sections G for south and north lanes, respectively.

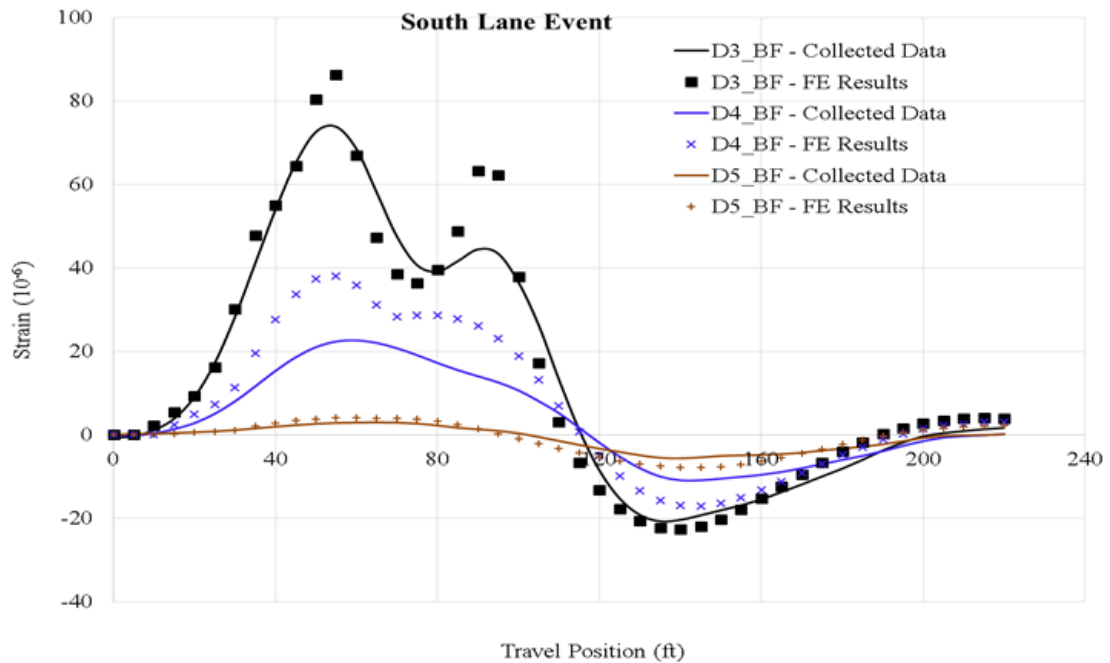
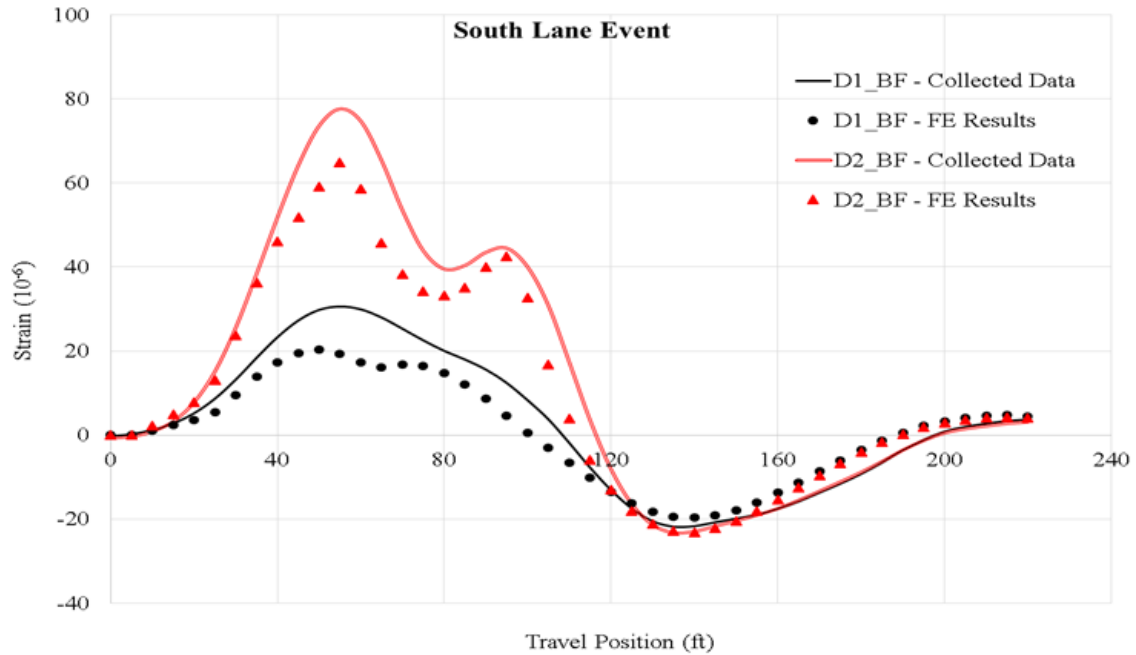


Figure 6.15. Comparisons of strain time histories between collected data and FE results using AAT approach – south-lane event and Section D (1 ft = 0.305 m)

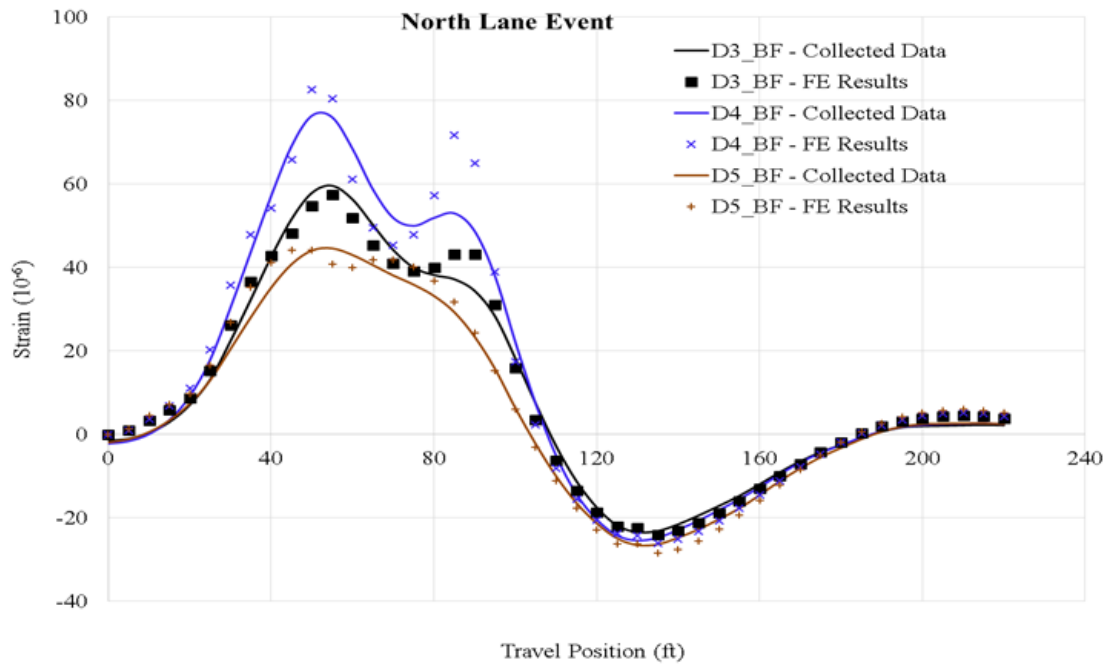
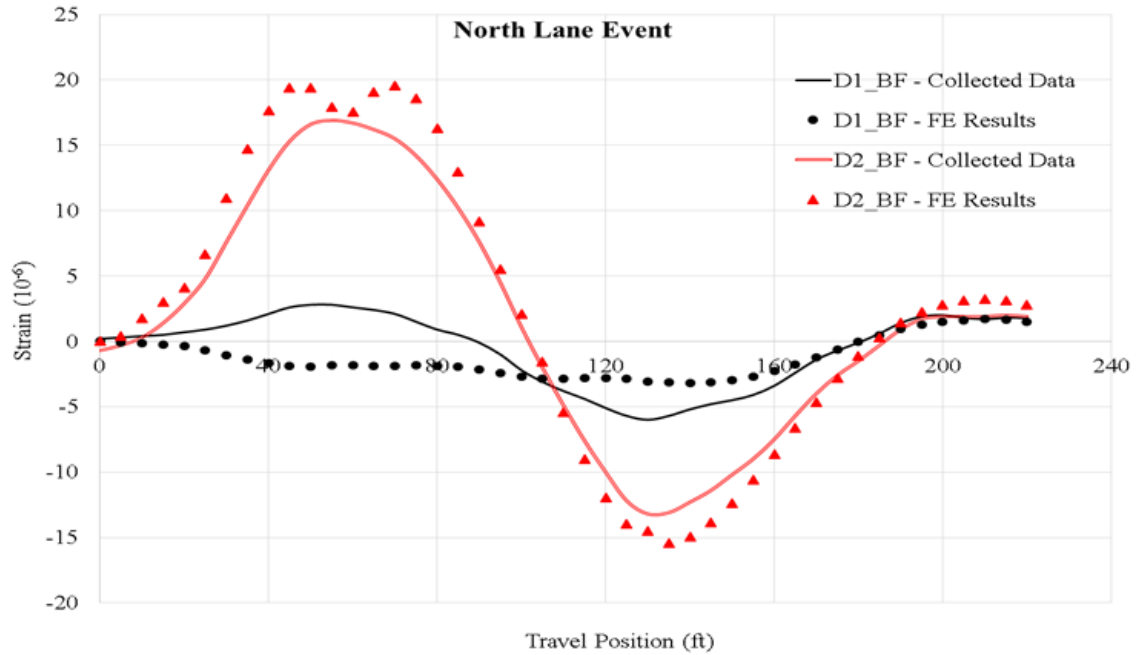


Figure 6.16. Comparisons of strain time histories between collected data and FE results using AAT approach – north-lane event and Section D (1 ft = 0.305 m)

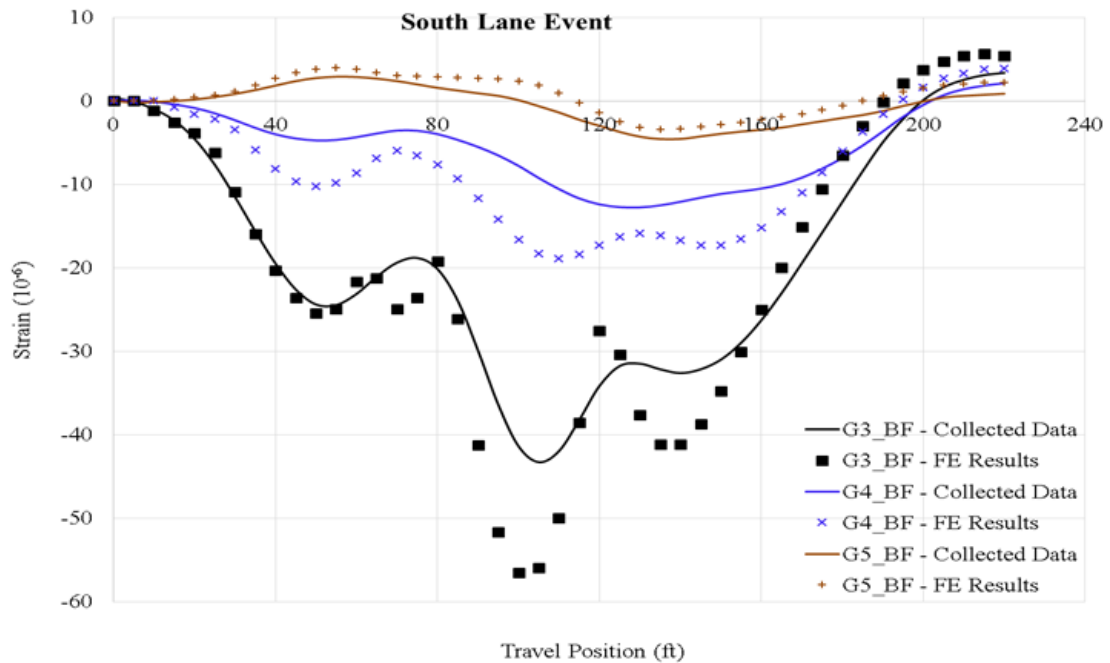
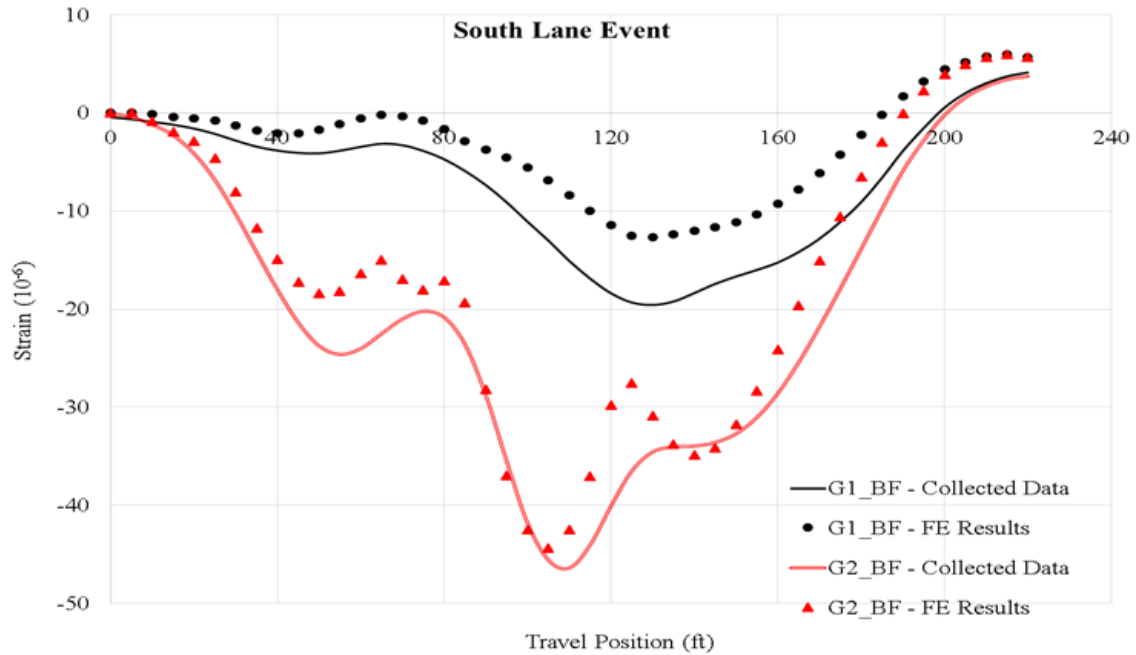


Figure 6.17. Comparisons of strain time histories between collected data and FE results using AAT approach – south-lane event and Section G (1 ft = 0.305 m)

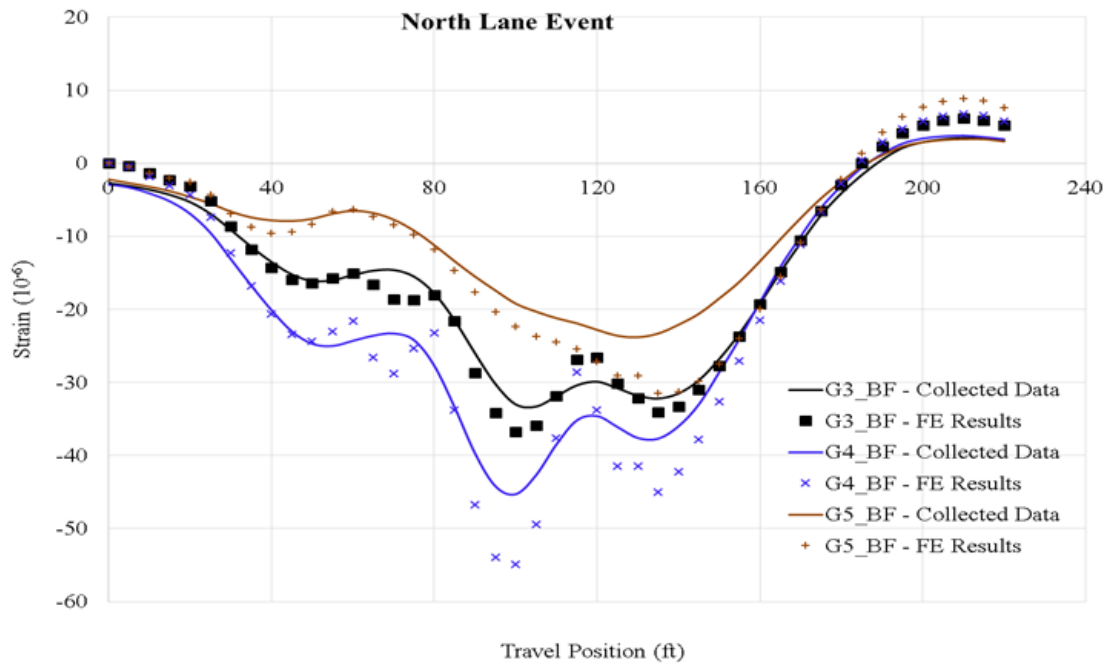
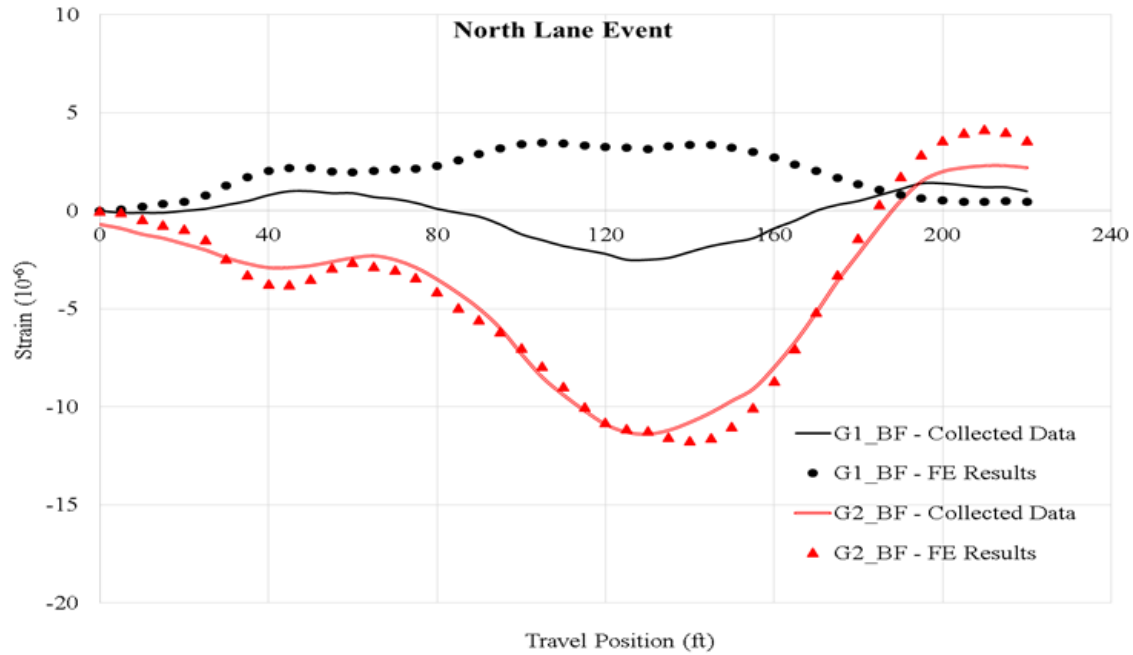


Figure 6.18. Comparisons of strain time histories between collected data and FE results using AAT approach – north-lane event and Section G (1 ft = 0.305 m)

6.5. Summary and Conclusions

An AAT approach was introduced for determining load ratings of steel girder bridges under ambient traffic. The AAT approach was developed by incorporating the truck detection process into an automated step-by-step procedure of bridge model calibration and load rating. The single

five-axle truck events extracted from the SHM system records were utilized for bridge model calibration. Accounting for the uncertainties of gross vehicle weight and axle weights, different sampling strategies were utilized to select bridge response and truck characteristics for bridge model calibration.

Load rating of the I-80 bridge using the TKT approach was performed to provide information for validating the adequacy of the AAT approach. The following conclusions were made from the load rating using the TKT approach:

- Small errors including percent error and scale error and good correlations were obtained.
- The bridge parameter values and rating factors were well determined.

Calibration and load rating results using the AAT approach with different sampling strategies were compared with those obtained using the TKT approach. The mean and standard deviation of converged parameter values, statistical values, and minimum rating factors were calculated for many runs of calibration and load rating using each sampling strategy. The following conclusions were made:

- When using Sampling Strategy C, the means and standard deviations of the statistical values and minimum rating factors were comparable to those obtained using the TKT approach.
- The mean values of bridge parameters using Sampling Strategy C were in agreement with the results using the TKT approach. The smallest spread of the minimum rating factor was obtained using Sampling Strategy C, which was closest to the result obtained using the TKT approach.
- A minimum rating factor of 1.28, obtained by the Iowa DOT using the single line girder method, was much lower than the mean of 1.60 using Sampling Strategy C. This indicated that an average increase in rating factor of 25% was obtained using calibrated bridge models for bridge load rating.
- The AAT approach was a reliable method for continuously estimating the load carrying capacity of bridges, and Sampling Strategy C was recommended for the AAT approach.

CHAPTER 7. IMPROVED LOAD RATING FACTOR THROUGH BETTER CAPACITY ESTIMATION

7.1. Overview

The load rating calculation can be used to estimate the safe load carrying capacity of a bridge. It helps to increase the public safety by reducing the risk of structural damage and collapse. The load rating factor, known as the rating factor (RF), is also a tool used to issue permits to heavy trucks and load postings on bridges. The AASHTO Manual of Bridge Evaluation (MBE) (AASHTO 2015) recommends two primary methods to calculate the rating factor of a bridge, the non-destructive load rating method, and analytical load rating method. The non-destructive load rating method involves load testing in the field, where the load tests are required traffic closures on bridges. The Allowable Stress Rating (ASR), Load Factor Rating (LFR), and Load and Resistant Factor Rating (LRFR) are three different general rating factor calculation methods. The main difference between these analytical load rating methods are the design philosophies underlying the associated rating specification. The basic idea of the rating factor is to assess the safety of a bridge at a critical section, and can be expressed in equation (24), which is a simplified version of AASHTO MBE equation 6A.4.2.1-1 (AASHTO 2015).

$$RF = \frac{\text{Strength Reduction Factor} \cdot M_n - \text{Load Factor for Permanent Loads} \cdot M_{DL}}{\text{Load Factor for Live Loads} \cdot M_{LL+IM}} \quad (24)$$

In equation (24), M_n represents the nominal flexural strength at a critical section. The M_{DL} and M_{LL+IM} are dead load moment and live load moment at the section, respectively. Analytical methods are used to calculate the M_{DL} and M_{LL+IM} in the above equation. The M_n can be calculated using theory of strength of materials and plastic moment principles given in Appendix D6.1 of the AASHTO Load and Resistance Factor Design (LRFD) Bridge Design Specifications (AASHTO 2014). Typically, the M_{DL} , M_{LL+IM} , and M_n are calculated based on nominal parameters, such as the section dimensions and the material properties listed in the bridge plans. The rating factor calculated in this way reflects the load rating of the bridge at the time of construction. However, the rating factor of the bridge could also be based on the section dimensions and the material properties at the time of the load rating.

7.1.1. Load Rating Using BECAS SHM System

In an attempt to improve the rating factor calculation, the BEC developed an SHM-based approach. Figure 7.1 shows the current approach to calculate the rating factor based on SHM data.

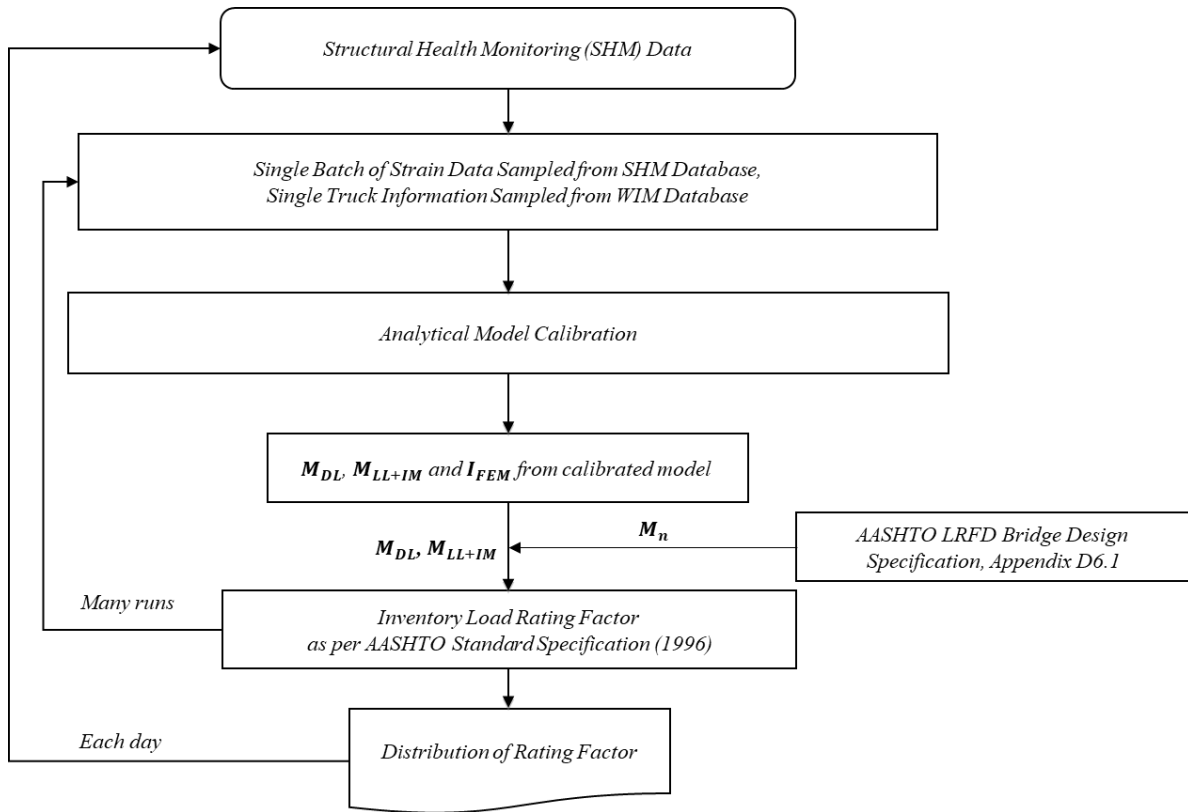


Figure 7.1. Current load rating process using SHM data

The truck detection program (Section 4.2) is capable of detecting and then characterizing five-axle semi-trucks as they cross a bridge. Even though the truck detection program is capable of detecting five-axle semi-trucks as well as determining truck speed and longitudinal position on the bridge, the program cannot precisely determine the gross weight of the trucks and axle weights. Thus, a single batch of strain data from the monitoring system and truck information from a WIM database are sampled to calibrate an FE model of the bridge (Section 6.2). The calibration is done by minimizing the percent error between measured and calculated strains by optimizing different bridge parameters. The calibrated FE model is used to obtain the M_{DL} and the M_{LL+IM} . The nominal moment capacity is calculated based on the LRFD Bridge Design Specifications (AASHTO 2014). With the above information, the load rating factor can be calculated as per the AASHTO Standard Specifications for Highway Bridges (AASHTO 1996). By sampling many different batches of strain data combined with different truck information from the WIM database, a probability distribution for the rating factor can be found.

In the current approach, the M_{DL} and M_{LL+IM} are estimated using the calibrated FE model of the bridge. As such, they represent the dead load moment and live load moment based on the section dimensions and the material properties at the time of the load rating. However, the above approach still uses the M_n , which is calculated based on LRFD Bridge Design Specifications (AASHTO 2014) guidelines and nominal properties of the bridge, which may not represent the flexural strength at the time of current load rating.

The material properties and section dimensions significantly affect the M_n of a bridge. Mans et.al. (2001) conducted two full-scale experiments on steel-concrete composite sections to investigate the effects of material properties on the flexural strength under positive bending moment. Both specimens were 40 ft long and loaded with a concentrated load at mid-span. Specimen 1 consisted of a 2.5 ft deep plate girder with a 5 ft wide, 7.25 in. thick concrete slab. Specimen 2 consisted of a similar plate girder, but a narrower bottom flange and a 7 ft wide, 7.25 in. thick concrete slab. Both girders had a nominal yield strength of steel 70 ksi. However, the measured steel material properties indicated that the yield strength of steel was between 80 and 85 ksi. Even though the specified strength of the concrete slab was not mentioned, the measured strength of the concrete was about 4.5 ksi for Specimen 1, whereas Specimen 2 was 7.5 ksi. The author used these section dimensions and material properties to calculate the M_n of Specimen 1 and Specimen 2 and compared them with the experimentally estimated flexural strength, M_{exp} . The results indicated that the M_n of Specimen 1 is 14% lower than the M_{exp} of the section and Specimen 2 showed 22% lower strength compared to the M_{exp} .

Gupta et.al. (2007) carried out an experiment to evaluate the ultimate flexural strength of a composite section. The steel-concrete composite section consisted of a 4 ft deep beam with 1.5 ft wide, 7 in. thick concrete slab. Two concentrated loads were applied at approximately the 1/3 location of a 33 ft long beam. The measured yield strength of the steel was about 47 ksi. The minimum specified strength of the concrete was not given in the article. However, the measured strength of the concrete is given as 6.5 ksi. The test results indicate that the M_{exp} was 7% higher than the M_n of the section.

Roberts (2004) conducted an experiment to understand the ductile behavior of steel-concrete composite sections under positive bending. The experiment consists of three full-scale composite sections. The first specimen was an 18 ft long simply supported beam with a 2 ft deep rolled steel beam with 3.5 ft wide, 7 in. thick concrete slab. Specimen 2 was a 30 ft long simply supported beam with a 2 ft deep plate girder. Specimen 1 and 2 had the same slab dimensions. Specimen 3 was similar to Specimen 2 except the top flange and web of Specimen 3 consisted of grade 50 steel, whereas the bottom flange consisted of HPS70W steel. The material test results indicated that the experimentally evaluated material properties were significantly higher than the nominal values. Probably for this reason, Specimen 1 showed a 14% higher M_{exp} and Specimen 2 showed a 24% higher M_{exp} compared to their M_n values. Specimen 3 did not reach the ultimate state during testing. However, the moment capacity at the maximum load was 10% higher than the M_n .

According to the above, typically the M_{exp} is significantly higher than the M_n of steel-concrete composite sections under positive bending moment. The probable reason for this difference is the measured material strength of both steel and concrete are significantly higher than the nominal values prescribed in the plans. However, there is no direct way to determine the material properties of a bridge component without doing a destructive test.

7.1.2. Objective

The objective of this part of the project was to further improve the rating factor calculation process by improving the estimate for flexural strength of steel-concrete composite sections. As mentioned in Section 7.1.1, the M_n value in the current rating factor calculation process is the only value that depends upon nominal bridge parameters. According to the experimental results shown in Section 7.1.1, typically the M_n is significantly smaller than the M_{exp} , which could lead to underestimating the rating factor of a bridge. By improving the estimate for flexural strength, a more meaningful value for the rating factor can be obtained.

7.2. Methodology

7.2.1. Hypothesis

Figure 7.2 shows the relationship between flexural strength and moment of inertia for non-composite sections obtained from the American Institute of Steel Construction Manual, hereafter referred to as AISC Specification (AISC 2015).

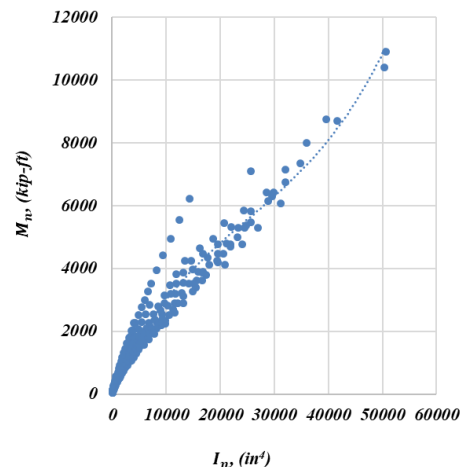


Figure 7.2. Relationship between flexural strength and moment of inertia

According to Figure 7.2 there is a trend, such that when flexural strength increases, the moment of inertia increases and vice versa. It is also noted that the relationship between strength and stiffness is not unique. The research group suspected that there was a similar trend between flexural strength and moment of inertia of steel-concrete composite sections. If that statement was true, then that relationship along with the I_{FEM} can be used to get an improved estimate for the flexural strength of the section, where the I_{FEM} is the moment of inertia from the calibrated FE model, and it represents the moment of inertia of the section based on the existing section dimensions and the material properties at the time of the load rating (Figure 7.1).

The relationship between flexural strength and moment of inertia was proposed to be developed using a Monte Carlo simulation. Figure 7.3 shows a schematic diagram of the expected relationship.

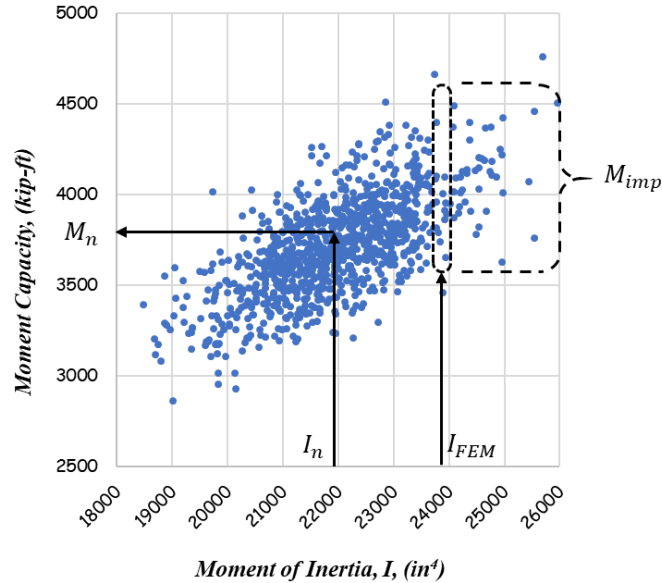


Figure 7.3. Relationship between capacity and moment of inertia of composite sections

The improved flexural strength, M_{imp} would be estimated from the I_{FEM} of the section. It is important to note that the M_{imp} does not necessarily mean a higher flexural strength compared to the M_n of a section. The M_{imp} could be smaller than or equal to the M_n of a section depending on its I_{FEM} . The M_{imp} would replace the M_n value in the current rating factor calculation process (equation (24)). The proposed improved rating factor calculating process using SHM data is shown in Figure 7.4.

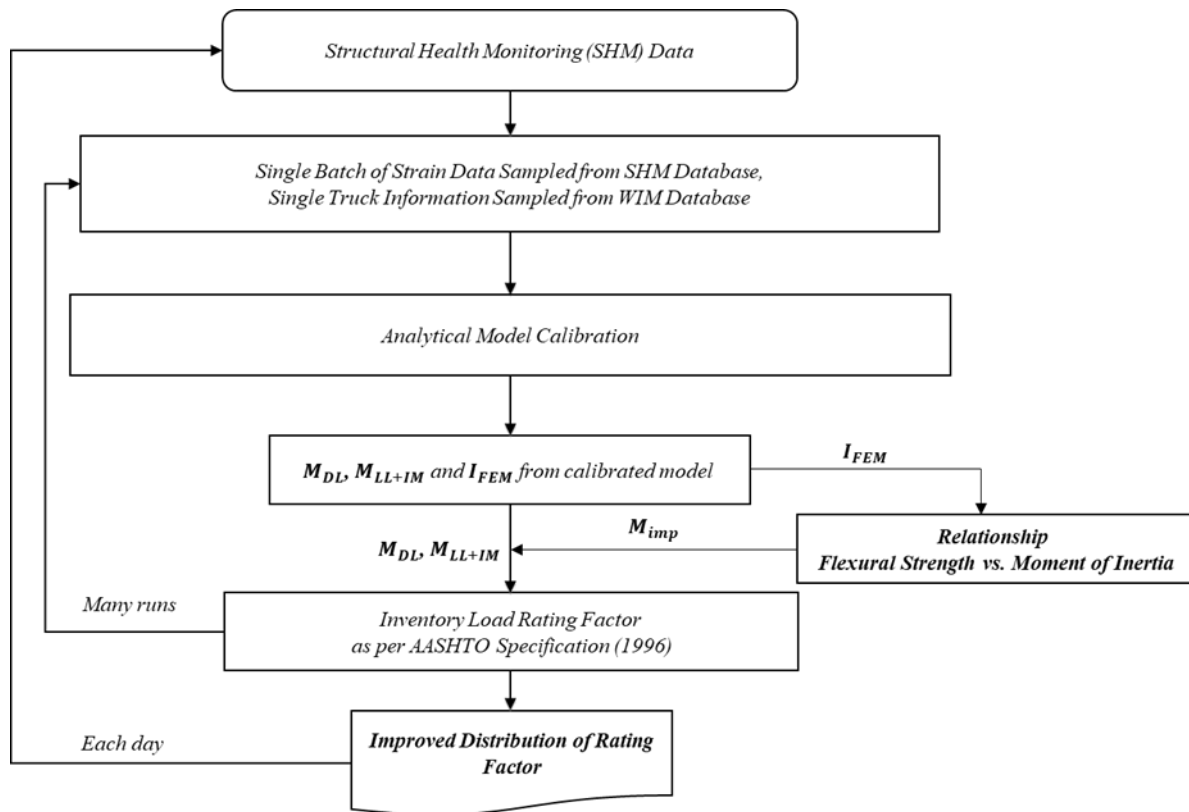


Figure 7.4. Improved load rating process using SHM data

7.2.2. Monte Carlo Simulation

When the existing material and geometric properties of a bridge element are known, the theory of strength of materials and the equations given in the LRFD Bridge Design Specifications (AASHTO 2014) can be used to develop a relationship between the moment of inertia and flexural strength of a section. However, the existing material properties of a bridge cannot be determined without performing material tests on the bridge components. To overcome the uncertainty of the existing section dimensions and material properties, statistical distributions of section dimensions and material properties can be used to represent the possible values for existing section dimensions and material properties. An extensive literature review was conducted by the research team to determine the parameters of the statistical distribution of section dimensions and material properties of bridge components. Significant research has proposed statistical distributions for material properties based on experiments (Melcher et al. 2004, Wiśniewski et al. 2012). As an example, Table 7.1 shows possible statistical parameters for Specimen A.

Table 7.1. Statistical distribution parameters of material properties

Parameter	Nominal value	Mean, (μ)	COV = σ/μ	Standard deviation, (σ)	Type of distribution
f'_c , (ksi)	4	4	0.20	0.8	Lognormal
F_y , (ksi)	50	50	0.05	2.5	
E_s , (ksi)	29000	29000	0.04	1160	

The nominal material properties of Specimen A were used as the mean. The mean (μ) and coefficient of variation (COV) were then used to determine the standard deviation (σ) of the lognormal distribution for each material property.

However, minimal research data were found regarding the statistical distribution of section dimensions (Bartlett et al. 2003). The COV and type of distribution are used to describe the section dimensions as was used for the material properties. The nominal dimension of the section was used as the mean value, and the COV was used to calculate the standard deviation of each lognormal distribution (Table 7.2).

Table 7.2. Statistical distribution parameters of section properties

Parameter	Nominal value	Mean, (μ)	COV = σ/μ	Standard deviation, (σ)	Type of distribution
b_s , (in.)	108	108	0.05	5.4	Lognormal
t_s , (in.)	8	8	0.05	0.4	
t_{tf} , (in.)	0.79	0.79	0.09	0.07	
b_{tf} , (in.)	12	12	0.02	0.25	
t_w , (in.)	0.6	0.6	0.08	0.05	
h_w , (in.)	34.02	34.02	0.02	0.68	
t_{bf} , (in.)	0.79	0.79	0.09	0.07	
b_{bf} , (in.)	12	12	0.02	0.25	

The Monte Carlo simulation along with the statistical distributions of section dimensions and material properties could be used to simulate the possible values for moment of inertia and flexural strength such that a relationship between the moment of inertia and flexural strength can be developed. The equations given in Appendix D6.1 of the LRFD Bridge Design Specifications (AASHTO 2014) were automated to perform the Monte Carlo simulation. The Monte Carlo simulation was carried out using the @Risk computer program version 7.5.1 Industrial Version using 50,000 iterations.

Figure 7.5 shows the probability distribution of moment of inertia of all four specimens obtained from the Monte Carlo simulation.

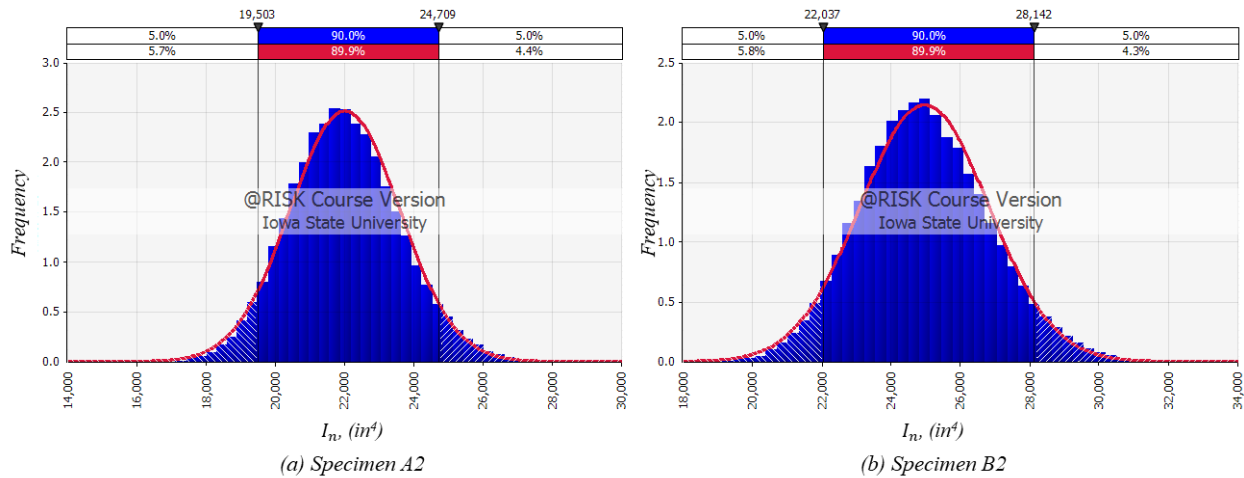


Figure 7.5. Monte Carlo simulation of composite I_n

Results show that the moment of inertia generally is normally distributed.

Similarly, Figure 7.6 shows the Monte Carlo simulation results for flexural strength of all four specimens.

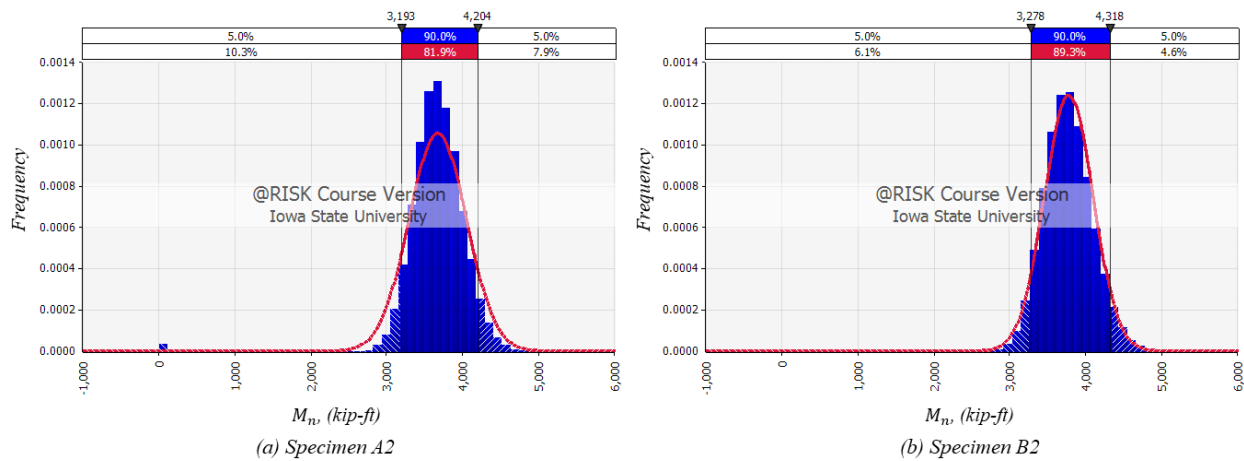
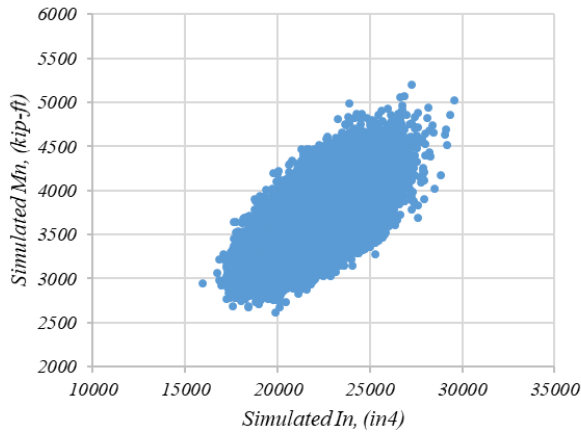


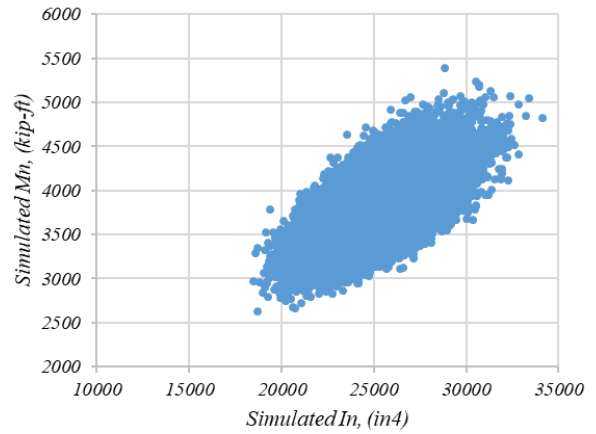
Figure 7.6. Monte Carlo simulation of composite M_n

Results indicate that the flexural strength of all four specimens are normally distributed.

The probability distributions of moment of inertia (Figure 7.5) and flexural strength (Figure 7.6) of each specimen were combined to develop the relationship between moment of inertia and flexural strength of the sections. Figure 7.7 shows the relationship between moment of inertia and flexural strength of all four specimens involved in the experimental study.



(a) Specimen A2



(a) Specimen B2

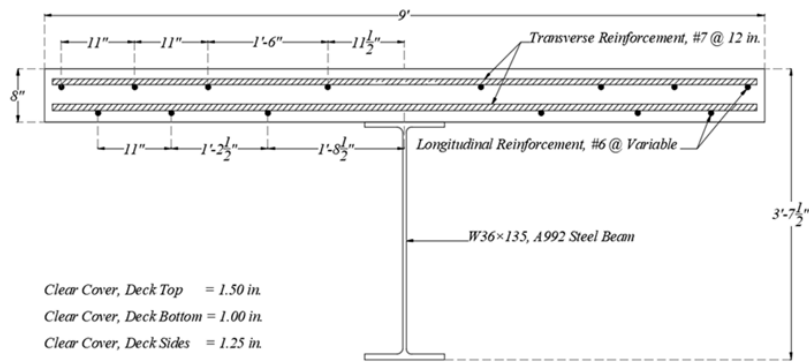
Figure 7.7. Relationship between M_n and I_n

According to the relationships shown in Figure 7.7, when the flexural strength increases the moment of inertia increases and vice versa, as suspected (Section 7.2.1). The experimental program described in the following section was conducted to provide validation of the use of I_{FEM} to get M_{imp} for the proposed rating factor calculation process.

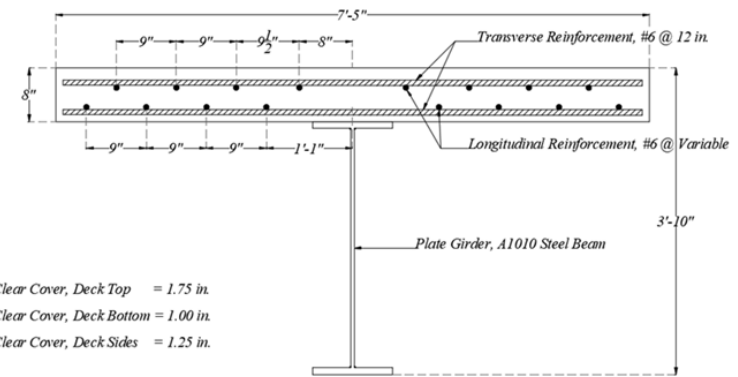
7.3. Experimental Program

7.3.1. Layout

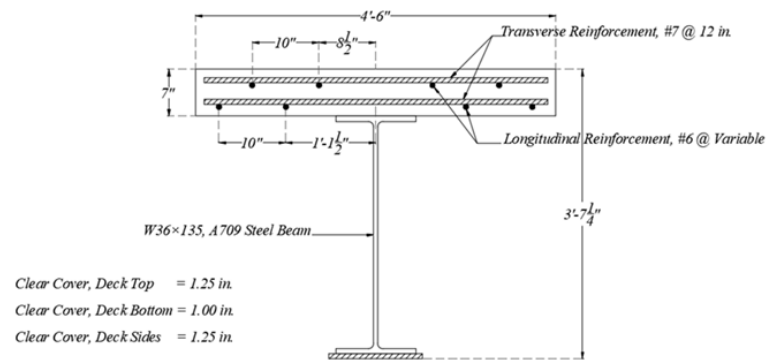
An experimental program was conducted at the Iowa State University Structural Engineering Research Laboratory to validate the hypothesis associated with this project objective. The experimental program consisted of the testing of four different steel-concrete composite specimens (Figure 7.8).



(a) Specimen A



(b) Specimen B



(c) Specimen C and D

Figure 7.8. Cross-sectional details

The moment of inertia and flexural strength of each specimen were experimentally determined to validate the (1) relationship between moment of inertia and flexural strength of the steel-concrete composite sections, and (2) use of moment of inertia from the calibrated FE model, I_{FEM} , to estimate flexural strength, M_{imp} , for the proposed rating factor calculation process.

Specimen A (Figure 7.8a) was a 40 ft long W36 x 135 mild-steel (A992 Steel) beam with a 9 ft wide, 8 in. thick concrete deck, whereas Specimen B (Figure 7.8b) was a 50 ft long stainless-steel (A1010 Steel) plate-girder with a 7.5 ft wide, 8 in. thick concrete deck. Specimen C and Specimen D (Figure 7.8c) consisted of a 45 ft long W36 x 135 mild-steel (A709 Steel) beam with a cover plate attached to the bottom flange and a 4.5 ft wide, 7 in. thick concrete deck. Compared to the cross section of Specimen A, the deck width of Specimen C and D were half as wide with a cover plate at the bottom flange. Theoretically, the narrower deck width and cover plate on the bottom flange should move the plastic neutral axis (PNA) of the cross section from the deck toward the steel girder. The only difference between Specimen C and Specimen D was that Specimen D was constructed with a lesser strength concrete to simulate the effects of a deteriorated concrete deck in the field. The reinforcing bar arrangement of the concrete deck for all four specimens were the same as those given in typical bridge plans. The shear studs were designed according to the LRFD Bridge Design Specifications (AASHTO 2014) Section 6.10.10.4, such that fully composite action can be achieved between the concrete and steel sections.

7.3.2. Section Dimensions

Table 7.3 shows the nominal dimensions of each specimen.

Table 7.3. Nominal dimensions of specimens

Nominal dimensions, (in.)	Specimen A	Specimen B	Specimen C	Specimen D
Deck width, b_s	108	89	54	54
Deck thickness, t_s	8	8	7	7
Top flange width, b_{tf}	12	12	12	12
Top flange thickness, t_{tf}	0.79	1.00	0.79	0.79
Web thickness, t_w	0.60	0.44	0.60	0.60
Web height, h_w	34.02	36	34.06	34.02
Bottom flange width, b_{bf}	12	12	12	12
Bottom flange thickness, t_{bf}	0.79	1.00	0.79	0.79
Cover plate width, b_{cp}	-	-	14	14
Cover plate thickness, t_{cp}	-	-	0.75	0.75
Span length, L	39 x 12	51.75 x 12	44 x 12	44 x 12

The actual dimensions of each specimen were measured to investigate the effects of actual dimensions on moment of inertia and flexural strength of each specimen. The difference between nominal and measured dimensions are significantly small. It should be pointed out that in an

actual bridge, the effective deck width is highly variable and mostly unknown. Therefore, the nominal dimensions given in Table 7.3 were used to initially estimate the moment of inertia and flexural strength of each specimen.

7.3.3. Material Properties

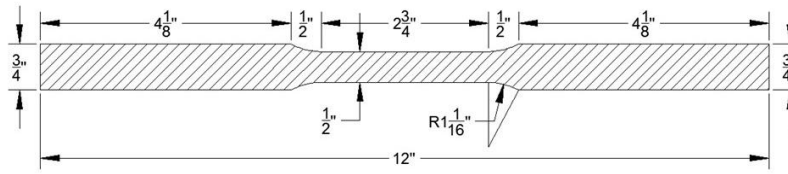
The nominal material properties of the concrete deck, steel girders, and cover plates for each specimen are listed in Table 7.4.

Table 7.4. Nominal material properties

Nominal material properties, (ksi)	Specimens A, B, C, and D
Strength of concrete deck, $f'_{c,n}$	4.00
Modulus of concrete deck, $E_{c,n}$	3640
Strength of steel girder, $F_{y,n}$	50
Modulus of steel girder, $E_{s,n}$	29000
Strength of steel cover plate, $F_{y,cp,n}$	50
Modulus of steel cover plate, $E_{s,cp,n}$	29000

The nominal strength of the concrete deck, $f'_{c,n}$ was obtained from the associated construction drawings of the I-80 bridge. The nominal modulus of elasticity of the concrete deck, $E_{c,n}$ was calculated based on the equation given in Section C5.4.2.4 of the LRFD Bridge Design Specifications (AASHTO 2014). The nominal strength of the steel girder $F_{y,n}$ and cover plate, $F_{y,cp,n}$ were obtained from the corresponding American Society for Testing and Materials (ASTM) standards (ASTM A992M 2015, ASTM A1010M 2013, ASTM A709M 2016). The nominal modulus of elasticity of the steel girder $E_{s,n}$ and cover plate, $E_{s,cp,n}$ were obtained based on LRFD Bridge Design Specifications (AASHTO 2014) Section 6.4.1.

The nominal material properties listed in Table 7.4 were experimentally determined to investigate the effects of measured material properties on moment inertia and flexural strength of each specimen. The material property experiments were conducted according the ASTM standards. The material properties of reinforcement in the concrete deck were not evaluated, since its contribution to the moment inertia and flexural strength of each specimen is small under positive bending behavior. ASTM A370 (2015) and ASTM E8/E8M (2016) were followed to determine the yield strength of steel girders, $F_{y,m}$, the Young's modulus of steel girders, $E_{y,m}$, the yield strength of cover plates, $F_{y,cp,m}$, and the Young's modulus of the cover plates, $E_{y,cp,m}$. Figure 7.9 shows the dimensions of the steel coupons used to conduct both yield strength and Young's modulus experiments.



Thickness of the specimen = 0.6"

Figure 7.9. Rectangular tension coupon details

Three coupons from each specimen were tested.

Two 6 mm (≈ 0.25 in.) foil strain gauges were attached on opposite sides at the middle of each coupon. A hydraulic test machine was used to apply a tensile load to each coupon until its failure. The applied load and average strain of two strain gauges were used to develop the engineering stress-strain response for each specimen. Figure 7.10a shows a sample stress-strain response obtained during the coupon tests of Specimens A, C, and D.

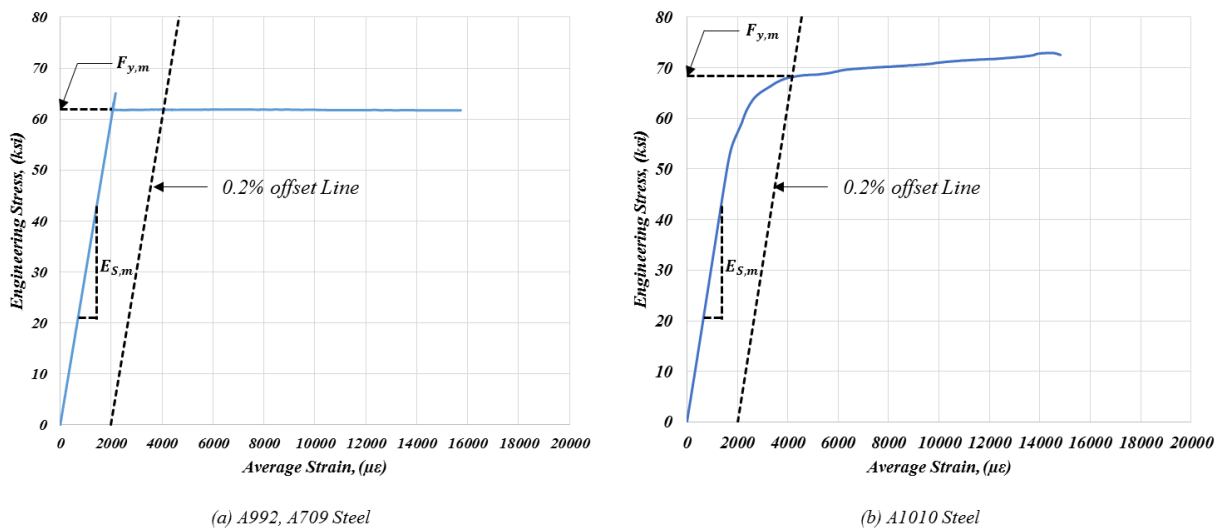


Figure 7.10. Typical applied load vs. average strain variation of a test specimen

The stress-strain curve shows a distinct yielding behavior. Figure 7.10b shows a typical stress-strain response obtained in the coupon tests of Specimen B. No distinct yielding behavior can be observed. The 0.2% offset method stated in ASTM A370 (2015) and ASTM E8/E8M (2016) was used to estimate the yield strength of the steel. The slope of the linear elastic region was used to calculate the Young's modulus of the steel. The experimentally determined material properties of steel are tabulated in Table 7.5. The average value was used in the calculations.

Table 7.5. Material test results, steel

Coupon No.	Experiment A		Experiment B		Experiment C				Experiment D			
	F_{y,m}	E_{s,m}	F_{y,m}	E_{s,m}	F_{y,m}	E_{s,m}	F_{y,cp,m}	E_{s,cp,m}	F_{y,m}	E_{s,m}	F_{y,cp,m}	E_{s,cp,m}
1	61.9	30010	68.2	31414	52.1	29884	60.5	30154	52.1	29884	60.5	30154
2	61.0	29742	68.0	31264	54.0	30161	62.2	29316	54.0	30161	62.2	29316
3	61.2	30753	70.9	31638	53.6	30010	61.0	30054	53.6	30010	61.0	30054
Average	61.4	30168	69.0	31439	53.2	30018	61.2	29841	53.2	30018	61.2	29841

The compressive strength of the concrete deck, $f'_{c,m}$ was experimentally determined based on the guidelines given in ASTM C39/C39M (2016). Following ASTM C469 (2002), a compressometer was used to experimentally determine the Young's modulus of the concrete, $E_{c,m}$. Three 4 in. diameter and 8 in. height concrete cylinders were prepared from each specimen's concrete. Each cylinder was attached to the compressometer and loaded to 40% of $f'_{c,n}$ to obtain the stress-strain response of concrete. The slope of the linear elastic region was used to calculate the Young's modulus of the concrete. Since the Young's modulus experiment is non-destructive, the same cylinders were used to measure the compressive strength of each concrete deck, $f'_{c,m}$. The cylinders were removed from the compressometer and loaded until failure. The maximum load was recorded and used to calculate the compressive strength of the concrete. The $f'_{c,m}$ and $E_{c,m}$ of each specimen are tabulated in Table 7.6. The average value was used in the calculations.

Table 7.6. Material test results, concrete

Cylinder No.	Experiment A		Experiment B		Experiment C		Experiment D	
	$f'_{c,m}$	$E_{c,m}$	$f'_{c,m}$	$E_{c,m}$	$f'_{c,m}$	$E_{c,m}$	$f'_{c,m}$	$E_{c,m}$
1	5.602	4807	6.509	6695	7.783	6280	3.710	5427
2	5.710	4621	6.460	6933	7.828	6144	3.529	5887
3	5.469	4724	6.322	6577	7.929	6019	3.740	5035
Average	5.594	4717	6.430	6735	7.847	6148	3.615	5450

Table 7.7 shows the experimentally evaluated material properties as a ratio to the nominal material properties.

Table 7.7. Measured material properties

Measured / Nominal	Specimen A	Specimen B	Specimen C	Specimen D
$f'_{c,m}/f'_{c,n}$	1.40	1.61	1.96	0.90
$E_{c,m}/E_{c,n}$	1.30	1.85	1.69	1.50
$F_{y,m}/F_{y,n}$	1.23	1.38	1.06	1.06
$E_{s,m}/E_{s,n}$	1.04	1.08	1.04	1.04
$F_{y,cp,m}/F_{y,cp,n}$	-	-	1.22	1.22
$E_{s,cp,m}/E_{s,cp,n}$	-	-	1.03	1.03

The experimentally measured material properties of Specimen A, B, and C were significantly greater than corresponding nominal material properties. The $f'_{c,m}$ of Specimen D was in the vicinity of its nominal value, because Specimen D was constructed with a weak concrete deck to simulate the deteriorated concrete deck in the field.

7.3.4. Experimental Setup and Instrumentation Plan

Figure 7.11a shows an elevation view of experimental setup of Specimen A.

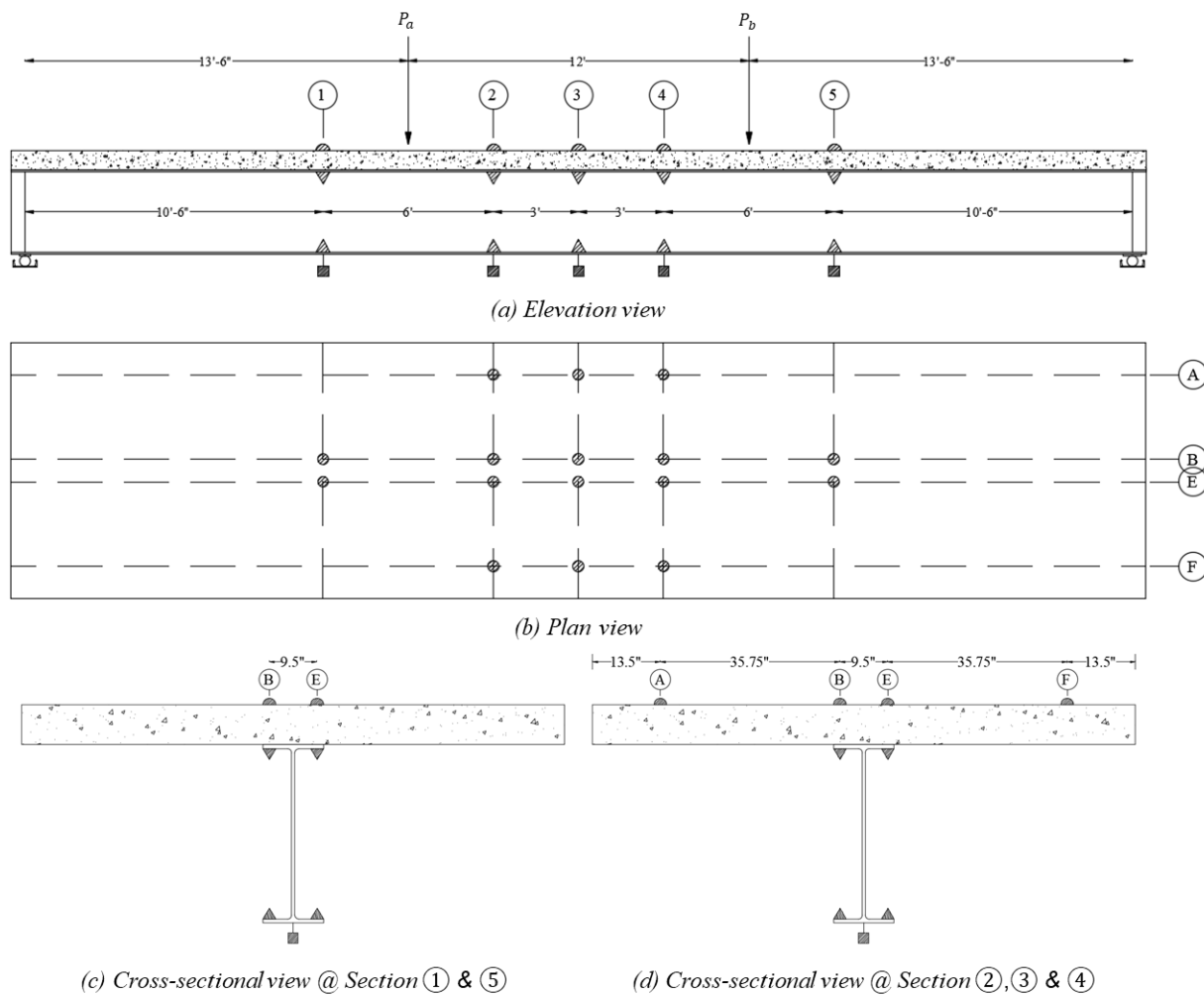


Figure 7.11. Experimental setup and instrumentation plan, Specimen A

The specimen was simply supported and two equal concentrated loads (P_a and P_b) were simultaneously applied approximately at the 1/3 span location to generate a constant moment region in the middle 1/3 of the specimen. Two sections outside the constant moment region (section 1 and section 5) and three sections within the constant moment region (section 2, section 3, and section 4) were instrumented to obtain the strain and displacement responses. Figure 7.11b shows the instrumentation plan on the concrete deck. Four foil strain gauges were placed across the width of the concrete deck at the sections within the constant moment region to obtain the strain responses and investigate the effective width of the section. Two foil strain gauges were installed at the sections outside the constant moment region to get the strain responses. As shown above, the instrumented cross sections in the transverse direction were labeled from 1 to 5, and the instrumented cross sections in the longitudinal direction were labeled as A, B, M, E, and F. The strain gauges are designated by their location, so for example, CT-A2 indicates the concrete top (CT) gauge along grid line A at section 2. During the experiment using Specimen A, no strain gauges were installed along grid line M.

Figure 7.11c and Figure 7.11d represent the instrumentation plan of cross sections outside the constant moment region and within the constant moment region, respectively. A similar labeling system was used to identify the strain gauges attached to the steel girder. For example, ST-B1 indicates the steel top flange (ST) gauge along grid line B at section 1, and SB-B1 indicates the steel bottom flange (SB) gauge along grid line B at section 1. The steel gauges and concrete gauges along the grid lines B and E were used to obtain the strain profile for each section. String potentiometers were attached to the bottom of the bottom flange at every section to measure deflection (Figure 7.11c and Figure 7.11d). Additionally, two string potentiometers were located very close to the supports (8.5 in. toward the mid-span from the support) to investigate displacements at the supports. The string potentiometers at each section were labeled from D-1 to D-5, where D stands for displacement and the number identifies the instrumented cross section.

An elevation view of the experimental setup for Specimen B is shown in Figure 7.12a.

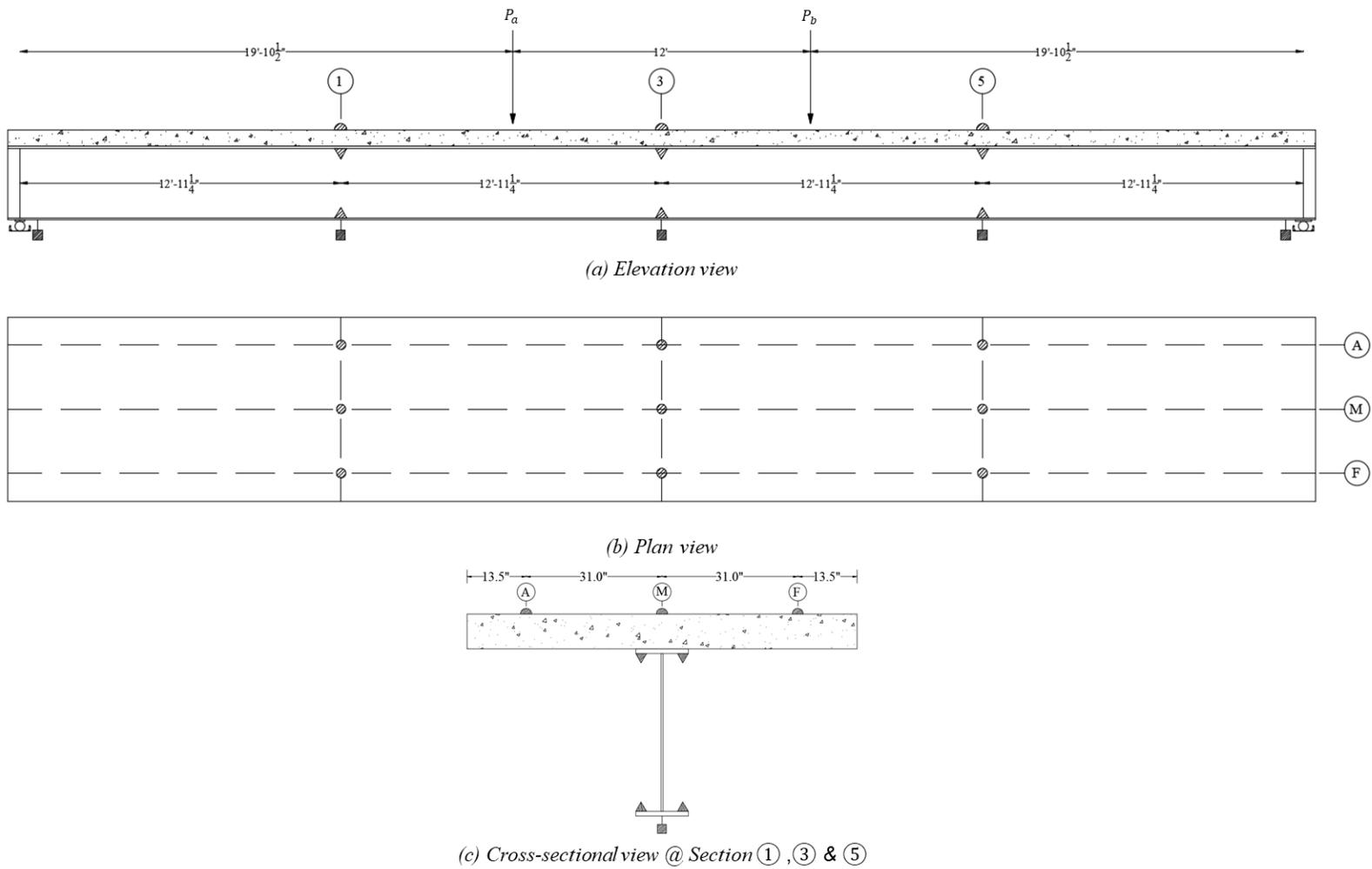


Figure 7.12. Experimental setup and instrumentation plan, Specimen B

Specimen B was simply supported and two equal concentrated loads (P_a and P_b) were simultaneously applied approximately 19 ft from each side of the beam. The two instrumented sections outside the constant moment region were labeled section 1 and section 5. The instrumented section within the constant moment region was labeled section 3. Figure 7.12b shows the instrumentation plan on the concrete deck. Three foil strain gauges were placed across the width of the concrete deck of all three cross sections to obtain the strain responses. A similar labeling system was used to identify the strain gauges on top of the concrete deck. Figure 7.12b shows the cross-sectional instrumentation plan. The average strain for each top and bottom strain gauge along grid lines B and E, and the strain data for concrete gauges along grid line M were used to develop the strain profile for each section. Similar to Specimen A, the string potentiometers were attached to the bottom of the bottom flange at every section to measure displacement (Figure 7.12b).

Figure 7.13 illustrates the instrumentation plan and loading arrangement of Specimens C and D.

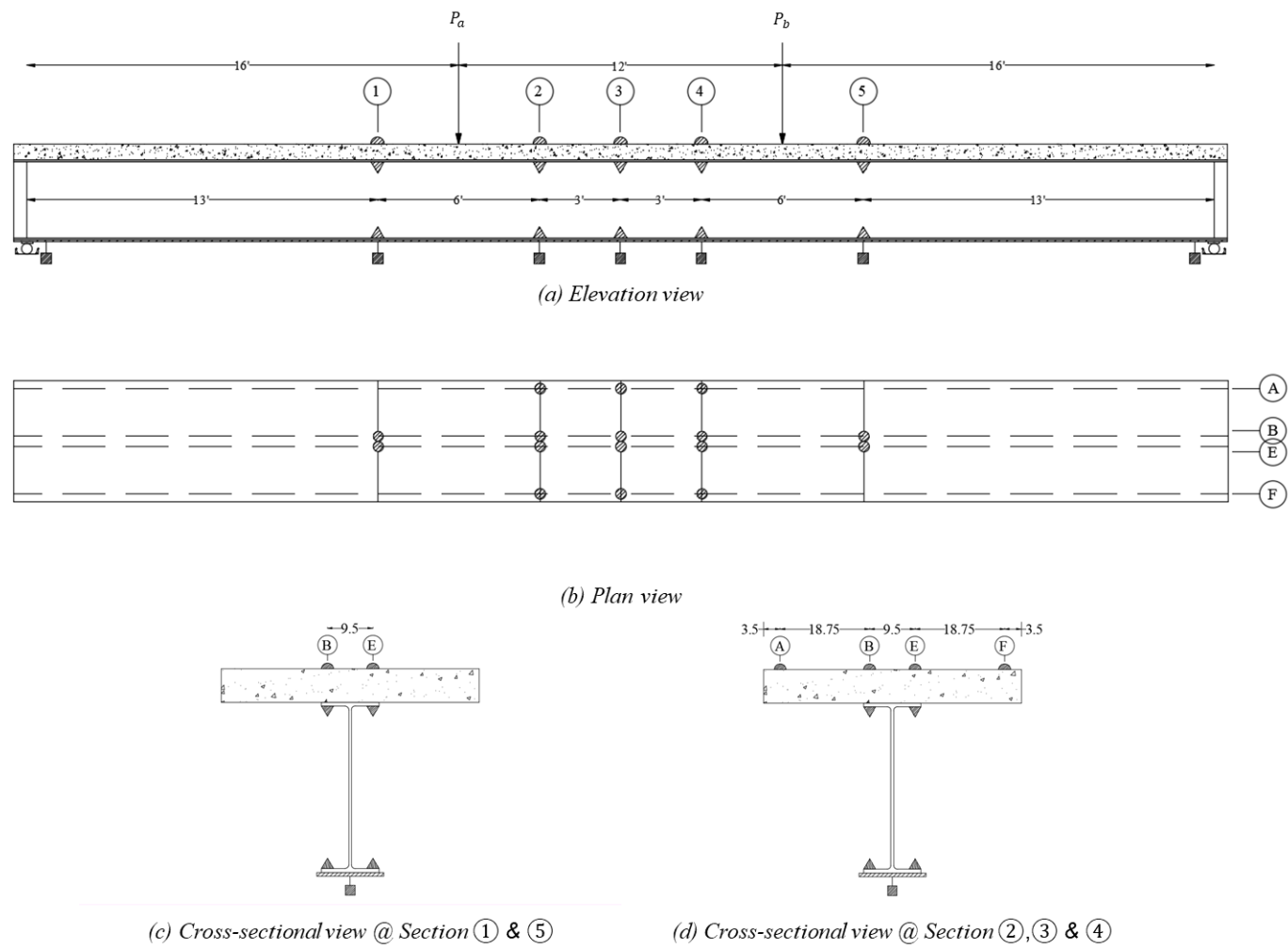


Figure 7.13. Experimental setup and instrumentation plan, Specimen C and Specimen D

The concept of the experimental setup shown in Figure 7.13 is similar to the experiment setup for Specimen A (Figure 7.11). However, the strain gauges and displacement gauges are at different locations due to the different section dimensions.

During the experiment, each specimen was loaded within the elastic limits to obtain the experimentally evaluated moment of inertia, I_{exp} , of each specimen. Later, the specimens were loaded until the failure to obtain the experimentally evaluated flexural strength, M_{exp} , of each specimen.

7.4. Moment of Inertia of a Composite Section

7.4.1. Based on Strength of Materials

When calculating the I_n of the steel-concrete composite sections, the effective width of the concrete deck plays an important role. The strain in the concrete away from the beam lags behind the strain of the concrete in the vicinity of the beam, a phenomenon known as shear-lag. Due to the shear-lag, the longitudinal stress distribution across the transverse direction of the composite section becomes non-uniform (Figure 7.14).

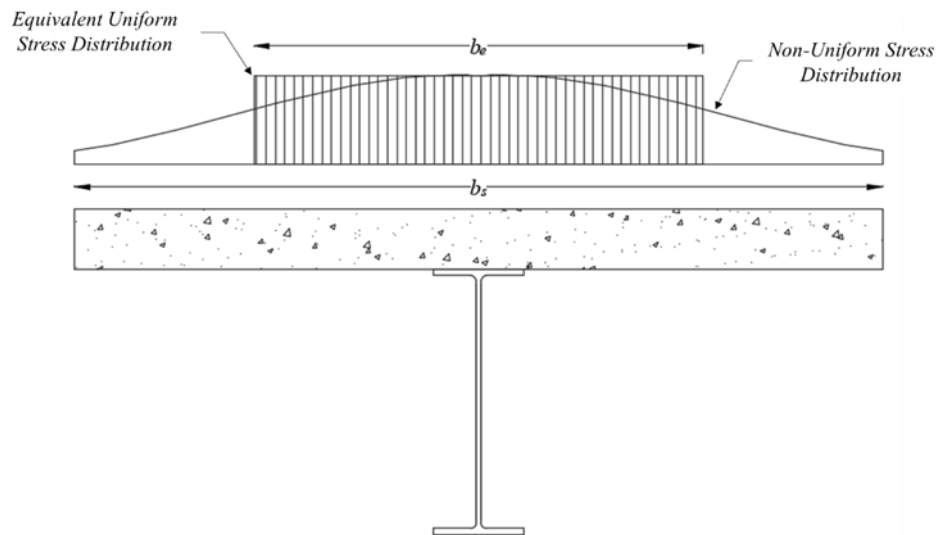


Figure 7.14. Effective width concept

The concept of effective width has been introduced to simplify the calculations, i.e., the non-uniform stress distribution is replaced by a uniform stress distribution with a reduced width of the slab, effective width, b_e (Figure 7.14).

Numerous researchers developed different simplified formulas to estimate the effective width of the steel-concrete composite sections under positive bending. Researchers have found that the effective width of a composite section primarily depends on the width of the deck (b_s), span length (L), and the loading condition of the composite section. Also, they have found that the

effective width during the elastic behavior is different from the plastic behavior. Based on an analytical investigation of several composite sections, Salama et al. (2011) proposed equation (25) to calculate the effective width of a steel-concrete composite deck in the elastic range. The b_s/L ratio of all four specimens are less than 0.25 (Table 7.3). Therefore, the full width of the concrete deck was used when calculating I_n for all four specimens.

$$b_e/b_s = 1 - 0.5(b_s/L) \text{ if } b_s/L > 0.25 \quad (25)$$

When estimating the effective width of the steel-concrete composite sections under positive bending at the ultimate limit state, Jian-Guo Nie et al. (2008) suggested that if $b_s/L < 0.5$, then the full width acts as the effective width of the section. Castro et al. (2007) also suggested the same criteria. Salama et al. (2011) have proposed equation (26) to estimate the effective width of a section at its ultimate limit state. According to the b_s/L ratios of all four specimens (Table 7.3), the deck width of every specimens is fully effective in its ultimate limit state.

$$b_e/b_s = 1 - 0.25(b_s/L) \text{ if } b_s/L > 0.25 \quad (26)$$

When calculating the I_n of the steel-concrete composite sections, the section is transformed into a single homogenous material; typically, the concrete deck is transformed into an equivalent steel deck by reducing the effective width of the deck by the ratio of E_s/E_c , which is known as the modular ratio, n , of the section. Once the steel-concrete composite section is transformed in to a homogeneous section, equation (27) can be used to calculate the neutral axis location of the cross section.

$$\bar{y} = \frac{\sum y_i A_i}{\sum A_i} \quad (27)$$

where, \bar{y} is the distance to the neutral axis from a datum; A_i is the area of a segment; and y_i denotes the centroid of each segment from the datum. For a homogeneous section within the elastic range, the location of the neutral axis coincides with the centroid of the section given that there is no axial force.

A typical steel-concrete composite section consists of at least four rectangular segments. Using parallel axis theorem, the second moment of area, or the moment of inertia of a composite section, for \bar{y} is defined in equation (28).

$$I_n = \sum \left(\frac{1}{12} b_i t_i^3 + A_i d_i^2 \right) \quad (28)$$

where, A_i is the area of each individual segment; d_i is the perpendicular distance between the centroid of each segment and the \bar{y} of the section; and b_i and t_i are the width and thickness of each rectangular segment, respectively.

7.4.2. Using Nominal Material Properties

Equation (27) and equation (28) along with the nominal section dimensions listed in Table 7.3 and nominal material properties listed in Table 7.4 were used to calculate the I_n of each specimen and tabulated in Table 7.8.

Table 7.8. The I_n of specimens

Moment of inertia, (in ⁴)	Specimen A	Specimen B	Specimen C	Specimen D
I_n	22,019	24,980	25,996	25,996

7.4.3. Using Measured Material Properties

Similarly, equation (27) and equation (28) along with the nominal section dimensions listed in Table 7.3 and measured material properties listed in Table 7.5 and Table 7.6 were used to calculate the I'_n of each specimen and listed in Table 7.9.

Table 7.9. The I'_n of specimens

Moment of inertia, (in ⁴)	Specimen A	Specimen B	Specimen C	Specimen D
I'_n	22,922	28,394	29,941	28,991

Compared to the I_n , the I'_n is significantly different due to the effects of the measured material properties of each specimen.

7.4.4. Based on Experimental Results

The moment of inertia of each composite specimen was experimentally evaluated using strain responses. The I_{exp} estimation process is somewhat similar to the I_{FEM} estimation process outlined in the current rating factor calculation process, which involves minimizing the percent error between the measured and the calculated strains or displacements by optimizing single parameter, which is the I_{exp} of the section. During each experiment, the strains were measured, ϵ_m , at the top of the concrete deck, bottom of the top flange, and top of the bottom flange of each specimen. The moment at each strain gauge location, M_m , was calculated based on the equilibrium. The distance to each strain gauge location from the neutral axis, y_m , was calculated based on the linear response of measured strains. The strain at any strain gauge location can be calculated using the theory of strength of materials principles, ϵ'_c (equation (29)), as the I_{exp} is the value to be determined.

$$\epsilon'_c = \frac{M_m y_m}{E_{s,m} I_{exp}} \quad (29)$$

The percent error between ϵ_m and ϵ'_c can be calculated using equation (30). The I_{exp} is selected such that it minimizes the percent error between ϵ_m and ϵ'_c , a procedure similar to I_{FEM} in the current load rating process explained in Section 6.1.

$$\text{Percent Error} = \frac{\sum_{\text{all gauges}} [\epsilon'_c - \epsilon_m]^2}{\sum_{\text{all gauges}} [\epsilon_m]^2} \quad (30)$$

To estimate the I_{exp} of each specimen, the loads P_a and P_b were slowly and simultaneously applied to create 40% the yield moment of each specimen at the mid-span (cross section 3). As an example, the strain responses obtained during the experiment using Specimen A is used to explain the I_{exp} calculation process. Figure 7.15a shows the variation of strain magnitude with the applied load at the top of the concrete deck at section 3 of Specimen A.

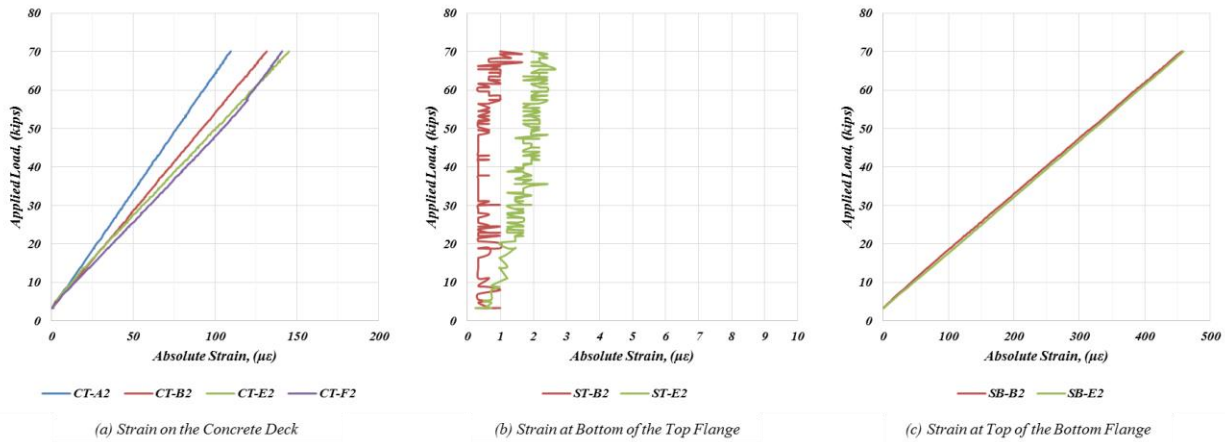


Figure 7.15. Typical strain measurements at a cross section

Figure 7.15b and Figure 7.15c show the variation of strain magnitudes of the top and bottom flange strain gauges at cross section 3 of Specimen A. Since the top flange gauges are very close to the neutral axis of the specimen, the strain responses of the top flange gauges are in the vicinity of the noise level of the strain gauges ($5 \mu\epsilon$) and were not used in the calculation process. According to Figure 7.15a and Figure 7.15c, a linear variation between measured strain versus applied load can be observed. Therefore, a single batch of strain data associated with P_a , which equals -66.77 kips, and P_b , which equals -65.14 kips, were selected for further calculations.

The strain data associated with the above loads are represented in Figure 7.16a.

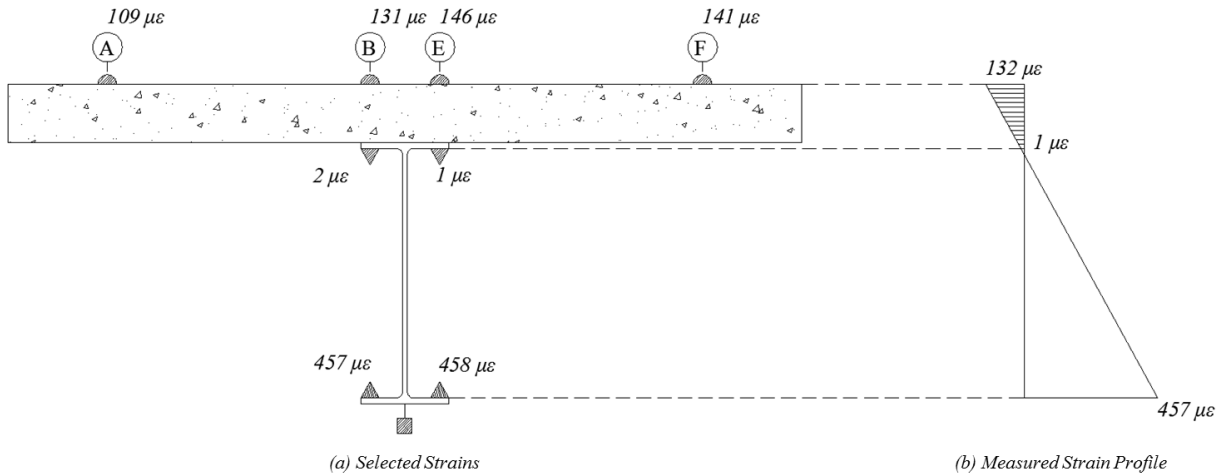


Figure 7.16. Typical strain measurements at a cross section

The strain measurements are non-uniform across the concrete deck, probably due to minor axis bending and torsional effects. The average strains were used to remove the effects of the minor axis bending and torsional effects, and Figure 7.16b shows the measured strain profile at section 3 of Specimen A. Later, the strain profile is used to calculate y_m at each section and the I_{exp} of the specimen.

The measured strains of every cross section for all four specimens are tabulated in Table 7.10 to Table 7.13.

Table 7.10. Summary of the average strains at each section, Specimen A

Specimen A Section No.	Strain ($\mu\epsilon$) at $P_a = -66.77$ kips, $P_b = -65.14$ kips			
	Concrete top (CT)		Steel bottom flange (SB)	
	ϵ_c	ϵ_m	ϵ_c	ϵ_m
1	-133	-106	424	357
2	-172	-132	545	457
3	-172	-132	545	421
4	-172	-136	545	467
5	-133	-134	424	360

Table 7.11. Summary of the average strains at each section, Specimen B

Specimen B Section No.	Strain ($\mu\epsilon$) at $P_a = -50.08$ kips, $P_b = -49.52$ kips			
	Concrete top (CT)		Steel bottom flange (SB)	
	ϵ_c	ϵ_m	ϵ_c	ϵ_m
1	-123	-86	357	322
3	-189	-138	549	468
5	-123	-85	357	301

Table 7.12. Summary of the average strains at each section, Specimen C

Specimen C Section No.	Strain ($\mu\epsilon$) at $P_a = -39.65$ kips, $P_b = -40.48$ kips			
	Concrete top (CT)		Steel bottom flange (SB)	
	ϵ_c	ϵ_m	ϵ_c	ϵ_m
1	-139	-103	207	188
2	-172	-123	255	235
3	-172	-121	255	233
4	-172	-118	255	235
5	-139	-100	207	194

Table 7.13. Summary of the average strains at each section, Specimen D

Specimen D Section No.	Strain ($\mu\epsilon$) at $P_a = -39.73$ kips, $P_b = -40.78$ kips			
	Concrete top (CT)		Steel bottom flange (SB)	
	ϵ_c	ϵ_m	ϵ_c	ϵ_m
1	-139	-104	207	201
2	-172	-134	255	245
3	-172	-156	255	247
4	-172	-139	255	236
5	-139	-118	207	184

For the purpose of comparison, the expected strain values based on nominal parameters, ϵ_c (use equation (29) with nominal parameters given in Table 7.3 and Table 7.4, and the average of P_a and P_b) are also listed in each table. The data suggest that ϵ_m is approximately 12% smaller than the ϵ_c of each specimen.

The above strain data along with equation (29) and equation (30) were used to calculate the I_{exp} of each specimen. The I_{exp} value was mathematically determined as a ratio to I_n . Variation of percent error with I_{exp}/I_n ratio for all four specimens are given in Figure 7.17, whereas the I_{exp}/I_n ratios, which minimizes the percent error, are tabulated in Table 7.14.

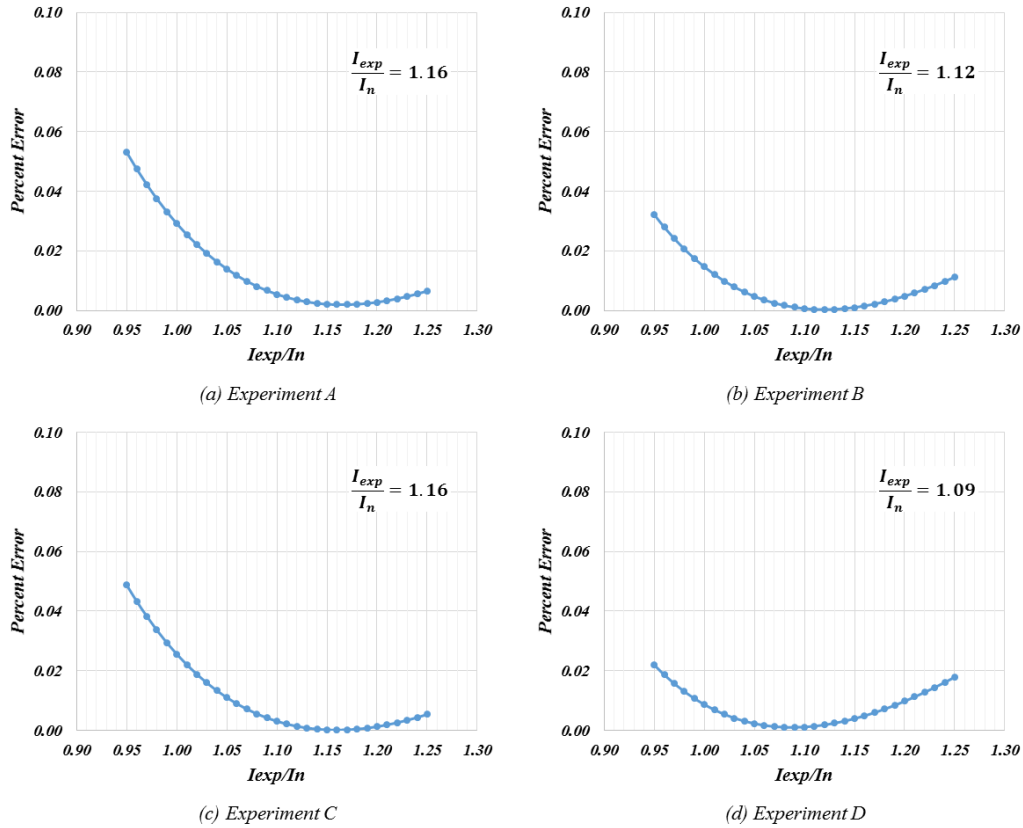


Figure 7.17. Percent error vs. I_{exp}/I_n variation

Table 7.14. The I_{exp} of the specimens

Moment of inertia, (in ⁴)	Specimen A	Specimen B	Specimen C	Specimen D
I_{exp}	25,542	27,978	30,155	28,336

According to Table 7.14, the I_{exp} value of each specimen is significantly different from I_n of the specimens.

7.5. Flexural Strength of a Composite Section

7.5.1. Based on Strength of Materials

Steel-concrete composite sections can be divided into three categories as compact, non-compact, and slender sections. Typically, compact sections can reach the maximum flexural resistance of the section at the ultimate state, which is the plastic moment capacity, M_p , of the section. Non-compact sections have a flexural strength above the yield moment, M_y , but do not reach the M_p . The slender sections will not attain M_y . Most bridges are designed to comply with the compact section limits recommended in the LRFD Bridge Design Specifications (AASHTO 2014)

Section 6.10.6.2.2, such that it can reach the maximum flexural resistance of the section at the ultimate state and reach to the M_p of the section. However, the compact sections under positive moments with a PNA close to the steel-concrete interface may not reach M_p , because part of the steel section close to the concrete-steel interface may not reach the yield stress. Based on Wittry (1993) and Yakel and Azizinamini (2005), the LRFD Bridge Design Specifications (AASHTO 2014) Section 6.10.7.1.2 states that the nominal flexural resistance of a compact section is equal to M_p if $D_p \leq 0.1D_t$, where D_t is total depth of the composite section and D_p is distance from the top of the concrete deck to the PNA. Otherwise, the flexural strength of a compact section can be calculated using equation (31).

$$M_n = M_p \left(1.07 - 0.7 \frac{D_p}{D_t} \right) \text{ if } D_p \geq 0.1D_t \quad (31)$$

According to equation (31), the flexural strength of a steel-concrete composite section primarily depends on the plastic moment capacity, location of the PNA, and total depth of the composite section. In fact, locating the PNA is the first step of determining the M_p of a composite section. Depending on possible PNA locations, seven different equations are given in LRFD Bridge Design Specifications (AASHTO 2014) Table D6.1-1 to calculate the location of the PNA of a composite section under positive bending. However, the definition of the PNA location is somewhat vague as to whether PNA is the depth to the zero-stress location or to the Whitney stress block when the PNA is at the concrete deck. Figure 7.18a shows a typical stress distribution of a composite section when the PNA is at the concrete deck.

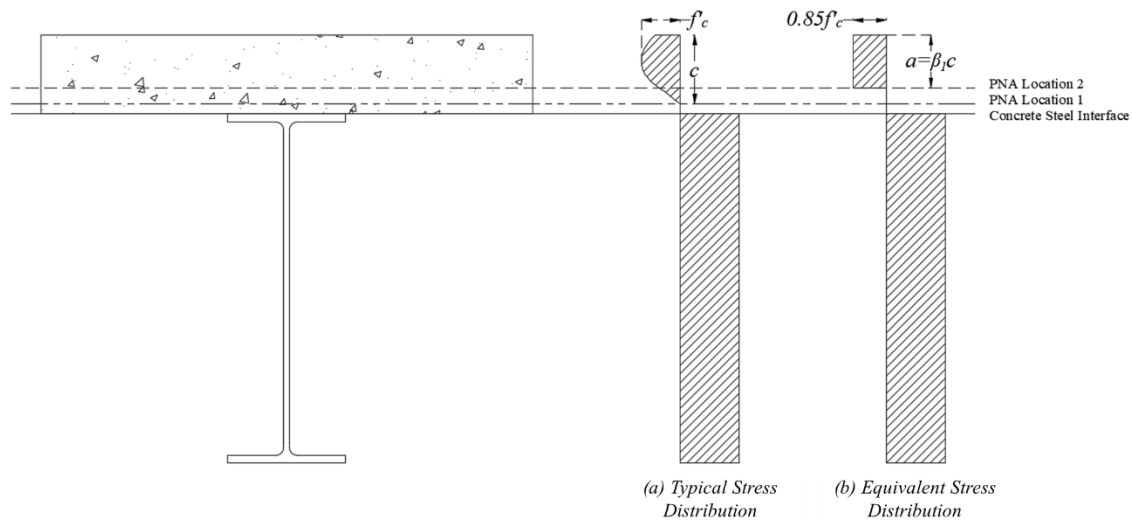


Figure 7.18. Definition of PNA location

Figure 7.18b shows the equivalent stress distribution based on both LRFD Bridge Design Specifications (AASHTO 2014) Section 5.7.2.2 and American Concrete Institute (ACI) Committee 318 Building Code Requirements for Structural Concrete (2014), hereafter referred to as ACI 318-14 Specification Section 22.2.2.4.1. Both sections define the PNA as the zero-stress location (Figure 7.18, PNA Location 1). The equations given in Table D6.1-1 of the LRFD

Bridge Design Specifications (AASHTO 2014) consider the plastic neutral axis location as depth to the stress block (Figure 7.18, PNA Location 2), which is equal to the factor β_1 times depth to the PNA Location 1. The factor β_1 depends on the f'_c of the concrete slab (LRFD Bridge Design Specifications [AASHTO 2014] 5.7.2.2. or ACI 318-14 Specification [ACI 2014] Table 22.2.2.4.3). Depending on the β_1 factor, the two PNA locations could be 35% different from each other. Although M_p of a section does not depend on the PNA location, M_n could be affected by the PNA location as it is directly related to the M_n of the section. The AASHTO method is selected for further calculations, because it is more commonly used in bridge design offices. The AASHTO method denotes the PNA by using either \bar{Y} or D_p .

Equations given in the LRFD Bridge Design Specifications (AASHTO 2014) Table D6.1-1 were used to calculate the M_p of the composite sections. In the equations, the plastic force induced in the concrete slab is calculated by using the equivalent stress block with maximum compressive strength as $0.85f'_c$ (LRFD Bridge Design Specifications [AASHTO 2014] Section 5.7.2.2). The plastic forces of the steel sections are calculated by multiplying the cross-sectional area by the yield strength of the steel. The concrete in tension and the plastic forces induced in the deck reinforcement were neglected.

7.5.2. Using Nominal Material Properties

Each specimen satisfies the compact section requirements given in the LRFD Bridge Design Specifications (AASHTO 2014) Section 6.10.6.2.2. However, the specimens cannot reach the M_p due to ductility limitations. Equation (31) along with the section dimensions given in Table 7.3 and material properties given in Table 7.4 were used to calculate the nominal flexural strength of the section and listed in Table 7.15.

Table 7.15. The PNA, M_p , and M_n of composite specimens

Parameter	Specimen A	Specimen B	Specimen C	Specimen D
D_t , (in.)	43.60	46.00	43.35	43.35
\bar{Y} or D_p , (in.)	5.36	6.58	12.13	12.13
D_p/D_t	0.12	0.14	0.28	0.28
$[1.07 - 0.7(D_p/D_t)]$	0.98	0.97	0.87	0.87
M_p , (kip-ft)	3,793	3,936	4,773	4,773
M_n , (kip-ft)	3,732	3,817	4,173	4,173

The PNA location of Specimen D is about 5 in. below the steel-concrete interface. Therefore, a significant reduction in flexural strength can be observed.

7.5.3. Using Measured Material Properties

Similarly, equation (31) along with the section dimensions given in Table 7.3 and material properties given in Table 7.5 and Table 7.6 were also used to calculate the flexural strength of each specimen and listed in Table 7.16.

Table 7.16. The PNA, M'_p , and M'_n of composite specimens

Parameter	Specimen A	Specimen B	Specimen C	Specimen D
D_t , (in.)	43.60	46.00	43.35	43.35
\bar{Y}' or D'_p , (in.)	4.69	5.59	7.20	16.73
D'_p/D_t	0.11	0.12	0.17	0.39
$[1.07 - 0.7(D'_p/D_t)]$	0.99	0.98	0.95	0.80
M'_p , (kip-ft)	4,709	5,481	5,845	5,167
M'_n , (kip-ft)	4,684	5,399	5,575	4,133

According to the results in given in Table 7.16, the M'_n shows a significant difference compared to the M_n value. This could be due to the significant difference shown in the measured material properties of each section (Table 7.7).

7.5.4. Based on Experimental Results

As the final step of the experiment program, the experimental flexural strength, M_{exp} of each steel-concrete composite specimen was determined. The loads were applied until the collapse of each specimen. The M_{exp} is defined as the maximum flexural strength right before the collapse. The M_{exp} was calculated using two different methods: (1) considering the equilibrium at ultimate and (2) using the strain profile at the ultimate.

As an example, the strain responses obtained with Specimen A are used to explain the M_{exp} calculation process. Figure 7.19a shows the variation of concrete strain with the applied load.

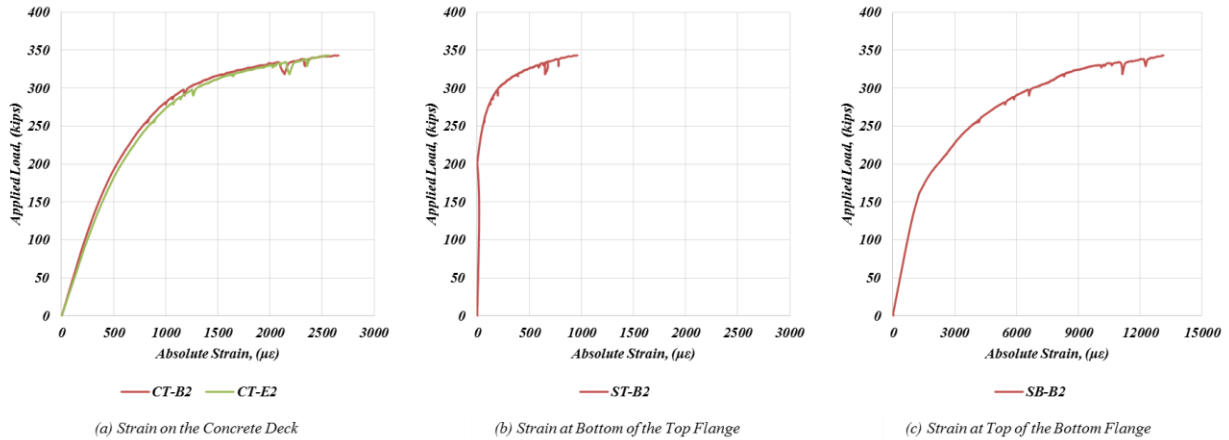


Figure 7.19. Variation of strain at each location at section 2 of Specimen A

According to Figure 7.19a, at the collapse the concrete, the strain reached to the crushing strain ($3,000 \mu\epsilon$) of the concrete. Figure 7.19b shows the variation of strain at the bottom of the top flange with the applied load, whereas Figure 7.19c shows the variation of strain at the top of the bottom flange with the applied load. The applied loads, P_a and P_b at the collapse were recorded as 342.8 kips and 346.2 kips. The average of P_a and P_b , 344.5 kips, and the distance to the loading point from the support, 13.5 ft, were used to calculate the M_{exp} of the specimen in the equilibrium method.

The strains at the ultimate loading condition ($P_a = 342.8$ kips and $P_b = 346.2$ kips) are shown in Figure 7.20a.

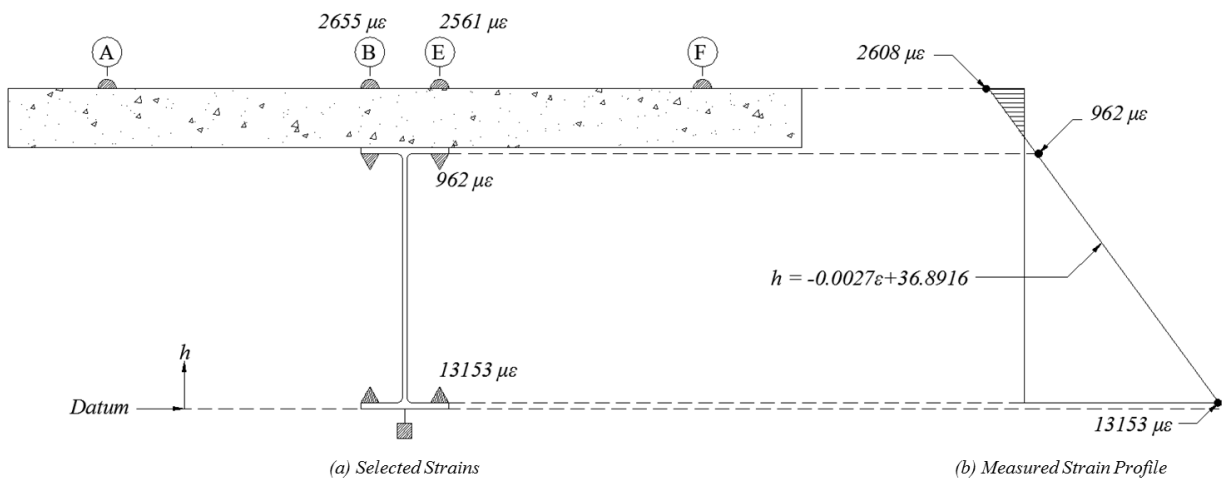


Figure 7.20. Typical strain measurements at a cross section

The average strains of the concrete gauges and the strain of steel gauges were used to develop the strain profile at the ultimate and shown in Figure 7.20b. Since the strain data are not in a

perfect linear relationship, a linear regression line was used to calculate the strains at any location of the cross section.

According to the regression line, the strain at the concrete, bottom of the top flange, and top of the bottom flange are $-2,453 \mu\epsilon$, $761 \mu\epsilon$, and $13,199 \mu\epsilon$, respectively. Typically, the strain of steel at strain hardening is $12,000 \mu\epsilon$. However, during steel material tests, no strain hardening was observed at the $12,000 \mu\epsilon$ strain level (Figure 7.10). Therefore, any possible strain hardening at the bottom flange was neglected. The stress-strain response obtained during the coupon test along with the measured strain profile of the cross section was used to develop the stress profile of the cross section (Figure 7.21).

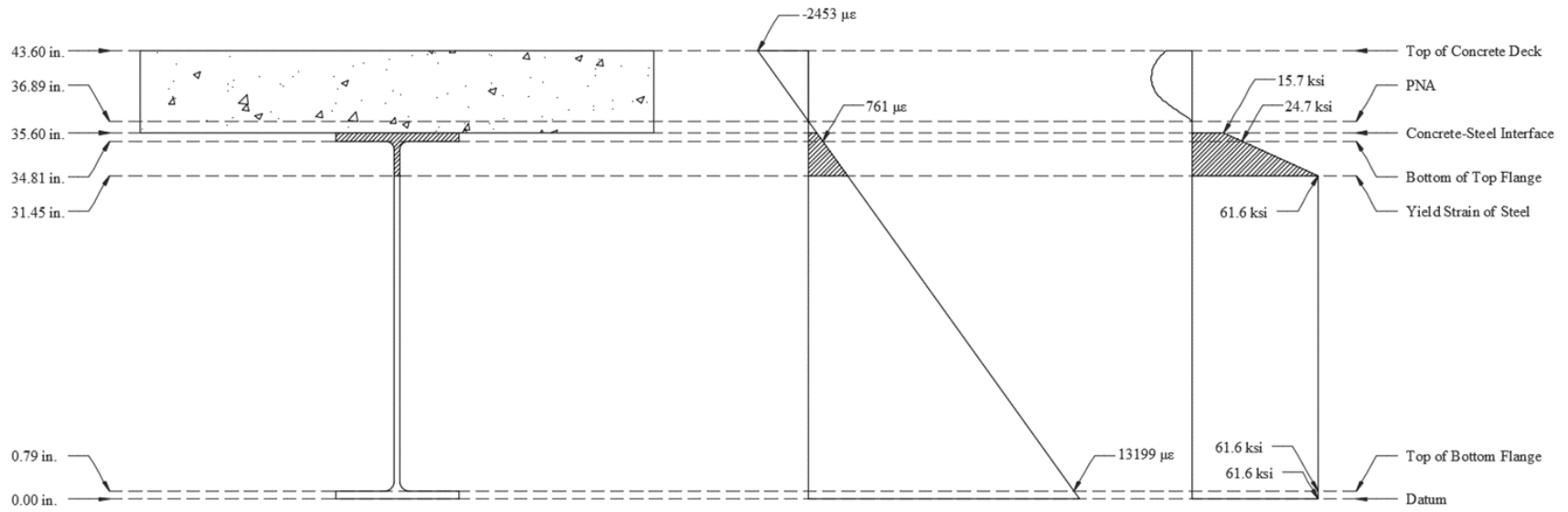


Figure 7.21. Strain and stress distribution at section 2 of Specimen A

As shown in Figure 7.21, the top flange and about 3.5 in. of the web did not reach the yield limit. The stress profile along with the steel section dimensions (Table 7.3.) were used to estimate the tensile force induced in the steel girder. Stress-strain responses were not recorded during the concrete cylinder test. In lieu of the stress-strain relationship on concrete, the Whitney rectangular stress block with maximum stress of $0.85 f'_c$ was considered to calculate the compressive force induced in the concrete deck, where the f'_c is the measured strength of the concrete. The depth of the PNA was adjusted to make the force equilibrium between tensile and compressive forces, and the distances to the plastic forces were calculated. The calculated plastic forces and distances were used to calculate the M_{exp} of the section. Strain and stress profiles used to calculate M_{exp} of each specimen are shown in Figure 7.22 to Figure 7.24.

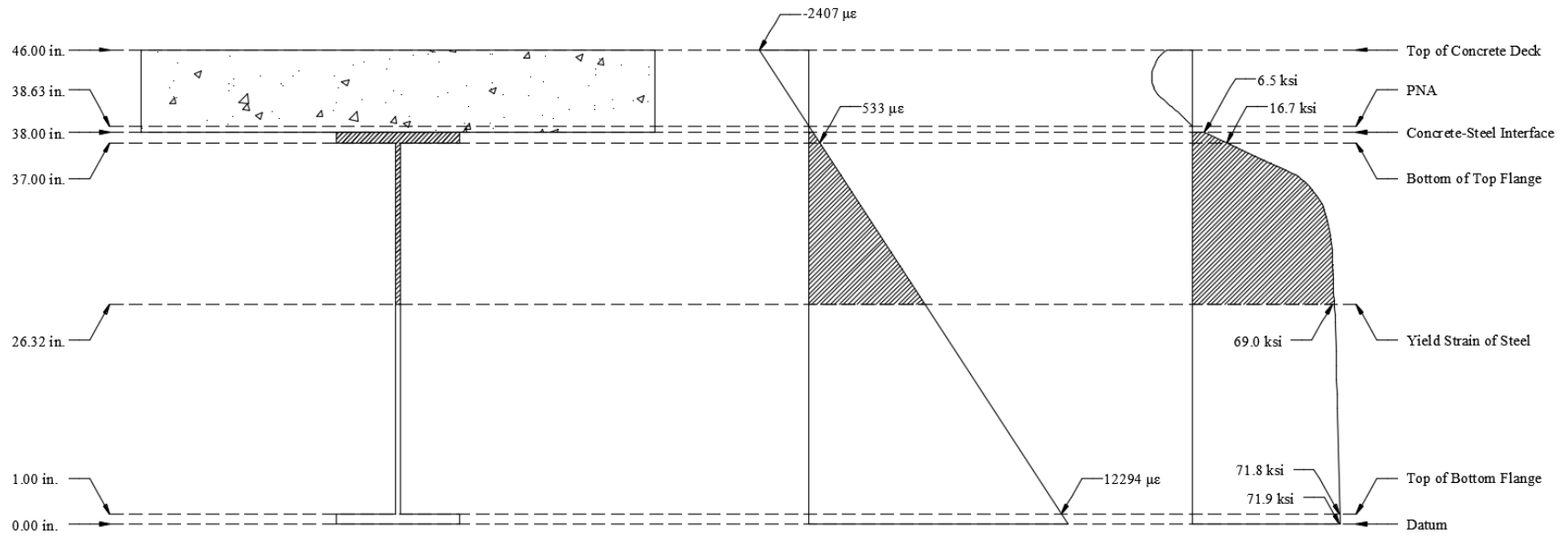


Figure 7.22. Strain and stress distribution at section 2 of Specimen B

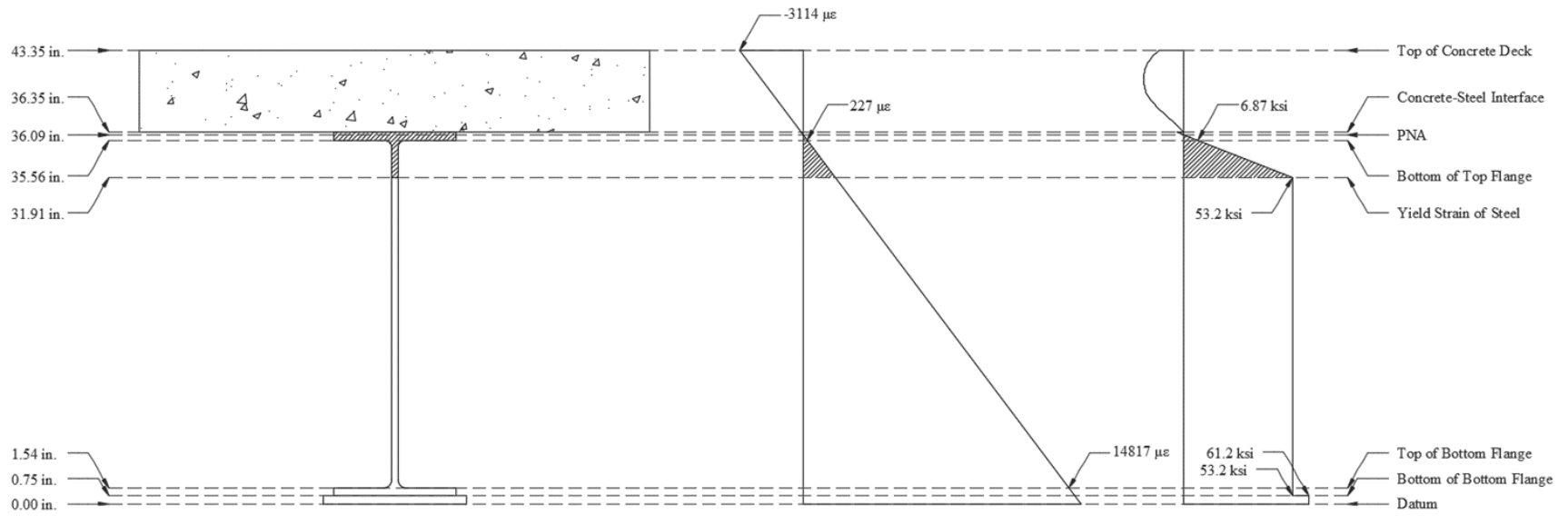


Figure 7.23. Strain and stress distribution at section 2 of Specimen C

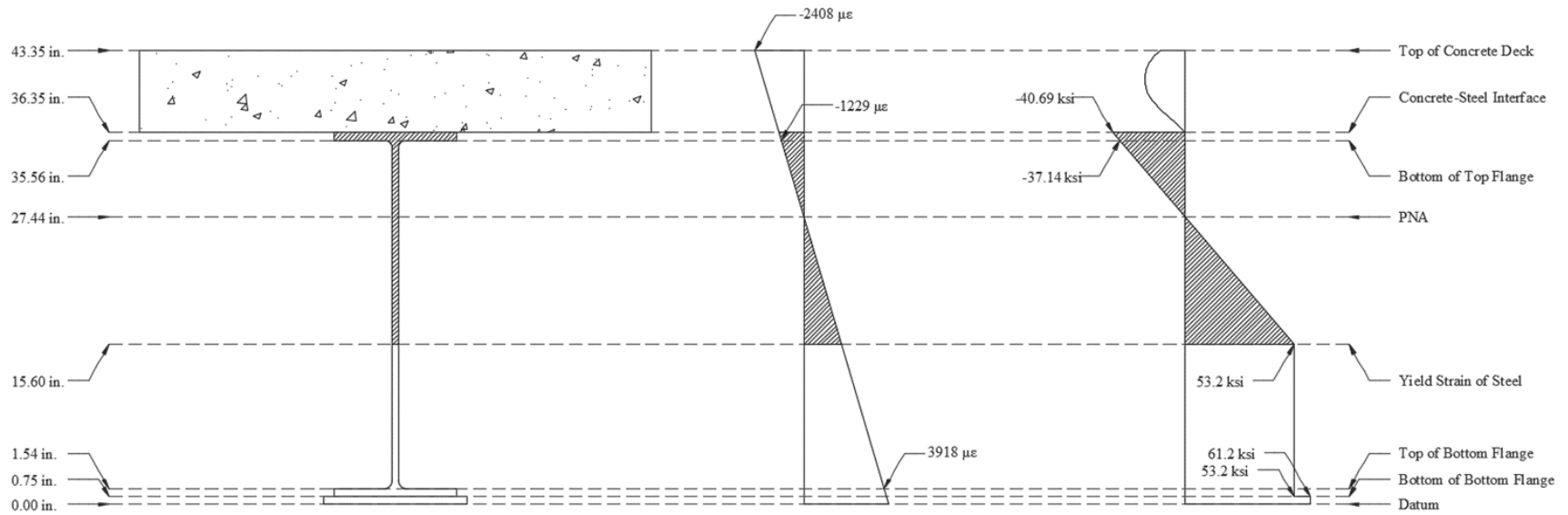


Figure 7.24. Strain and stress distribution at section 2 of Specimen D

The M_{exp} calculated based on equilibrium at ultimate and stress-strain profile are tabulated in Table 7.17.

Table 7.17. The M_{exp} of composite specimens

Average of P_a of P_b	Distance to the load from the support, (ft)	M_{exp} from the equilibrium at ultimate	M_{exp} from the strain profile at ultimate
344.5	13.5	4,651	4,586
265.3	19.875	5,273	5,447
359.4	16	5,750	5,868
310.4	16	4,966	4,510

The results from both methods are approximately the same. Compared to the nominal flexural strength, the M_{exp} values are significantly greater than the M_n values, probably due to the material properties of the section. Through the remaining report, only the M_{exp} obtained from equilibrium at ultimate is considered.

7.6. Validation of the Proposed Method

7.6.1. Relationship between Capacity and Moment of Inertia

The moment of inertia based on measured properties, I'_n , and the experimentally estimated moment of inertia, I_{exp} , are listed in Table 7.18 as a ratio to the nominal moment of inertia, I_n , of each specimen.

Table 7.18. Comparison of moment of inertia values

Specimen	$I_{exp}/I_n \approx (I_{FEM}/I_n)$	I'_n/I_n
A	1.16	1.04
B	1.12	1.14
C	1.16	1.15
D	1.09	1.12

The I_{exp} and I'_n values are significantly different compared to the I_n value of each specimen. However, the I_{exp}/I_n and I'_n/I_n ratios are approximately equal, suggesting (1) the difference between I_{exp} and I_n is due to the difference between measured and nominal material properties, and (2) the theory of strength of materials along with measured material properties can be used to accurately estimate the moment of inertia of a steel-concrete composite specimen.

Similarly, the flexural strength based on measured properties, M'_n , and the experimentally estimated flexural strength, M_{exp} , are listed in Table 7.19 as a ratio to the nominal flexural strength, M_n , of each specimen.

Table 7.19. Comparison of flexural strength values

Specimen	M_{exp}/M_n	M'_n/M_n
A	1.25	1.26
B	1.38	1.41
C	1.38	1.34
D	1.19	0.99

The M_{exp} and M'_n are significantly higher than the M_n . However, the M_{exp}/M_n and M'_n/M_n ratios are approximately the same. This suggests that (1) the difference between M_{exp} and M_n is due to the difference between measured and nominal material properties, and (2) the guidelines given in Appendix D6.1 of the LRFD Bridge Design Specifications (AASHTO 2014) can be used along with the measured material properties to get an accurate estimate of the flexural strength of the steel-concrete composite sections.

7.6.2. Improved Load Rating Factor Calculation

Figure 7.25 (same as Figure 7.7a) shows the relationship between moment of inertia and flexural strength of Specimen A.

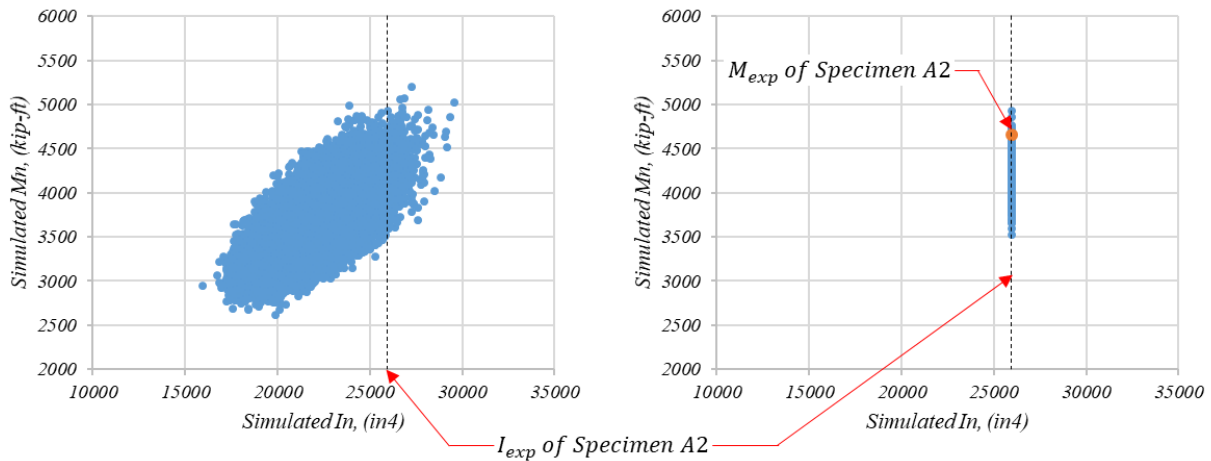


Figure 7.25. Validation of proposed procedure with Specimen A

According to Table 7.7 and Table 7.14, I_{exp} of Specimen A can be calculated as 25,542 in⁴. It is important to remember that the I_{exp} and I_{FEM} represent the same concept, which is the moment of inertia of the specimen under the existing condition at the time of the load rating. The possible flexural strength values corresponding to the I_{exp} of the specimen can be obtained from Figure

7.25, left, and shown in Figure 7.25, right. According to Figure 7.25, on average, the M_{imp} values are higher than the M_n of the section, implying that the higher the moment of inertia, the higher the flexural strength. Also, the flexural strength values corresponding to the I_{exp} of the specimen are smaller than the M_{exp} of the section.

Similarly, Figure 7.26 shows the relationship between moment of inertia and nominal flexural strength of Specimen B.

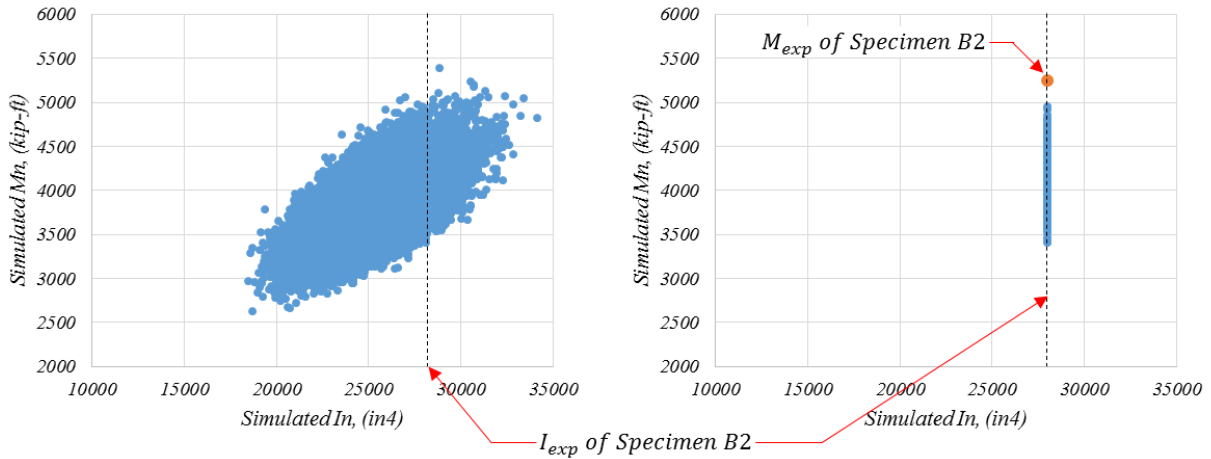


Figure 7.26. Validation of proposed procedure with Specimen B

The improved estimation for the flexural strength, (M_{imp}) corresponds to the I_{exp} of the section. According to Table 7.8 and Table 7.14, the I_{exp} of Specimen B can be calculated as 27,978 in⁴. On average, the M_{imp} values are higher than the M_n of the section. Also, the M_{exp} of the section is larger than the M_{imp} values, suggesting that the M_{imp} values can be used to improve the rating factor calculation process.

Finally, the relationship between moment of inertia and the flexural strength of Specimen C and Specimen D are shown in Figure 7.27.

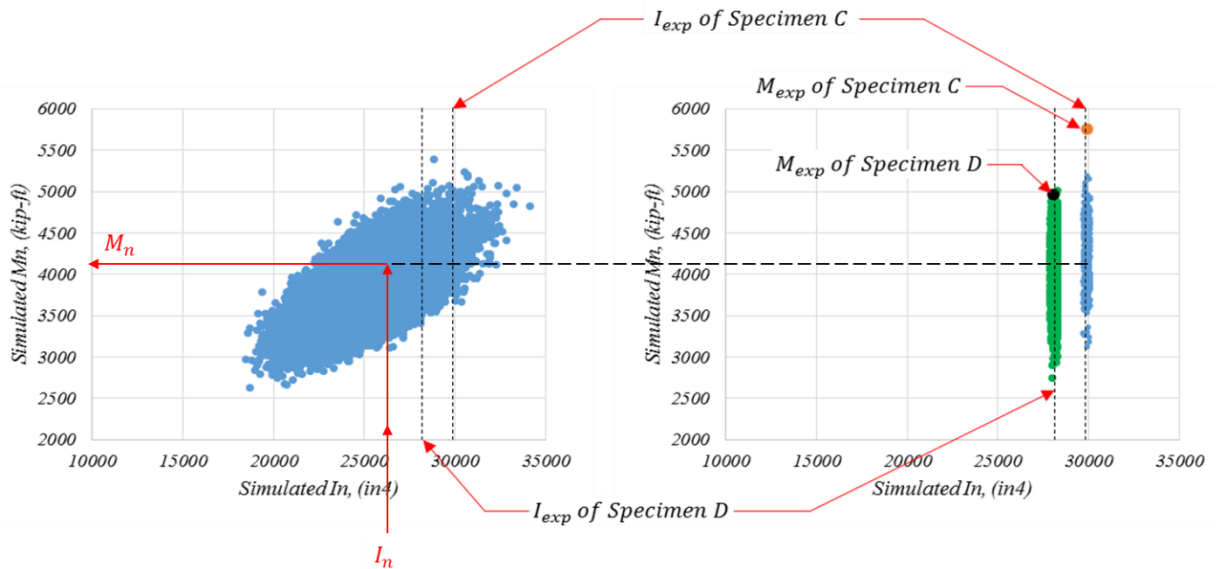


Figure 7.27. Validation of proposed procedure with Specimen C and Specimen D

Both Specimens C and D had the same relationship due to the same nominal properties of the specimen. However, due to the different measured concrete strength, Specimen C has a higher I_{exp} value than the I_{exp} value of Specimen D. The M_{imp} values corresponding to the I_{exp} of Specimen C show a larger value compared to M_n and significantly lower than the M_{exp} of the specimen. The I_{exp} of Specimen D is smaller than the I_{exp} of Specimen C, which means the M_{imp} values are smaller than the M_{imp} values. Again, this suggested that there is a trend, such that when flexural strength increases, the moment of inertia increases and vice versa. Also, the M_{exp} of Specimen D is higher than the M_{imp} values of the section.

The above results show that the I_{exp} of each specimen can be used in combination with a Monte Carlo simulation to obtain an improved flexural strength of a steel-composite section. Since the I_{exp} is calculated similar to the I_{FEM} calculation process, the I_{FEM} can be used to obtain an improved flexural strength of a bridge without doing a destructive test and interrupting the traffic on the bridge.

7.7. Summary and Conclusions

7.7.1. Summary

The load rating factor is a measurement DOTs use to describe the load carrying capacity of a bridge, issue permits to heavy trucks, and to determine load postings on bridges. It helps to increase safety by reducing the risk of structural damage and collapse. According to AASHTO's Manual for Bridge Evaluation, the rating factor of a bridge can be calculated in two ways: (1) non-destructive load rating method and (2) analytical load rating method. The non-destructive load rating method represents a realistic value for a bridge under existing conditions, because it involves load tests on bridges in the field. However, the load tests typically require traffic

closures. The BEC has developed a method to improve the non-destructive load rating method using continuous SHM data from an actual bridge site that does not require traffic disruptions. In the current load rating factor calculation approach, the BEC calculates the live load moments and dead load moments using health monitoring data. However, the M_n is based on the nominal section dimensions and material properties of the bridge and may not represent the actual capacity of the bridge or its elements. The objective of the present research study was to further improve the rating factor calculation process by estimating an improved flexural strength for composite sections. The research team suspected that there was a relationship between moment of inertia and flexural strength of composite sections. The idea, then, was to use the I_{FEM} from the current load rating process to get an improved estimate of the flexural strength.

To validate the project hypothesis related to capacity estimation, an experimental program was conducted at the ISU Structural Engineering Research Laboratory. Four steel-concrete composite sections were used to obtain the experimentally evaluated moment of inertia of the section and flexural strength, such that the research team could (1) develop a relationship between moment of inertia and flexural strength of steel-concrete composite sections and (2) validate the use of I_{FEM} to get an improved flexural strength of steel-concrete composite sections. The beams were simply supported, and two concentrated loads were applied to create a constant moment region over the middle of the beam. Instrumentation of the beams consisted of strain gauges on the top of the concrete deck, top flange of the steel girder, and bottom flange of the steel girder. Also, displacement gauges were attached to the bottom of each beam.

To calculate the I_{exp} , each specimen was loaded to 40% of the expected yield moment. The strain responses and the measured parameters along with the beam theory was used to calculate the calculated strain. The percent error between the calculated strains and the measured strain were minimized by optimizing the moment of the inertia of the section. Both strain gauge data and displacement data were used to calculate and compare the I_{exp} results. As expected, the I_{exp} values are significantly higher than the I_n of each specimen. Then, loads were applied to each beam until failure of each specimen to obtain the experimentally determined strength of the section. The M_{exp} of each section was significantly higher than the M_n of the section.

According to the experimental results, the theory of strength materials and the guidelines given in Appendix D6.1 of the LRFD Bridge Design Specifications (AASHTO 2014) along with the actual material properties (if available) of the bridge can be used to evaluate the moment of inertia and the flexural strength of the steel-concrete composite sections. However, in lieu of existing properties of bridge components, the Monte Carlo simulation was used to develop a relationship between moment of inertia and flexural strength of steel-concrete composite sections. The improved flexural strength was noticeably higher than the nominal strength and the improved strength is smaller than the measured ultimate strength of each section thereby giving improved but conservative estimates.

7.7.2. Conclusions

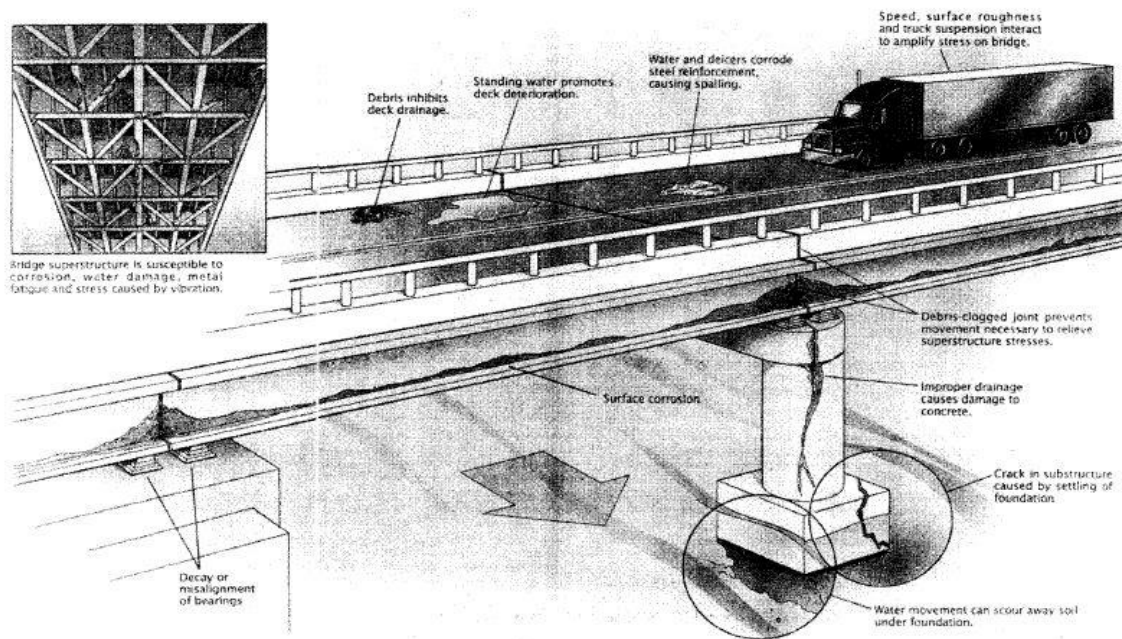
The experimental results show that the moment of inertia and the flexural strength of steel-concrete composite sections calculated based on nominal material properties are significantly different than the actual moment of inertia and the flexural strength of the section. Therefore, the load rating factor calculated using nominal values underestimates the rating factor of bridges by 20% to 40%. The experimental results indicated that the theory of strength of materials and the AASHTO guidelines along with actual material properties (when available) can accurately predict the moment of inertia and flexural strength of the section. In the absence of actual material properties, a Monte Carlo simulation along with the I_{exp} from the calibrated load rating model may significantly improve the rating factor of a bridge.

CHAPTER 8. PREDICTION OF FUTURE BRIDGE CONDITION RATINGS

8.1. Introduction

According to the Manual for Bridge Evaluation (AASHTO 2015), a bridge is defined as a structure that supports moving loads with a length more than 20 ft over obstructions, such as water, highway, or railway. Elements of a typical bridge can be grouped into three primary components: (1) deck, (2) superstructure, and (3) substructure. The deck of a bridge is defined as the component that directly carries the moving loads. The superstructure is defined as the component that supports the deck and connects to the substructure. The superstructure consists of every element below the deck and above the bearings. The substructure is responsible for support of both deck and superstructure of the bridge and responsible for distributing loads to the ground. The substructure consists of every element below the bearings, including diaphragm, piers, and components of the foundation. The wing walls and the abutments of a bridge are also considered as substructure components.

Bridges are continuously exposed to the environment and dynamic loading effects due to moving loads. Therefore, bridges can deteriorate relatively quickly. Figure 8.1 shows the leading causes of typical bridge deterioration.



Dunker and Rabbat 1993 (taken from Ramey and Wright 1997), © 1993 Scientific American

Figure 8.1. Causes of deterioration of a typical bridge

Hairline cracks on a bridge deck propagate due to freeze-thaw effects of water, which seeps through the hairline cracks. Also, the water and deicing salt inside the cracks accelerate corrosion of the deck reinforcement. Ineffective drainage systems could accelerate the corrosion of superstructure and substructure. Debris clogged inside the joints may prevent the intended degree

of freedoms that leads to misalignment such that the structure may not be able to release the necessary stresses. Scour damages the foundation and washes away the soil under the foundation causing excessive settlements of the bridge. The continuous dynamic effects, especially from the moving heavy traffic, amplify the stresses and may induce fatigue damage.

Bridge deterioration is a critical problem in the US. According to the infrastructure report card of ASCE (2017), as of 2016, out of 614,387 bridges in the US, almost 1 in 11 (9.1%) bridges are rated as structurally deficient. A structurally deficient bridge is defined as a bridge with a condition rating of 4 or less for either the deck, superstructure, or substructure, where the condition rating is a condition assessment scale from 0 to 9, where 0 is the failed condition and 9 is the excellent condition. Structurally deficient bridges are not necessarily unsafe to the traffic, but they can quickly become unsafe without proper inspection and maintenance. Even though high-traffic volume bridges may have a lower probability of being structurally deficient, in 2016 an average of 188 million trips per day were recorded on structurally deficient bridges (ASCE 2017). Figure 8.2 shows the total number of bridges and total number of structurally deficient bridges in the US from 2002 to 2012.

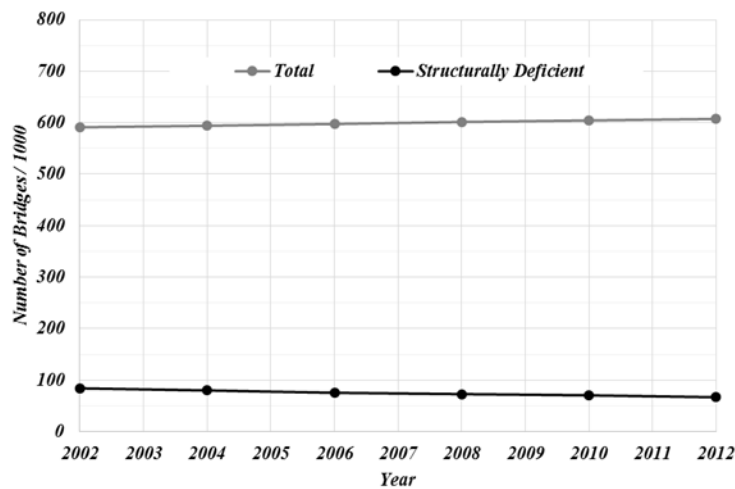


Figure 8.2. Statistical data of structurally deficient bridges in the US

As the number of bridges increases, the number of structurally deficient bridges decrease. However, out of 600,000 bridges, approximately 100,000 (1/6) are still rated as structurally deficient.

Figure 8.3 illustrates the condition of each bridge component in 2012.

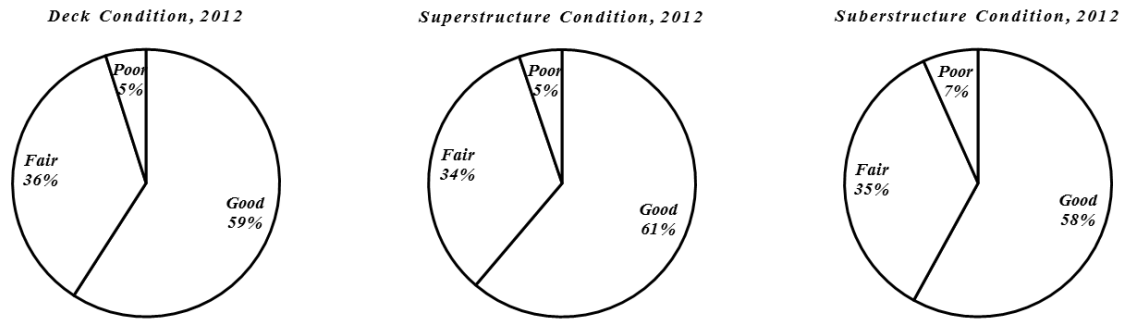


Figure 8.3. Condition of each bridge component in the US in 2012

The bridge components with condition rating greater than 6 are classified as good, while the bridge components with condition rating lower than 5 are classified as poor. The bridge components with a condition rating of 5 and 6 are classified as fair. According to Figure 8.3, about 40% of each bridge component has a condition rating of 6 or less, which implies that there are a large number of bridges getting closer to the structurally deficient limits.

The design life of many bridges was originally 50 years. The average age of a bridge in the US is 43 years. Figure 8.4 shows the percentage of bridges in different age groups and the portion of structurally deficient bridges in each age group.

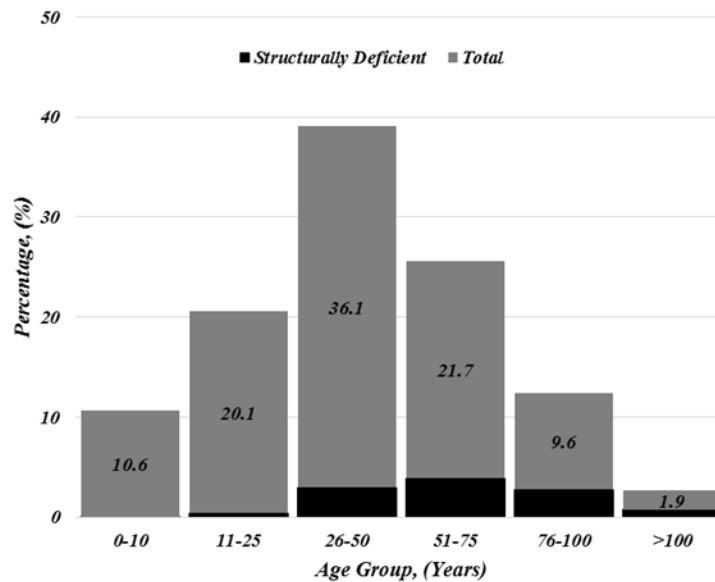


Figure 8.4. Statistical data of structurally deficient bridges in US

According to Figure 8.4, approximately 4 out of 10 (40%) bridges are older than 50 years. As of 2016, the American Society of Civil Engineers estimates that rehabilitation of these bridges could cost about \$123 billion, suggesting that even though there is a high repair and maintenance demand, available resources are very limited.

This indicates the necessity of proper bridge management plans to keep the nation's transportation system functioning. Predicting future conditions and estimating the remaining service life are important so that owners can prioritize repair and maintenance activities while minimizing the required resources. According to the literature, many researchers carried out different methods to develop future condition rating prediction models. Each method has its own limitations. However, it may be noticed that the best way to predict the future behavior to estimate the remaining service life is to use the NBI bridge condition rating database.

8.2. Historical Behavior of Bridges in the US

8.2.1. National Bridge Inventory Database

The NBI database contains historical bridge condition information for bridges in the US. The NBI database was created after the Silver Bridge collapse in 1967, which was used to connect the Ohio and West Virginia across the Ohio River. After the incident, the FHWA mandated that every state maintain records of their bridges regarding its (1) geometric properties, such as span length, width of the deck, etc.; (2) operational conditions that include the traffic volume and age of the bridge; and (3) condition of every component of the bridges with physical inspections. Currently, DOTs in each state commonly conduct three types of inspections, namely (1) initial inspection, (2) routine inspection, and (3) in-depth inspection. The initial inspection of a bridge is conducted after the construction or rehabilitation of the bridge to establish a baseline for the bridge condition and identify any problems that may exist. Routine inspections are performed at intervals not less than 24 months. The inspection interval can be increased up to a maximum of 48 months with written FHWA approval only if past inspection analysis justifies it. The in-depth inspections are carried out independent of the scheduled routine inspections to identify any problems that cannot be identified during the routine visual inspections.

Typically, the initial inspection and routine inspections are visual inspections. According to Recording and Coding Guide for the Structure Inventory and Appraisal of the Nation's Bridges, hereafter referred to as the NBI Coding Guide (FHWA 1993), concrete decks should be inspected for possible cracks, scaling, spalling, leaching, chloride contamination, potholes, delamination, and full-depth and partial-depth failures. The condition of the wearing surface, joints, expansion devices, curbs, sidewalks, and parapets are not considered in evaluating the overall deck condition. Also, decks integral with the superstructure are rated as a deck only and not how they may influence the superstructure rating. The superstructures are inspected for signs of distress, which may include cracking, deterioration, section loss and malfunction, and misalignment of bearings. Except in extreme situations, the conditions of bearings, joints, and paint systems are not included in the superstructure condition ratings. When the deck is integral with the superstructure, the superstructure condition rating may be affected by the deck condition. All substructure elements should be inspected for visible signs of distress including cracking, section losses, settlement, misalignments, scour, collision damages, and corrosions of piers, abutments, piles, footings, or other components. Substructure rating is independent of the deck and superstructure ratings.

During the initial and routine inspections, the condition of each component of the bridge is rated according to the condition rating system given in Table 8.1.

Table 8.1. Description of condition ratings for deck, superstructure, and substructure

Code	Rating	Description
N	Not applicable	
9	Excellent condition	
8	Very good condition	No problems noted.
7	Good condition	Some minor problems.
6	Satisfactory condition	Structural elements show some minor deterioration.
5	Fair condition	All primary structural elements are sound, but may have minor section loss, cracking, spalling, or scour.
4	Poor condition	Advanced section loss, deterioration, spalling, or scour.
3	Serious condition	Loss of section, deterioration, spalling, or scour have seriously affected primary structural components. Local failures are possible. Fatigue cracks in steel and shear crack in concrete may be present.
2	Critical condition	Advanced deterioration of primary structural elements. Fatigue cracks in steel or shear cracks in concrete may be present or scour may have removed substructure support. Unless closely monitored, it may be necessary to close the bridge until corrective action is taken.
1	“Imminent” failure condition	Major deterioration or section loss present in critical structural components or obvious vertical or horizontal movement affecting structure stability. Bridge is closed to traffic, but corrective action may put back in light service.
0	Failed condition	Out of service, beyond corrective action.

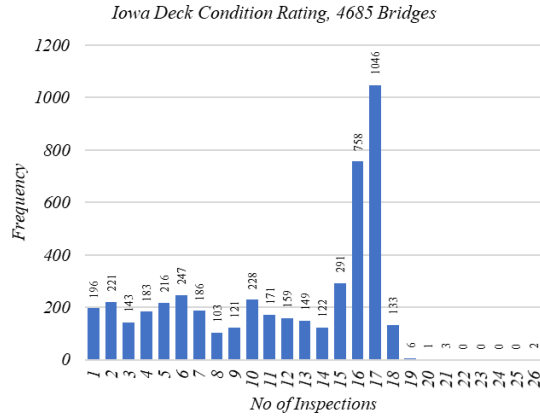
The rating system scale ranges from 0 to 9 on an integer scale, where condition rating 0 represents a failed condition and condition rating 9 represents an excellent condition. As mentioned in Section 8.1, a bridge with either deck, superstructure, or substructure rating of 4 or less is defined as a structurally deficient bridge.

8.2.2. Historical Bridge Condition Statistics, Iowa and Wisconsin

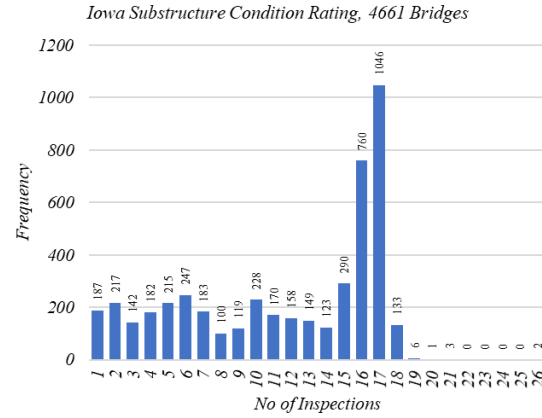
The NBI condition rating database is the best available database to describe the historical condition of bridges in the US. Though the NBI condition rating database was started around 1970, the condition rating data are available from 1982 for the interstate bridges in Iowa and the condition rating data are available from 1990 for the interstate bridges in Wisconsin. The NBI condition rating histories of both Iowa and Wisconsin bridge components were analyzed to

understand any possible trend of each bridge component in each state. The analysis results were also used to strengthen the results of future condition rating prediction models.

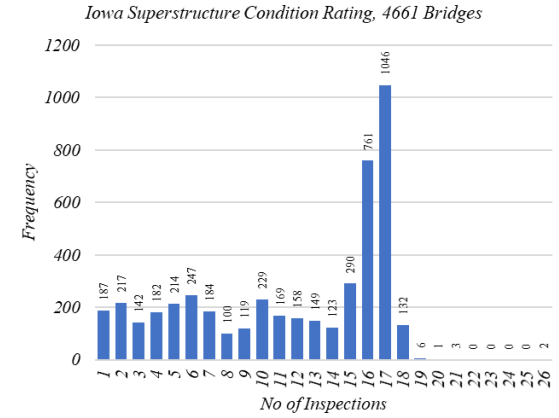
Figure 8.5 shows the frequency of inspection of each bridge component during last three decades.



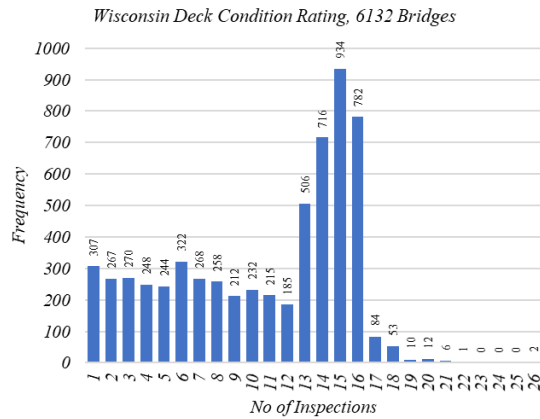
(a)



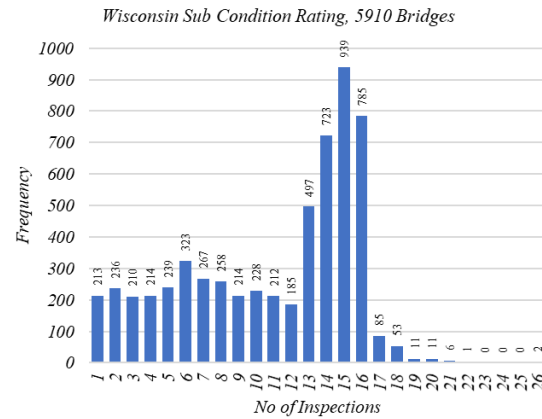
(b)



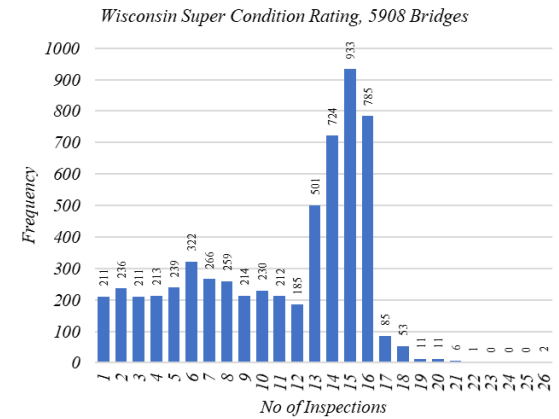
(c)



(d)



(e)

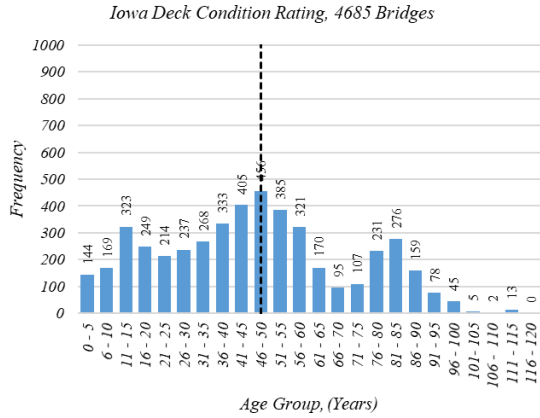


(f)

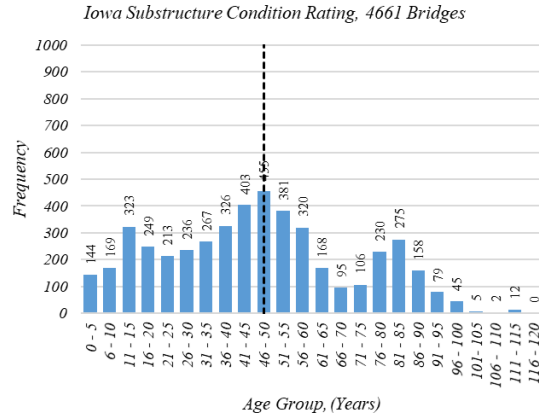
Figure 8.5. Frequency vs. number of inspections for bridges in Iowa and Wisconsin

There was no significant difference between any of the bridge components in both the Iowa and Wisconsin databases. According to Figure 8.5, more than 65% of bridges had at least 10 inspections during last three decades. This implies that these condition rating histories describe around 1/3 of bridge life; hence, these condition rating histories may be useful in predicting future bridge conditions.

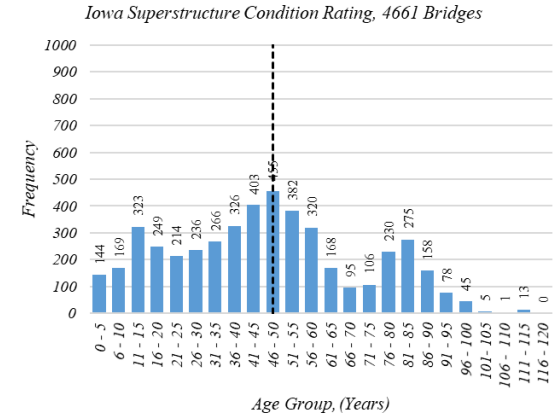
Figure 8.6 illustrates the frequency of each bridge component in five-year age groups.



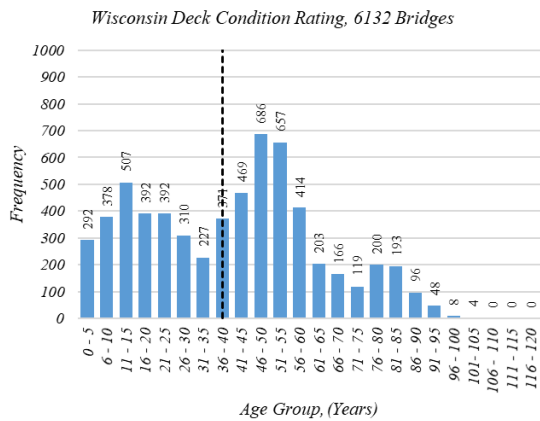
(a)



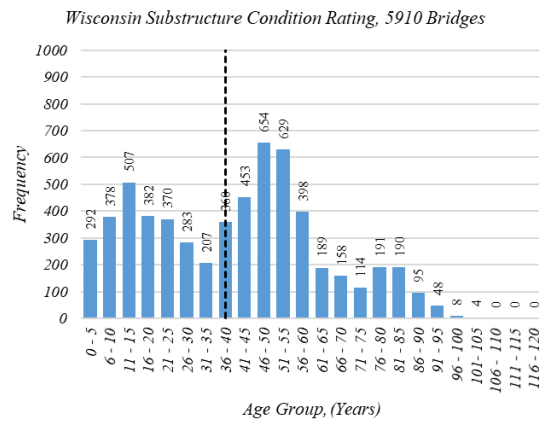
(b)



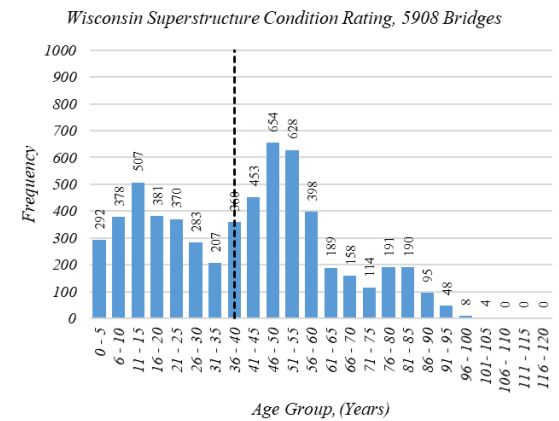
(c)



(d)



(e)



(f)

Figure 8.6. Frequency vs. age group for bridges in Iowa and Wisconsin

There was no significant difference between the histograms for each bridge component in the Iowa condition rating database. Similarly, there was no noticeable difference between the histograms for each bridge component in the Wisconsin condition rating database.

However, the histograms of the Iowa condition rating data and the Wisconsin condition rating data showed a significant difference. The average age of any Iowa bridge component is about 46.0 years, whereas the average age of any Wisconsin bridge component is about 38.5 years. The age of the Iowa bridges is greater than the average age of the nation's bridges (43 years). The age of the Wisconsin bridges is younger than the average age of the nation's bridges. Also, the ASCE Infrastructure Report Card (2017) ranked Iowa as the state with highest number of structurally deficient bridges.

Figure 8.7 shows the percentage of each condition rating number given to each bridge component over the last three decades for both Iowa and Wisconsin bridges.

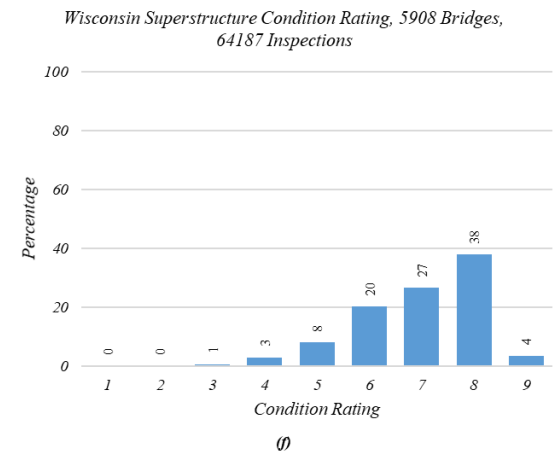
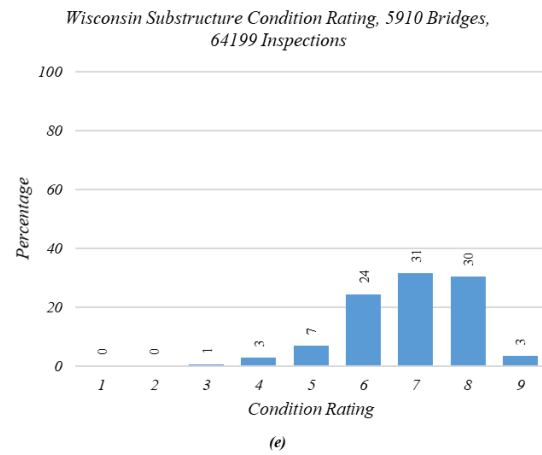
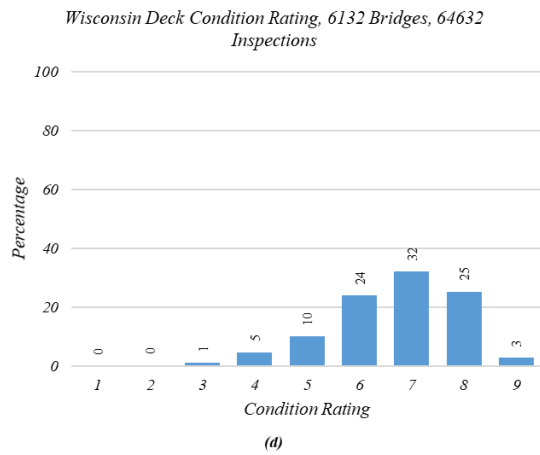
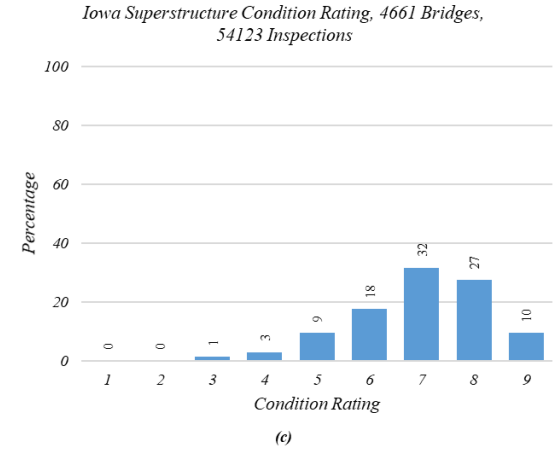
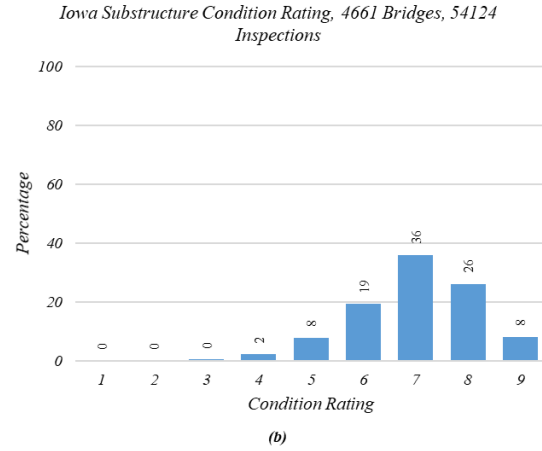
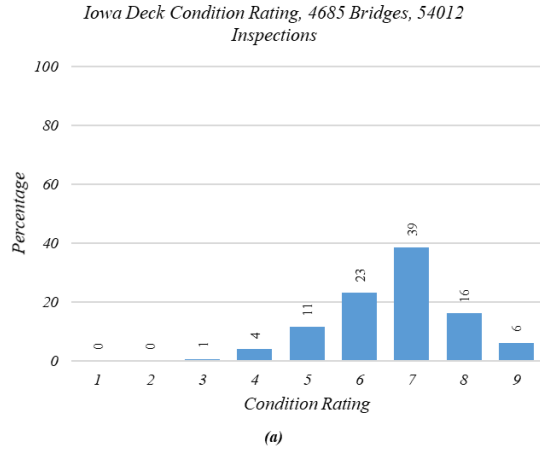


Figure 8.7. Percentage vs. condition rating for bridges in Iowa and Wisconsin

According to Figure 8.7, most of the bridge decks in both Iowa and Wisconsin were at condition rating 7. Most of the superstructures and substructures in both Iowa and Wisconsin were at condition rating 7 or condition rating 8. This implies that the deck deteriorates somewhat faster than the substructure and superstructure, probably because the bridge decks are continuously and directly exposed to both traffic and environmental changes. Figure 8.7 also shows that few bridges are at condition rating 3 or less.

Figure 8.8 illustrates the age span of each condition rating for all bridge components in both Iowa and Wisconsin databases.

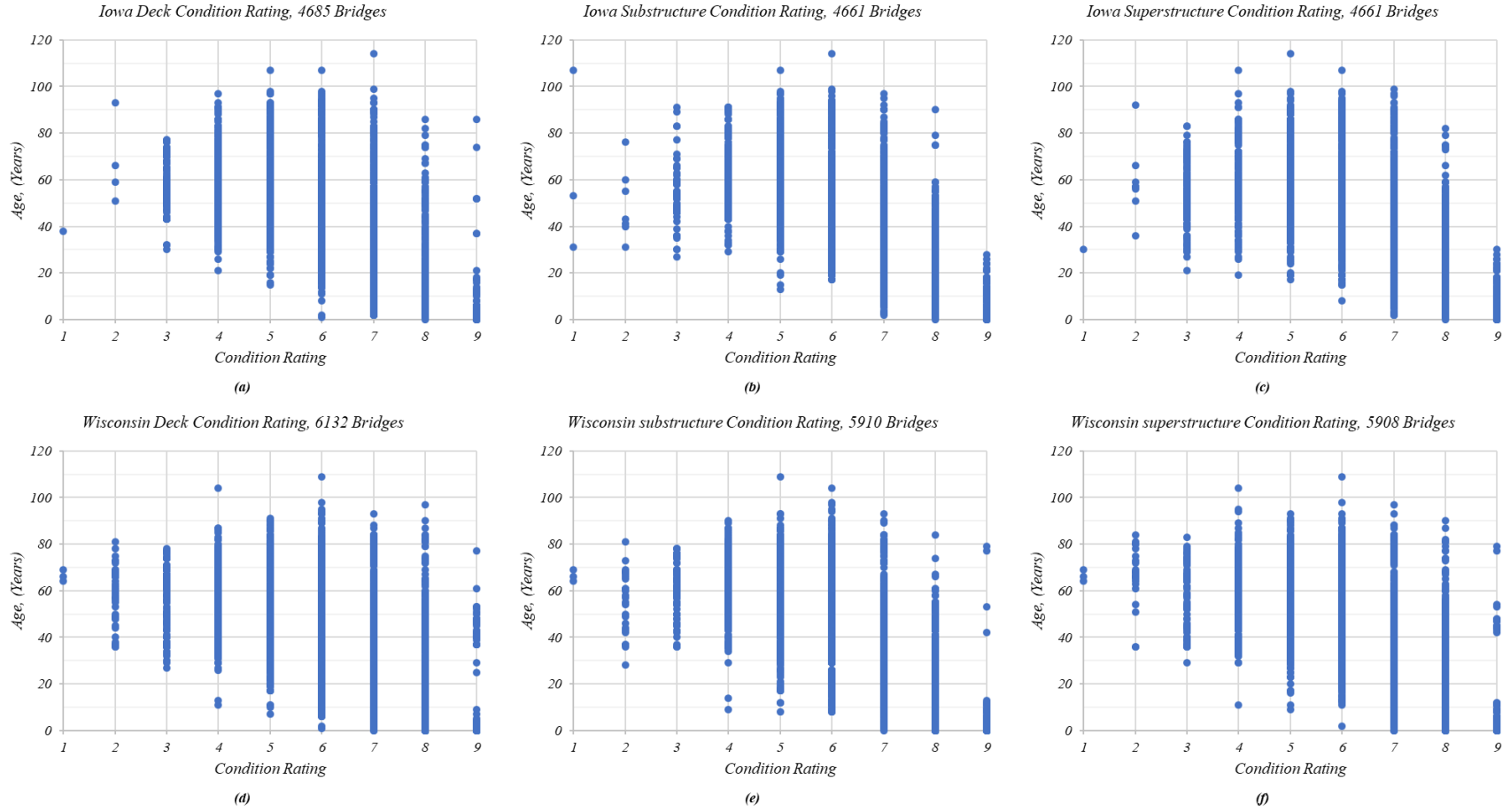


Figure 8.8. Condition rating vs. age for bridges in Iowa and Wisconsin

The age span of each condition rating in both Iowa and Wisconsin bridges showed a similar trend with some minor differences. The condition rating 6 and 7 has a wider age span, ranging from 5 years to 100 years, whereas condition rating 9 has a narrower age span, ranging from 1 year to 15 years.

8.3. Objective

The objective of this portion of the project was to develop a mathematical model that can be used to predict future condition ratings of each bridge component, and more specifically, to estimate the probability of each bridge component being at any condition rating at any future year. The research group was interested in developing two different types of prediction models. The first type was called the current practice model (CPM), which is capable of simulating the effects of historical maintenance activities when predicting the future condition rating probabilities. The second type was called the deterioration prediction model (DPM), which does not consider the historical maintenance activities when predicting the future condition rating probabilities. Both models could be useful when making bridge management decisions. For example, CPM and DPM can be used to investigate the effects of current maintenance practices while making repair and maintenance decisions, such that bridge management decisions can be optimized while minimizing the required resources.

8.4. Methodology

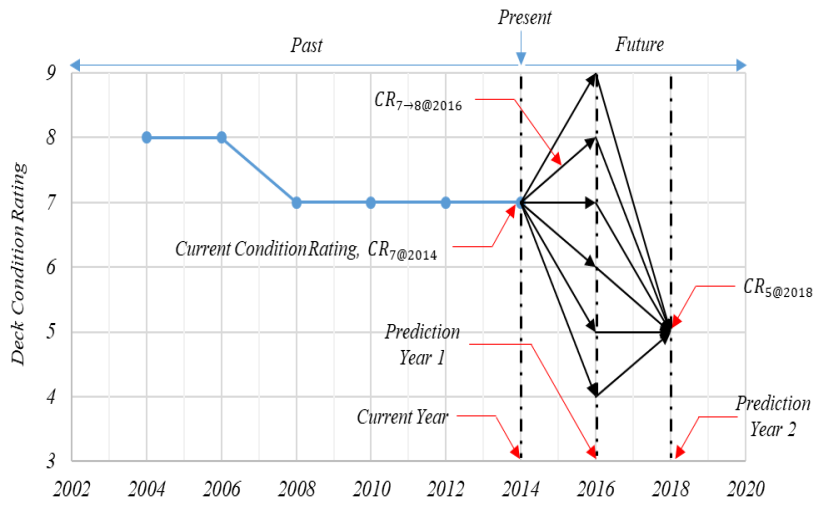
8.4.1. Current Practice Model

The methodology behind the development of the CPM is explained in this section. As discussed in previous sections, the models were developed using the historical condition rating data available in the NBI condition rating database. As shown in Section 8.2.2, there are very few bridges at condition rating 3 or less. Therefore, this methodology of calculating the probability of a bridge component being at any condition rating is limited to between 4 and 9 in any future year.

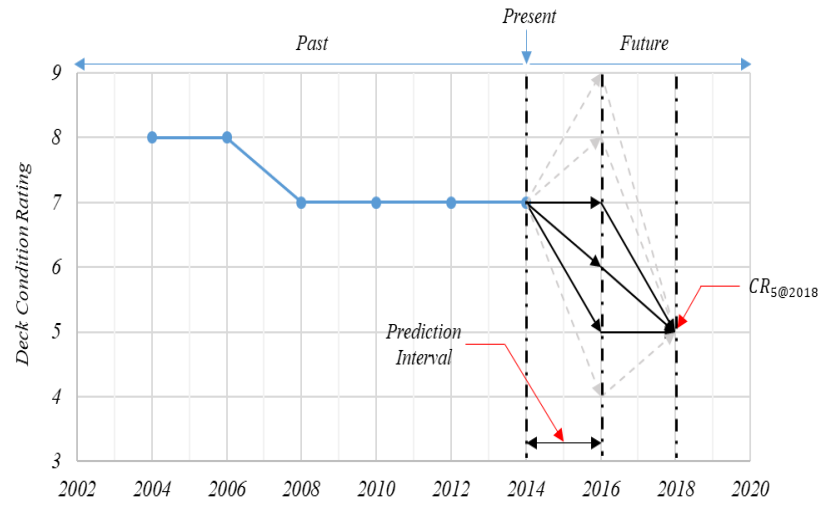
The NBI condition rating data recorded until 2014 were considered to develop the CPM. Therefore, 2014 was assumed as the present year and 2016, 2018, 2020, etc. were considered as the future years. Since the typical routine-inspection interval is two years, the probability of a bridge being at any condition rating between 4 and 9 was calculated in two-year intervals and defined as the prediction interval. The most recent inspection year and the most recent condition rating were defined as current year and current condition rating. The subsequent future years at the end of each prediction interval were termed as prediction years. The possible paths to transition from one condition rating to another condition rating were defined as transition paths. Both the condition ratings and transition paths were labeled such that the rating number, year, and transition path are clearly understandable. For example, $CR_{7@2014}$ indicates the condition rating of the bridge deck in 2014 was 7. Also, $CR_{7 \rightarrow 8@2016}$ indicates the condition rating transition from $CR_{7@2014}$ to $CR_{8@2016}$, whereas $CR_{7 \rightarrow 8 \rightarrow 5@2018}$ indicates the condition rating transition from $CR_{7@2014}$ to $CR_{8@2016}$ and then $CR_{5@2018}$. Also, the CPM assumes that the

previous maintenance practices will continue; i.e., with respect to the current condition rating, the future condition rating can increase, decrease, or stay the same.

A hypothetical condition rating history of a bridge deck is used to illustrate the CPM development process (Figure 8.9a).



(a) CPM, Possible Transition Paths to Reach $CR_{5@2018}$



(b) DPM, Possible Transition Paths to Reach $CR_{5@2018}$

Figure 8.9. CPM development process, possible future deck condition ratings

As an example, the methodology of calculating the probability of the bridge deck being at $CR_{8@2016}$ and $CR_{5@2018}$ are discussed. When calculating the probability of a bridge being at a given condition rating, it is important to identify every possible transition path to reach that condition rating. For example, Figure 8.9a shows that there is one possible transition path available to reach $CR_{8@2016}$, that is $CR_{7 \rightarrow 8@2016}$. Also, Figure 8.9 shows that there are six possible transition paths available to reach $CR_{5@2018}$, i.e., $CR_{7 \rightarrow 9 \rightarrow 5@2018}$, $CR_{7 \rightarrow 8 \rightarrow 5@2018}$, $CR_{7 \rightarrow 7 \rightarrow 5@2018}$, $CR_{7 \rightarrow 6 \rightarrow 5@2018}$, $CR_{7 \rightarrow 5 \rightarrow 5@2018}$, and $CR_{7 \rightarrow 4 \rightarrow 5@2018}$. This suggests that there are total of 36 possible transition paths available when calculating the probability of the bridge being at any condition rating in 2020 (prediction year 3). The number of transition paths increases with the number of prediction intervals, such that representation of every possible path in Figure 8.9 is problematic. A tree diagram can be used to clearly represent every possible transition path for any number of prediction intervals, and it can be used to develop the probability theory to calculate the bridge deck being at each condition rating at a given year (Figure 8.10).

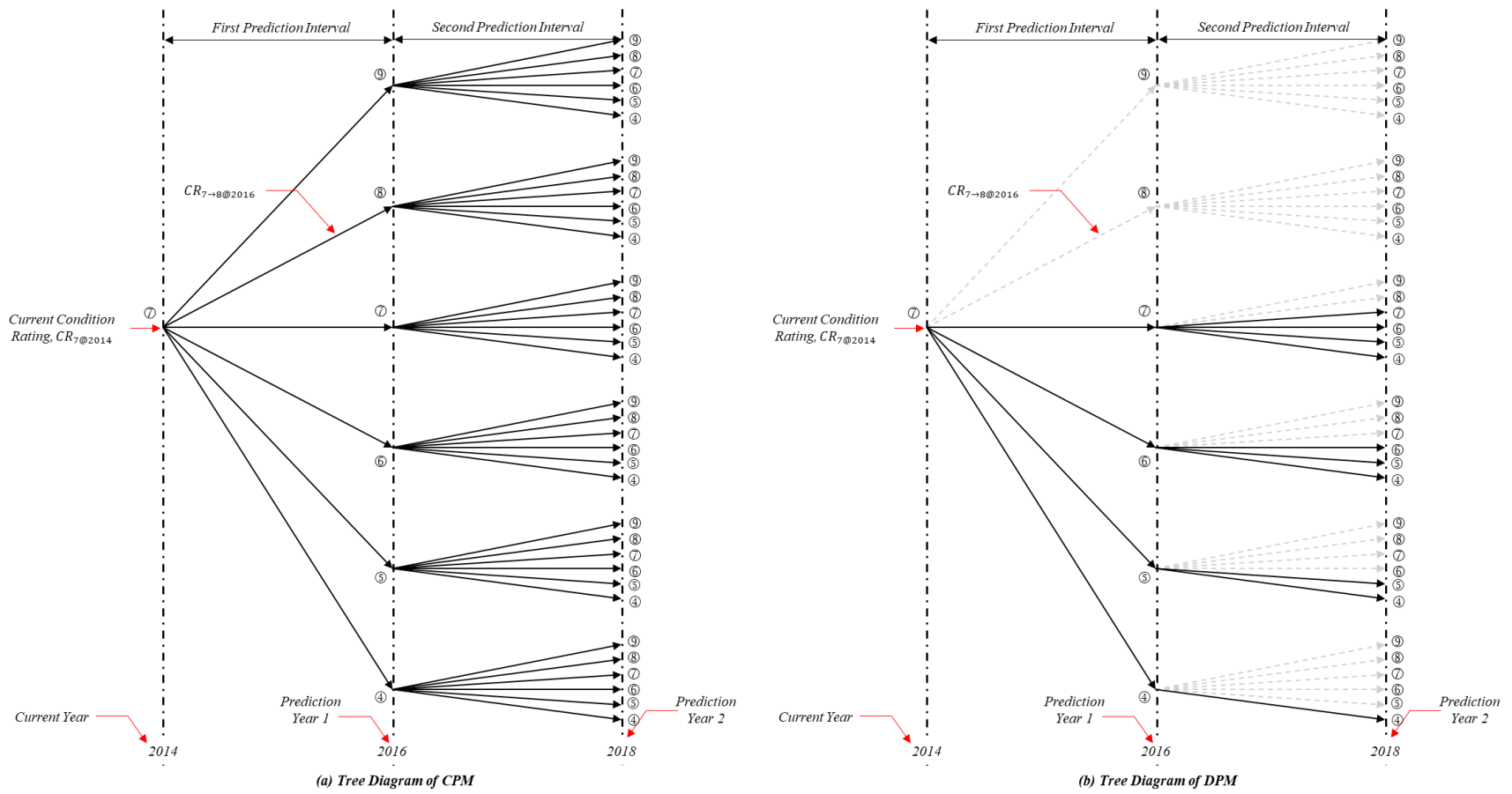


Figure 8.10. Possible future condition ratings using tree diagram

8.4.2. Deterioration Prediction Model

The development of DPM was similar to the development of CPM; however, the DPM did not assume current maintenance practices would continue; i.e., with respect to the current condition rating, the future condition ratings cannot be increased with time, but it can continue to stay the same or decrease with time. The labeling system used in the CPM modeling process was used in the DPM to label condition ratings and the transition paths.

The same hypothetical condition rating history was used to illustrate the methodology behind DPM, and the calculation of the probability of a bridge being at $CR_{8@2016}$ and $CR_{5@2018}$ are discussed. As mentioned in Section 8.4.1, $CR_{7 \rightarrow 8@2016}$ is the only possible path to reach $CR_{8@2016}$. Since the DPM does not consider current maintenance practices, $CR_{7 \rightarrow 8@2016}$ is not a valid transition path, such that the probability of the bridge deck being at $CR_{8@2016}$ is zero. When calculating the probability of bridge being at $CR_{5@2018}$, three possible transition paths are available, i.e., $CR_{7 \rightarrow 7 \rightarrow 5@2018}$, $CR_{7 \rightarrow 6 \rightarrow 5@2018}$, and $CR_{7 \rightarrow 5 \rightarrow 5@2018}$. All invalid transition paths are shown in a light dashed line (Figure 8.9b). Compared to the CPM, the DPM consists of a smaller number of transition paths. However, to clearly explain the methodology behind the DPM development process, it is also illustrated in a tree diagram and shown in Figure 8.10b.

8.4.3. Probability Theory

The use of tree diagrams to calculate the probability of being at each condition rating at a given year consists of two steps: (1) calculation of probability of each possible transition path and (2) summation of probabilities of every possible transition path. These steps are explained by calculating the probability of the bridge deck being at $CR_{5@2018}$. As a part of the first step of the probability calculation, the probability of having $CR_{7 \rightarrow 9 \rightarrow 5@2018}$ path is calculated and defined as Event B_9 . Event B_9 can be simplified in to two events as Event A_1 and Event A_2 , where Event A_1 , is defined as $CR_{7 \rightarrow 9@2016}$ and Event A_2 , is defined as $CR_{9 \rightarrow 5@2018}$. In statistical terms, the transition path $CR_{7 \rightarrow 9 \rightarrow 5@2018}$ can be written as shown in equation (32). The probability of having $CR_{7 \rightarrow 9 \rightarrow 5@2018}$ transition path can be written as shown in equation (33).

$$B_9 = CR_{7 \rightarrow 9 \rightarrow 5@2018} = CR_{7 \rightarrow 9@2016} \cap CR_{9 \rightarrow 5@2018} = A_1 \cap A_2 \quad (32)$$

$$P(B_9) = P(CR_{7 \rightarrow 9 \rightarrow 5@2018}) = P(CR_{7 \rightarrow 9@2016} \cap CR_{9 \rightarrow 5@2018}) = P(A_1 \cap A_2) \quad (33)$$

According to the probability multiplicative rule, if an experiment consists of dependent events $A_1, A_2, A_3, \dots, A_m$, then the probability of having every event is given in equation (34), where $P(A_2|A_1)$ is the conditional probability of Event A_2 given that Event A_1 has already happened.

$$P(A_1 \cap A_2 \cap A_3 \cap \dots \cap A_m) = P(A_1) \cdot P(A_2|A_1) \cdot P(A_3|A_1 \cap A_2) \cdots P(A_m|A_1 \cap A_2 \cap A_3 \cap \dots \cap A_{m-1}) \quad (34)$$

Event A_1 and A_2 defined above are independent events because the probability of Event A_2 is dependent upon the occurrence of Event A_1 . Following the probability multiplicative rule, the probability of the condition rating transition path $CR_{7 \rightarrow 9 \rightarrow 5@2018}$ can be written as shown in equation (35) and equation (36).

$$P(B_9) = P(A_1 \cap A_2) = P(A_1) \cdot P(A_2|A_1) \quad (35)$$

$$P(CR_{7 \rightarrow 9 \rightarrow 5@2018}) = P(CR_{7 \rightarrow 9@2016} \cap CR_{9 \rightarrow 5@2018}) = P(CR_{7 \rightarrow 9@2016}) \cdot P(CR_{9 \rightarrow 5@2018}|CR_{7 \rightarrow 9@2016}) \quad (36)$$

According to Figure 8.9a, there are five other possible transition paths available to reach $CR_{5@2018}$, which are $CR_{7 \rightarrow 8 \rightarrow 5@2018}$, $CR_{7 \rightarrow 7 \rightarrow 5@2018}$, $CR_{7 \rightarrow 6 \rightarrow 5@2018}$, $CR_{7 \rightarrow 5 \rightarrow 5@2018}$, and $CR_{7 \rightarrow 4 \rightarrow 5@2018}$. These events were defined as Event B_8, B_7, \dots, B_4 , respectively. The same procedure was followed to calculate the probability of these five transition paths to reach $CR_{5@2018}$. In statistical terms, every possible path that could reach to $CR_{5@2018}$ can be written as shown in equation (37). The probability of having $CR_{5@2018}$ can be written as shown in equation (38).

$$CR_{5@2018} = CR_{7 \rightarrow 9 \rightarrow 5@2018} \cup CR_{7 \rightarrow 8 \rightarrow 5@2018} \cup \dots \cup CR_{7 \rightarrow 4 \rightarrow 5@2018} = B_9 \cup B_8 \cup \dots \cup B_4 \quad (37)$$

$$P(CR_{5@2018}) = P(CR_{7 \rightarrow 9 \rightarrow 5@2018} \cup CR_{7 \rightarrow 8 \rightarrow 5@2018} \cup \dots \cup CR_{7 \rightarrow 4 \rightarrow 5@2018}) = P(B_9 \cup B_8 \cup \dots \cup B_4) \quad (38)$$

However, the bridge deck can take only one possible path to reach $CR_{5@2018}$, implying that these six possible paths are independent from each other. Such events are defined as mutually exclusive events. The probability of mutually exclusive events can be calculated using the additive rule given in equation (39). Following the additive rule, the probability of being at $CR_{5@2018}$ can be calculated as shown in equation (40). The same procedure can be applied to calculate the probability of being at any condition rating at any given year.

$$P(B_1 \cup B_2 \cup \dots \cup B_n) = P(B_1) + P(B_2) + \dots + P(B_n) \quad (39)$$

$$P(CR_{5@2018}) = P(CR_{7 \rightarrow 9 \rightarrow 5@2018}) + P(CR_{7 \rightarrow 8 \rightarrow 5@2018}) + \dots + P(CR_{7 \rightarrow 4 \rightarrow 5@2018}) \quad (40)$$

8.4.4. Sojourn Time

When predicting future condition ratings of bridge components, the time spent at each condition rating is important. The time spent at any given condition rating until it transitions to a different condition rating is defined as the sojourn time of the condition rating. Throughout this study, the sojourn time is designated as A_i , where i represents the condition rating and A represents the time spent at condition rating i . The A_i of a bridge component can be easily calculated by transforming the actual NBI condition rating history to a simplified condition rating history. Whenever the condition rating of a bridge component transitioned from one condition rating to

another, the former condition rating was assumed to remain just before the latter condition rating, such that the actual NBI condition rating history can be transformed to a simplified condition rating history of the bridge component.

The simplified condition rating history was very useful in defining the sojourn time of a bridge component and quantifying the history of the bridge component before and after the sojourn time, and thereby mathematically modeling the future condition rating prediction models. Figure 8.11 shows a schematic representation of an actual NBI condition rating history and the simplified condition rating history of a bridge deck.

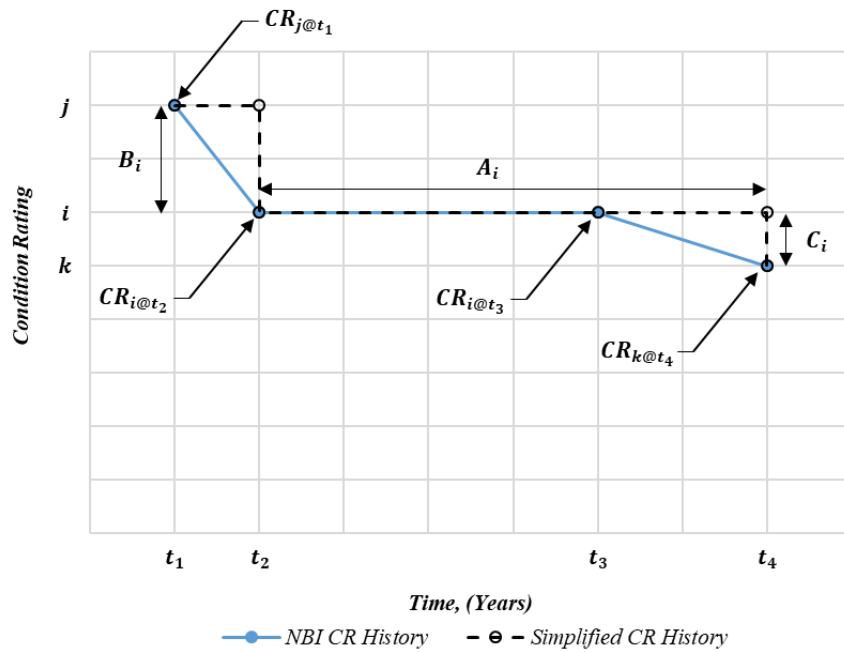


Figure 8.11. Schematic representation of actual and simplified rating histories

The condition rating of the bridge deck at any inspection was labeled such that the condition rating and the year of inspection can be easily understood. For example, $CR_i@t_2$ indicates the bridge deck is rated as condition rating i in year t_2 . As mentioned earlier, the A_i value represents the sojourn time of the bridge deck at condition rating i . The B_i value represents the condition rating transition of the bridge deck before the $CR_i@t_2$, i.e., right before the sojourn time A_i , whereas the C_i value represents the condition rating transition of the bridge deck after the $CR_i@t_3$, i.e., right after the sojourn time A_i , where the $CR_i@t_2$ and $CR_i@t_3$ should be the same. Positive B_i or C_i values suggest possible maintenance effects on the bridge deck, whereas negative B_i or C_i values represent the possible effects due to deck deterioration. Degree of maintenance or deterioration is related to the magnitude of the B_i or C_i values.

Depending upon the sign of the B_i value and C_i value, nine different types of sojourn times can be identified (Figure 8.12).

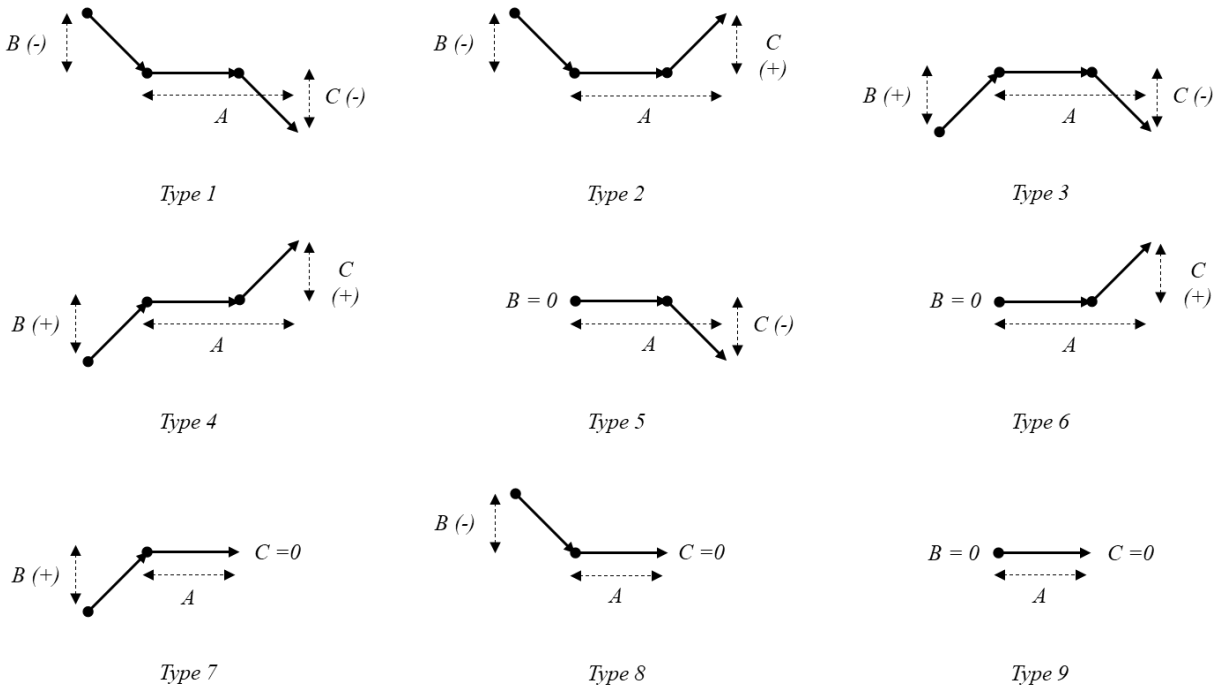


Figure 8.12. Sojourn time types

These nine sojourn time types are capable of representing every possible transition in condition rating of a bridge component throughout its entire life.

As an example, an actual condition rating history of a bridge deck in Iowa (Figure 8.13) is used to illustrate the concept of a simplified condition rating history, sojourn time, and different types of sojourn time.

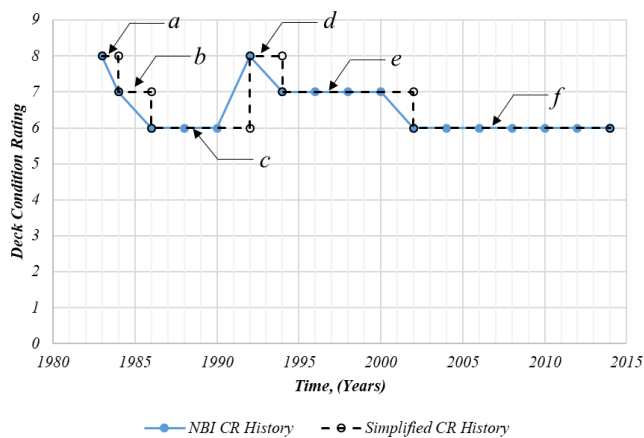


Figure 8.13. Actual and simplified rating histories of an actual bridge deck

The continuous line in Figure 8.13 shows the actual NBI condition rating history, which was obtained during the routine inspections process. The dashed line shows the simplified condition

rating history of the bridge deck. It is clear that the simplified condition rating history is nothing but the actual condition rating history with instantaneous transitions. As shown in Figure 8.13, six different sojourn time types can be identified and used to describe the deck condition rating history of the bridge.

A summary of the sojourn times shown in Figure 8.13 is tabulated in Table 8.2. The bridge was built in 1980, and the condition rating inspection data was available from 1983.

Table 8.2. Summary of sojourn times

No.	Year		Age _i	CR _i	B _i	A _i	C _i	Sojourn time type
	From	To						
a	1983	1984	3	8	0	1	-1	5
b	1984	1986	4	7	-1	2	-1	1
c	1986	1992	10	6	-1	6	2	2
d	1992	1994	12	8	2	2	-1	3
e	1994	2002	20	7	-1	8	-1	1
f	2002	2014	34	6	-1	12	0	8

The parameter Age_i in Table 8.2 represents the age of the bridge deck at each inspection corresponding to the condition rating transition of the NBI condition rating history.

Table 8.2 suggests that for a given condition rating history there can be several sojourn times with different combinations. Also, Table 8.2 describes the historical behavior of the bridge deck in details in numerical format, which would be very helpful to develop the future condition rating prediction models.

8.4.5. Sojourn Time Database and Characteristics

As discussed previously, the sojourn time, A_i, along with parameters B_i and C_i can be used to describe the condition rating history in a quantifiable manner, and it can be used to train the future condition rating prediction models. For the purpose of developing future condition rating prediction models, the parameters listed in Table 8.2. were extracted from each NBI condition rating history of each bridge component.

Characteristics of the sojourn time database were investigated to understand the statistics of sojourn times and significance of each sojourn time type. Figure 8.14 shows the time span of sojourn time at each condition rating of each bridge component in both Iowa and Wisconsin, regardless the sojourn time type.

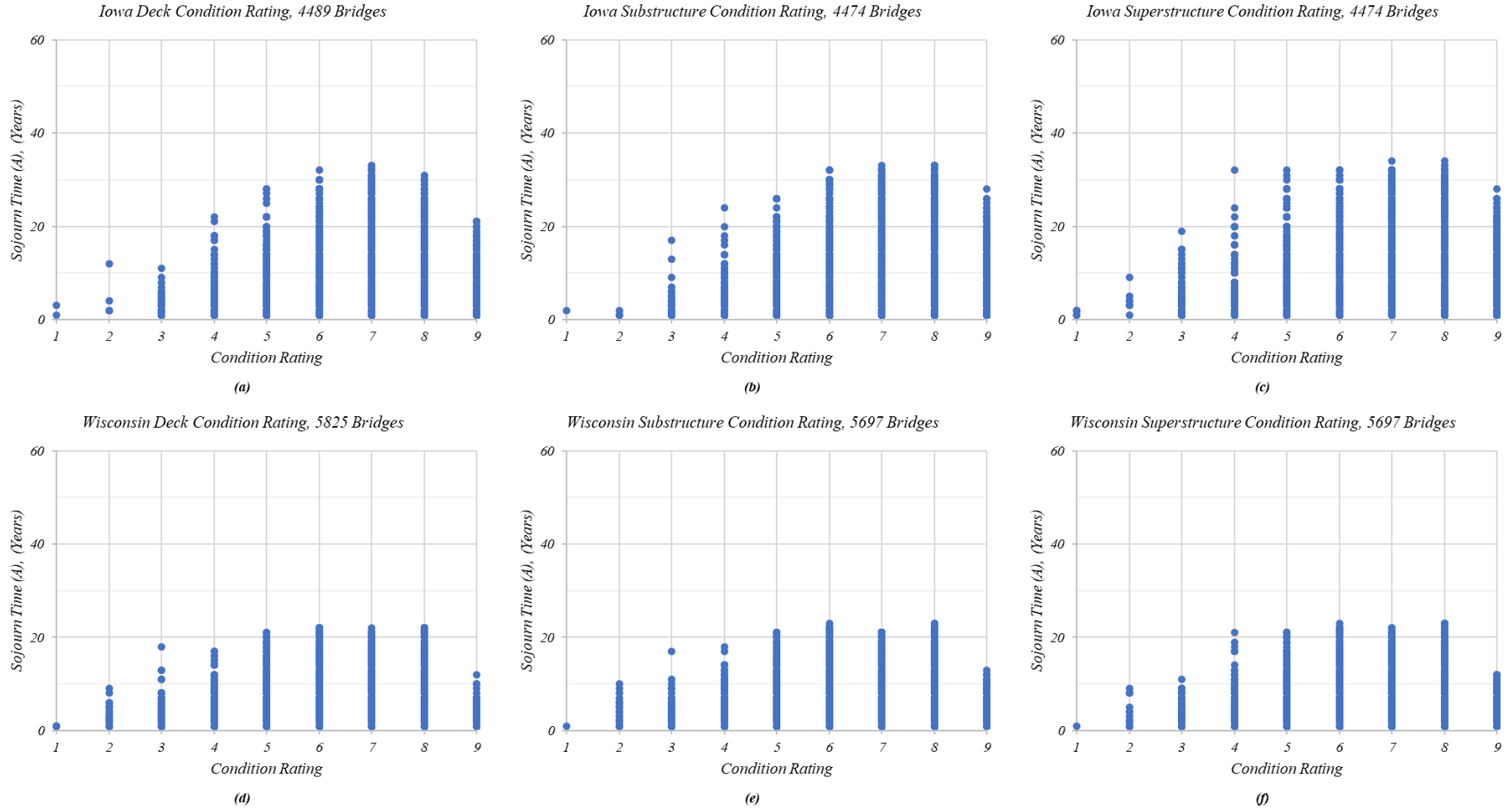


Figure 8.14. Sojourn time of each bridge component for Iowa and Wisconsin bridges

There is no significant difference between the behaviors of sojourn time of each Iowa bridge component. Similarly, Wisconsin bridge components show no noticeable difference between the behaviors of sojourn time. However, the sojourn time span of Wisconsin bridges are smaller than that of the Iowa bridge components, probably because Wisconsin bridge components have had fewer inspections than Iowa bridge components.

According to Section 8.2.2 and Figure 8.14, the characteristics of condition rating and sojourn time of each bridge component are similar in both Iowa and Wisconsin databases. Therefore, only sojourn time databases of the deck condition rating of both Iowa and Wisconsin data were used to graphically illustrate the characteristics of sojourn time types. Figure 8.15 and Figure 8.16 show the time span of each sojourn time type of both Iowa and Wisconsin deck condition ratings data.

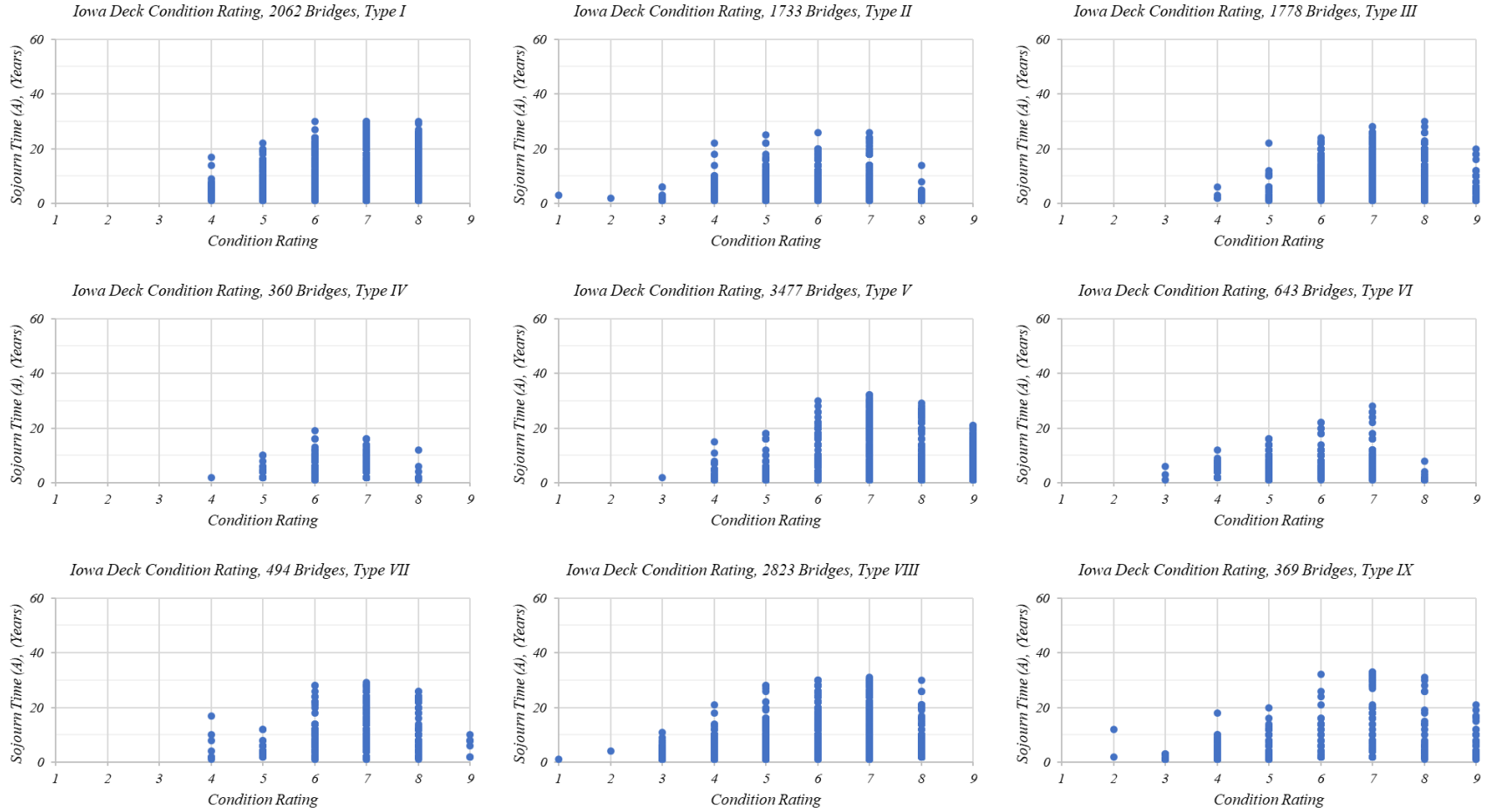


Figure 8.15. Sojourn time type of Iowa deck condition ratings

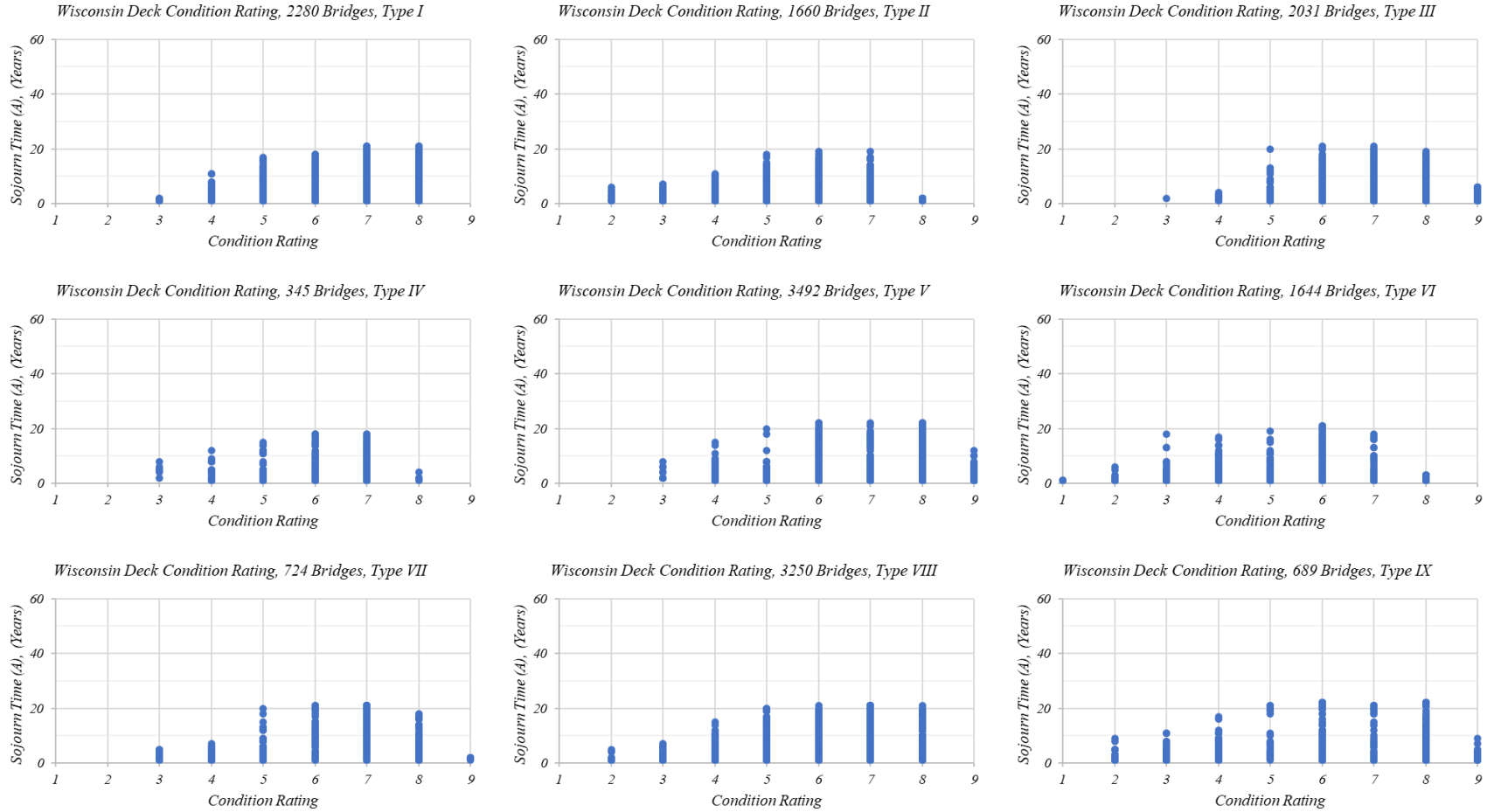


Figure 8.16. Sojourn time type of Wisconsin deck condition ratings

The time span of each sojourn time of both data sets show similar behavior. Each sojourn time type has a significant span of sojourn time, which implies that each different type of sojourn time is important when developing future condition rating prediction models. Also, the time span of each sojourn time of condition rating 3 and lower is significantly small. The average sojourn time of each sojourn time type for each condition rating of every bridge component for both Iowa and Wisconsin condition rating data are tabulated in Table 8.3 to Table 8.8.

Table 8.3. Iowa deck condition rating, average sojourn time

	Average sojourn time, (years)								
	1	2	3	4	5	6	7	8	9
Type I				5.0	5.6	7.1	10.2	8.1	
Type II	3.0	2.0	2.2	3.9	4.6	5.2	6.2	2.9	
Type III				3.3	5.2	7.4	9.0	7.9	4.4
Type IV				2.0	3.7	4.1	4.7	3.9	
Type V			2.0	3.1	3.2	5.0	7.1	3.9	4.2
Type VI			3.3	4.0	4.2	5.8	7.8	2.3	
Type VII				6.3	5.1	7.5	10.1	11.0	6.3
Type VIII	1.0	4.0	3.3	4.8	6.2	7.3	9.0	6.6	
Type IX		7.0	1.7	4.0	5.8	7.5	17.1	9.4	5.9

Table 8.4. Iowa substructure condition rating, average sojourn time

	Average sojourn time, (years)								
	1	2	3	4	5	6	7	8	9
Type I			1.0	3.7	5.3	8.3	11.0	10.8	
Type II	2.0	1.0	2.8	4.1	4.2	4.5	5.8	5.7	
Type III				1.0	4.4	7.4	8.9	10.1	7.9
Type IV				2.0	3.7	3.8	4.1	6.4	
Type V			1.0	2.6	3.8	5.9	7.7	7.3	5.3
Type VI		2.0	1.9	5.4	4.5	6.2	8.6	7.3	
Type VII			2.0	6.3	6.1	7.0	12.0	15.6	6.7
Type VIII		1.0	2.8	4.9	6.8	8.9	9.8	8.9	
Type IX			2.8	3.8	5.7	9.9	21.0	18.7	8.6

Table 8.5. Iowa superstructure condition rating, average sojourn time

	Average sojourn time, (years)								
	1	2	3	4	5	6	7	8	9
Type I		9.0	2.0	3.4	4.5	7.4	9.9	10.5	
Type II	1.8	2.5	3.0	3.7	4.0	4.7	5.4	5.9	
Type III			1.0	1.0	4.2	7.1	8.7	9.6	7.4
Type IV				2.0	5.7	4.3	3.4	2.9	
Type V			1.3	3.0	3.5	4.0	7.0	5.6	5.8
Type VI			6.2	4.0	3.7	4.9	7.8	8.4	
Type VII			1.0	6.0	13.6	8.8	13.7	15.5	9.5
Type VIII	1.0	4.0	3.7	4.9	6.8	8.3	9.0	9.0	
Type IX		3.0	3.6	4.0	7.5	13.0	19.8	21.9	8.5

Table 8.6. Wisconsin deck condition rating, average sojourn time

	Average sojourn time, (years)								
	1	2	3	4	5	6	7	8	9
Type I			1.3	3.6	4.3	5.1	5.9	5.7	
Type II		2.9	2.9	3.6	4.3	5.1	4.7	1.7	
Type III			2.0	2.2	3.8	4.9	5.1	4.0	1.9
Type IV			5.0	4.8	4.4	5.0	6.4	2.3	
Type V			4.3	4.5	3.7	5.7	5.6	5.7	2.2
Type VI	1.0	1.7	2.8	3.3	2.2	3.6	2.0	1.5	
Type VII			2.7	3.0	4.6	7.2	8.6	4.7	1.9
Type VIII		2.0	3.0	4.5	5.4	6.8	8.0	6.0	
Type IX		3.0	3.8	4.7	8.7	10.0	8.5	6.4	2.9

Table 8.7. Wisconsin substructure condition rating, average sojourn time

	Average sojourn time, (years)								
	1	2	3	4	5	6	7	8	9
Type I			1.3	3.9	4.8	5.9	7.1	6.8	
Type II	1.0		2.4	2.8	4.9	5.8	4.2	2.2	
Type III			3.0	2.0	4.4	5.6	5.7	5.3	2.8
Type IV				2.7	5.6	5.9	5.4		
Type V			8.0	4.2	7.3	6.0	5.2	6.7	2.9
Type VI		2.6	3.1	3.4	2.1	4.1	1.7	1.9	
Type VII			1.0	4.8	8.2	8.9	9.6	7.5	7.0
Type VIII		1.7	3.2	3.5	5.7	7.9	9.4	7.7	
Type IX		4.1	4.5	5.1	7.3	13.5	15.6	12.9	3.9

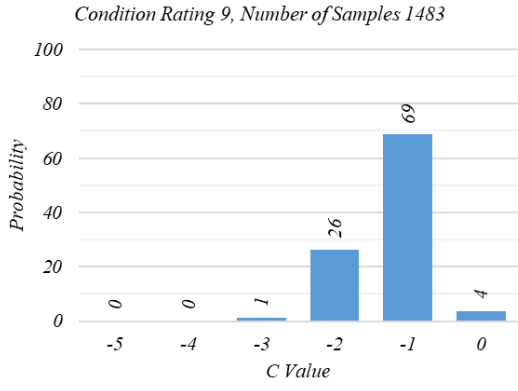
Table 8.8. Wisconsin superstructure condition rating, average sojourn time

	Average sojourn time, (years)								
	1	2	3	4	5	6	7	8	9
Type I			1.3	3.4	4.9	5.6	6.5	7.3	
Type II	1.0	3.3	4.7	3.2	4.8	5.0	4.5	2.1	
Type III				3.3	4.6	5.6	5.0	5.3	2.3
Type IV			5.0	3.6	5.2	7.6	4.6	1.2	
Type V			5.0	4.1	3.4	5.1	6.6	6.9	3.0
Type VI		1.8	2.5	3.2	4.2	4.0	2.4	1.7	
Type VII			5.0	2.4	7.5	9.4	7.5	7.0	3.8
Type VIII		1.8	3.4	4.6	5.3	7.0	8.9	8.0	
Type IX		3.7	3.9	5.0	8.2	10.3	10.8	13.5	3.9

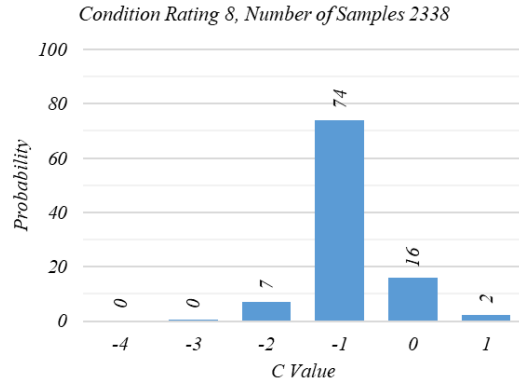
8.4.6. Transition Probabilities of Condition Ratings

The previous section explained the theory of calculating the probability of being at each condition rating at a given year, given that the transition probability of each individual transition path is known. This current section is focused on calculating the transition probability of each transition path of the tree diagram. The transition probability of each transition path can be represented as the relative frequency of the C_i value for each condition rating. For a given condition rating, the C_i value represents the possible transition paths, and the relative frequencies give the probability of taking each transition path and being at any condition rating at the next prediction time. For example, $CR_{7 \rightarrow 8@2016}$ represents the transition path of condition rating from $CR_{7@2014}$ to $CR_{8@2016}$ (See Figure 8.9a). However, it indirectly represents the C_i value ($C_7 = +1$) of the transition path with respect to the most recent inspection. Similarly, $CR_{7 \rightarrow 5@2016}$ represents $C_7 = -2$. Since, these models predict condition rating being between 9 and 4, depending on the most recent condition rating, the C_i value could be anything between ± 5 . In the current example, the most recent condition rating is 7. Therefore C_7 value could be any value between -3 to +2.

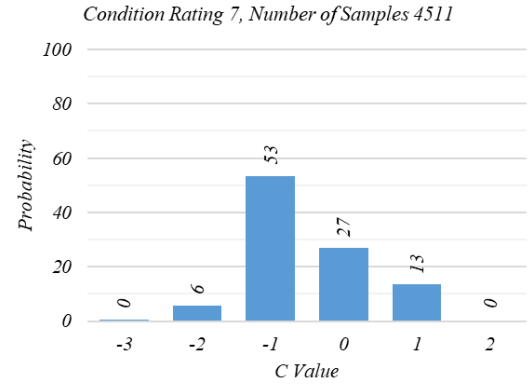
The sojourn time database can be used to find the possible C_i values for each condition rating. As mentioned in Section 8.4.4, the sojourn time database of a bridge component consists of Age_i , CR_i , B_i , A_i , and C_i . Therefore, the sojourn time database can be filtered with respect to each CR_i and C_i to calculate the relative frequency of C_i of each condition rating, in other words, the probability of a bridge component being at any condition rating in the future. As an example, the sojourn time database of Iowa bridge decks were filtered with respect to each CR_i and C_i to calculate the relative frequency of C_i for each condition rating as shown in Figure 8.17.



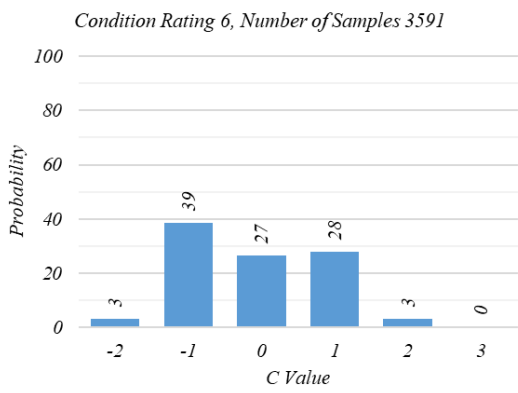
(a)



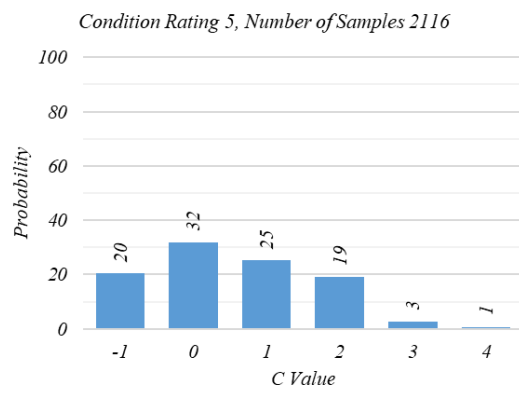
(b)



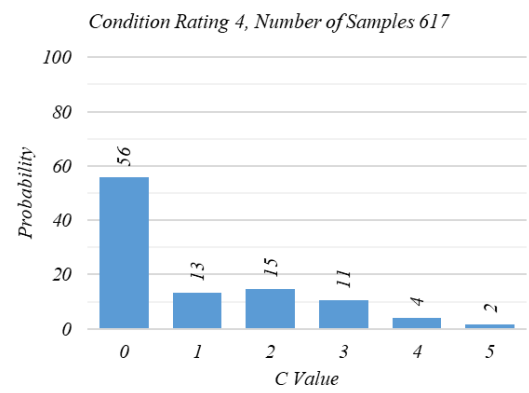
(c)



(d)



(e)



(f)

Figure 8.17. Relative frequency histogram of C value for Iowa bridge decks

These transition probabilities along with the probability theory discussed in Section 8.4.3 can be used to calculate the probability of being at any condition rating in the future.

8.4.7. Sample Size

According to Figure 8.17, each probability histogram is based on a different number of samples. In some situations, these sample sizes could be significantly small, raising a question on required minimum sample size to calculate the transition probability. Since the transition probability histograms do not follow any standard statistical distribution, a normal distribution for transition probability histograms was assumed such that a baseline for minimum sample size could be established. To obtain an estimate with $100(1 - \alpha)\%$ confidence level for mean of a normally distributed population, the required minimum sample size is given in equation (41). The σ^2 is population variance and E is the half-width of the confidence interval.

$$n = \frac{(z_{\alpha/2})^2 \sigma^2}{E^2} \quad (41)$$

Since the population variance is unknown, equation (42) was used to calculate the reasonable estimate of the population variance. The condition rating changes between six condition ratings, and the range can be expressed as the number of condition ratings minus one.

$$\hat{\sigma} = \frac{\text{Range}}{4} = \frac{\text{Number of Condition Ratings}-1}{4} \quad (42)$$

The error E was assumed as 1, implying that the possible error between condition ratings as 1. The minimum required samples were calculated as seven. To be conservative, the minimum required sample size was set as 15 samples.

8.4.8. Filtering Methods

As discussed in Section 8.4.6, the transition probabilities of each transition path can be simply calculated by filtering the sojourn time database with respect to each CR_i and C_i . Although these probabilities represent an overall idea about future condition rating transitions, they do not entirely represent the effects of historical events that occurred at the bridge. To consider the effects of historical events that occurred at the bridge, the sojourn time database can be filtered in many different ways. Future condition rating of a bridge component primarily depends on four factors, namely (1) most recent condition rating, (2) age at most recent condition rating Age_i , (3) most recent B_i value, and (4) most recent A_i value (sojourn time) of the bridge. The most recent condition rating is important, because it represents the most recent condition of the bridge component. The age of the bridge component at the most recent condition rating is related to where in the deterioration process the bridge might be. For example, an older bridge component has a higher probability of transitioning to a lower condition rating than a new bridge component. The most recent B_i value reflects the most recent deterioration or maintenance activity of the bridge component. As an example, a most recent B_i value of +3 suggests that there

was major maintenance recently. Depending upon the most recent A_i value, the condition rating of the bridge component could go up, down, or stay at the same. Further, the longer the A_i value the higher the probability of condition rating transition. To accommodate the effects of historical events that occurred at the bridge and to study the effects of the different parameters on the future condition rating, the research group came up with five different filtering methods, named Method I to Method V. The filtering methods were applied to both the CPM and DPM.

A sample condition rating history of a bridge (Figure 8.18) can be used to explain each filtering method.

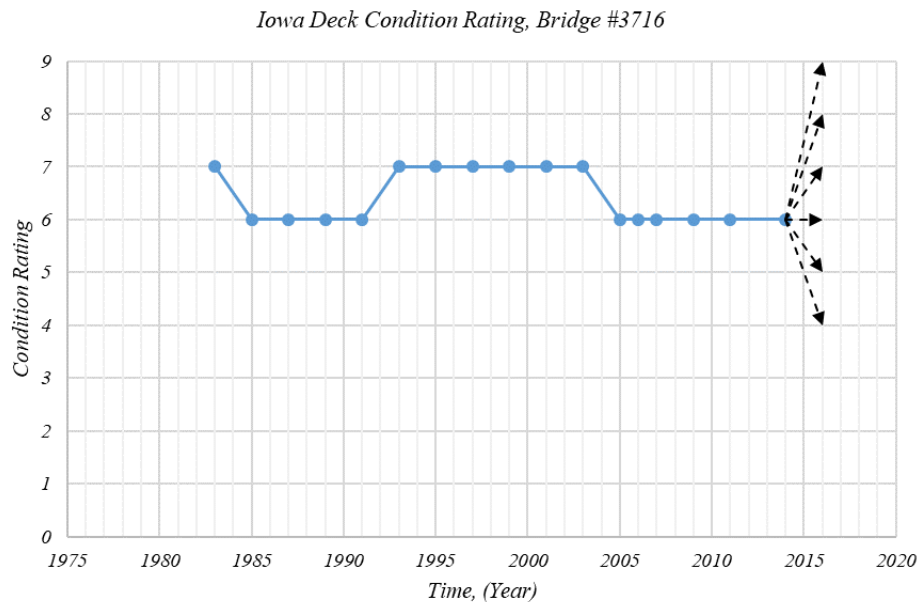
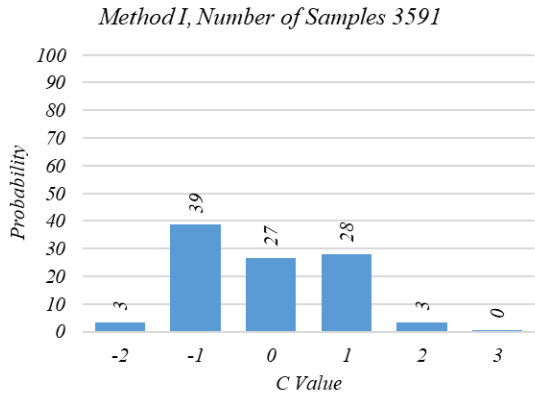


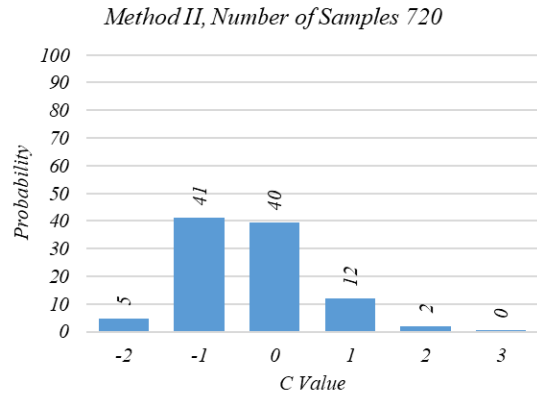
Figure 8.18. Sample condition rating history

Figure 8.18 shows a condition rating history of a bridge deck in Iowa. The objective in this example is to illustrate the five different filtering methods to calculate the probability of the bridge deck being at any condition rating in 2016 (from $CR_{9@2016}$ to $CR_{4@2016}$). All possible transition paths are shown as dotted arrow lines.

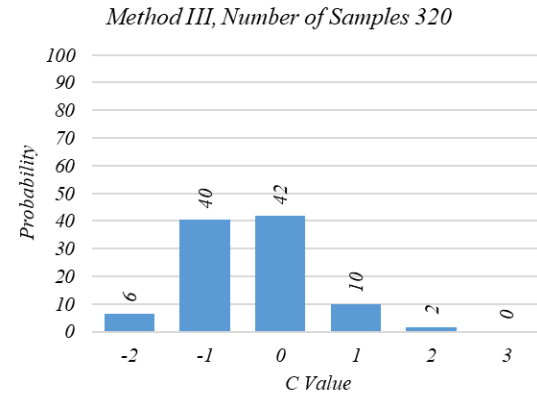
As mentioned in Section 8.4.6, the probability of the bridge being at any condition rating in 2016 can be simply calculated by filtering the sojourn time database by CR_i and C_i alone. The probability histogram calculated that way is represented in Figure 8.19a.



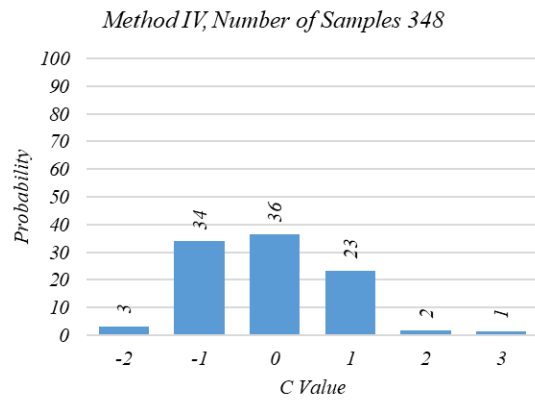
(a)



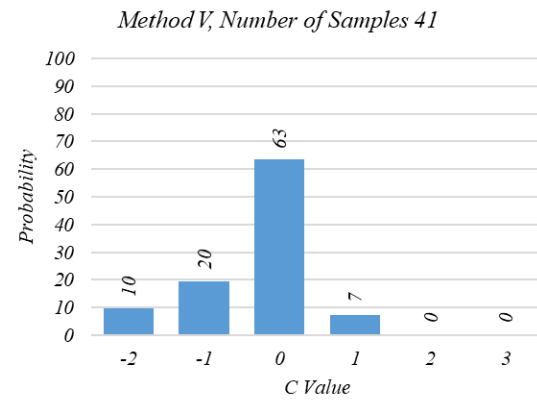
(b)



(c)



(d)



(e)

Figure 8.19. Different filtering methods

The probability calculation could be refined based on the age of the bridge deck. The age at the current condition rating ($CR_{6@2014}$) of this bridge deck is 48 years. Therefore, the sojourn time database can be filtered based on the age. Filtering the sojourn time database by the exact age might give a small number of samples. Therefore, the sojourn time database was filtered in 5- and 15-year age groups. Figure 8.19b shows filtering Method II, which considers the large age groups (15-year age groups), and Figure 8.19c shows filtering Method III, which considers the small age groups (5-year age groups). Data filtering Method IV was developed to include the effects of sojourn time, A_i , and the most recent B_i of the bridge deck (Figure 8.19d). Data filtering Method V consists of the effects of sojourn time, A_i , the most recent B_i , and Age_i (five-year groups) of the bridge deck (Figure 8.19e)

Filtering Method I only depends on the CR_i and C_i values. Therefore, the transition probability histogram of a given condition rating is constant for the same bridge component. Similarly, the filtering Method II and Method III depend on the CR_i , C_i , and Age_i values. Therefore, the transition probability histogram of a given condition rating at a given age group is constant for the same bridge component. However, the probability values of Method IV and V are unique at each and every transition path. According to Figure 8.19, a different filtering method gives a somewhat different probability value. An important thing to notice is that the number of samples from Method I to Method V significantly decreases. In some situations, there may not be enough samples (15 samples) to calculate the transition probabilities. In such situations, the transition probabilities were calculated based on the base filtering method, Method I. The accuracy of each filtering method was quantitatively and qualitatively studied in the next sections.

8.5. Validation of Current Practice Model

The previous sections illustrate the methodology of developing the CPM and different methods to filter the sojourn time database to calculate the probability of a bridge component being at each condition rating at a given year. This section further describes the representation of CPM, validation of CPM, and sample quantitative and qualitative results of the CPM validation.

8.5.1. Overview of CPM Predictions

The condition rating history of the bridge deck used in Section 8.4.8 was used to explain CPM visual representation. CPM Method I is used in the following example for easy explanation. However, the same procedure could be applied to all methods. The methodology explained in Section 8.4 was used to estimate the probability of the bridge deck being at any condition rating in years 2016, 2018, and 2020. The probability histograms obtained using Method I are shown in Figure 8.20, left.

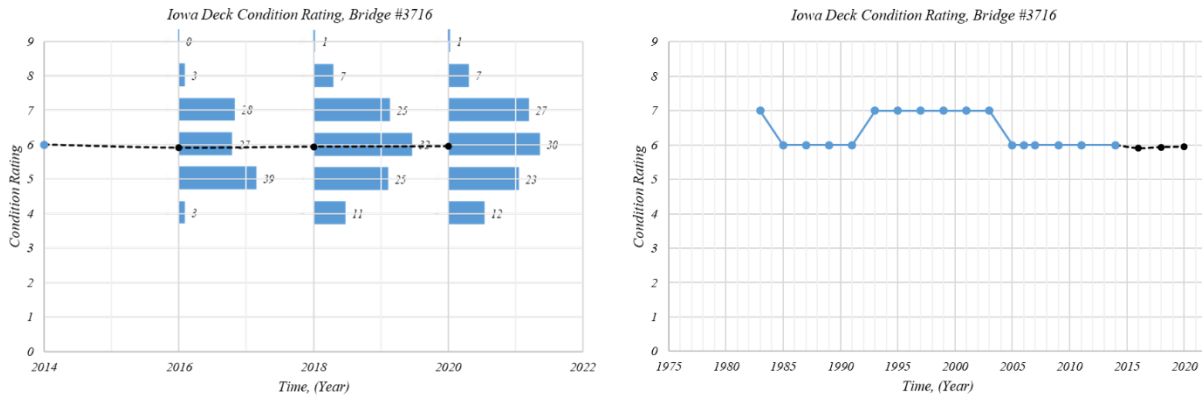


Figure 8.20. Representation of CPM Method I for Iowa bridge deck

The dotted line shown in Figure 8.20, left, represents the line passing through the centroid of each probability histogram, which is a statistical estimate of the most likely future condition rating path of the bridge deck. The most likely condition ratings are not integer numbers like in the NBI condition rating scale. However, the statistical values can be used to understand the future trend of bridge condition, such that it can be used to develop bridge management and maintenance schedules. The predicted and most likely future condition rating path along with historical condition rating data of the bridge deck is shown in Figure 8.20, right.

8.5.2. Hindcasting of CPM

All five different CPMs were quantitatively and qualitatively studied to increase the confidence of using CPMs and to identify the best filtering method. Also, the results were useful in identifying the most important parameters affecting future condition ratings. For the purpose of CPM evaluation, the subset of condition rating histories were selected from each condition rating database. Each subset of condition rating histories consisted of at least 15 inspections and 30 years of condition rating history. Each CPM method was then used to hindcast the condition rating. The hindcasting was performed from the middle of the actual condition rating history. Each CPM prediction length is 16 years. Figure 8.21 shows the same condition rating history used in previous examples.

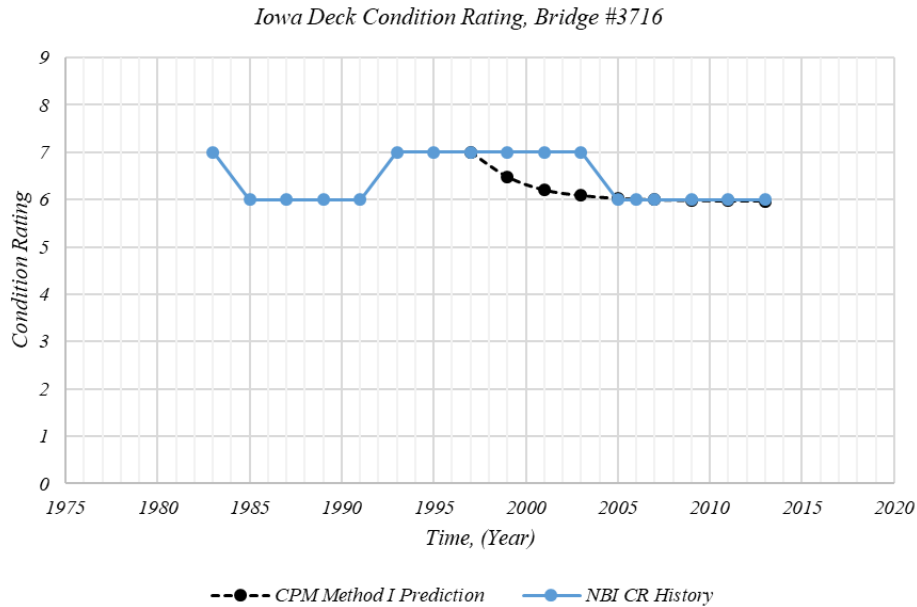


Figure 8.21. CPM validation example

The dotted line shows the condition rating prediction results of CPM Method I. Both actual condition rating history and prediction results were visually compared to qualitatively evaluate the model. According to Figure 8.21, the prediction and historical condition rating data are in somewhat good agreement.

According to Figure 8.21, the prediction starts from 1997, the middle of the actual condition rating history of the bridge. The historical condition ratings from 1997 and the predicted condition ratings were used to calculate the mean squared error (MSE) (Equation (43)), such that the models can be quantitatively evaluated. The MSE value between ± 1 indicates a very good condition rating prediction.

$$\text{Mean Squard Error} = \frac{\sum(CR_{i,\text{Predicted}} - CR_{i,\text{Actual}})^2}{\text{Number of Inspections}} \quad (43)$$

Twenty bridges from the subset of condition rating histories were randomly selected to present the results. The average MSE value of each condition rating database is calculated and tabulated in Table 8.9 and Table 8.10.

Table 8.9. CPM validation results for Iowa condition rating data

Data filtering method	Iowa condition rating data, CPM		
	Deck	Substructure	Superstructure
I	0.82	0.72	1.19
II	0.84	0.80	1.24
III	0.83	0.85	1.21
IV	0.78	0.59	0.87
V	0.74	0.62	0.89

Table 8.10. CPM validation results for Wisconsin condition rating data

Data filtering method	Wisconsin condition rating data, CPM		
	Deck	Substructure	Superstructure
I	0.78	0.75	1.09
II	0.84	0.54	0.97
III	0.84	0.58	0.93
IV	0.81	0.75	1.20
V	0.78	0.67	0.89

According to Table 8.9 and Table 8.10, the CPM Method IV shows the lowest MSE value, probably because the Method IV accommodates sojourn time, A_i , and B_i values. Method V showed the second lowest MSE value. Although Method V included the filtering parameters of Method IV, plus Age_i , Method V showed the second lowest MSE value. This is probably due to not having enough samples to accurately calculate the probability histogram, such that it may occasionally refer to the CPM Method I. In addition, filtering a bridge with respect to the age did not significantly affect the MSE value, probably because the maintenance activities throughout the life of the bridge span could alter the actual aging process of the bridge.

The CPM validation results for randomly selected six condition ratings for each bridge component for both Iowa and Wisconsin condition rating databases are shown in Figure 8.22 to Figure 8.27 for the purpose of qualitative evaluation.

8.5.3. Example Validations of CPM

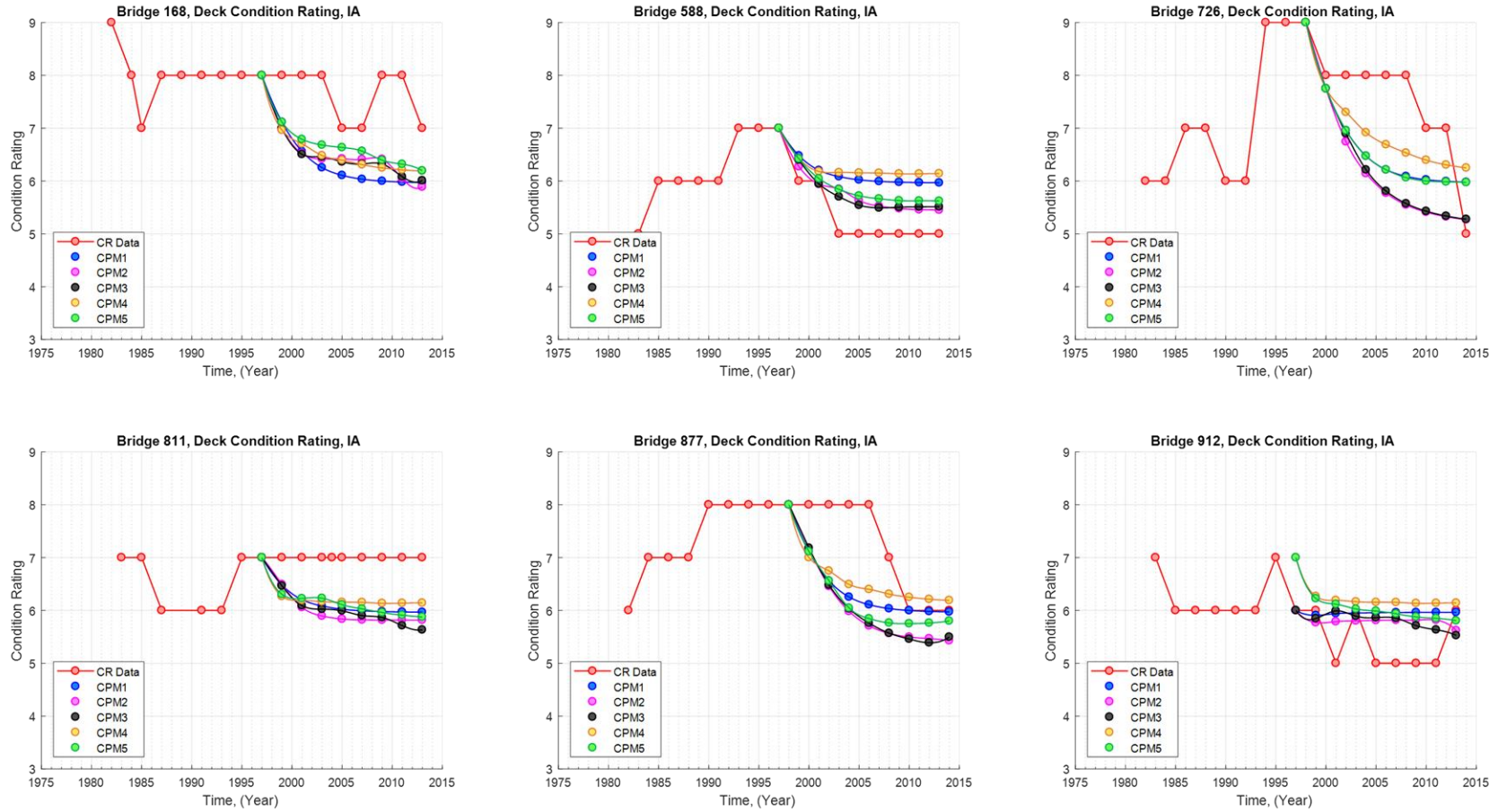


Figure 8.22. CPM validation results for Iowa deck condition rating data

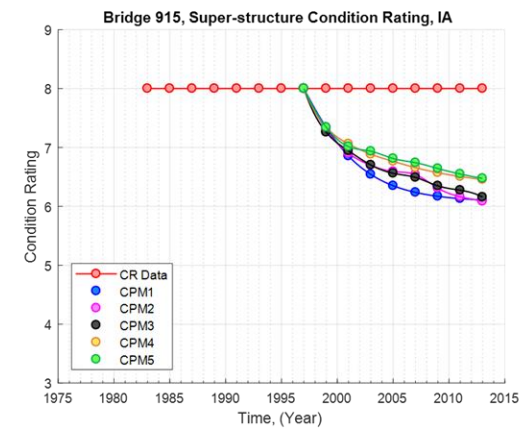
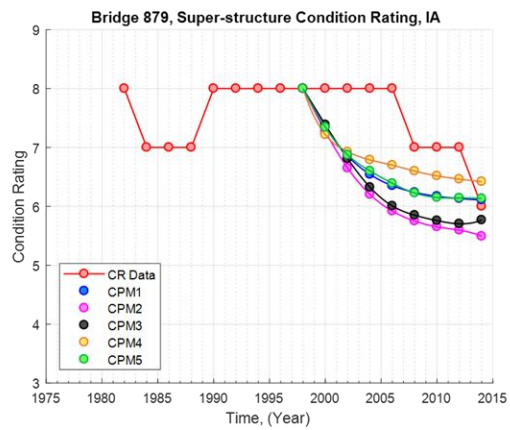
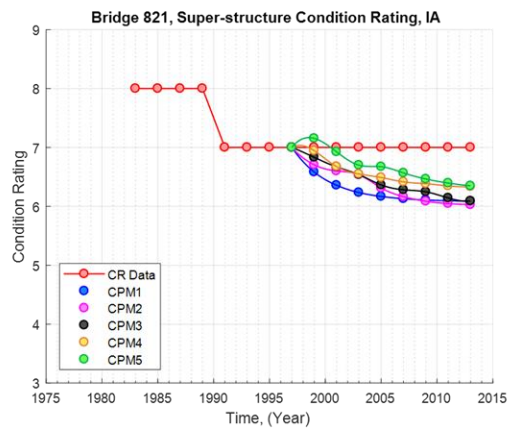
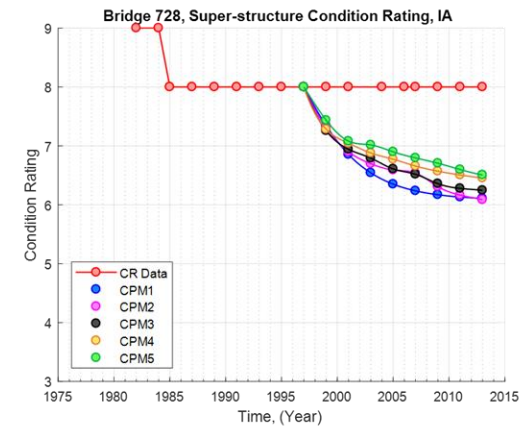
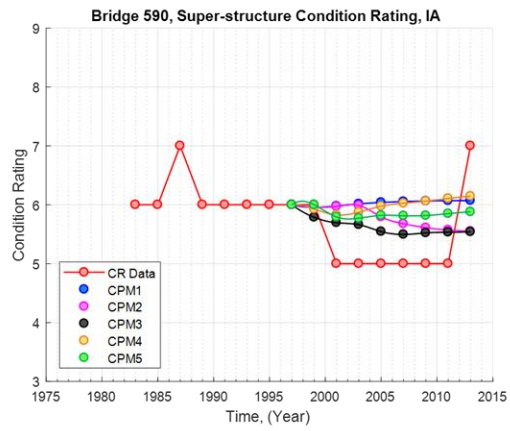
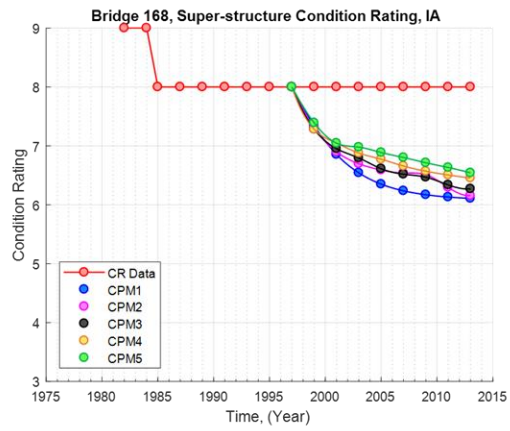


Figure 8.23. CPM validation results for Iowa superstructure condition rating data

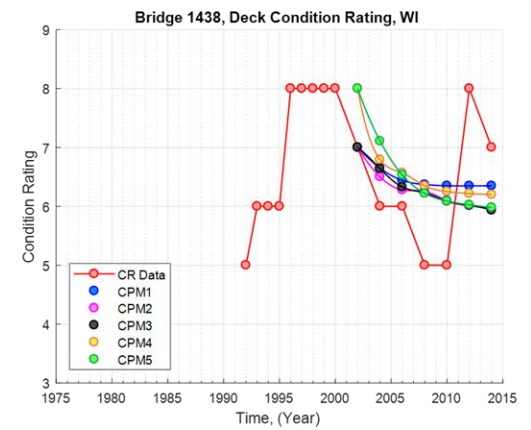
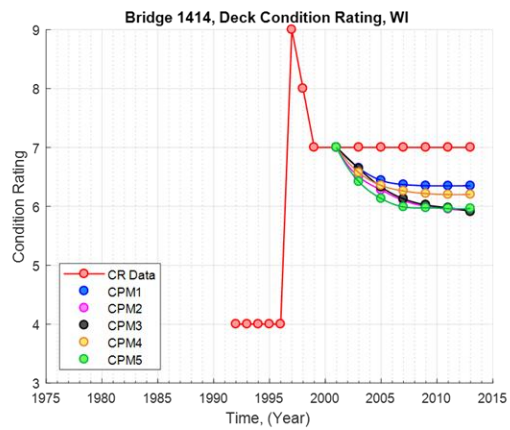
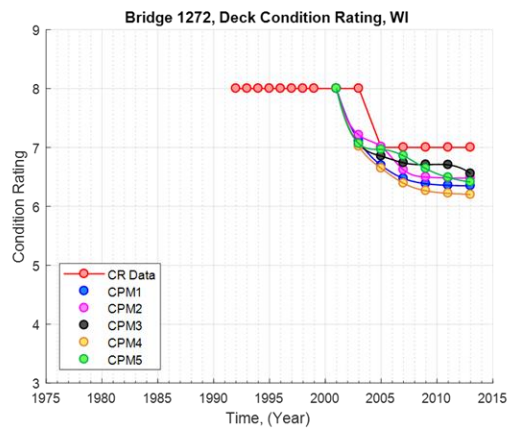
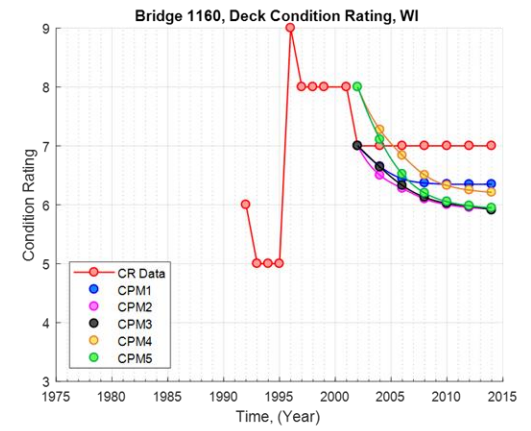
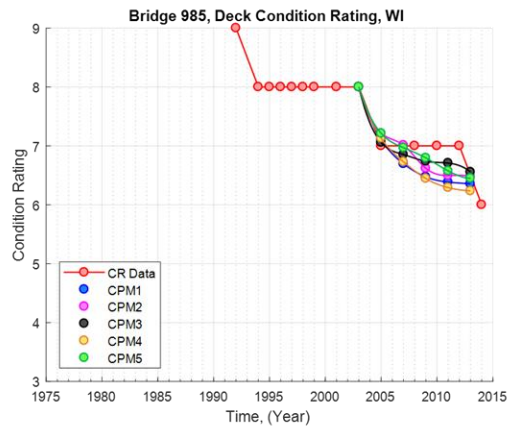
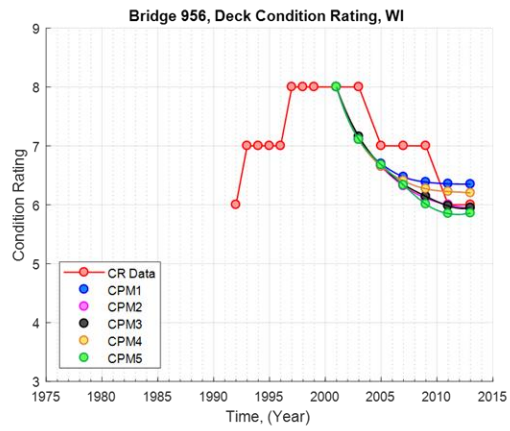


Figure 8.25. CPM validation results for Wisconsin deck condition rating data

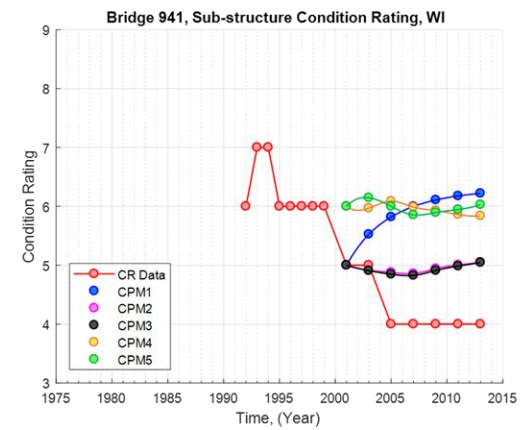
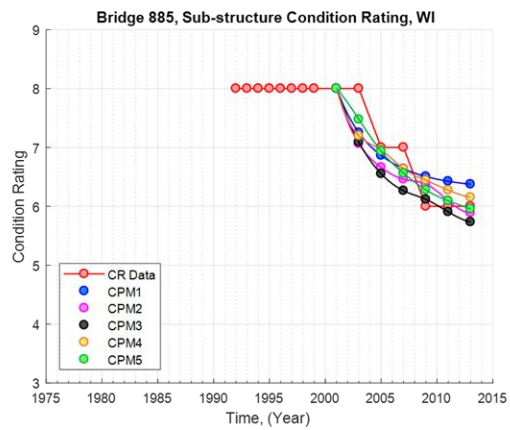
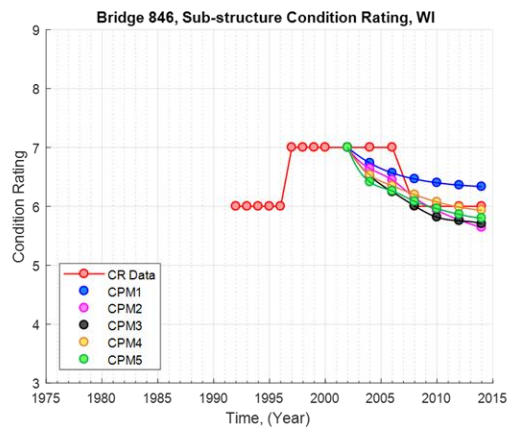
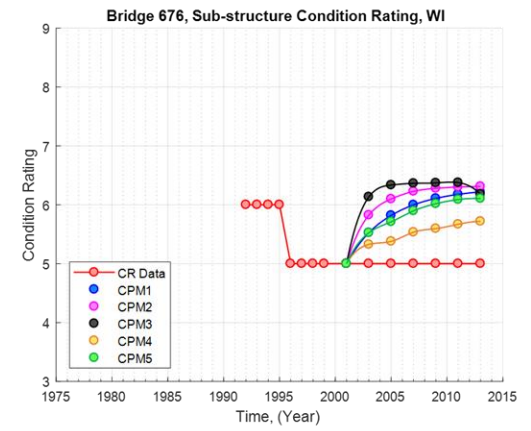
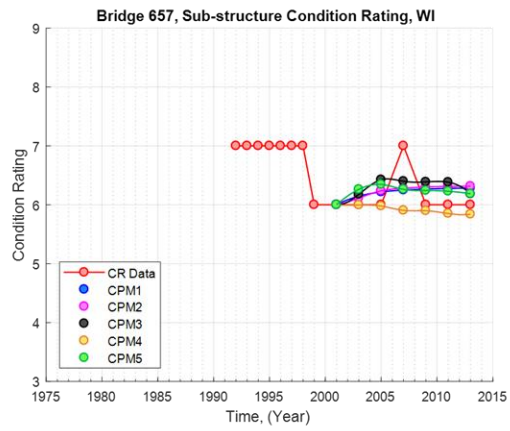
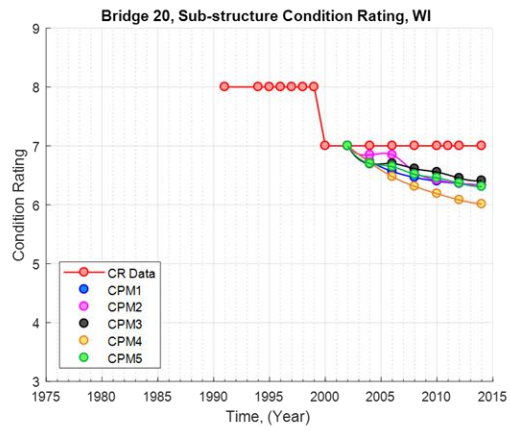


Figure 8.27. CPM validation results for Wisconsin substructure condition rating data

8.6. Validation of Deterioration Prediction Model

As discussed in Section 8.4, the methodology for developing CPM and DPM are almost the same, but DPM does not consider the effects of maintenance practices. The evaluation of DPM is also similar, and the current section describes the visual representation of DPM, DPM validation, and sample quantitative and qualitative DPM evaluation results.

8.6.1. Overview of DPM Prediction

The visual representation of DPM is explained using the same condition rating history used in the previous section. Similar to the previous section, DPM representation is explained with data filtering Method I. The probability histograms obtained using data filtering Method I for years 2016, 2018, and 2020 is shown in Figure 8.28, left.

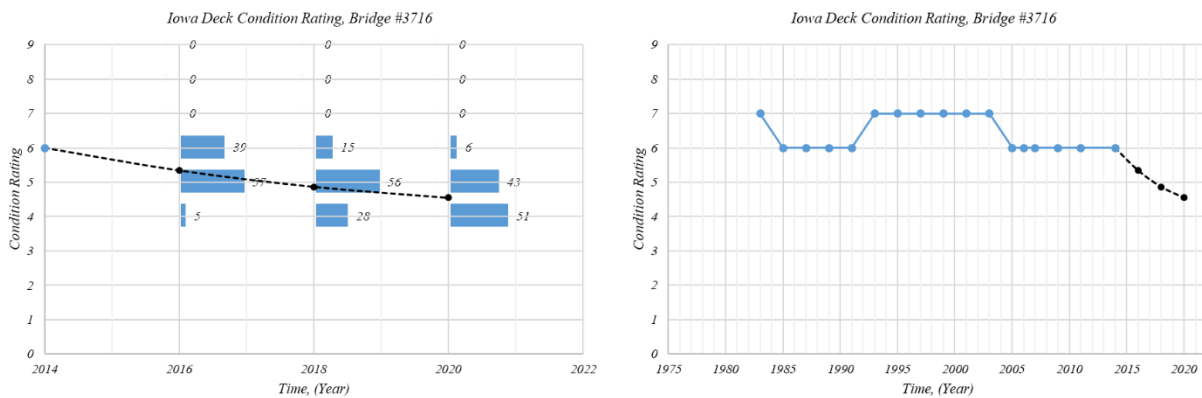


Figure 8.28. Representation of DPM Method I for Iowa bridge deck

The dotted line shown in Figure 8.28, left, represents the line that passes through the centroid of the probability histogram, illustrating the statistical future path of the bridge deck without any maintenance activities. Compared to Figure 8.20, left, Figure 8.28, left, shows the probability of a bridge deck being below the current condition rating, $CR_{6@2014}$, because DPMs do not consider that the condition rating can increase with time. The predicted most likely path along with the historical condition rating data of the bridge deck is shown in Figure 8.28, right.

8.6.2. Hindcasting of DPM

Five different DPMs were quantitatively and qualitatively evaluated to increase the confidence of using a DPM to predict future bridge condition ratings. For the purpose of validation, a subset of bridge condition rating histories with at least 10 inspections and 20 years of history were selected from each condition rating database. Each subset of bridge condition rating histories did not contain any condition rating increasing events. DPMs were used to predict the probability of condition ratings from the middle of the actual condition rating history of the bridge (Figure 8.29).

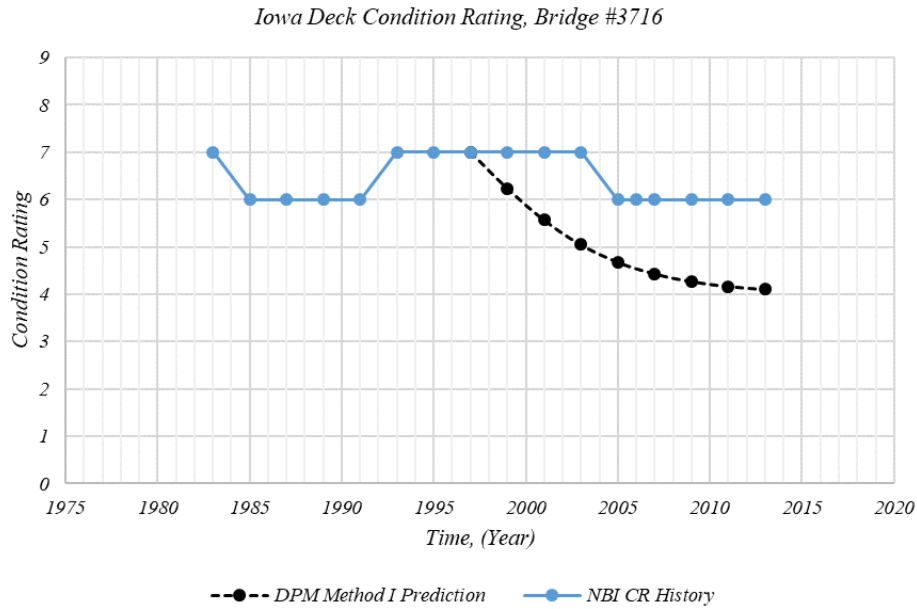


Figure 8.29. DPM validation example

The prediction length was 16 years. Figure 8.29 shows an example condition rating history, and the dotted line shows the condition rating prediction of DPM Method I. Both actual condition rating history and prediction results were visually compared to qualitatively validate the model. Similar to CPMs, the MSE (equation (43)) values were used to quantitatively validate the DPMs.

Twenty bridges from each condition rating history subset were randomly selected to present the results here. The average MSE value of each condition rating database was calculated and is tabulated in Table 8.11 and Table 8.12.

Table 8.11. DPM validation results for Iowa condition rating data

Data filtering method	Iowa condition rating data, DPM		
	Deck	Substructure	Superstructure
I	2.78	2.87	3.42
II	3.16	3.59	4.20
III	3.27	3.21	4.45
IV	2.04	1.65	2.39
V	2.22	1.98	2.88

Table 8.12. DPM validation results for Wisconsin condition rating data

Data filtering method	Wisconsin condition rating data, DPM		
	Deck	Substructure	Superstructure
I	1.09	1.40	1.47
II	1.12	1.40	1.44
III	0.95	1.26	1.28
IV	0.73	0.93	0.96
V	0.86	0.95	0.88

According to Table 8.11 and Table 8.12, DPM Method IV shows the lowest MSE value and DPM Method V shows the second lowest MSE value, and the results are consistent with CPM results. This also implies the importance of the use of A_i and B_i values in predicting the future condition rating of a bridge.

The DPM evaluation results for randomly selected six condition ratings for each bridge component history for both Iowa and Wisconsin condition rating databases are shown in Figure 8.30 to Figure 8.35, for the purpose of qualitative validation of DPM models.

8.6.3. Example Validations of DPM

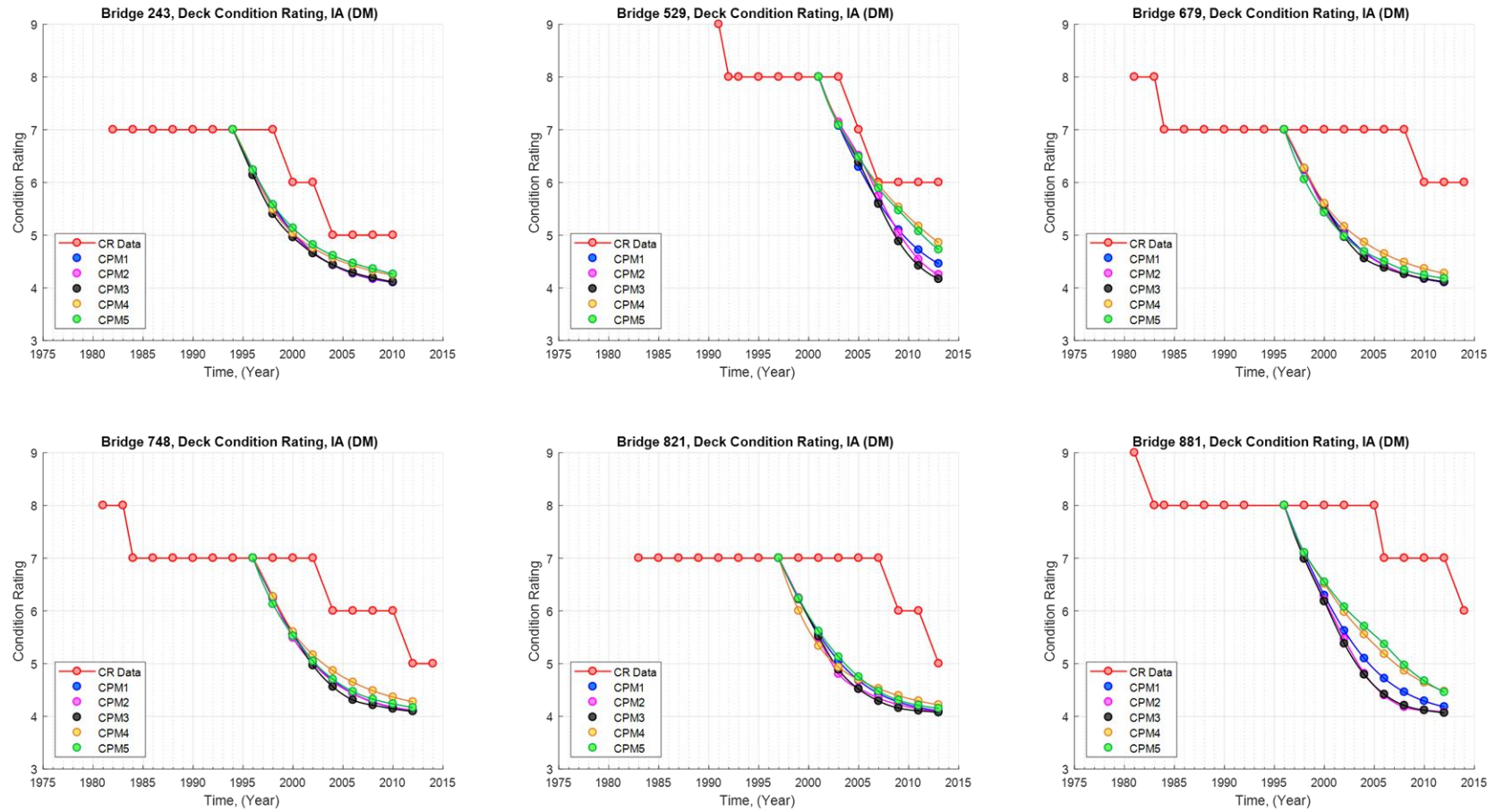


Figure 8.30. DPM validation results for Iowa deck condition rating data

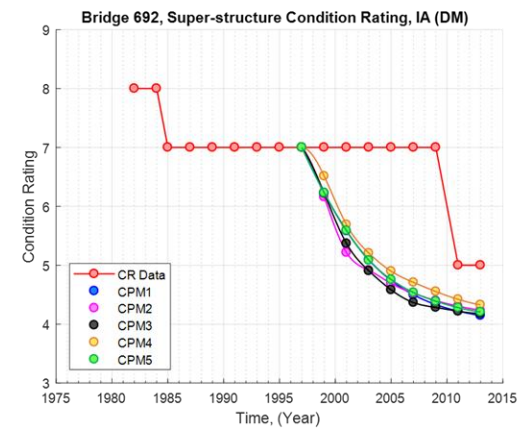
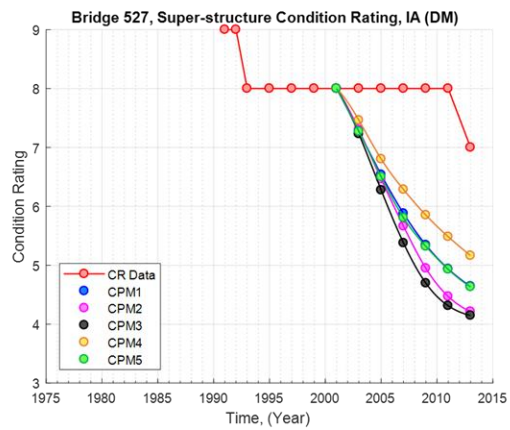
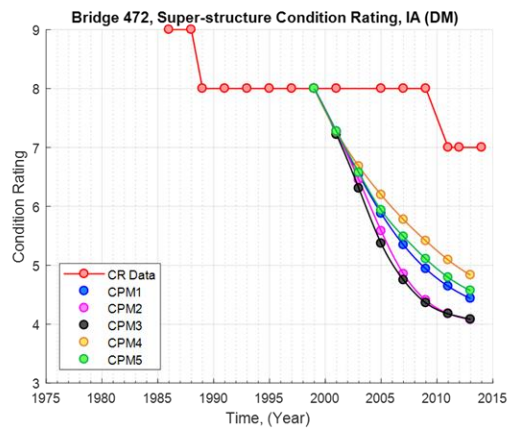
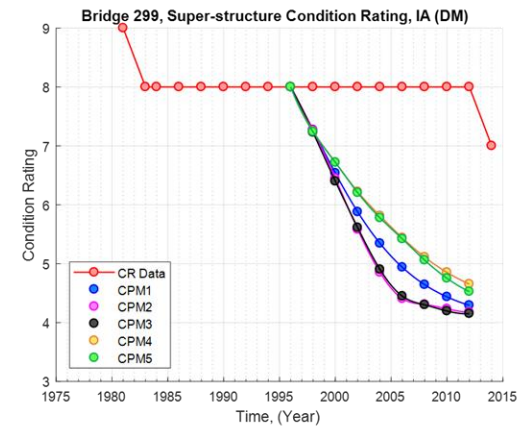
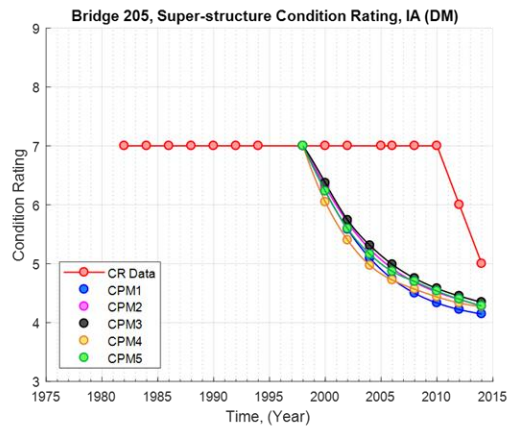
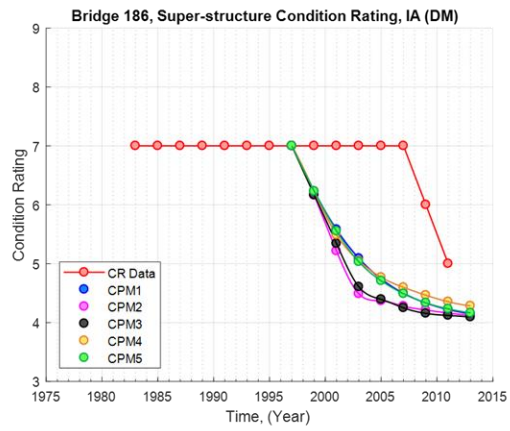


Figure 8.31. DPM validation results for Iowa superstructure condition rating data

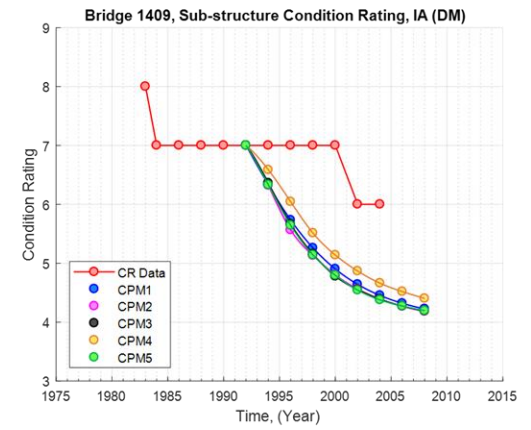
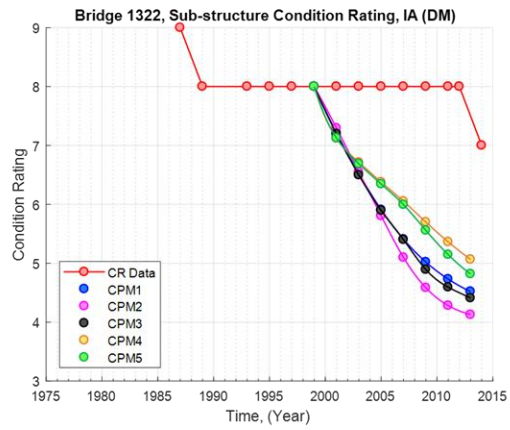
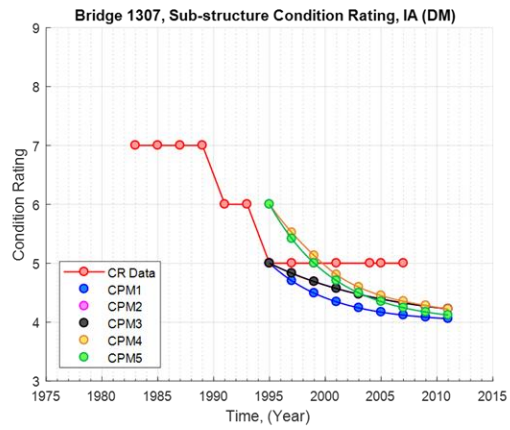
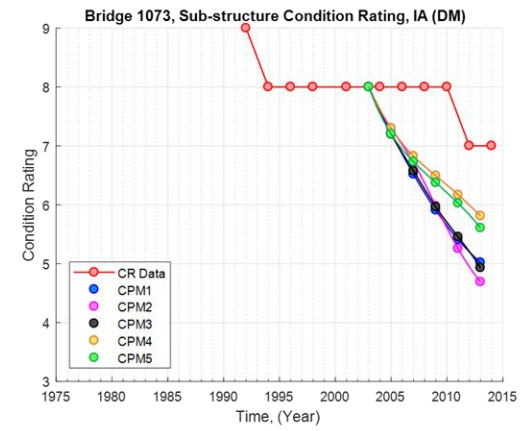
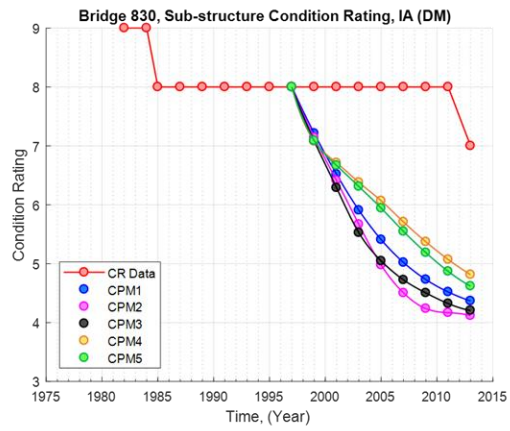
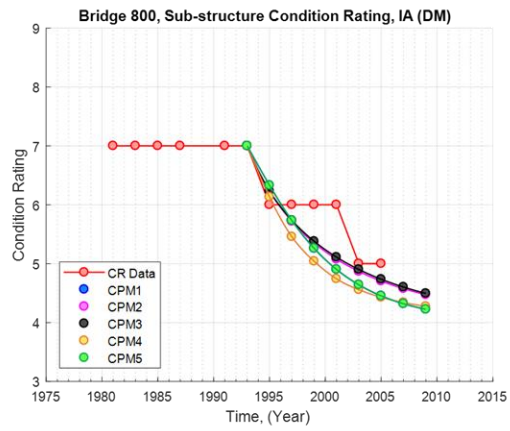


Figure 8.32. DPM validation results for Iowa substructure condition rating data

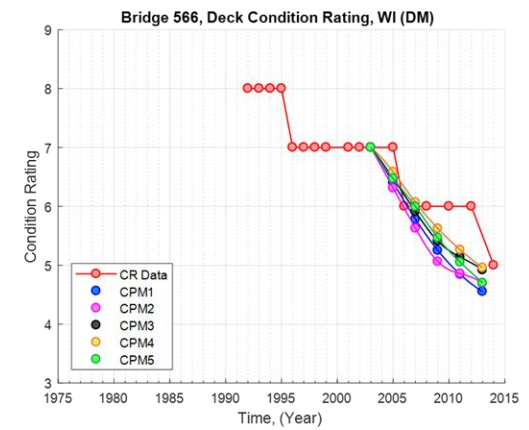
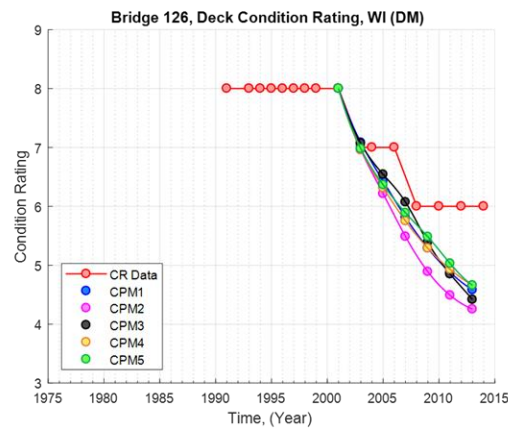
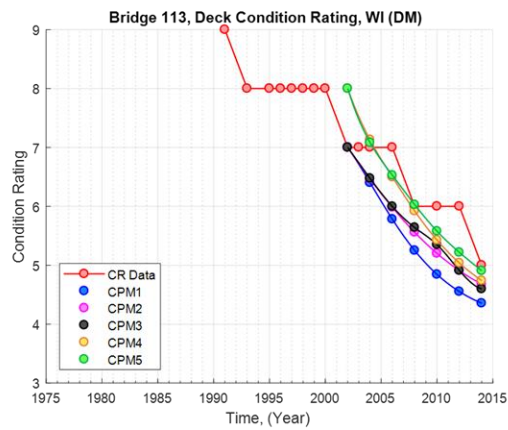
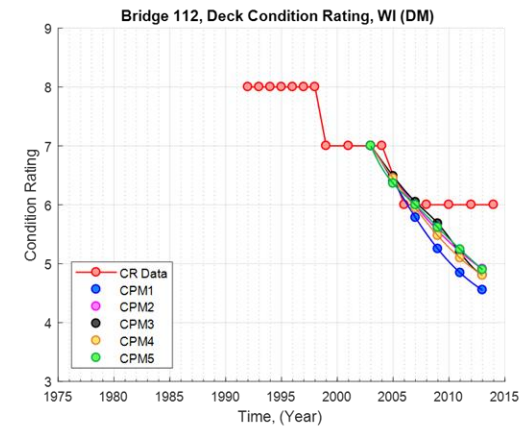
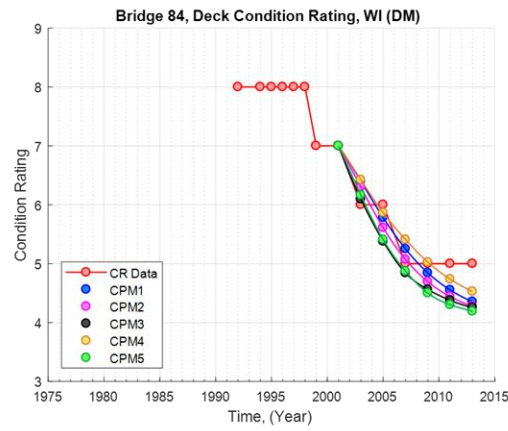
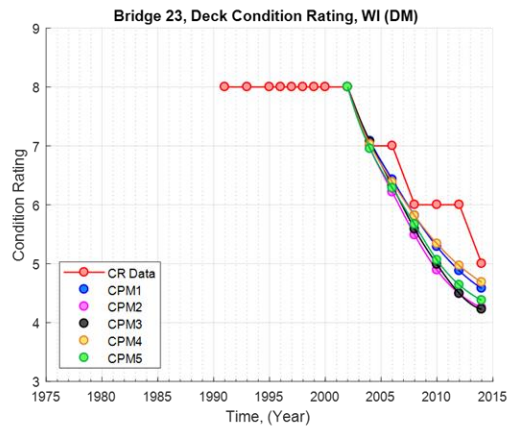


Figure 8.33. DPM validation results for Wisconsin deck condition rating data

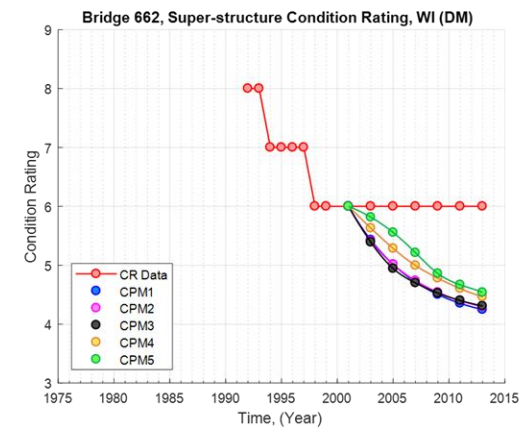
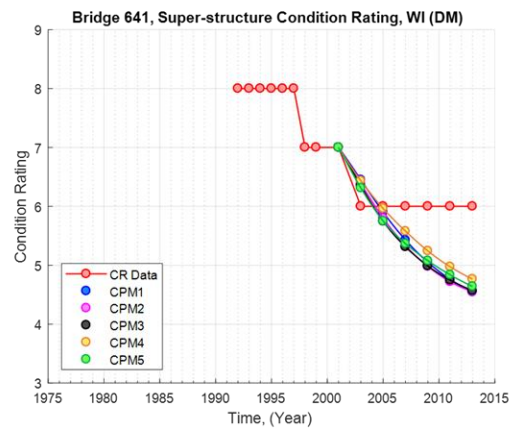
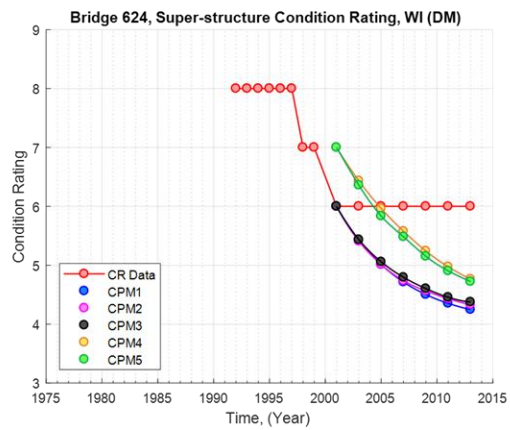
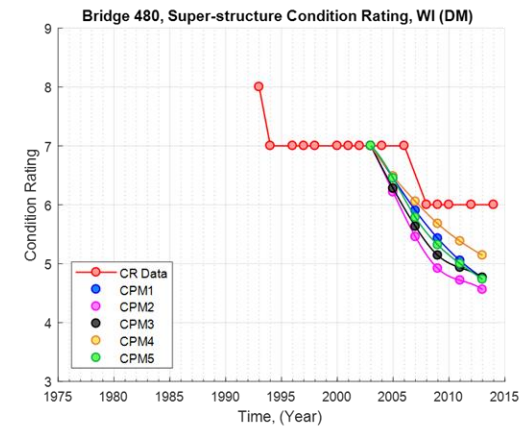
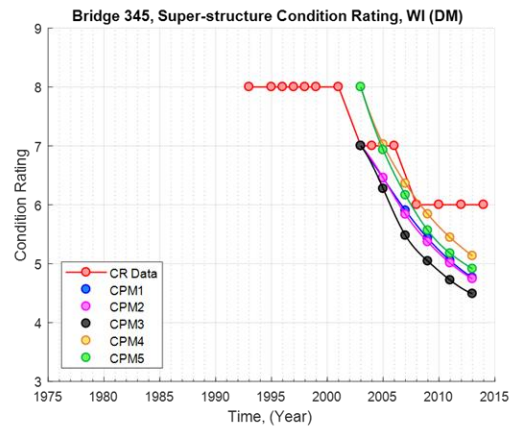
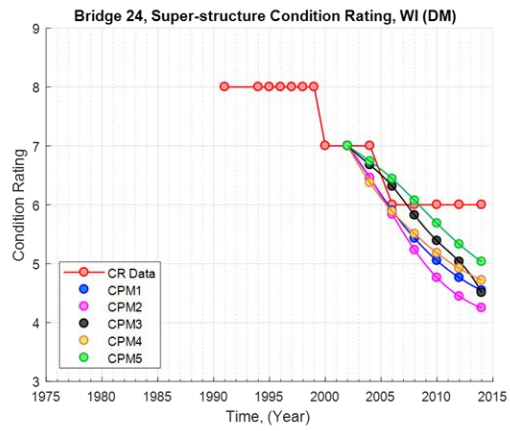


Figure 8.34. DPM validation results for Wisconsin superstructure condition rating data

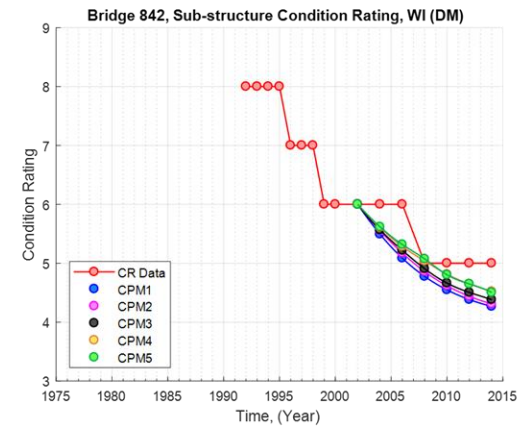
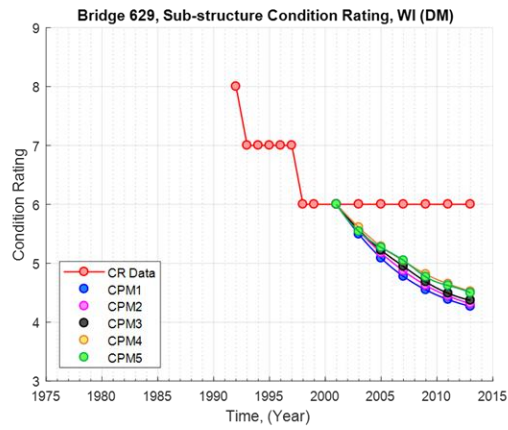
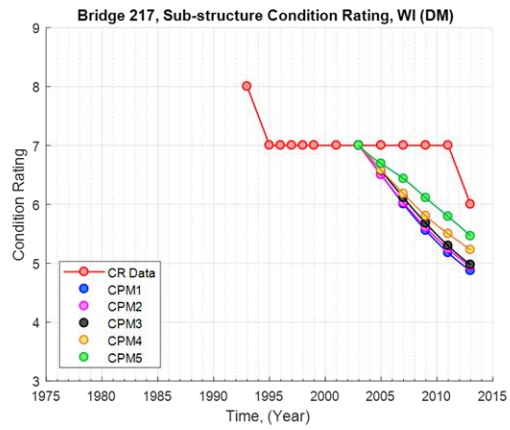
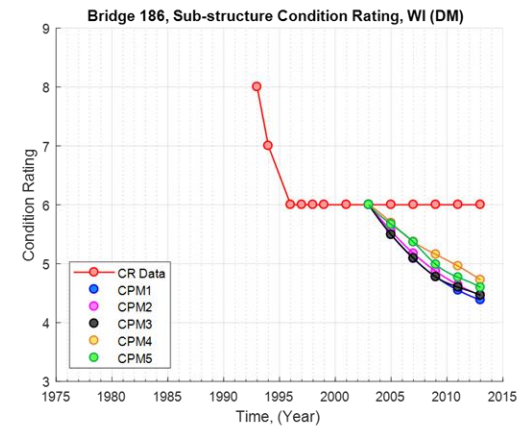
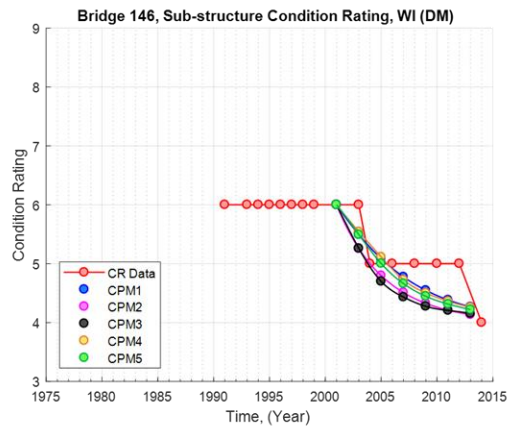
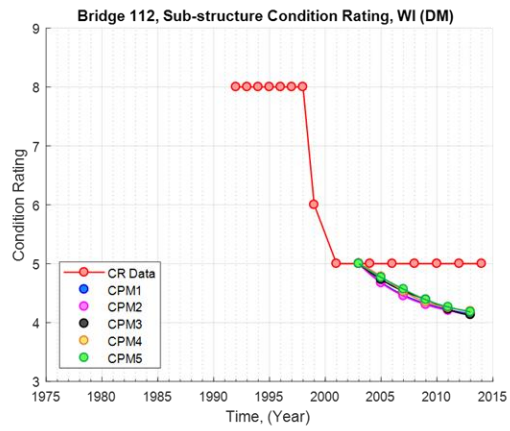


Figure 8.35. DPM validation results for Wisconsin substructure condition rating data

8.7. Summary and Conclusion

8.7.1. Summary

Bridges are continuously exposed to environmental changes and dynamic loading effects due to moving loads. As a result, bridge deterioration is a critical problem in the US. According to the ASCE Infrastructure Report Card (2017), as of 2016, almost 9.1% of bridges are rated as structurally deficient. The structurally deficient bridges are not necessarily unsafe to traffic, but they can quickly become unsafe without proper inspections and maintenance. The average age of a bridge in the US is 43 years, and approximately 40% bridges are older than 50 years. The ASCE estimates that rehabilitation of these bridges could cost about \$123 billion, suggesting that even though there is a high repair and maintenance demand, the available resources are very limited.

The NBI database contains historical bridge condition information for bridges in the US, and it is the best available database for describing the historical condition of bridges in the US. The NBI database contains condition rating data of bridges rated during visual inspections, on an integer scale from 0 to 9, where condition rating 0 represents a failed condition and condition rating 9 represents an excellent condition. The condition rating history data of Iowa and Wisconsin bridge components were statistically analyzed to understand the general trend of bridge behavior. More than 65% of bridge components in each state have more than 10 inspections spanning over 20 years. The average age of any Iowa bridge component is about 46.0 years. Most of the bridge decks in both Iowa and Wisconsin are at condition rating 7. Most of the superstructures and substructures in both Iowa and Wisconsin are at condition rating 7 or condition rating 8.

When predicting future condition ratings of bridge components, the time spent at each condition rating is very important, and it is defined as sojourn time of the condition rating of a bridge component. There are nine different types of sojourn times that can be defined (see Figure 8.12). These nine sojourn time types are capable of representing every possible transition in condition rating of a bridge component throughout its entire life. The characteristics of sojourn time type for each bridge component was investigated to understand the importance of sojourn time on predicting future condition ratings of bridges.

The research group developed two different types of future condition rating prediction models, namely current practice model (CPM) and deterioration prediction model (DPM). CPM is capable of simulating the effects of historical maintenance activities when predicting the future condition rating probabilities, whereas DPM does not consider the effects of historical maintenance activities when predicting the future condition rating probabilities. The sojourn time database was filtered in five different ways to calculate the transition probabilities for different prediction methods. Both CPMs and DPMs were quantitatively and qualitatively evaluated to increase the confidence of using CPMs and to identify the best filtering method.

8.7.2. *Conclusions*

Quantitative evaluation results of both CPMs and DPMs show data filtering Method IV is the best method for predicting future condition ratings. Also, it shows that sojourn time is an important parameter when predicting future condition ratings, whereas the age of the bridges does not play as an important role in predicting the future condition ratings of bridges. According to the qualitative evaluation results, some bridges show very good agreement with the prediction results and some bridges do not. However, it is important to understand that these predictions are entirely dependent on the original historical data of the bridges, which are subjective. The CPMs tend to converge to condition rating 6 within 15 years, whereas the DPMs tend to converge to condition rating 4 with 15 years. This suggests that conducting current maintenance activities helps to keep the nation's bridges in at least satisfactory condition. However, not performing any maintenance could lead bridges to be structurally deficient within 15 years.

CHAPTER 9. SHM-FACILITATED CONDITION-BASED MAINTENANCE PRIORITIZATION SYSTEM

As stated previously, in recognition of the limitations of the state of the practice in bridge maintenance and management decision-making approaches, a new SHM-CBM maintenance prioritization system was developed in this research and is described in this chapter. With this system, maintenance priority is established using a ranking index. A higher ranking index means a lower maintenance funding priority. The ranking index was computed using both bridge inventory (NBI) data (represented by the inventory index [II]) and SHM data (represented by a single SHM modifier, which was determined from long-term, continuous, qualitative data), as shown in Figure 9.1.



Figure 9.1. Ranking index computed using bridge inventory and SHM data

9.1. Inventory Index

The II was calculated from NBI data, which are primarily obtained from biennial bridge inspections (e.g., condition ratings for different components) and codified structural analyses (e.g., inventory rating and operating rating). In many decision-making approaches, the II or another similar condition quantification mechanism plays a central role in prioritization. The II illustratively utilized throughout this chapter was non-specific and any numerical system can be utilized in combination with the SHM modifier (SHMM) to integrate continuous performance monitoring data into the ranking index. For example, the II could simply be the sufficiency rating (SR) that is directly available from NBI data. The approach described below shows that the SHMM allows users to alter the II based on the quantified SHM data. For example, the II could simply be the sufficiency rating (SR) that is directly available from NBI data.

The SR provides a method of evaluating highway bridges by calculating four separate factors to obtain a numerical value that is indicative of a bridge's sufficiency to remain in service. The result of this method is a percentage, where 100% represents an entirely sufficient bridge and 0% represents an entirely insufficient or deficient bridge. The formula considers the structural adequacy, functional obsolescence, level of service, and essentiality for public use (FHWA 1996). The SR had been used by the FHWA and other bridge owners for many years as an important factor in determining bridge maintenance funding qualification, although it is currently not being utilized as a primary indicator.

With the introduction of the Moving Ahead for Progress in the 21st Century Act (MAP-21), a data-driven decision-making approach is now required by law. Many bridge owners are trying to modify the SR into a more agency-specific index. For example, the Iowa DOT has developed a bridge condition index (BCI). The BCI is calculated and reported in the Iowa DOT's bridge management system. Since being implemented, this index has played an important role in the Iowa DOT bridge maintenance prioritization process.

The calculation of the BCI is similar to that of the FHWA’s SR but modified to be more sensitive to minor condition changes, which should allow for more timely corrective measures to be made. Table 9.1 summarizes the major differences between the SR and the BCI.

Table 9.1. Comparison of SR and BCI calculations

	Sufficiency rating	Bridge condition index
S1	Considers the impact of load rating and condition ratings. Only the lowest rating of superstructure, substructure, or culvert rating applies. Ratings above 5 are considered to be the same.	In addition to load rating, all condition ratings of deck, superstructure, substructure, or culvert condition rating apply. Unlike the SR, all ratings above 2 are considered different.
S2	Considers the impact of deck condition, structural evaluation, deck geometry, underclearances, waterway adequacy, approach road alignment, roadway width, and vertical clearance. Ratings above 5 are considered to be the same.	Only considers the impact of underclearances, waterway adequacy, and roadway width (deck condition rating is covered in S1 and structural evaluation; deck geometry is a computed item).
S3 Essentiality for public use	Considers the impact of S1, S2, ADT, detour length, and whether the bridge is on the Strategic Highway Network (STRAHNET).	Same as the SR, except that the NHS highway classification is used rather than whether the bridge is on the STRAHNET.
S4	Considers the impact of detour length, structure type, and traffic safety features.	Considers the impact of fractural criticality, fatigue vulnerability, and channel protection.

As mentioned above, and as the Iowa DOT has done with the proposed SHM-CBM framework, bridge owners can easily design and implement their own index to reflect an agency-specific emphasis of certain parameters.

9.2. SHM Modifier

Due to the relatively limited availability of SHM systems, using SHM data as a tuning factor rather than the dominant factor is the most practical way to implement SHM in the short term and may well be more practical over the long term as well. The continuous real-time or near real-time SHM sensing data or derived data are fed into an equation to compute an SHMM. The SHMM is then applied as a multiplier to the II to tune its value up or down to reflect the impact

of up-to-date bridge condition information and the bridge owner’s opinion as to how the SHM data should affect maintenance decision making.

9.2.1. Parameters and Weighting Factors Used in the SHMM Calculation

Seven parameters (F_1 to F_7) are used in the SHMM calculation, and each parameter has a user-configurable weighting factor associated with it (γ_1 to γ_7 , respectively).

$$\text{SHMM} = (F_1^{\gamma_1}) (F_2^{\gamma_2}) (F_3^{\gamma_3}) (F_4^{\gamma_4})(F_5^{\gamma_5}) (F_6^{\gamma_6}) (F_7^{\gamma_7}) \quad (44)$$

where,

F_1 = Load rating ratio

F_2 = Load rating rate of change

F_3 = Behavior change

F_4 = Service level stress rate of change

F_5 = Service level stress margin

F_6 = Expert opinion

F_7 = Reduced uncertainty

γ_1 to γ_7 = weighting factors associated with F_1 to F_7 , respectively

The first five of the seven parameters— F_1 through F_5 —are calculated from the outputs of the SHM system (i.e., load rating ratio, average load rating rate of change, behavior change, service level stress rate of change, and service level stress margin). These are updated in a real-time or near real-time fashion to reflect the most up-to-date bridge condition and performance information. The other two parameters (F_6 and F_7) are user inputs that are designed to reflect the bridge owner’s opinion as to how the SHM data should affect maintenance decision making.

9.2.1.1. SHMM Parameters F_1 to F_7

- F_1 : Load rating ratio

$$\text{Load Rating Ratio, } F_1 = \frac{\text{Final Average Monitored Load Rating}}{\text{Codified Load Rating}} \quad (45)$$

F_1 is the ratio of the load rating determined by using the SHM system divided by the load rating based on codified provisions. In most cases, this ratio is greater than 1.0 and, as such, demonstrates how valuable SHM data can be in accurately reflecting actual bridge behavior and performance.

- F_2 : Load rating rate of change = 1 + average load rating rate of change

Average load rating rate of change is an output of the SHM system. It reflects the general trend in bridge capacity change, including both magnitude and rate of change over time. Due to

structural deterioration, the value of the average load rating rate of change is, in general, expected to be negative with a very small absolute value.

F_2 is defined as $1 +$ average load rating rate of change. For example, in the demonstration system application that follows, the average load rating rate of change since system installation is -0.3% . F_2 is, therefore, calculated as 99.7% . A factor smaller than 1.0 would be applied in the SHMM calculation to reduce the final ranking index and reflect the gain in maintenance priority due to the decrease in structural capacity.

- F_3 : Behavior change

The F_3 parameter reflects how much the system performance is deviating from its baseline performance. Using the BECAS system, this parameter is defined as one minus the smaller value of the violation rates calculated from the F-test and the strain range method. A higher violation rate indicates a more significant deviation from the system's baseline level, and, as a result, a higher maintenance priority should be assigned. For example, when the violation rate is 2% , the behavior change parameter (F_3) would be 98% . This value is always less than or equal to 1 .

- F_4 : Service level stress rate of change = $1 -$ service level stress rate of change

Service level stress rate of change is an output of the SHM system that indicates the change trend in measured maximum strain (i.e., maximum strain in each minute). It could be either positive or negative, and, in general, its absolute value is small. A positive value means the service stress level is going up, and therefore, a higher maintenance priority is appropriate, and vice versa.

- F_5 : Service level stress margin

$$\text{Service Level Stress Margin, } F_5 = \frac{\text{Codified Strain of HS20 with impact}}{\text{Max Monitored Strain}} \quad (46)$$

F_5 is a measure of how the predicted service level strain compares with the measured strains. A value greater than 1.0 indicates that the designed live load strain is higher than the monitored service level live load strain. A larger value indicates that the structural system has a higher live load capacity reserve, and therefore, a lower maintenance priority can be assigned.

- F_6 : Expert opinion (1.25)

The F_6 parameter is used to allow a trained SHM engineer to provide an expert analysis of all of the collected data, which can then be used to increase or decrease the maintenance priority. In an operational sense, the expert opinion factor would be determined by the organization preparing an annual summary report based on the collected data.

- F_7 : Reduced uncertainty (default value $1/0.85$)

By using the real-time or near real-time bridge condition/performance data collected by an SHM system in maintenance decision making, the uncertainty of bridge performance is reduced. This factor is applied to offset the uncertainties introduced during codified calculation.

9.2.1.2. Use of the Weighting Factors γ_1 to γ_7

A weighting factor value can be applied to each of the F_1 to F_7 values parameters to reflect the priorities of an individual agency. In some ways, this can be considered as representing the values of the agency. For example, if capacity is the highest priority, the weighting factor values for the capacity-related parameters can be adjusted to reflect that.

In the demonstration application shown in Section 9.3, the value of γ_1 is set to 1.0. This reflects a baseline value of the weighting factor and indicates that the user wants to take full advantage of the factor of F_1 . A weighting factor higher than 1.0 indicates a higher maintenance decision-making impact, while 0 means that the user does not want that specific factor to play any role in decision making.

In the demonstration application shown in Section 9.3, γ_2 through γ_4 are set to 2, because F_2 , F_3 , and F_4 all represent long-term global changes to a structure. Their impacts on maintenance decision making are profound. The values of F_2 through F_4 are typically stable and close to 1.0. However, any significant change in these factors' parameter values indicates sizable structural performance changes that should be given significant attention.

When one factor parameter value is significantly larger than other factors, to prevent it from overwhelmingly affecting the final ranking index, a smaller weighting factor should be assigned to it. In the demonstration development bridge application, γ_5 is set to 0.2 to roughly normalize its impact to be equivalent to the impact of F_7 .

9.2.2. Use of the SHMM Calculation

The equation for the SHMM is given below. As described below, the equation contains seven factors coupled with seven weighting factors. The combination of quantitative data and user configurability with the calculation for the SHMM (equation (47)) allows an owner agency to customize its approach to meet agency goals.

$$\text{SHMM} = (F_1^{\gamma_1}) (F_2^{\gamma_2}) (F_3^{\gamma_3}) (F_4^{\gamma_4})(F_5^{\gamma_5}) (F_6^{\gamma_6}) (F_7^{\gamma_7}) \quad (47)$$

A product equation rather than a summation equation is used in the SHMM calculation for two major reasons: (1) all of the factors used in the calculation are ratios or percentages instead of differences, and (2) research has shown that simple multiplication can avoid the complicated normalization procedure for each factor and still keep the final ranking reasonable (Tofallis 2015).

The meaning and typical values of F_1 to F_7 and γ_1 to γ_7 were discussed in the previous section. The computed SHMM is then applied as a modifier in the computation of the ranking index to show the impacts of SHM. For bridges without an SHM system installed, the SHMM has a value of one. By comparing ranking indexes among bridges, the condition-based maintenance priorities are established.

9.3. Demonstration Application

As a demonstration, an Excel spreadsheet was developed using 21 bridges from the Iowa bridge inventory. Twenty of the bridges are not configured using the BECAS SHM system, and one bridge has the SHM system available (the I-80 Sugar Creek Bridge, FHWA #22380). In this application, IIs are obtained from NBI data, and the SHMM is calculated with the inputs from the SHM system and the user-configurable weighting factors.

For the II, the user has the opportunity to select either SR or BCI. Either of these is directly importable from the NBI data and has a value between 0 and 100 for any bridge. Table 9.2 and Figure 9.2 present the SR and BCI for each of the 21 bridges. As can be seen from Figure 9.2, the SR and BCI share similar change trends.

Table 9.2. SR and BCI of all 21 bridges

Bridge index	FHWA #	SR	BCI
1	3410	48.40	47.40
2	3825	57.00	40.70
3	3826	58.80	51.20
4	4111	88.80	78.80
5	4271	99.30	92.20
6	7901	80.10	69.60
7	7911	79.40	59.30
8	12411	85.00	80.90
9	12491	96.90	81.10
10	12511	98.20	84.20
11	12920	74.40	60.70
12	12970	42.70	43.50
13	12980	68.60	55.20
14	12990	68.10	57.20
15	13010	46.70	92.90
16	13040	61.50	59.70
17	13050	74.80	61.10
18	13060	74.10	64.60
19	13101	97.00	85.10
20	13111	97.00	84.10
21	22380	96.30	70.00

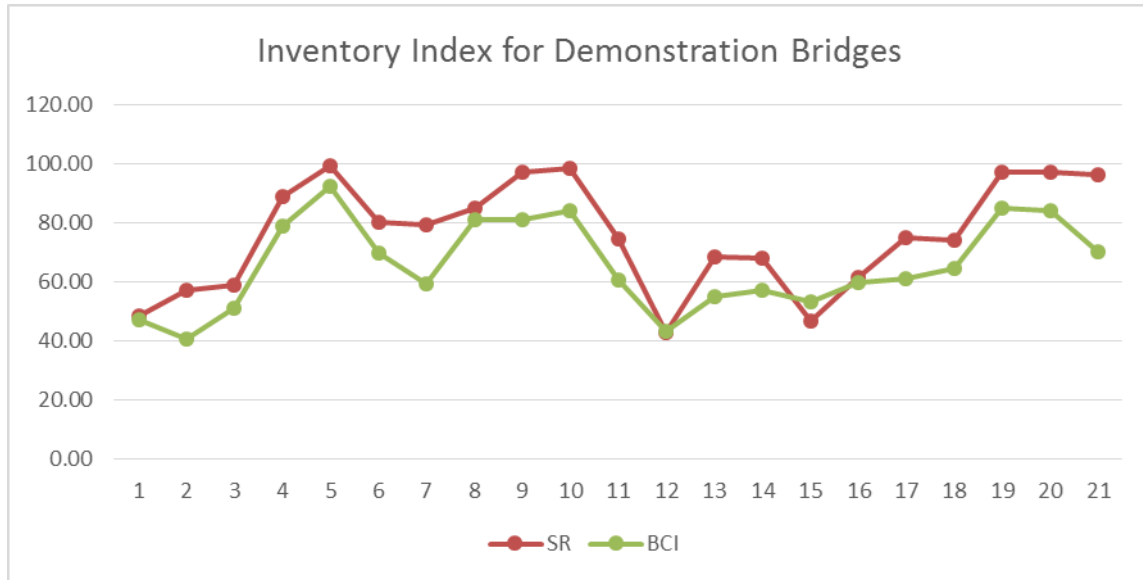


Figure 9.2. SR and BCI of all 21 demonstration bridges

For the 20 bridges without SHM instrumentation, the SHMM is simply 1.0. That means that the maintenance priorities of the bridges are totally determined by bridge inventory data.

For the instrumented bridge (FHWA #22380), the SHMM is calculated by using the SHM input data, which are represented by F_1 to F_5 , along with the user inputs for F_6 (expert opinion parameter) and F_7 (reduced uncertainty parameter). A snapshot of the values of F_1 to F_5 (which are updated in real-time or near real-time) and typical values of F_6 and F_7 for the demonstration bridge are shown in Table 9.3.

Table 9.3. Values of F_1 to F_7 used in SHMM computation for bridge FHWA#22380

Parameters	Value	Weighting factor
F_1 (load rating ratio)	1.37	1
F_2 (load rating rate of change factor)	0.997	2
F_3 (behavior change factor)	0.98	2
F_4 (service level stress rate of change factor)	1.000001	2
F_5 (service level stress margin)	1.68	0.2
F_6 (expert opinion factor)	1.25	1
F_7 (reduced uncertainty factor)	1.18	1

The values of the weighting factors that are associated with F_1 to F_7 are also presented in Table 9.3 in the right-hand column.

F_1 (load rating ratio) = 1.37 indicates that at the specific time, the monitored load rating is 37% higher than the codified load rating. In the SHMM computation, any factor with a value larger

than one will potentially increase the final ranking index and thereby reduce the maintenance priority. F_1 is used here to reflect the maintenance priority impact caused by the monitored live load capacity. A weighting factor of 1 is used for F_1 to show that the extra live load capacity gained from SHM should be fully used in maintenance decision making.

F_2 (load rating rate of change) = 0.997. The monitored load rating has decreased by 0.3% annually since the SHM system was installed, and F_2 is calculated as $1 - 0.3\% = 0.997$. The generally decreasing trend in load rating indicates an increasing demand for maintenance. The value slightly smaller than 1 is applied to show this impact.

F_3 (behavior change) = 0.98 because the maximum strain range violation rate is 2% since the installation of the system. This violation rate of 2% is the smaller of the violation rates obtained from different violation rules. A higher violation rate indicates a more significant deviation of the structural performance from its baseline (i.e., as-designed performance), and therefore, a higher maintenance priority is required.

F_4 (service level stress rate of change) = 1.000001 because the measured maximum strain of each minute for the control location (D2_BF) has been decreasing at a rate of 10^{-6} since the system was installed. The decreasing trend in live load effect indicates a decreasing demand for bridge maintenance.

The values of F_2 to F_4 are typically stable and close to one. But once any of the factors show a significant change, it is an indication of a significant structural change, and therefore, more attention should be paid to maintenance decision making. Values larger than one are more appropriate for γ_2 to γ_4 . In this demonstration application, values of 2 are used.

F_5 (service level stress margin) = 1.68 indicates that the codified HS-20 strain at the control location is 68% higher than the monitored maximum strain. This factor measures the margin between the strain produced by the HS-20 truck and the maximum strain to which the bridge has been exposed. A larger value indicates a larger capacity reservation and, therefore, that a longer service life can be expected and the maintenance priority can be lowered. The value of F_5 can be large and can drop significantly due to a single event, so a relatively smaller weight factor is appropriate. The value of 0.2 is used here to roughly normalize its impact to the same level of F_7 .

F_6 (expert opinion) and F_7 (reduced uncertainty) are the two user-input parameters in this system. Values of 1.25 and 1.18 are used, respectively, in this demonstration application. The expert opinion parameter was set at 1.25 after reviewing all available data and making an expert assessment of bridge performance. The value of the reduced uncertainty parameter was set to $1/0.85$ (1.18) to offset the uncertainties introduced during codified calculation. Weighting factors of 1 are used for these two parameters.

Using the values of F_1 to F_7 and γ_1 to γ_7 shown in Table 9.3, the SHMM and the final ranking index are summarized in Table 9.4.

Table 9.4. Ranking index with $\gamma_1, 6, 7 = 1, \gamma_2$ to $\gamma_4 = 2,$ and $\gamma_5 = 0.2$

	SR	BCI
FHWA #22380	96.30	70.00
SHMM	2.14	2.14
Ranking index	206.08	149.80

A ranking index higher than 100 indicates that the replacement priority of the bridge is lower than that of the bridges with an SR or BCI equal to 100.

Table 9.5 and Table 9.6 show bridge age data as related to the SR and the BCI of the bridge.

Table 9.5. SR and corresponding bridge age

SR	Average bridge age	Std dev
96.30	38.6	8.1
100	18.1	12.6

Table 9.6. BCI and corresponding bridge age

BCI	Average bridge age	Std dev
70.00	39.1	15.2
100	2	0

The average age for bridges with SR = 100 is 18.1 years, and the average age is 38.6 when SR = 96.3. When the bridge's ranking index increases from 96.3 (without SHM) to > 100 (with SHM), the equivalent bridge age is reduced by at least 20 years. That may mean that bridge replacement can be postponed by 20 years because the bridge is performing notably better than expected. Similarly, when the BCI is used as the II, results show that bridge replacement may be able to be postponed by 37 years.

CHAPTER 10. SUMMARY, CONCLUSIONS, AND RECOMMENDATIONS

10.1. Summary

Approximately 11% of bridges in the US are categorized as structurally deficient. There is a marked need to realistically evaluate the true structural capacity of bridges to provide a high fidelity bridge preservation tool. The FHWA requires that bridges carrying a public road should be regularly inspected and evaluated for safety within an interval of no more than two years. However, visual inspections are difficult to perform, can put the traveling public in dangerous roadway situations, and require inspectors to work in somewhat precarious situations. Many transportation agencies have been interested and active in finding methods to evaluate bridge damage and the associated impact on the effectiveness of the bridge to provide service.

The literature shows many examples of general load testing methods and bridge maintenance and assessment to manage bridge inventories. One option for managing bridges identified as structurally deficient is to perform diagnostic load testing to more accurately assess load carrying ability. Frequently, diagnostic load tests reveal strength and serviceability characteristics that exceed those predicted with codified parameters. Usually, codified parameters are very conservative at predicting lateral load distribution characteristics and the influence of other structural attributes. As a result, the predicted rating factors are often conservative.

SHM systems can provide a timely indication of the need for maintenance, repair, rehabilitation, and replacement of bridges and can greatly improve the apportionment and management of limited resources. Beginning approximately 20 years ago, the BEC at Iowa State University, in cooperation with the Iowa DOT, has worked toward developing and evolving an autonomous SHM system to assess the safety of bridge structures and to determine the remaining life of bridges. This research report was funded by a transportation pooled fund (TPF) program with multiple DOTs, the FHWA, and the U.S. Department of Agriculture (USDA) Forest Products Laboratory. An automated ambient traffic (AAT) approach is used for determining load rating of and for identifying damage to bridges monitored by the BECAS SHM system under ambient traffic.

The AAT approach was developed through a process integration of truck detection, bridge model calibration, bridge load rating, real-time evaluation of bridge response, and statistical evaluation of changes in behavior over time. The quasi-static bridge strain response and the characteristics of associated trucks are collected, and multiple trucks are randomly sampled from a historic weigh-in-motion (WIM) database as well as a bridge-specific training period. For each combination of strain response and truck selection, a finite element (FE) model and/or a statistical model is calibrated and used to calculate a load rating and to determine if changes in condition have occurred. Sampling strategies were discussed for appropriately quantifying the influence of uncertainties of truck characteristics on the calibration and load rating results. It was concluded that the AAT approach using the BECAS SHM system is a reliable method for continuously estimating the load carrying capacity of bridges.

10.2. Conclusions

Based on past performance of the SHM system in implementation over approximately the past five years, the system is working well and providing useful information for bridge engineers. The SHM system provides comprehensive and significant information for assessing bridge condition in real time. The SHM system has multiple capabilities including (1) bridge engineering condition assessment, (2) truck detection methodology, (3) strain-based damage detection, (4) changes in bridge behavior, (5) load rating using ambient traffic, (6) prediction of bridge condition ratings, and (7) bridge condition-based prioritization system using SHM and CBM.

A brief and specific list of observations will be useful for bridge engineers and provides some general detail of how the data may be of use. The observations are as follows:

- Identify the percent of truck events within a driving lane (e.g., the driving lane is typically very large compared to other lanes on a bridge).
- Identify the highest stressed location on a girder (typically occurs in a driving lane). Inspections can be performed more effectively with these data.
- Identify bridge usage (based on one-minute maximum, minimum, and strain range). These data allow engineers to address fatigue in the bridge, particularly for fracture critical bridges.
- Identify threshold exceedances that can show that large strain events do occur with three or more trucks on a bridge at the same time. During construction activity, these exceedances can result in closing one of the normal traffic lanes.
- Identify load ratings with the collected data in real time, and the data can show changes in the load rating over time.
- Identify critical areas on the bridge using the long-term data. For an example, the strain data could alert the bridge engineer that a bearing is frozen or partially frozen, or some other structural anomaly. Over time, it is possible to create excessive stresses at the abutment.

10.3. Recommendations

A recently developed comprehensive SHM system has been implemented on current bridges within multiple states. These bridges provide an opportunity to evaluate the potential effectiveness of the bridge evaluation system. This new system requires a commitment and investment to implement the SHM system. The hardware and software are commercially available. Appropriate staffing is needed to implement the field and office hardware and software, as well as identifying staffing to manage and process the significant data.

REFERENCES

- AASHTO. 2009. *The Bottom Line Report*. American Association of State Highway and Transportation Officials, Washington, DC.
- AASHTO. 2014. *LRFD Bridge Design Specifications*, 7th Edition. American Association of State Highway and Transportation Officials, Washington, DC.
- AASHTO. 2015. *Manual for Bridge Evaluation*, 2nd Edition. American Association of State Highway and Transportation Officials, Washington, DC.
- AASHTO. 1996. *Standard Specifications for Highway Bridges*, 16th Edition. American Association of State Highway and Transportation Officials, Washington, DC.
- ACI Committee 318. 2014. *Building Code Requirements for Structural Concrete*. ACI 318-14. American Concrete Institute, Farmington Hills, MI.
- Adey, B. T., L. Klatter, and J. S. Kong. 2010. *Overview of Existing Bridge Management Systems*. The International Association for Bridge Maintenance and Safety (IABMAS) Bridge Management Committee.
- AISC. 2015. *Steel Construction Manual*, 14th Edition. American Institute of Steel Construction, Chicago, IL.
- Aktan, A. E., D. N. Farhey, D. L. Brown, V. Dalal, A. J. Helmicki, V. J. Hunt, and S. J. Shelley. 1996. Condition Assessment for Bridge Management. *Journal of Infrastructure Systems*, Vol. 2, No. 3, pp.108–117.
- Aktan, A. E., A. J. Helmicki, and V. J. Hunt. 1998. Issues in Health Monitoring for Intelligent Infrastructure. *Smart Materials and Structures*, Vol. 7, No. 5, pp. 674–692.
- ASCE. 2017. *The American Infrastructure Report Card*. American Society of Civil Engineers, Reston, VA.
- ASTM A992/A992M *Standard Specification for Structural Steel Shapes*. ASTM International, West Conshohocken, PA.
- ASTM A1010/A1010M *Standard Specification for Higher-Strength Martensitic Stainless Steel Plate, Sheet, and Strip*. ASTM International, West Conshohocken, PA.
- ASTM A709/A709M *Standard Specification for Structural Steel for Bridges*. ASTM International, West Conshohocken, PA.
- ASTM A370 *Standard Test Methods and Definitions for Mechanical Testing of Steel Products*. ASTM International, West Conshohocken, PA.
- ASTM E8/E8M *Standard Test Methods for Tension Testing of Metallic Materials*. ASTM International, West Conshohocken, PA.
- ASTM C39/C39M *Standard Test Method for Compressive Strength of Cylindrical Concrete Specimens*. ASTM International, West Conshohocken, PA.
- ASTM C469 *Standard Test Method for Static Modulus of Elasticity and Poisson's Ratio of Concrete in Compression*. ASTM International, West Conshohocken, PA.
- Bartlett, F. M., R. J. Dexter, M. D. Graeser, J. J. Jelinek, B. J. Schmidt, and T. V. Galambos. 2003. Updating Standing Shape Material Properties Database for Design and Reliability. *Engineering Journal*, Vol. 40, pp. 2–14.
- Benedettini, O., T. S. Baines, H. W. Lightfoot, and R. M. Greenough. 2009. State-of-the-Art in Integrated Vehicle Health Management. *Proceedings of the Institution of Mechanical Engineers, Part G: Journal of Aerospace Engineering*, Vol. 223, No. 2, pp.157–170.

- Bentley Systems, Inc. n.d. *LARS Bridge: Load-Rating for Better Bridges*. Bentley Systems, Inc., Exton, PA. <https://www.bentley.com/en/products/product-line/bridge-analysis-software/lars-bridge>
- Bridge Diagnostics Inc. (BDI). 2003. *Integrated Approach to Load Testing Instruction Manual*. Boulder, CO.
- Cadick, J. and G. Traugott. 2009. *Condition-Based Maintenance: A White Paper Review of CBM Analysis Techniques*. Technical Bulletin TB-017. Cadick Corporation, Garland, TX.
- Carroll, R. J. and D. Ruppert. 1996. The Use and Misuse of Orthogonal Regression in Linear Errors-in-Variables Models. *The American Statistician*, Vol. 50, No. 1, pp. 1–6.
- Castro, J. M., A. Y. Elghazouli, and B. A. Izzuddin. 2007. Assessment of Effective Slab Widths in Composite Beams. *Journal of Constructional Steel Research*, Vol. 63, No. 10, pp. 1317–1327.
- Catbas, F. N., R. Zaurin, M. Susoy, and M. Gul. 2007. *Integrative Information System Design for Florida Department of Transportation: A Framework for Structural Health Monitoring of Movable Bridges*. University of Central Florida, Orlando, FL.
- Chajes, M. J., D. R. Mertz, and B. Commander. 1997. Experimental Load Rating of a Posted Bridge. *Journal of Bridge Engineering*, Vol. 2, No. 1, pp. 1–10.
- Connor, R. J. and J. R. McCarthy. 2006. *Report on Field Measurements and Uncontrolled Load Testing of the Lehigh River Bridge (SR-33)*. ATLSS Report No. 06-12. Advanced Technology for Large Structural Systems Engineering Research Center, Lehigh University, Bethlehem, PA.
- Connor, R. J. and B. J. Santosuosso. 2002. *Field Measurements and Controlled Load Testing on the Lehigh River Bridge (SR-33)*. ATLSS Report No. 02-07. Advanced Technology for Large Structural Systems Engineering Research Center, Lehigh University, Bethlehem, PA.
- Deraemaekera, A., E. Reynders, G. De Roeck, and J. Kullaa. 2008. Vibration-Based Structural Health Monitoring Using Output-Only Measurements under Changing Environment. *Mechanical Systems and Signal Processing*, Vol. 22, No. 1, pp. 34–56.
- Doornink, J. D. 2006. Monitoring the Structural Condition of Fracture-Critical Bridges Using Fiber Optic Technology. PhD dissertation. Iowa State University, Ames, IA. [43] [33]
- Dunker, K. F. and B. G. Rabbat. 1993. Why America's Bridges are Crumbling. *Scientific American*, Vol. 268, No. 3, pp. 66–72.
- Fanouf, F., L. F. Greimann, D. Petermeier, and Z. Yuan. 1991. *Essential Parameters for an Iowa Bridge Management System*. Midwest Transportation Center, Iowa Transportation Center, Iowa State University, Ames, IA.
- FHWA. 1993. *The Status of the Nation's Highways, Bridges, and Transit: Conditions and Performance*. FHWA-PL-93-017. Federal Highway Administration, Washington, D.C.
- FHWA. 1995. *Recording and Coding Guide for the Structure Inventory and Appraisal of the Nation's Bridges*. FHWA-PD-96-001. Federal Highway Administration, Washington, DC.
- Fugate, M. L., H. Sohn, and C. R. Farrar. 2001. Vibration-Based Damage Detection Using Statistical Process Control. *Mechanical Systems and Signal Processing*, Vol. 15, No. 4, pp. 707–721.
- Fuller, W. A. 1987. *Measurement Error Models*. John Wiley & Sons, Inc., Hoboken, NJ.
- Ghasemi, H., J. Penrod, and J. M. Hooks. 2009. Developing Advanced Methods of Assessing Bridge Performance. *Public Roads*, Vol. 73, No. 3.

- Gupta, V. K., Y. Okui, N. Inaba, and M. Nagai. 2007. Effect of Concrete Crushing on Flexural Strength of Steel-Concrete Composite Girders. *Doboku Gakkai Ronbunshuu A*, Vol. 63, No. 3, pp. 475–485.
- Harman, D. 1981. The Aging Process. *Proceedings of the National Academy of Sciences of the United States of America*, Vol. 78, No. 11, pp. 7124–7128.
- IAEA. 2007. *Implementation Strategies and Tools for Condition Based Maintenance at Nuclear Power Plants*. IAEA-TECDOC-1551. International Atomic Energy Agency, Vienna, Austria.
- Ikegami, R., and E. D. Haugse. 2001. Structural Health Management for Aging Aircraft. *SPIE's 8th Annual International Symposium on Smart Structures and Materials*, August, pp.60–67.
- Kareem, A., T. Kijewski, and Y. Tamura. 1999. Mitigation of Motions of Tall Buildings with Specific Examples of Recent Applications. *Wind and Structures*, Vol. 2, No. 3, pp.201–251.
- Kijewski-Correa, T. and M. Kochly. 2007. Monitoring the Wind-Induced Response of Tall Buildings: GPS Performance and the Issue of Multipath Effects. *Journal of Wind Engineering and Industrial Aerodynamics*, Vol. 95, No. 9, pp.1176–1198.
- Kijewski-Correa, T., D. K. Kwon, A. Kareem, A. Bentz, Y. Guo, S. Bobby, and A. Abdelrazaq. 2013. SmartSync: An Integrated Real-Time Structural Health Monitoring and Structural Identification System for Tall Buildings. *Journal of Structural Engineering*, Vol. 139, No. 10, pp.1675–1687.
- Kijewski-Correa, T. and J. D. Pirnia. 2007. Dynamic Behavior of Tall Buildings under Wind: Insights from Full-Scale Monitoring. *The Structural Design of Tall and Special Buildings*, Vol. 16, No. 4, pp.471–486.
- Koch, P. N. 2002. *Probabilistic Design: Optimizing for Six Sigma Quality*. 43rd AIAA/ASME/ASCE/AHS/ASC Structures, Structural Dynamics, and Materials Conference, April 22–25, Denver, CO.
- Kullaa, J. 2003. Damage Detection of the Z24 Bridge Using Control Charts. *Mechanical Systems and Signal Processing*, Vol. 17, No. 1, pp. 163–170.
- Lu, P. 2008. A Statistical Based Damage Detection Approach for Highway Bridge Structural Health Monitoring. PhD dissertation. Iowa State University, Ames, IA.
- Lu, P., B. Phares, L. Greimann, and T. Wipf. 2010. Bridge Structural Health-Monitoring System Using Statistical Control Chart Analysis. *Transportation Research Record: Journal of the Transportation Research Board*, No. 2172, pp.123–131.
- Lu, P., B. M. Phares, T. J. Wipf, and J. D. Doornink. 2007. A Bridge Structural Health Monitoring and Data Mining System. *Proceedings of the 2007 Mid-Continent Transportation Research Symposium*, August 16–17, Ames, IA.
- Magalhães, F., A. Cunha, and E. Caetano. 2012. Vibration Based Structural Health Monitoring of an Arch Bridge: From Automated OMA to Damage Detection. *Mechanical Systems and Signal Processing*, Vol. 28, pp. 212–228.
- Mans, P., A. J. Yakel, and A. Azizinamini. 2001. Full-Scale Testing of Composite Plate Girders Constructed Using 485-MPa High-Performance Steel. *Journal of Bridge Engineering*, Vol. 6, No. 6, pp. 598–604.
- Melcher, J., Z. Kala, M. Holický, M. Fajkus, and L. Rozlívka. 2004. Design Characteristics of Structural Steels Based on Statistical Analysis of Metallurgical Products. *Journal of Constructional Steel Research*, Vol. 60, Nos. 3–5, pp. 795–808.

- Mishalani, R. G. and S. M. Madanat. 2002. Computation of Infrastructure Transition Probabilities Using Stochastic Duration Models. *Journal of Infrastructure Systems*, Vol. 8, No. 4, pp. 139–148.
- Mosavi Khandan Haghghi, A. A. 2010. Vibration-Based Damage Detection and Health Monitoring of Bridges. PhD dissertation. North Carolina State University, Raleigh, NC.
- Ni, Y. Q. and K. Y. Wong. 2012. Integrating Bridge Structural Health Monitoring and Condition-Based Maintenance Management, *Proceedings of the Civil Structural Health Monitoring Workshop (CSHM-4)*, Berlin, Germany.
- Nie, J.-G., C.-Y. Tian, and C. S. Cai. 2008. Effective Width of Steel–Concrete Composite Beam at Ultimate Strength State. *Engineering Structures*, Vol. 30, No. 5, pp. 1396–1407.
- NYSDOT. 2010. Pavement Condition Assessment. V2.0w, New York State Department of Transportation, Albany, NY.
- Okasha, N. M. and D. M. Frangopol. 2012. Integration of Structural Health Monitoring in a System Performance Based Life-Cycle Bridge Management Framework. *Structure and Infrastructure Engineering*, Vol. 8, No. 11, pp. 999–1016.
- Phares, B. M., T. J. Wipf, P. Lu, L. Greimann, and M. Pohlkamp. 2011. *An Experimental Validation of a Statistical-Based Damage-Detection Approach*. Bridge Engineering Center, Iowa State University, Ames, IA.
- Phares, B. 2001. *Highlights of Study of Reliability of Visual Inspection. Presentation at the Annual Meeting of TRB Subcommittee A2C005(1): Non-Destructive Evaluation of Structures*. (Report is also available from the FHWA Turner-Fairbanks Research Center).
- Ramey, G. E. and R. L. Wright. 1997. Bridge Deterioration Rates and Durability/Longevity Performance. *Practice Periodical on Structural Design and Construction*, Vol. 2, No. 3, pp. 98–104.
- Roberts, N. R. 2004. Evaluation of the Ductility of Composite Steel I-Girders in Positive Bending. MS thesis. West Virginia University, Morgantown, WV.
- Rytter, A. 1993. Vibrational Based Inspection of Civil Engineering Structures. PhD dissertation. Aalborg University, Aalborg, Denmark.
- Salama, T. and H. H. Nassif. 2011. Effective Flange Width for Composite Steel Beams. *Journal of Engineering Research*, Vol. 8, No. 1, pp. 28–43.
- Sohn, H. C. R. Farrar, F. M. Hemez, D. D. Shunk, D. W. Stinemates, B. R. Nadler, and J. J. Czarnecki. 2004. *A Review of Structural Health Monitoring Literature: 1996–2001*. LA-13976-MS. Los Alamos National Laboratory, Los Alamos, NM.
- Spencer, B. F., Jr. and S. Nagarajaiah. 2003. State of the Art of Structural Control. *Journal of Structural Engineering*, Vol. 129, No. 7.
- Tennant, G. 2001. *Six Sigma: SPC and TQM in Manufacturing and Services*. Gower Publishing, Ltd., Aldershot, UK.
- Tofallis, C. 2015. A Better Measure of Relative Prediction Accuracy for Model Selection and Model Estimation. *Journal of the Operational Research Society*, Vol. 66, pp. 1352–1362.
- Vis, J. M. 2007. Evaluation of a Structural Health Monitoring System for Steel Girder Bridges. Creative component report. Iowa State University, Ames, IA.
- Wipf, T. J., B. M. Phares, J. D. Doornink, L. F. Greimann, and D. L. Wood. 2007. Evaluation of Steel Bridges (Volume I): Monitoring the Structural Condition of Fracture-Critical Bridges using Fiber Optic Technology. Bridge Engineering Center, Iowa State University, Ames, IA.

- Wiśniewski, D., P. J. S. Cruz, A. A. R. Henriques, and R. A. D. Simões, 2012. Probabilistic Models for Mechanical Properties of Concrete, Reinforcing Steel and Pre-Stressing Steel. *Structure and Infrastructure Engineering*, Vol. 8, No. 2, pp. 111–123.
- Wittry, D. M. 1993. An Analytical Study of the Ductility of Steel Concrete. MS thesis. University of Texas at Austin, Austin, TX.
- Xu, J. and L. Xu. 2013. Integrated System Health Management-Based Condition Assessment for Manned Spacecraft Avionics. *Proceedings of the Institution of Mechanical Engineers, Part G: Journal of Aerospace Engineering*, Vol. 227, No. 1, pp. 19–32.
- Xu, J., F. Guo, and L. Xu. 2013. Integrated System Health Management-Based State Evaluation for Environmental Control and Life Support System in Manned Spacecraft. *Proceedings of the Institution of Mechanical Engineers, Part I: Journal of Systems and Control Engineering*, Vol. 227, No. 5, pp.461–473.
- Yakel, A. J. and A. Azizinamini. 2005. Improved Moment Strength Prediction of Composite Steel Plate Girders in Positive Bending. *Journal of Bridge Engineering*, Vol. 10, No. 1, pp. 28–38.
- Yan, A.-M., G. Kerschen, P. De Boe, and J.-C. Golinval. 2005. Structural Damage Diagnosis under Varying Environmental Conditions—Part I: A Linear Analysis. *Mechanical Systems and Signal Processing*, Vol. 19, No. 4, pp. 847–864.

APPENDIX A. DEMONSTRATION OF AUTOMATED SHM SYSTEM FOR BRIDGES

Data processed using the SHM system for three bridges (I-80 in Iowa, I-280 in Illinois, and US 151 in Wisconsin) are shown in this appendix. The intent is to inform bridge engineers about the availability of useful data from the SHM system.

A.1. Demonstration Bridge 1

A.1.1. Overall Bridge Description

The eastbound I-80 bridge crosses Sugar Creek near a weigh station in Dallas County, Iowa (Figure A.1).



Figure A.1. I-80 bridge

The bridge was built in 1966. The bridge has three spans with an overall span of 208 ft 7 in. out-to-out, with two end spans of 61 ft and a center span of 78 ft. The bridge is a three-span continuous steel girder structure. The bridge width is 42 ft 4 in. out-to-out with a skew of 15 degrees. The concrete deck is 7½ in. thick, supported by five continuous steel girders with girder spacing of 9 ft 6 in.

A.1.2. Instrumentation Plan—I-80 Bridge

The SHM system of Demonstration Bridge 1 consists of 71 electrical resistance strain gauges on the steel girders as shown in Figure A.2.

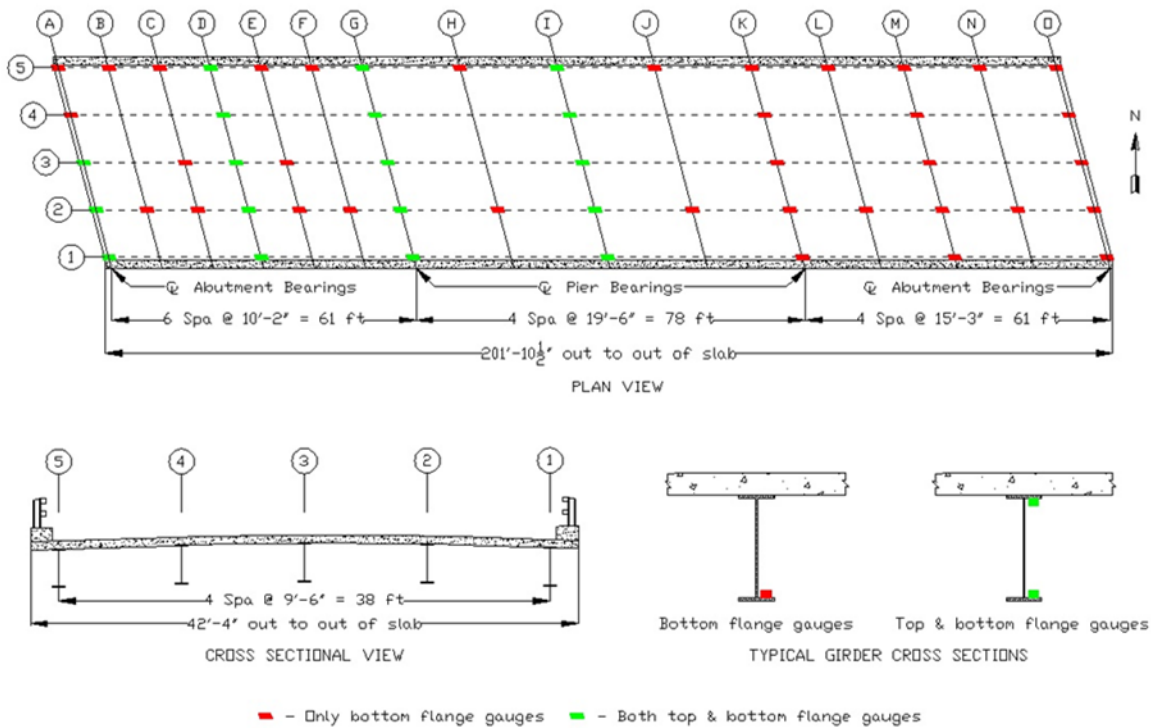


Figure A.2. I-80 bridge, instrumentation plan

In the figure, the red disks represent 35 strain gauges installed only at the top of the bottom flange of the steel girders, whereas, green disks represent the total of 36 strain gauges installed on both top of the bottom flange and bottom of the top flange of steel girders. The bridge cross sections with instrumentation were labeled from A to O, and the girder lines were labeled from 1 to 5. The nomenclature of the sensor designation used to represent strain gauge location by cross section, girder line, and flange location. As an example, sensor designation D2_BF represents a sensor installed at the intersection of cross section D and girder line 2, and at the bottom flange (BF) of the girder, whereas sensor designation D2_TF represents a sensor installed at the intersection of cross section D and girder line 2, and at the top flange (TF) of the girder.

The SHM system of the I-80 bridge also consists of eight electrical resistance strain gauges installed at the bottom of the concrete deck. These strain gauges are in two rows of four strain gauges in each row and are located perpendicular to the girder lines. The deck strain gauges are used to identify the vehicle travel lane, axle number and spacing, and vehicle speed.

A.1.3. Observation Summary of the SHM System

A.1.3.1. Usage

The usage represents the utilization of a bridge by trucks in terms of average summation of recorded strain in each strain gauge throughout the monitoring period. The general measure of bridge usage is expressed using the one-minute maximum, minimum, and strain range data

collected throughout the monitoring period. Usage data for Demonstration Bridge 1 are shown in Figures A.3 through A.5 for years 2015, 2016, and 2017.

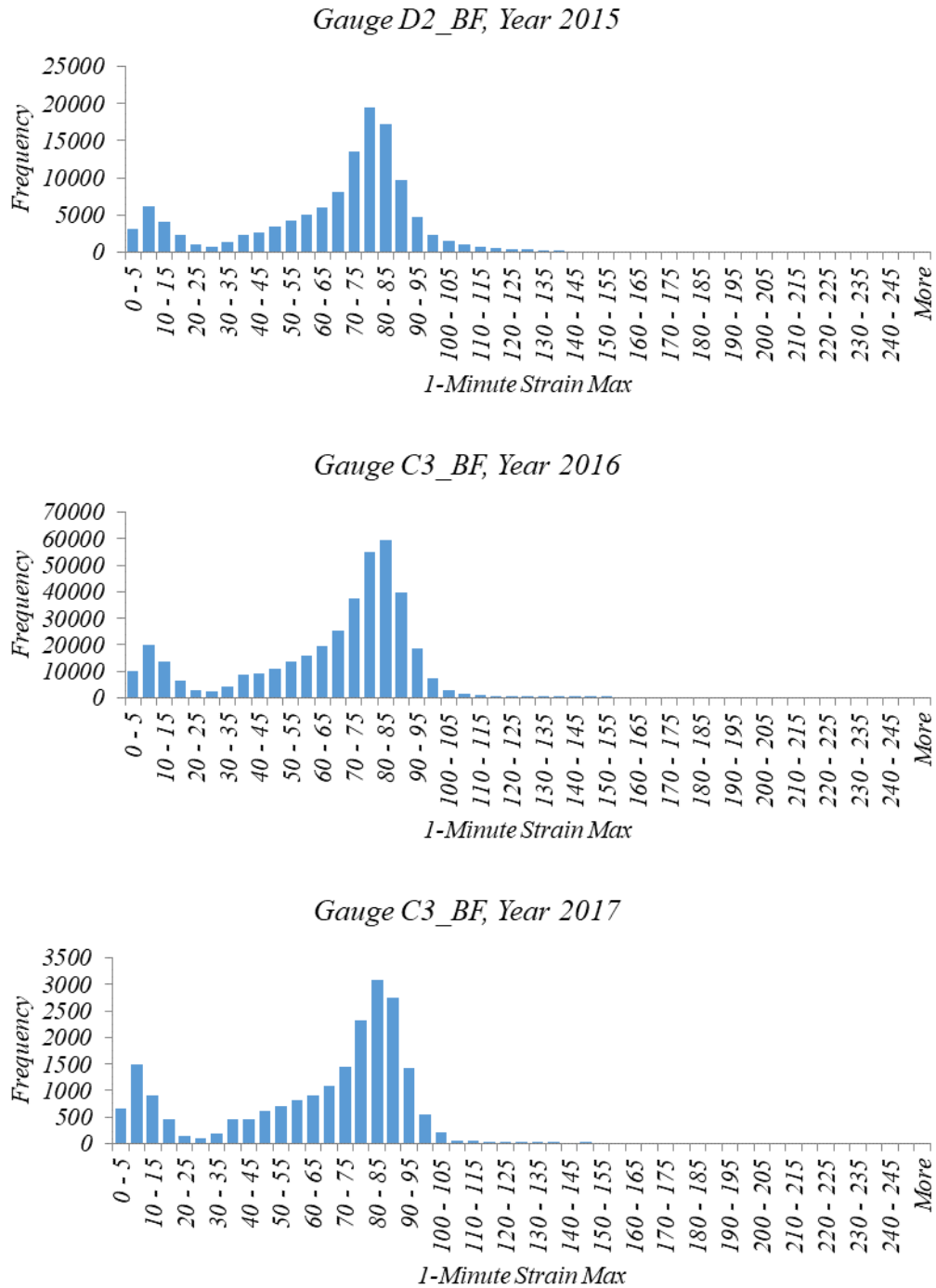
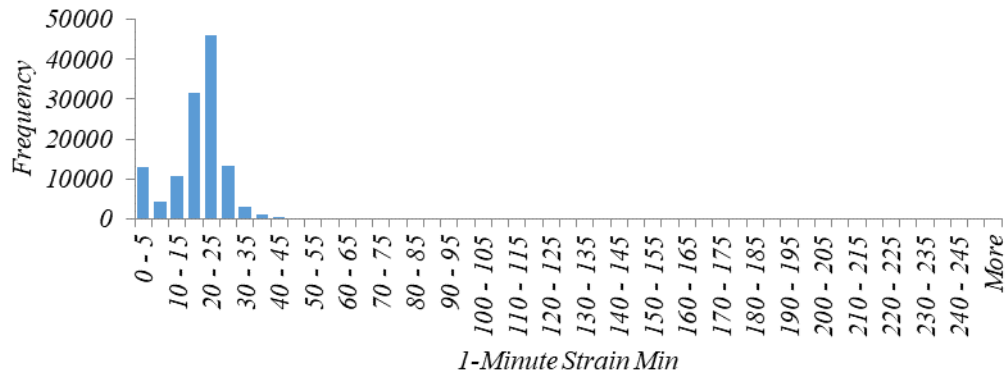
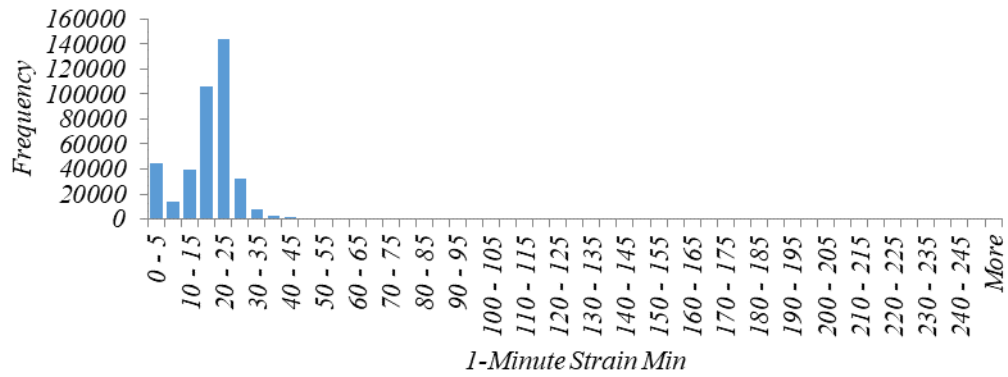


Figure A.3. Demonstration Bridge 1 usage based on maximum strain response

Gauge D2_BF, Year 2015



Gauge C3_BF, Year 2016



Gauge D3_BF, Year 2017

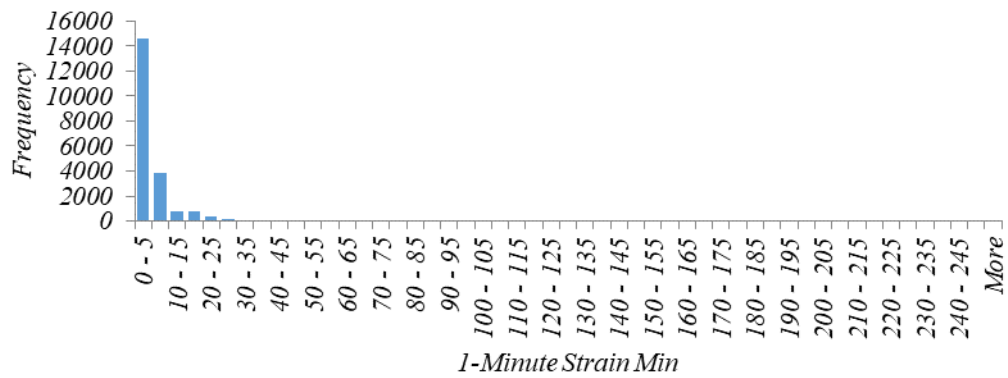


Figure A.4. Demonstration Bridge 1 usage based on minimum strain response

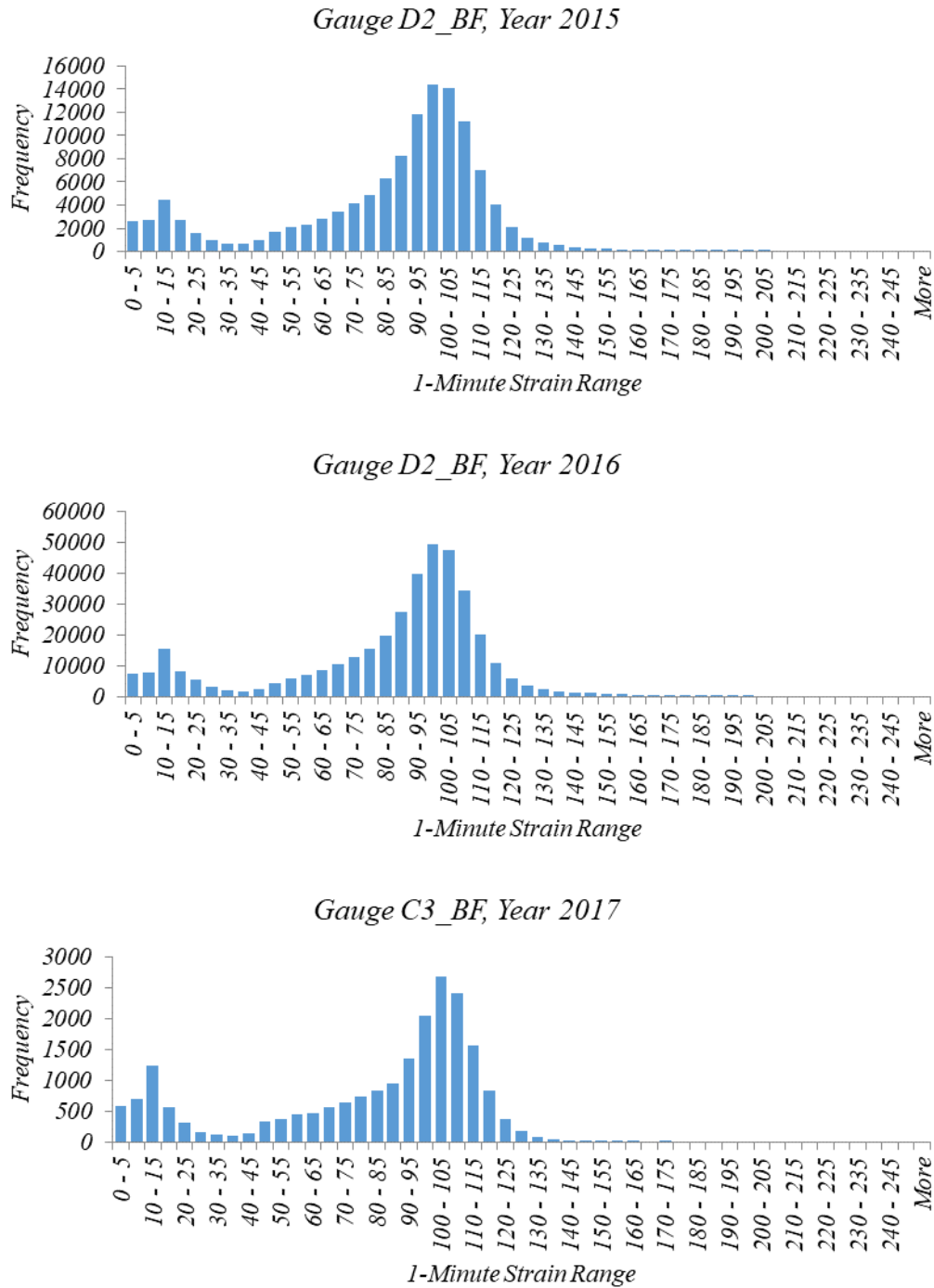


Figure A.5. Demonstration Bridge 1 usage based on strain range response

Throughout the monitoring period, the strain gauges D2_BF and C3_BF showed the highest strains, minimum strain response, and the maximum strain ranges throughout the monitoring period.

A.1.3.2. Load Rating

The load rating of Demonstration Bridge 1 calculated based on the ambient traffic response is shown in Figure A.6.

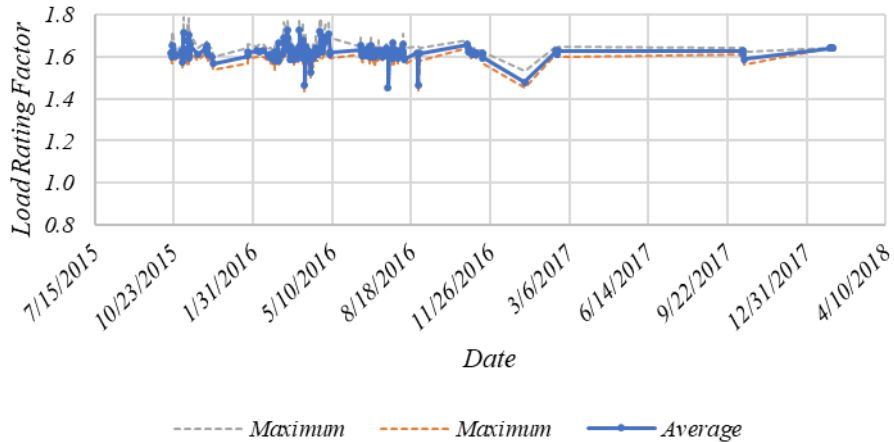


Figure A.6. Demonstration Bridge 1 load rating factor variation

Maximum, minimum, and average load rating factors were calculated. The average load rating of the bridge at the beginning of the monitoring period was 1.61. The average load rating of the bridge at the end of the monitoring period was recorded as 1.64. The average load rating throughout the monitoring period was 1.62 bounded by the average minimum load rating of 1.45 and average maximum load rating of 1.73. Figure A.7 shows the frequency of the load rating factor.

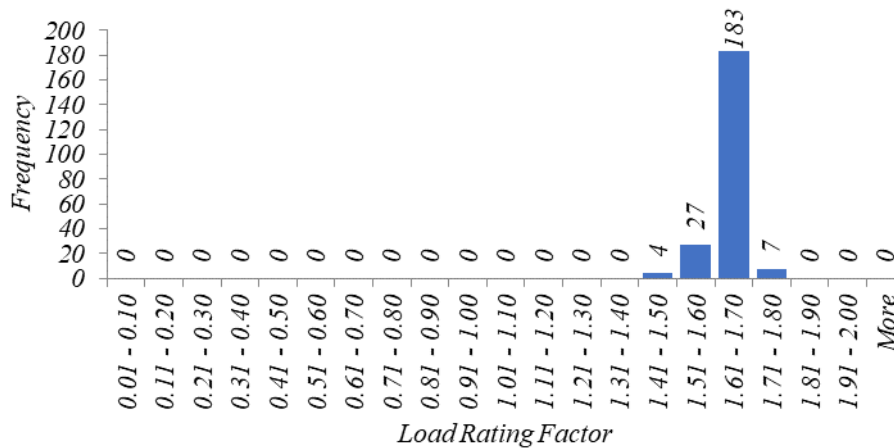


Figure A.7. Demonstration Bridge 1 load rating factor frequency

A.1.3.3. Behavior Change

A significant change in strain change can trigger a rule violation of these methods, suggesting that there is a significant structural change in the bridge at a specific location. Gauge A2_BF and A4_BF show the maximum F-test rule violations during the monitoring period (Figure A.8), and gauge A2_BF shows the maximum strain range rule violations during the monitoring period (Figure A.9).

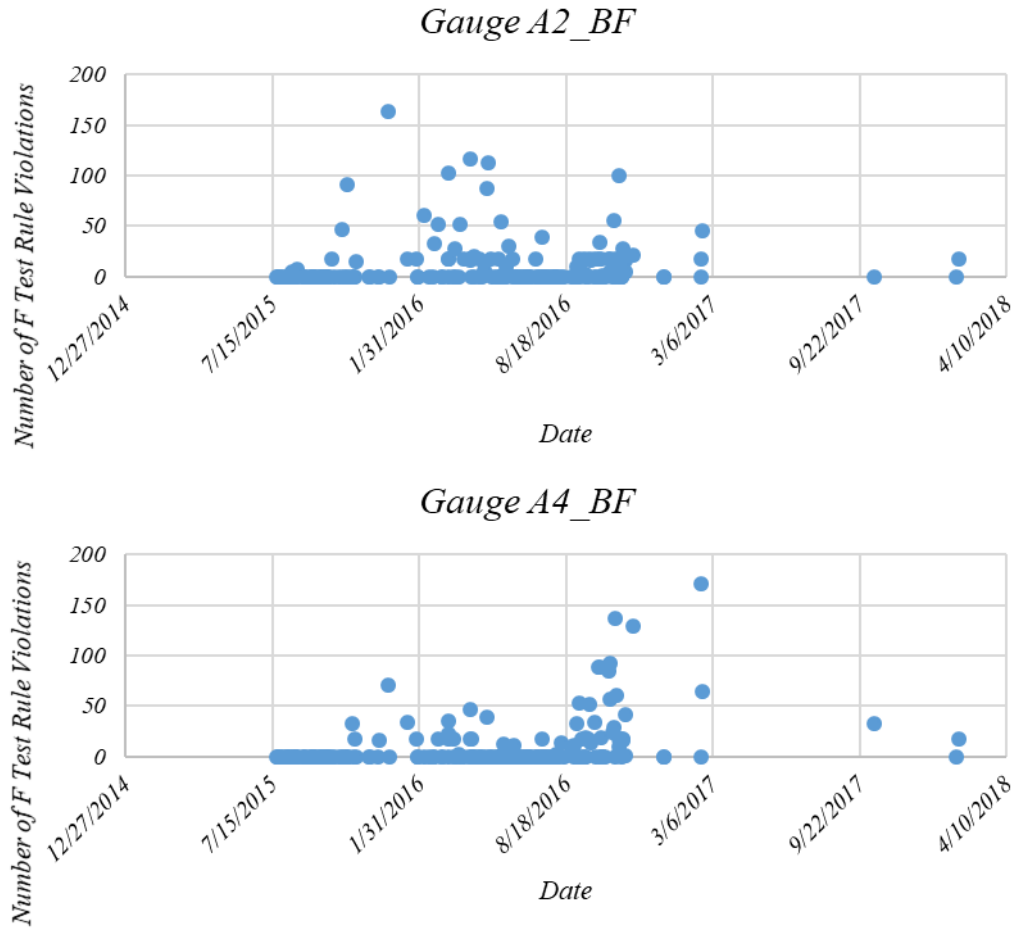
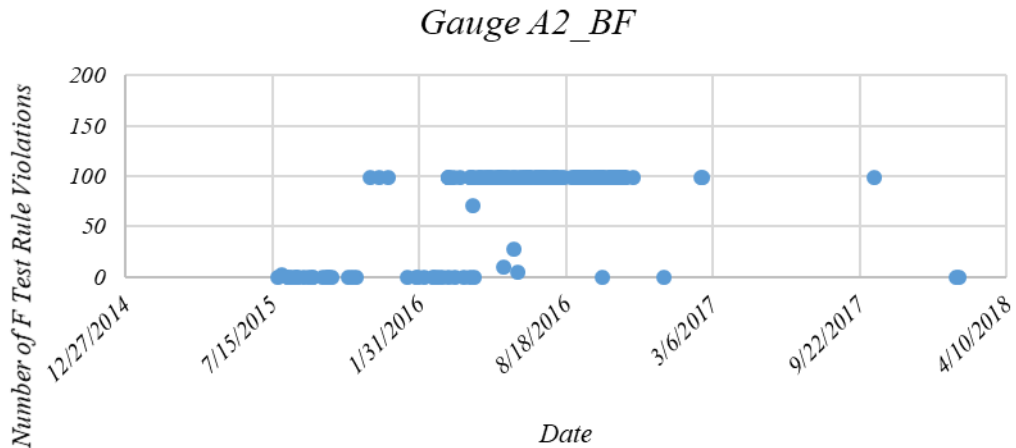


Figure A.8. F-test rule violations, Demonstration Bridge 1



A.2.2. Instrumentation Plan—I-280 Bridge

The SHM system of Demonstration Bridge 2 consists of 40 electrical resistance strain gauges installed on the steel girders as shown in Figure A.11.

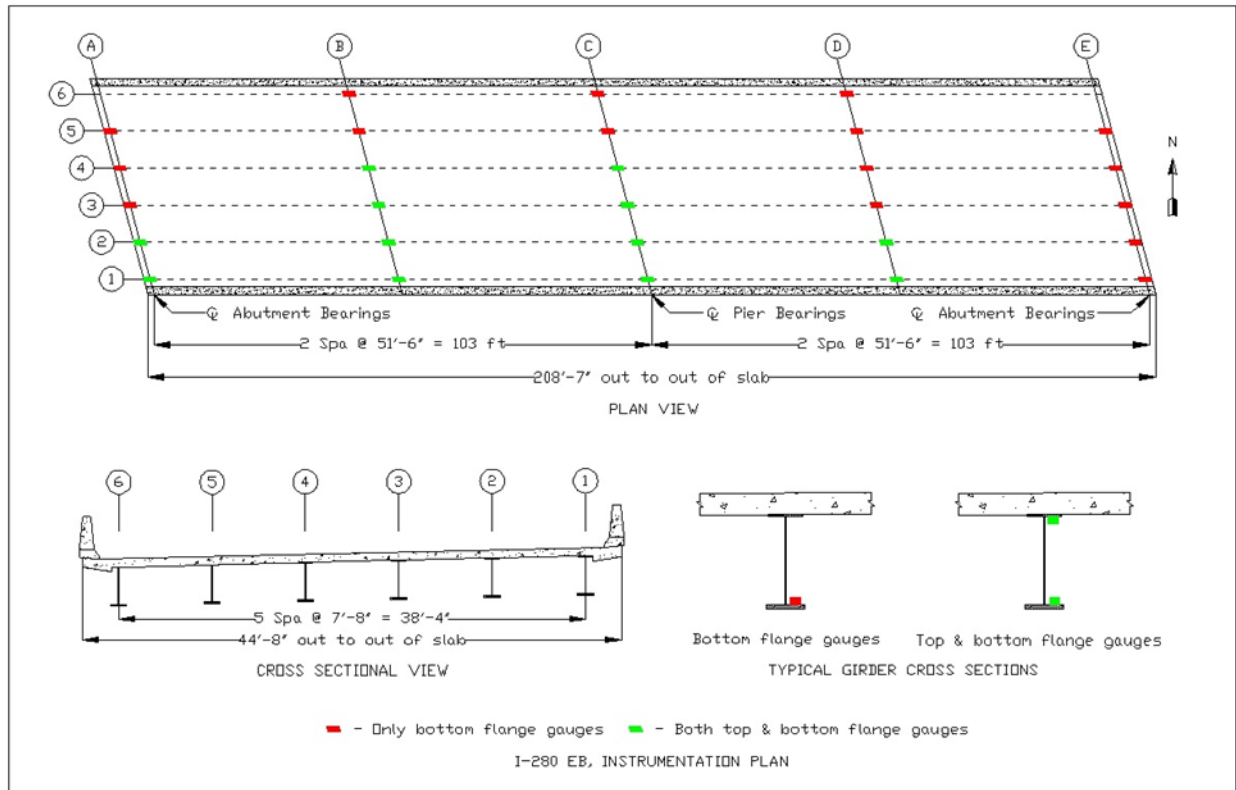


Figure A.11. I-280 bridge, instrumentation plan

In the figure, the red disks represent 16 strain gauges installed only at the top of the bottom flange of the steel girders, whereas, green disks represent total of 24 strain gauges installed on both top of the bottom flange and bottom of the top flange of steel girders. The bridge cross sections with instrumentation were labeled from A to E, and the girder lines were labeled from 1 to 6. The SHM system of I-280 bridge also consists of eight electrical resistance strain gauges installed at the bottom of the concrete deck. These strain gauges are in two rows of four strain gauges in each row and are located perpendicular to the girder lines. The deck strain gauges are used to identify vehicle travel lane, axle number and spacing, and vehicle speed.

A.2.3. Observation Summary of the SHM System

A.2.3.1. Usage

Usage data for Demonstration Bridge 2 are shown in Figure A.12 through Figure A.14 for structural health monitoring data for years 2015, 2016, and 2017.

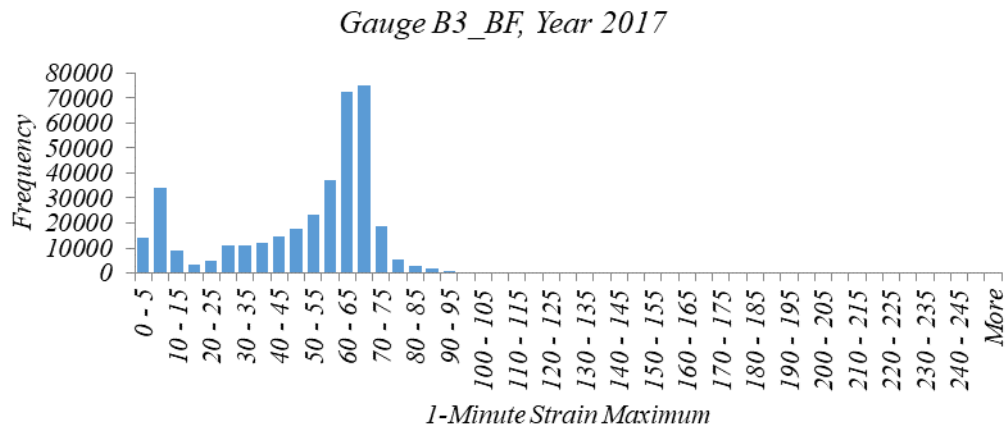
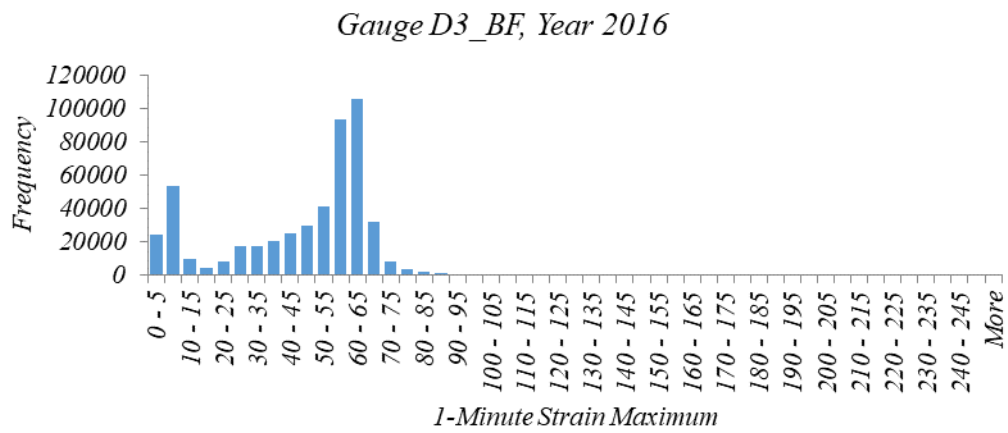
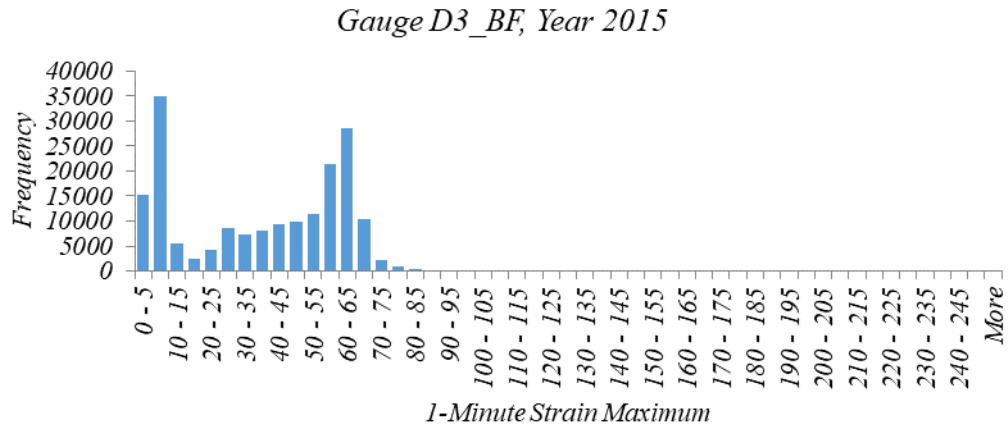


Figure A.12. Demonstration Bridge 2 usage based on maximum strain response

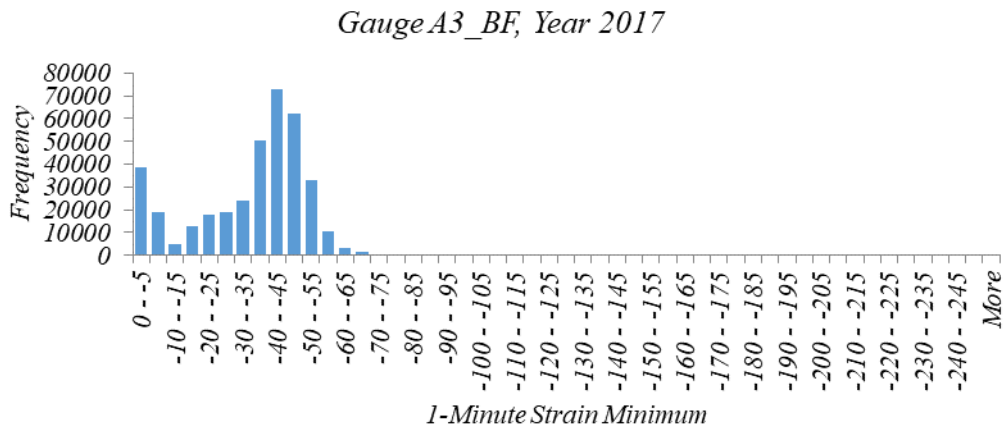
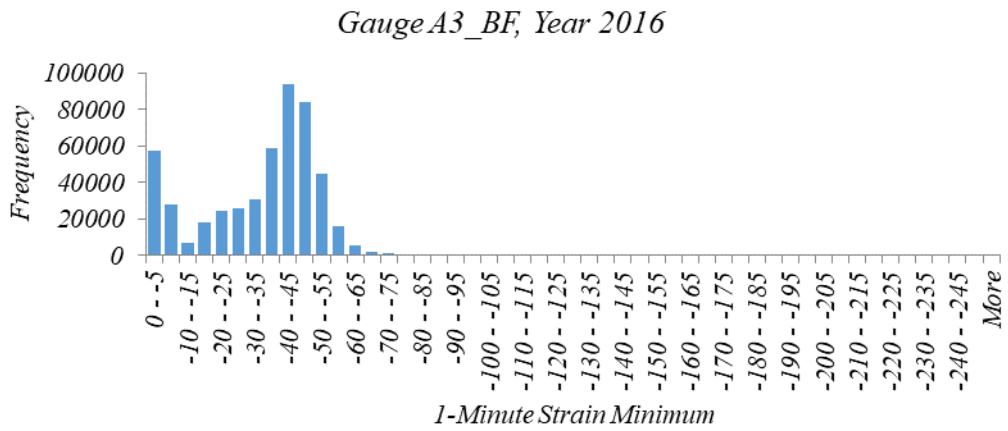
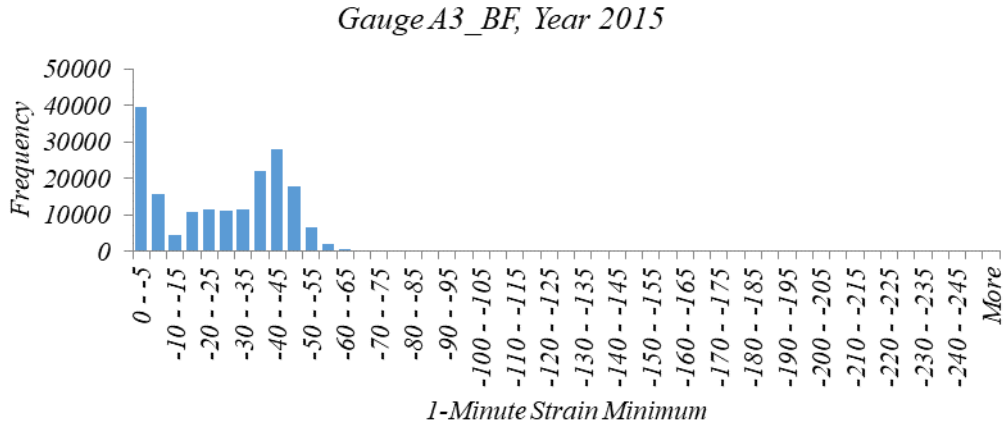


Figure A.13. Demonstration Bridge 2 usage based on minimum strain response

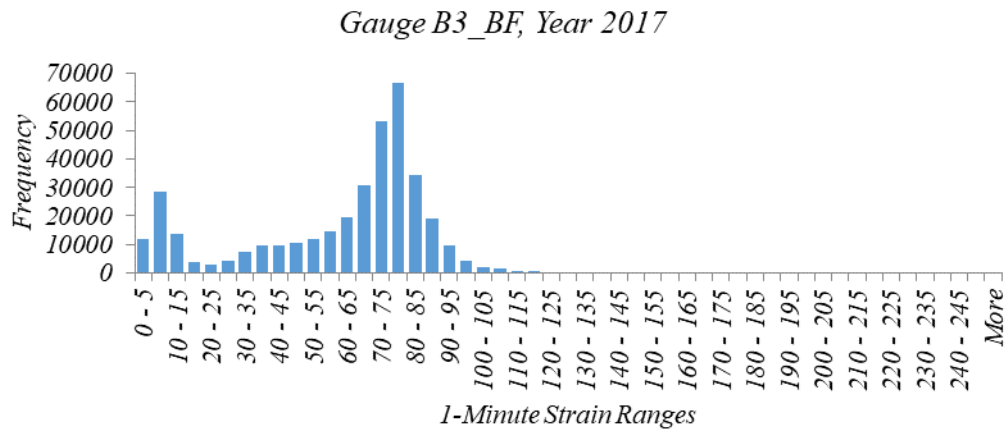
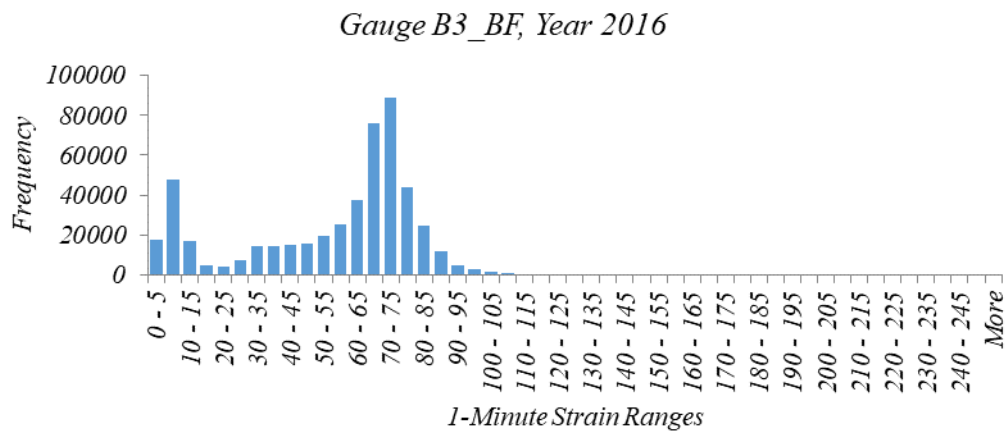
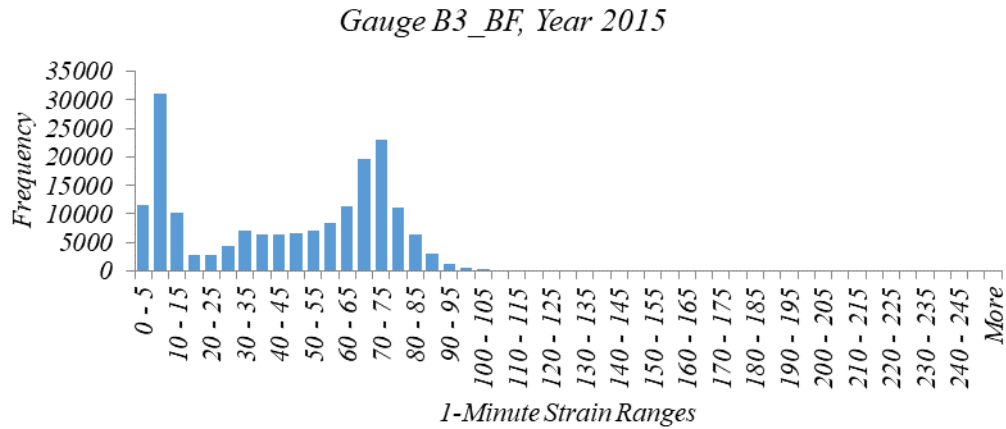


Figure A.14. Demonstration Bridge 2 usage based on strain range response

Throughout the monitoring period, strain gauge D3_BF showed the highest strains, whereas gauge A3_BF showed the minimum strain response. Strain gauge B3_BF showed the maximum strain ranges throughout the monitoring period.

A.2.3.2. Load Rating

The load rating of the bridge was also calculated based on the ambient traffic response and is shown in Figure A.15.

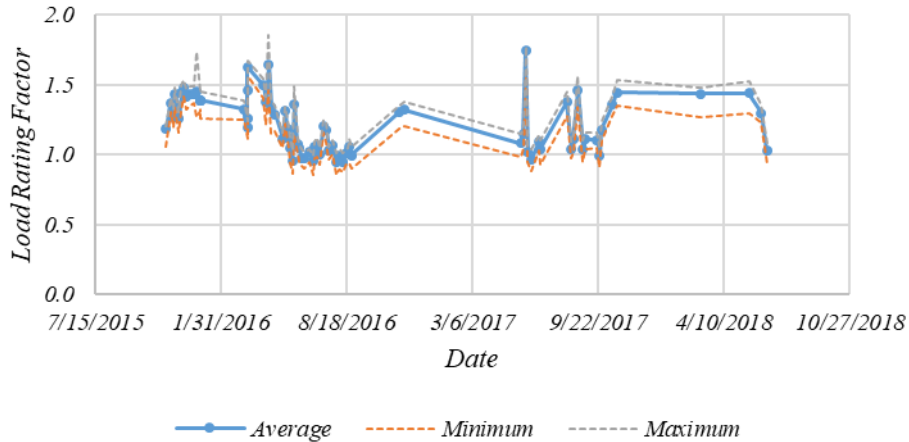


Figure A.15. Demonstration Bridge 2 load rating factor variation

Maximum, minimum, and average load rating factors were calculated. The average load rating of the bridge at the beginning of the monitoring period was 1.18. The average load rating of the bridge at the end of the monitoring period was recorded as 1.02. The average load rating throughout the monitoring period was 1.22, bounded by the average minimum load rating of 0.85 and average maximum load rating of 1.85. Figure A.16 shows the frequency of load rating factor.

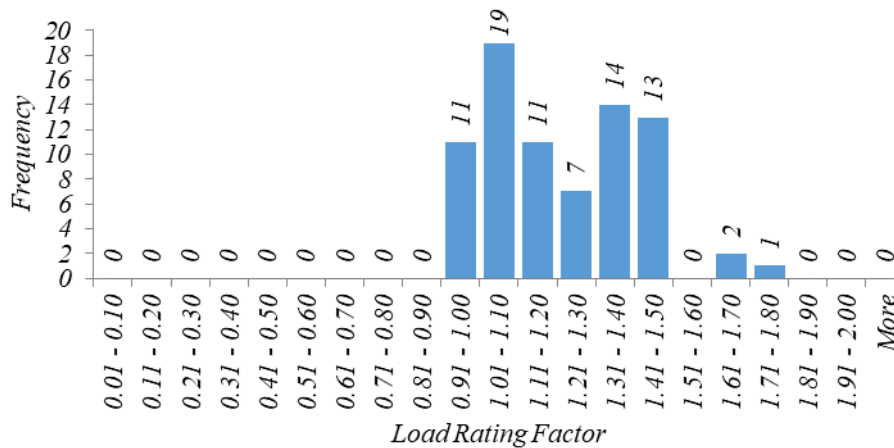


Figure A.16. Demonstration Bridge 2 load rating factor frequency

A.2.3.3. Behavior Change

The current SHM system measures the change in strain response with two primary methods: (1) F-test and (2) strain range method. A significant deviation in strain change will trigger a rule violation of these methods, suggesting that there is a significant structural change in the bridge at a specific location. Gauges B4_TF, C3_BF, and D2_TF of Demonstration Bridge 2 showed the maximum F-test rule violations during the monitoring period (Figure A.17), and gauge C3_BF showed the maximum strain range rule violations during the monitoring period (Figure A.18).

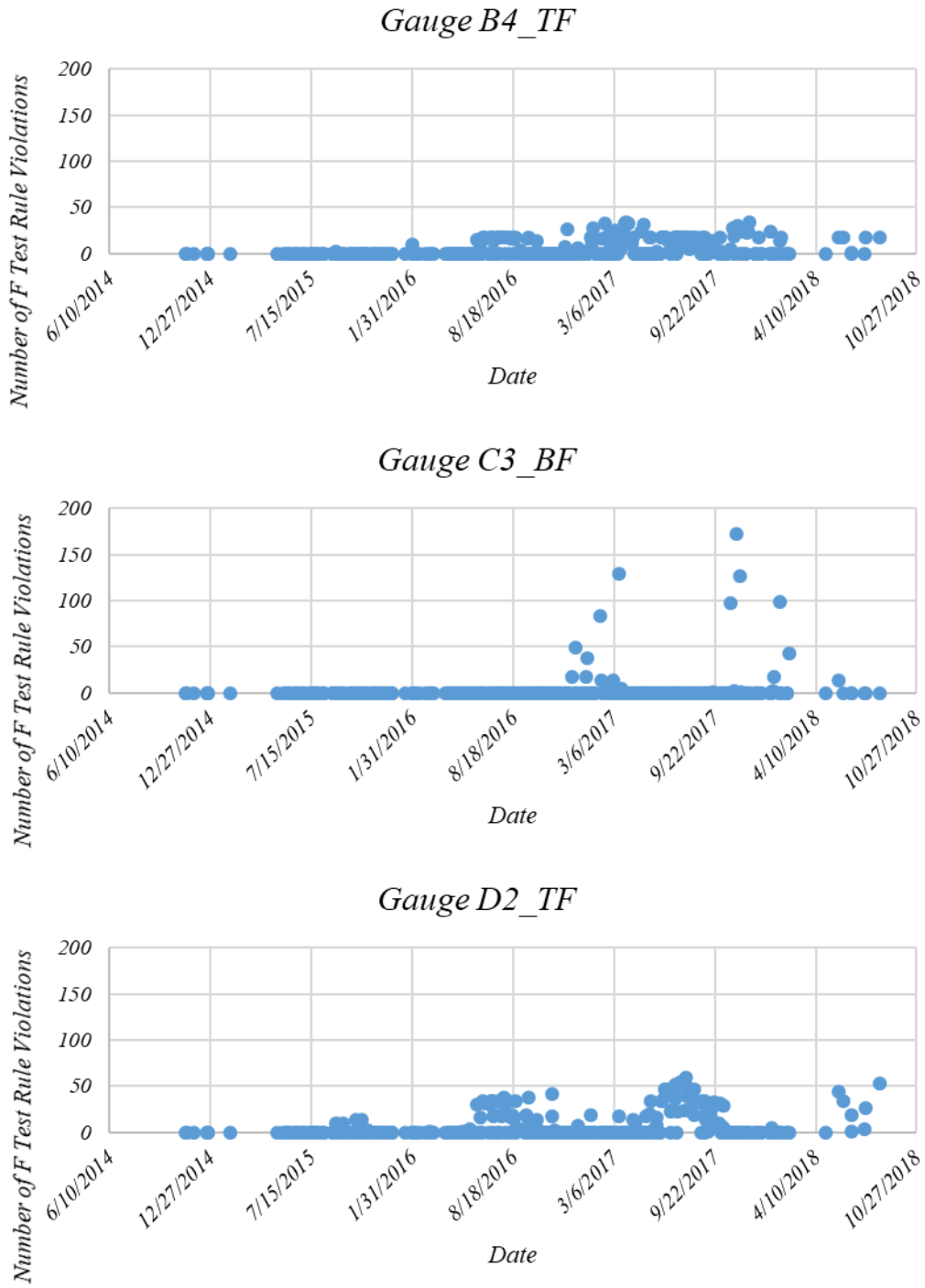


Figure A.17. F-test rule violations, Demonstration Bridge 2

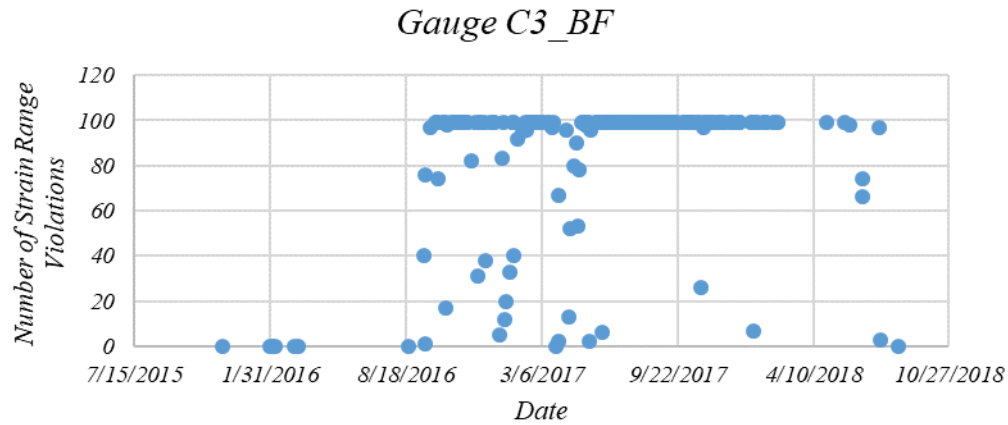


Figure A.18. Strain range rule violations, Demonstration Bridge 2

A.3. Demonstration Bridge 3

A.3.1. Overall Bridge Description

Demonstration Bridge 3, built in 1966, is located on US 151 northbound over County Road H north of Dubuque, Iowa and Kieler, Wisconsin (Figure A.19).



Figure A.19. US 151 bridge

The three span precast, prestressed concrete girder bridge has three simple spans with an overall length of 143 ft out-to-out and a skew of 15 degrees with a curve. The two end spans have lengths of 42 ft, and the center span has length of 59 ft. The cast-in-place reinforced concrete

deck is 7½ in. thick and is supported by four continuous precast, prestressed concrete girders. The spacing between the girders is 12 ft.

A.3.2. Instrumentation Plan—US 151 Bridge

The SHM system of Demonstration Bridge 3 consists of 28 electrical resistance strain gauges installed on the prestressed girders as shown in Figure A.20.

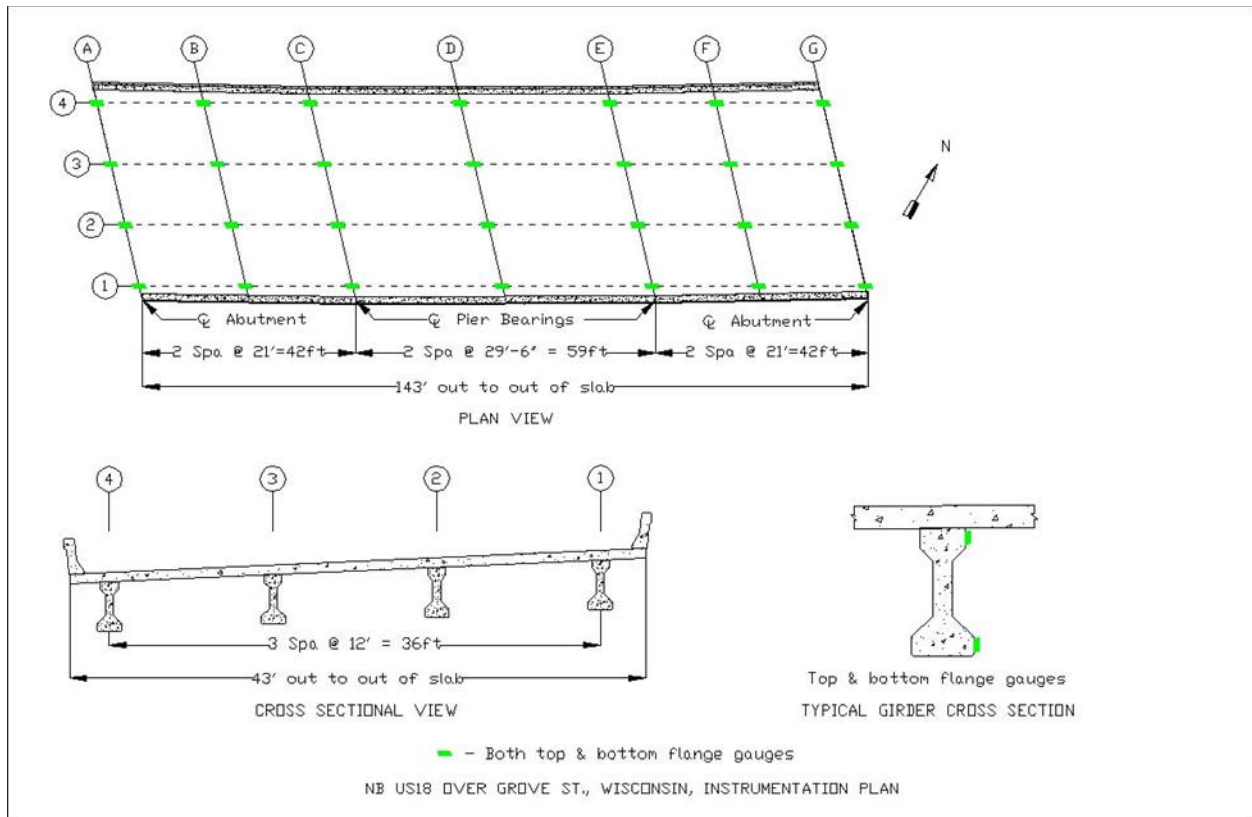


Figure A.20. US 151 bridge, instrumentation plan

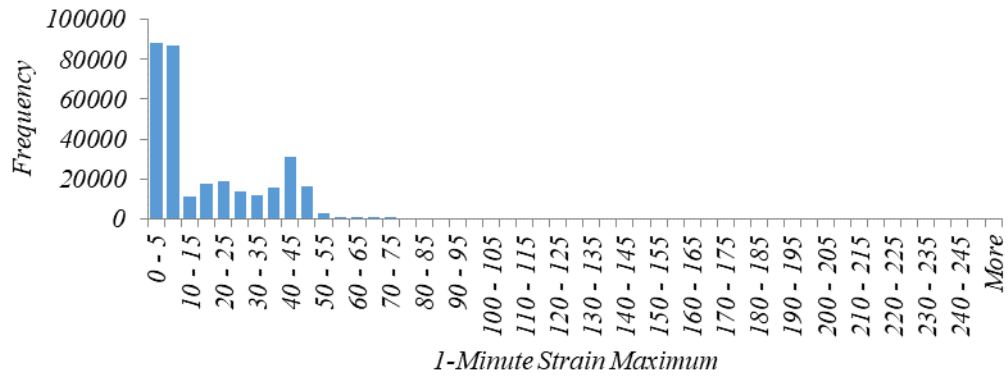
In the figure, the strain gauges were installed on both top and bottom flanges of the girders. Similar strain gauge designations as used for Demonstration Bridges 1 and 2 were used to designate the strain gauges attached to Demonstration Bridge 3. The SHM system of the US 151 bridge consists of eight electrical resistance strain gauges installed at the bottom of the concrete deck. These strain gauges are in two rows of four strain gauges in each row and are located perpendicular to the girder lines. The deck strain gauges are used to identify vehicle travel lane, axle number and spacing, and vehicle speed.

A.3.3. Observation Summary of the SHM System

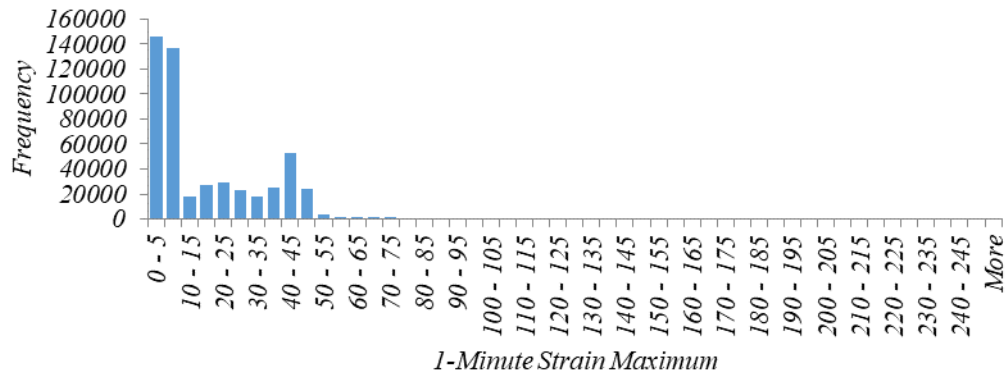
A.3.3.1. Usage

Usage data for Demonstration Bridge 3 are shown in Figure A.21 through Figure A.23 for structural health monitoring data for years 2016, 2017, and 2018.

Gauge D2_BF, Year 2016



Gauge D2_BF, Year 2017



Gauge D2_BF, Year 2018

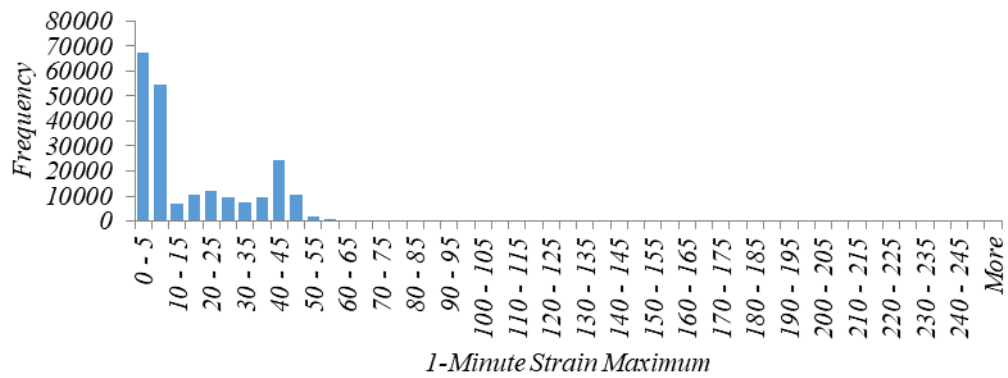
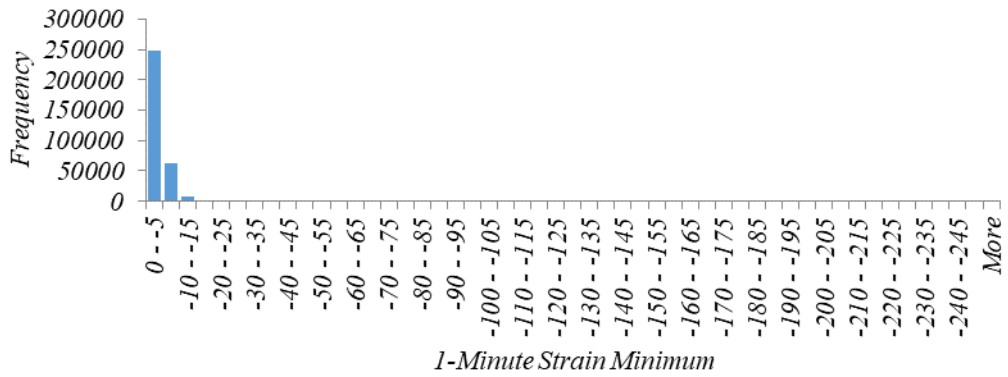
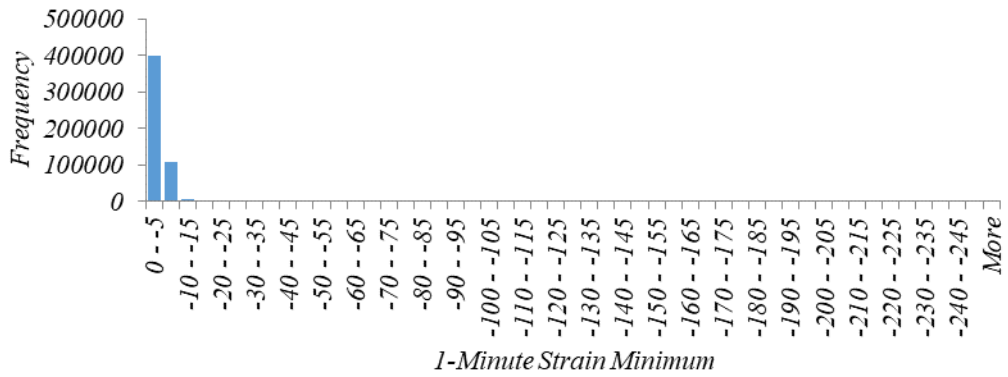


Figure A.21. Demonstration Bridge 3 usage based on maximum strain response

Gauge E3_BF, Year 2016



Gauge E3_BF, Year 2017



Gauge E3_BF, Year 2018

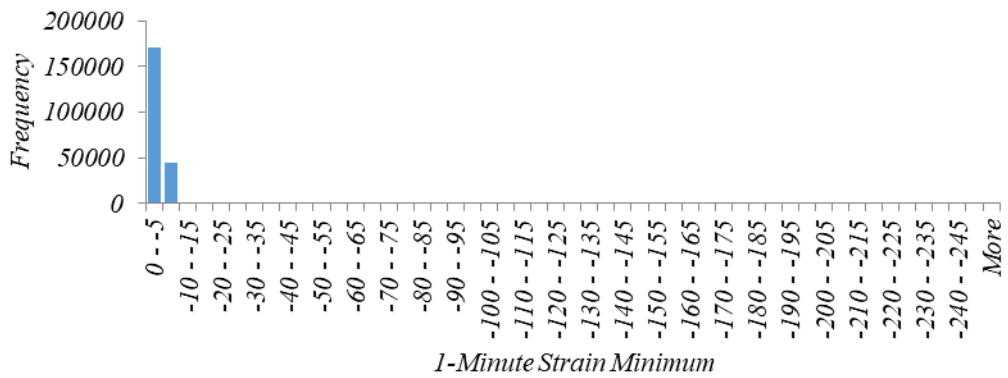
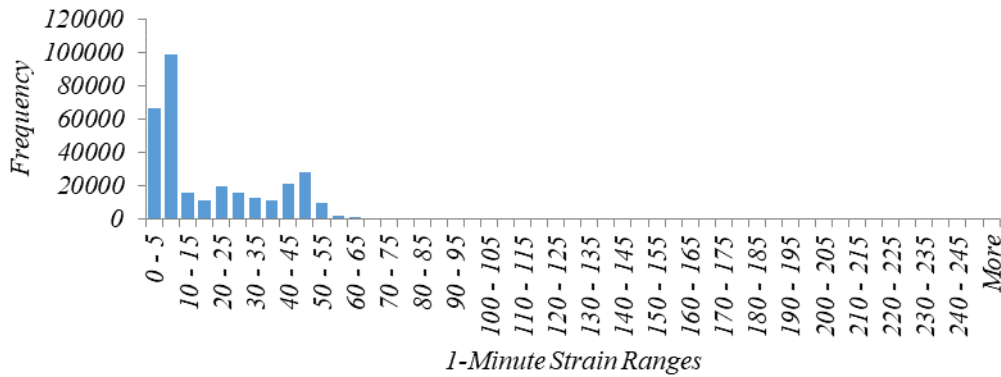
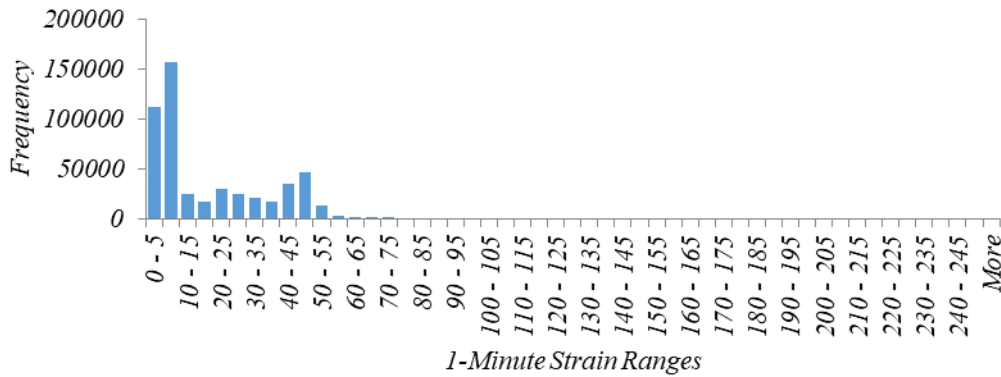


Figure A.22. Demonstration Bridge 3 usage based on minimum strain response

Gauge D2_BF, Year 2016



Gauge D2_BF, Year 2016



Gauge D2_BF, Year 2018

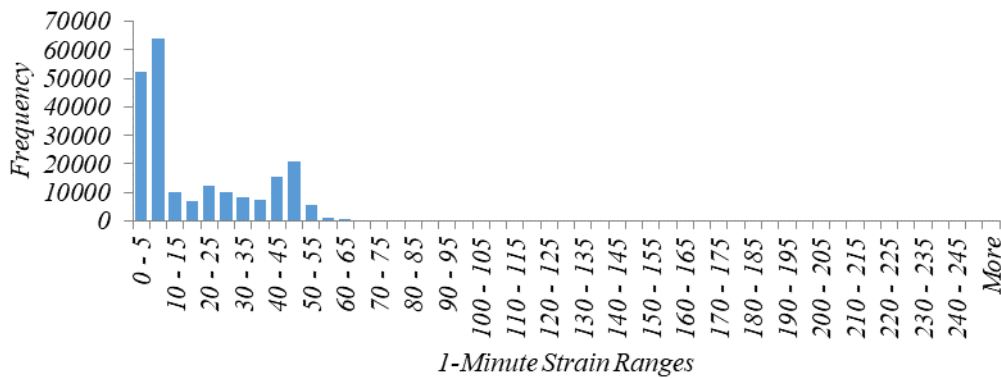


Figure A.23. Demonstration Bridge 3 usage based on strain range response

Throughout the monitoring period strain gauges D2_BF showed the highest strains, whereas gauge E3_BF showed the minimum strain response. Strain gauge D2_BF showed the maximum strain ranges throughout the monitoring period.

A.3.3.2. Load Rating

The load rating of Demonstration Bridge 3 was calculated based on the ambient traffic response and is shown in Figure A.24.

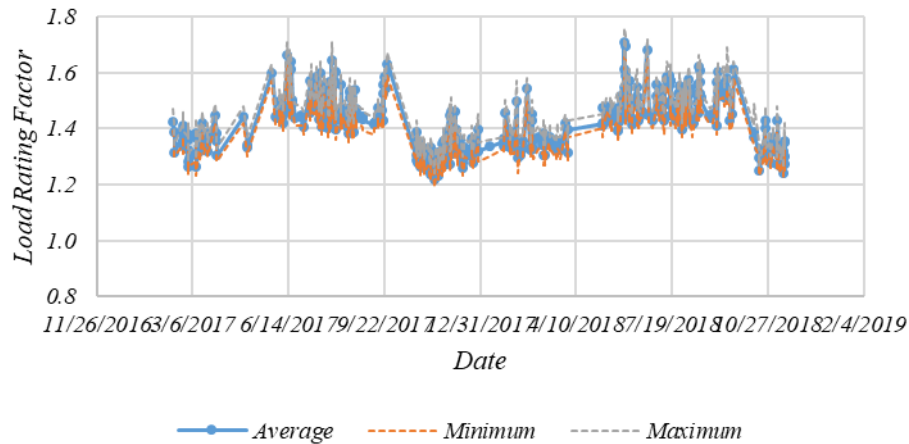


Figure A.24. Demonstration Bridge 3 load rating factor variation

Maximum, minimum, and average load rating factors were calculated. The average load rating of the bridge at the beginning of the monitoring period was 1.43. The average load rating of the bridge at the end of the monitoring period was recorded as 1.27. The average load rating throughout the monitoring period was 1.42, bounded by the average minimum load rating of 1.19 and average maximum load rating of 1.76. Figure A.25 shows the frequency of load rating factor.

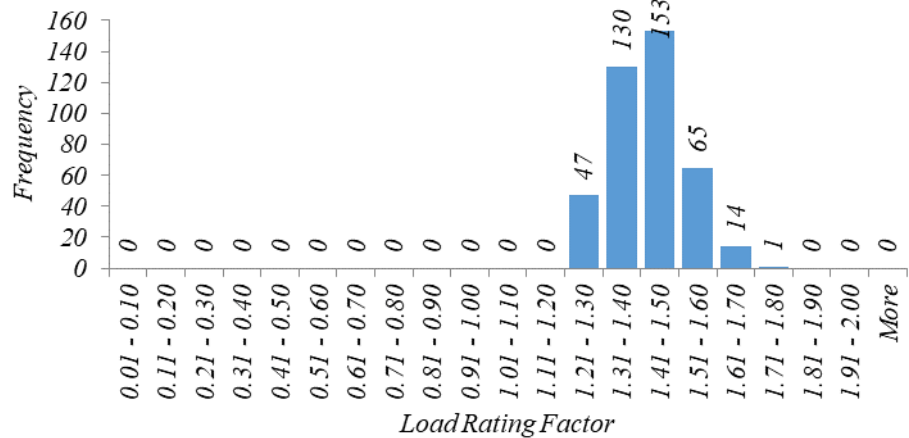


Figure A.25. Demonstration Bridge 3 load rating factor frequency

A.3.3.3. Behavior Change

As explained in the Section A.1.3.3, a significant change in strain change trigger a rule violation of these methods, suggesting that there is a significant structural change in the bridge at a specific location. Figure A.26 shows gauges A3_TF and A4_TF demonstrating the maximum F-test rule violations during the monitoring period.

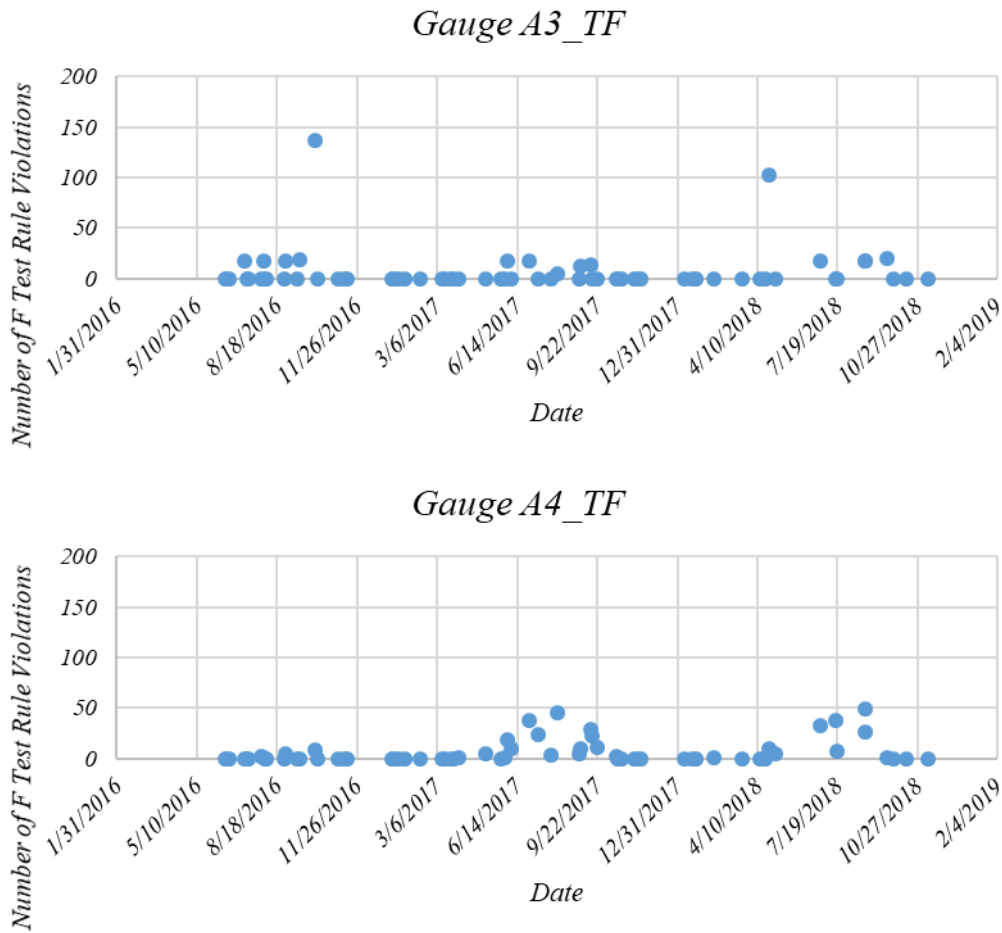


Figure A.26. F-test rule violations, Demonstration Bridge 3

Similarly, Figure A.27 shows results for gauge E3_TF based upon the maximum strain range rule violations during the monitoring period.

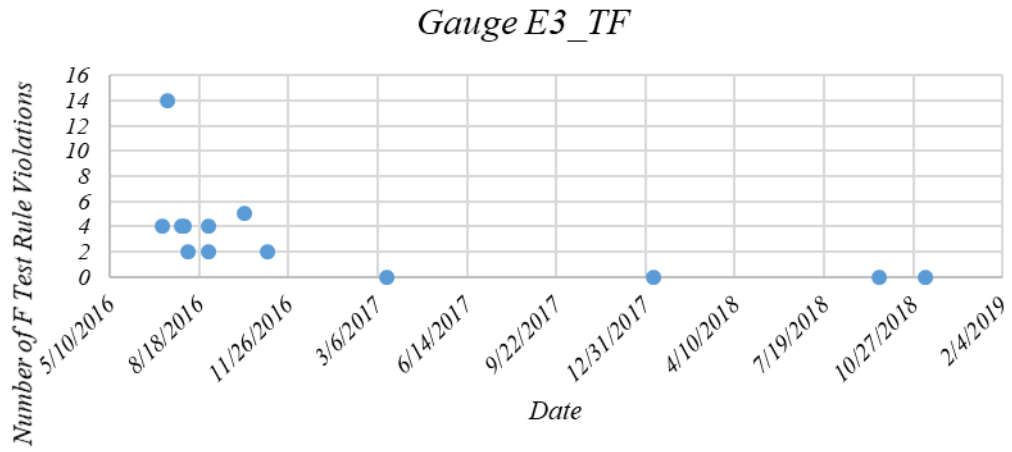


Figure A.27. Strain range rule violations, Demonstration Bridge 3